Dipl. - Ing. Walter Schmidt

Zur Li-Ionendynamik in batteriierelevanten Festkörpern: Li(4)Ti(5)O(12) und Li-haltige Granate

DISSERTATION

zur Erlangung des akademischen Grades

Doktor der technischen Wissenschaften

eingereicht an der

Technischen Universität Graz

Betreuer

Univ. - Prof. Dr. Martin Wilkening

Institut für Chemische Technologie von Materialien
(ICTM)

Graz, Dezember 2015

EIDESSTATTLICHE ERKLÄRUNG

Ich erkläre an Eides statt, dass ich die vorliegende Arbeit selbstständig verfasst, andere als die angegebenen Quellen/Hilfsmittel nicht benutzt, und die den benutzten Quellen wörtlich und inhaltlich entnommenen Stellen als solche kenntlich gemacht habe. Das in TUGRAZonline hochgeladene Textdokument ist mit der vorliegenden Dissertation identisch.

Datum

Unterschrift

Kurzfassung

Batterien spielen in unserer Zeit als mobile und stationäre Energiespeicher mittlerweile eine zentrale und unverzichtbare Rolle. Dabei nimmt die fast allgegenwärtige Li-Ionen-Batterie als eine der bedeutendsten wiederaufladbaren Systeme einen besonderen Platz ein. Aktuelle Forschung widmet sich der Entwicklung immer leistungsfähigerer und insbesondere umweltfreundlicherer Materialien. Als *emerging technology* sind *all-solid-state* Batterien ohne flüssige Bestandteile, d.h. mit festen Li-Elektrolyten, zurzeit ein *hot topic* der *battery community*. Die Li-Ionendynamik stellt eine der Kerneigenschaften dar, die es gilt umfassend zu beschreiben, um bei der Entwicklung neuer Speichersysteme zu helfen.

In dieser Arbeit wurde die Ionendynamik und elektrochemische Leistungsfähigkeit von nano- und mikrokristallinem $Li_{4+x}Ti_5O_{12}$ (LTO), das sich durch sein herausragendes Zyklisierverhalten auszeichnet, mit elektrochemischen Methoden sowie festkörperspektroskopischen Techniken, insbesondere der Li-Kernspinresonanz (engl. *nuclear magnetic resonance*, NMR), untersucht. Im Detail ist der Frage nachgegangen wie sich das Zyklisierverhalten bei mechanischer Behandlung durch Kugelmahlen ändert. An einer Reihe von chemisch interkalierten LTO-Proben ist die Li-Ionendynamik mit ^{7}Li-NMR-Relaxationsmessungen im rotierenden Koordinatensystem eingehend studiert worden. Es zeigte sich, dass bereits bei kleinem x ein erheblicher Anstieg der Li-Diffusivität in dem dann gemischtleitenden LTO erfolgt. Zusammen mit hochauflösende ^{6}Li-NMR-Messungen wurde ein Lithiierungsmechanismus abgeleitet, der bei kleinen Insertionsgraden die Bildung einer *solid solution* beinhaltet.

Der zweite Teil der Dissertationsschrift beschäftigt sich mit der Lithium-Dynamik in schnellen oxidischen Ionenleitern mit Granatstruktur. Li-Linienformmessungen und relaxometrische Untersuchungen an z.B. Al- und Ga-haltigen Granaten geben Aufschluss über Li-Bewegungsprozesse auf unterschiedlichen Längen- und Zeitskalen. Die Ergebnisse werden mit Strukturdaten der Granate verglichen.

Abstract

Batteries, serving as both mobile and stationary energy storage systems, play a central and essential role in our daily life. In particular, the lithium-ion battery represents one of the most important rechargeable device. Current research is devoted to develop more powerful and sustainable materials. Currently, all-solid-state batteries, taking advantage of a solid Li-ion electrolyte, are in the spotlight of battery research. Understanding lithium-ion dynamics in details is necessary to help develop new energy storage systems.

In this work ion dynamics and battery performance of $Li_{4+x}Ti_5O_{12}$ (LTO), characterized by outstanding cyclability, was evaluated by using electrochemical techniques and solid-state nuclear magnetic resonance (NMR), in particular. The thesis is also aimed at answering the question whether mechanical treatment, *i.e.*, high-energy ball milling, influences cyclying performance or induces ageing of LTO-based anodes. The main part focusses on ion dynamics, particularly on the change of Li-diffusivity upon chemical Li insertion into LTO. Surprisingly, ^{7}Li spin-locking NMR relaxometry reveals a steep increase in Li diffusivity at the early stages of lithiation. Together with high-resolution ^{6}Li NMR a refined lithiation mechanism is proposed that includes the formation of a solid solution at the beginning of Li insertion.

The second part of this thesis is devoted to the in-depth study of Li-ion dynamics in garnet-type oxides showing high ionic conductivity. As an example, Li ion diffusion in Al- and Ga-bearing garnets was studied by NMR line shape analyses and relaxometry. The data obtained, which characterizes ionic hopping processes on a different time-scales and length-scales, is compared with structural properties of the garnets studied.

Danksagung

In den letzten Jahren durfte ich in meiner Zeit als Dissertant am Institut für Chemische Technologie von Materialien der TU Graz viele interessante Erfahrungen machen. Viele Menschen traten in mein Leben und hatten Ihren Anteil am Gelingen dieser Arbeit.

Als allererstes bedanke ich mich bei Prof. Dr. Martin Wilkening für die intensive Betreuung der Dissertation und die zahllose Möglichkeiten meine Arbeit durch Poster oder Vorträge im In- oder Ausland zu präsentieren. Die Zusammenarbeit hat mir einen tiefen Einblick in die Abläufe wissenschaftlicher Tätigkeiten an der TU Graz und auf internationaler Ebene gegeben. Dr. Wilkening hat mir eindrucksvoll vorgelebt, wie eine Arbeitsgruppe erfolgreich geleitet werden kann, ohne dass der menschliche Kontakt dabei zu kurz gekommen wäre. Ich bin für die letzten drei Jahre sehr dankbar und überzeugt, dass diese Erfahrungen für meine zukünftige Entwicklung maßgebend sein werden.

Weiters bedanke ich mich bei Prof. Dr. Franz Mautner und Dr. Brigitte Bitschnau für die Durchführung der XRD-Messung und für die Hilfe bei der Interpretation der Daten. Mein besonderer Dank gilt Prof. Dr. Hansjörg Weber für die fruchtbaren Diskussionen rund um NMR-Spektroskopie.

In der Arbeitsgruppe um Prof. Wilkening gab es einige besondere Menschen, die ich auch dankend erwähnen möchte. Dr. Ilie Hanzu hatte immer für mich Zeit, wenn es ein elektrochemisches Problem gab und Dr. Michael Sternad bestach durch wertvolle, hilfreiche Kommentare wenn es um industrielle Batterieanwendungen oder Patente ging. Allen anderen Mitgliedern der Arbeitsgruppe Wilkening danke ich für die gemeinsame Zeit, die wir verbringen konnten, im Speziellen den Kollegen aus dem gemeinsamen Büro. Ich fand es sehr schön, mit Denise Prutsch, Marlena Uitz und Veronika Pregartner so viele gemeinsame fröhliche, traurige, ernste und spaßige Stunden verbracht zu haben.

Einige Kollegen aus dem nicht-wissenschaftlichen Bereich möchte ich noch dankend erwähnen, denn ohne sie wären alle Arbeiten am Insititut nicht so reibungslos abgelaufen. Georg Hirtler, der immer eine helfende Hand hatte, Christina Albering, die die Chemikalienausgabe fest in ihrer Hand hatte, Johann Schlegl für die Unterstützung im grobmechanischen Bereich und Margareta Maierhofer, dass alles immer so strahlend sauber war.

Last but not least danke ich Liane Hochgatterer als Sekretärin des Institutes ganz herzlich für Ihre Geduld mit allen Studenten und für alles was sie für mich getan hat.

Wenn ich an die Menschen abseits der technischen Universität Graz denke, die zum Gelingen dieser Schrift beigetragen haben, nenne ich an erster Stelle meine Frau Martina. Danke für Deine Unterstützung und Deinen immerwährenden Rückhalt in den letzten Jahren! Ich danke des Weiteren noch meiner Familie, in erster Linie meiner Mutter und meiner Schwester für die vielen Ermunterungen.

Meinem Vater, der diesen Tag leider nicht erleben konnte, gilt ebenso mein Dank, ich bin sicher, dass ihn diese Arbeit mit Stolz erfüllt hätte.

Inhalt

1 Einleitung ... 3

2 Batterien ... 5

3 $L_4T_5O_{12}$ und Zellalterung ... 7

4 Festkörperelektrolyte-Granate ... 9

5 Theoretische Grundlagen ... 11

5.1 Grundlagen von Sprungprozessen in Festkörpern ... 11

5.2 Kernspinresonanz ... 11

5.3 Kernspinrelaxation und Diffusion ... 18

6 Experimentelle Details ... 22

6.1 Elektrochemische Untersuchungen ... 22

6.1.1 Probenvorbereitung ... 22

6.1.2 Meßzelle für elektrochemische Untersuchungen ... 23

6.2 Elektrochemische Methoden ... 24

6.2.1 GCPL (galvanostatic cycling with potential limitation) ... 24

6.3 NMR-Relaxometrie und NMR-Spektroskopie: Techniken ... 25

7 Resultate: Publizierte und noch unveröffentlichte Arbeiten ... 27

7.1 Alterungsuntersuchungen an Li-Zellen mit LTO-Anoden ... 27

7.1.1 Nanokristalline Materialien durch Kugelmahlen: Mahlparameter ... 27

7.1.2 Röntgendaten ... 28

7.1.3 Elektrochemische Untersuchungen ... 29

7.2 Li-Diffusion in chemisch interkalierten LTO-Proben ... 32

7.2.1 Small Change - Great Effect: Steep Increase of Li Ion Dynamics in $Li_4Ti_5O_{12}$ at the Early Stages of Chemical Li Insertion ... 35

7.2.2 Discriminating the Mobile Ions from the Immobile Ones in $Li_{4+x}Ti_5O_{12}$: ^6Li NMR Reveals the Li^+ Diffusion Pathway and Proposes a Refined Lithiation Mechanism ... 51

7.2.3 Diffusion-induced ^7Li NMR spin-lattice relaxation of non-lithiated $Li_4Ti_5O_{12}$ and fully lithiated, mixed-conducting $Li_7Ti_5O_{12}$ battery materials ... 69

7.2.4 Einfluß von CO_2 auf die Ionenleitfähigkeit von mikrokristallinem LTO ... 81

7.2.5 Untersuchungen an Nanostrukturierten Proben ... 85

7.3 Zusammenfassung der LTO-NMR-Ergebnisse ... 92

7.4 Granate (LLZO) als Festkörperelektrolyte ... 95

7.4.1 Site Occupation of Ga and Al in Stabilized Cubic $Li_{7-3(x+y)}Ga_xAl_yLa_3Zr_2O_{12}$ Garnets As Deduced from ^{27}Al and ^{71}Ga MAS NMR at Ultrahigh Magnetic Fields 97

7.4.2 Ion Dynamics in Solid Electrolytes: NMR Reveals the Elementary Steps of Li^+ Hopping in the Garnet $Li_{6.5}La_3Zr_{1.75}Mo_{0.25}O_{12}$ 111

7.5 Zusammenfassung: LLZO-basierte Festelektrolyte 127

8 Resümee und Ausblick 128

A. Anhang 130

A.1 Geräte für die NMR-Messungen 130

A.2 Geräte zur Homogenisierung / Nanostrukturierung 131

A.3 Rakelautomat 132

A.4 Gloveboxen 132

A.5 Software 133

A.6 NMR-Pulsfolgen 134

B. Konferenzbeiträge und Publikationen 135

B.1 Posterbeiträge 135

B.2 Vorträge 135

B.3 Publikationen 136

B.4 Eingereichte Manuskripte 136

Literaturverzeichnis 137

1 Einleitung

In unserer modernen Welt würden alle Aktivitäten ohne mobile oder stationäre Energiespeicher wohl ganz anders aussehen oder gar nicht möglich sein. Viele Anwendungen und Erfindungen profitierten von der Möglichkeit, elektrische Energie direkt vor Ort zu speichern. Unsere moderne Welt ist dadurch deutlich mobiler und flexibler geworden.

Schon in der Antike war es möglich, elektrochemische Energiespeichersysteme zu entwickeln, wie die sogenannte Bagdad-Batterie[1] zeigt; ihr genaue Nutzen ist bis heute jedoch unklar. Eine wirkliche Beschleunigung der Entwicklung hat in den späten 1800ern und frühen 1900ern begonnen, als fundierte Forschung mit wissenschaftlicher Methodik an Bedeutung zunahm.

Forschung wurde vorangetrieben, um immer bessere Speicher hervorzubringen.[2] Zunächst wurden einmalig verwendbare Batterien eingesetzt; später haben sich wiederaufladbare Batterien als umweltfreundlicher und effizienter herausgestellt. Parallel dazu haben sich tragbare elektronische Geräte, wie Taschenlampen, Radios etc. entwickelt, deren Realisierung ohne mobile Energiespeichersysteme gar nicht möglich gewesen wären.[3,4] Es war und ist wichtig, die Langlebigkeit, das Energiespeichervermögen und natürlich die Art der Materialien, hinsichtlich Gefährdungspotential und Nachhaltigkeit zu optimieren. Zunächst gab es auf dem Markt Nickel-Cadmium und Nickel-Metallhydrid-Akkumulatoren. Als momentaner Stand der Technik hat sich ein System herauskristallisiert, dass bei geringem Gewicht eine hohe Leistungsdichte und ausreichende Zyklenstabilität vorzuweisen hat: Li-Ionenbatterie.[5,6] Und wiederum hat sich parallel dazu eine ganz neue Generation von tragbaren elektronischen Geräten entwickelt, wobei hier dem Einfallsreichtum kaum Grenzen gesetzt sind. Die Li-Ionenbatterie besitzt im Vergleich zu vielen Systemen eine hohe gravimetrische und volumetrische Energiedichte, was sie dadurch *in puncto* Gewicht und Abmessungen ideal für mobile Applikationen in Werkzeugen oder elektronischen Geräten, wie Laptops oder Mobiltelefone macht. Natürlich macht auch diese Entwicklung nicht vor der Fahrzeugindustrie Halt. Womöglich sind elektrochemische Speichersysteme geeignet, die nahezu ausgereifte Technologie des Verbrennungsmotors zu ergänzen bzw. gegebenenfalls zu ersetzen. Beide Technologien blicken auf eine lange Entwicklungsgeschichte zurück. Im Hinblick auf realisierte elektrochemische Energiespeicher stellt der Tesla Roadstar,[7] ein vollständig elektrifiziertes Fahrzeug, ein gutes Beispiel für diese Entwicklung dar.

In der Stromerzeugung zeichnet sich immer stärker ein Trend zu nachhaltigeren Systemen ab. Energieerzeugung aufgrund fossiler oder nuklearer Rohstoffe hat den Vorteil, dass die Verfügbarkeit des Rohstoffes die einzige Einschränkung für den Betrieb darstellt - bei ausreichendem Vorrat ist ein Betrieb tageszeitunabhängig möglich. Im Gegensatz dazu sind solare Anlagen

oder Windkraftwerke immer von der Verfügbarkeit von Wind oder Sonne abhängig. Dadurch ist die Entwicklung stationärer Energiespeicher von sehr großer Bedeutung, um Produktionsspitzen und -engpässe abfangen zu können und somit den aktuellen Strombedarf sicherzustellen. Auch hier können teilweise die bestehenden physikalischen Energiespeicher noch aushelfen, aber betreffend Wirkungsgrad sind elektrochemische Systeme weitaus besser geeignet. Große stationäre Energiespeicher mit geeigneten elektrochemischen Systemen[8] unweit der unregelmäßig Strom erzeugenden Kraftwerke, wäre ein sinnvoller Ansatz für eine gute zukünftige Energieversorgung.

Li-Ionenbatterien haben sich in vielen Bereichen aufgrund ihrer großen Vorteile durchgesetzt, in manchen Bereichen aber auch mangels Alternativen. Li-basierte Systeme weisen auch Nachteile auf: Da in vielen Fällen umweltgefährdende oder gar giftige Materialien für den Bau verwendet werden, stellen sich für die Sicherheit während des Betriebs und vor allem für das Recycling neue Herausforderungen. Die verwendeten Elektrolyte bestehen meist aus organischen Verbindungen, die oftmals intensiv mit Feuchtigkeit oder Luft reagieren und bei Funkenschlag entzündbar sind.[9]

In vielerlei Hinsicht ist es daher unverzichtbar, neue Materialien zu entwickeln und auf ihre Tauglichkeit in Batteriesystemen hin zu untersuchen. Bereits bekannte Materialien und ihre Eigenschaften eingehender verstehen zu lernen mag bei der Entwicklung von neuen Funktionsmaterialien jedoch ebenso entscheidend sein.

Im Rahmen dieser Arbeit wurde ein in der Batterietechnologie bereits bekanntes Aktivmaterial, nämlich der Spinell $Li_4Ti_5O_{12}$ (LTO),[10] genauer hinsichtlich seiner Li-Ionendynamik und Leistungsfähigkeit als Anodenmaterial in Li-Ionen-Batterien untersucht. Gerade bei bereits kommerziell eingesetzten Materialien sind oft viele grundlegende Zusammenhänge bezüglich lokaler Struktur und elektrochemischen Eigenschaften kaum oder unvollständig verstanden. Diese Lücken zu schließen kann helfen, die Materialien für ihren Einsatz in wiederaufladbaren Batterien zu optimieren.

LTO wird schon seit längerem in der Batterieindustrie als Aktivmaterial eingesetzt, die grundlegenden ionischen Transporteigenschaften und Li-Insertionsmechanismen sind aber noch nicht vollständig aufgeklärt. Basierend auf früheren Ergebnissen an einer lithiierten LTO-Probe konnte in dieser Arbeit z.B. gezeigt werden, wie sich bereits in den frühen Stadien der Li-Insertion in $Li_4Ti_5O_{12}$ die elektronischen und dynamischen Eigenschaften des Materials stark verändern. Die Ionendynamik in einer Serie von $Li_{4+x}Ti_5O_{12}$-Proben ist vor allem mit Hilfe der NMR-

Relaxometrie im sog. rotierenden Koordinatensystem mit *locking*-Feldern im kHz-Bereich untersucht worden. Mittels hochauflösenden ^{6}Li-NMR-Messungen unter schneller Probenrotation konnten erstmals detaillierte Einblicke gewonnen werden, wie sich aus Sicht der NMR-Spektroskopie die Li-Ionen während der Li-Insertion in der Spinellstruktur umlagern. Der Teilbereich $Li_{4+x}Ti_5O_{12}$ wird ergänzt durch elektrochemische Studien zur Zylenfestigkeit von mikro- und nanokristallinem LTO, das durch Hochenergiekugelmahlen hergestellt wurde.

Neben LTO bilden NMR-Untersuchungen zur Li^+-Dynamik in Festelektrolyten ein weiteres Forschungsthema, das in die vorliegende Dissertationsschrift eingeflossen ist. Im Speziellen widmen sich die NMR-Studien der Stoffklasse der Granate. Der Pionierarbeit von Weppner und Thangadurai[11] folgend bilden Li-haltige, oxidische Granate heutzutage vielversprechende Ionenleiter mit Leitfähigkeiten von 10^{-3} S/cm bei Raumtemperatur. NMR-Linienformanalysen und Relaxationsmessungen können dazu beitragen, die Ursachen der hohen Leitfähigkeit zu verstehen.

Bevor im Hauptkapitel 7 die Ergebnisse zu den beiden Teilbereichen präsentiert werden, werden einleitend Begriffe zum Thema Batterien und elektrochemische Untersuchungen sowie der Hauptuntersuchungsmethode, der NMR-Relaxometrie[12], kurz skizziert. Noch nicht publizierte Ergebnisse und weiterführende Arbeiten, z.B. den Einsatz von LTO in Natrium-Ionenbatterien, werden mit bzw. im Anschluss an die publizierten Einheiten dargestellt.

2 Batterien

Grundlage einer jeden Batterie[13,13,14] ist die elektrochemische (Halb-)Zelle, die aus einer Elektrolytlösung und einer Elektrode besteht. Zwischen der Elektrode und dem Elektrolyten stellt sich mit der Zeit ein elektrochemisches Gleichgewicht ein.

Die so genannte galvanische Zelle, benannt nach ihrem Entdecker, Luigi Galvani, besteht aus zwei elektrochemischen Zellen mit unterschiedlichen Elektrodenmaterialien und einer gemeinsamen Elektrolytlösung. Nimmt man beispielsweise unterschiedliche Metalle als Elektroden und verbindet diese mit einem elektrischen Leiter, kommt es im Kontakt zum Elektrolyten an der einen Elektrode zu einer Oxidation (Metall löst sich und geht als Metallionen in Lösung) und an der anderen Elektrode zu einer Reduktion (Metallionen scheiden sich aus der Lösung als Festkörper ab). Wenn dieser Vorgang spontan abläuft, kann aus dem System elektrische Energie gewonnen werden, indem man einen Verbraucher zwischen die Elektroden schaltet. Dabei bestimmt die sogenannte Potentialdifferenz zwischen Anode (negative Elektrode) und Kathode (Positive Elektrode) die effektive Spannung die die Batterie zur Verfügung stellen kann. Laut

der elektrochemischen Spannungsreihe weisen alle Materialien je nach ihren Eigenschaften ein unterschiedlich hohes Redoxpotential auf. Wenn man zwei Materialien mit unterschiedlich hohem Redoxpotential kombiniert, kann man dem System aufgrund der entstandenen Spannungsdifferenz Energie entziehen und durch Laden wieder zuführen. Primärzellen sind nach dem Entladen nicht mehr wieder aufladbar und müssen entsorgt werden, während sekundäre Batterien durch das Anlegen eines Gleichstromes wieder aufladbar sind.

Thema der vorliegenden Schrift sind Materialien, die in Li-Ionen-Batterien[15,16] eingesetzt werden können. Während des Ladens nimmt die Anode Li-Ionen und die zugehörigen Elektronen auf - in den konventionellen Fällen dienen Insertionselektroden als Wirt für die Li-Ionen.[17] Schichtförmig aufgebaute Materialien, wie z.B. Graphit[17] auf der Anodenseite, bieten sich dazu sehr gut an, während auf der Kathodenseite gerne, oftmals auch schichtstrukturierte, Metalloxide[18] verwendet werden. Die dazu nötige elektrische Energie muss der Batterie extern zur Verfügung gestellt werden. Während des Entladevorganges diffundieren die Li-Ionen durch den elektronisch isolierend wirkenden Elektrolyten und lagern sich in der Kathode wieder ein. Die Elektronen bewegen sich parallel durch die Stromableiter durch den Verbraucher. Kathode und Anode müssen für diese Prozesse eine hohe Reversibilität mitbringen, nur so kann eine hohe Zyklenstabilität gewährleistet werden.

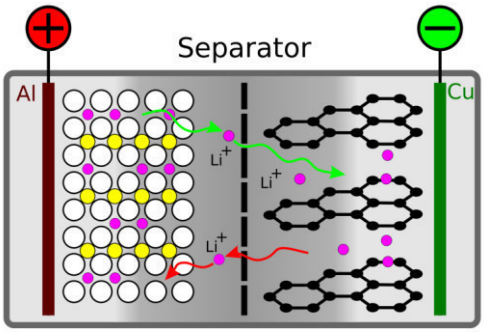

Abbildung 1: Schema einer Batterie mit Graphit als Anodenmaterial. Die Stromableiter bestehen aus Al und Cu. Ein Separator getränkt mit flüssigem Elektrolyten trennt beide Halbzellen voneinander.

Die Materialien, die sich aktiv an der Insertion von Ionen beteiligen, nennt man Aktivmaterialien. Auf diese Materialien beziehen sich Kenngrößen, wie beispielsweise die spezifische Kapazität. Ein zugefügter Binder verklebt das meist pulverförmige Aktivmaterial mit sich selbst und der Elektrode, während bei der Anodenseite oft auch Leitruß beigemengt wird, um die elektronische Leitfähigkeit zu erhöhen. Da sich diese Stoffe nicht an den Batterieprozessen beteiligen, wird versucht, diese Beimengungen weitestgehend zu reduzieren.

Elektrolyte besitzen die wichtige Aufgabe, die Kathode und die Anode so zu verbinden, dass ein möglichst ungestörter Ionentransport möglich ist. Hingegen muss der Elektrolyt als elektronischer Isolator wirken, um einen elektrischen Kurzschluss der Batterie zu verhindern. Organische Verbindungen mit Li-ionenhaltigen Salzen bieten sich hierbei gut an. Als Nachteile sind die Entflammbarkeit und die moderate elektrochemische Stabilität gegenüber den Elektroden zu erwähnen. Der Separator liegt ebenfalls zwischen Anode und Kathode uns sorgt für eine definierte räumliche Trennung von Kathode und Anode. In der Praxis werden Batterien während des Produktionsprozesses stark komprimiert, der Separator verhindert einen Kontakt der Elektroden. Freilich muss er durchgängig sein für den Elektrolyten, damit der Ionentransport ungestört von statten gehen kann. Abbildung 1 zeigt den schematischen Aufbau einer Batterie und die Wanderungsrichtung der Li-Ionen beim Laden (grün) und Entladen (rot) durch den Elektrolyten und den strichliert angedeuteten Separator.

3 $L_4T_5O_{12}$ und Zellalterung

$Li_4Ti_5O_{12}$ kristallisiert in der Spinellstruktur[10,19] und folgt dabei der kristallographischen Besetzung $[Li]_{8a}[Ti_{5/3}Li_{1/3}]_{16d}[O_4]_{32e}$ (Fd3m). Diese Struktur wurde mehrfach durch Röntgen[20,21,22]-und Neutronenbeugungsexperimente[23,24] bestätigt. Man sieht, dass anfangs die Positionen 8a und 16d mit Lithium in einem Verhältnis von 3:1 besetzt sind, während Ti die restlichen Oktaederplätze auf 16d ausfüllt. Für einen dreidimensionalen Li-Migrationspfad würden die Positionen 16c (neben vorhandenen Fehlstellen) zur Verfügung stehen[25].

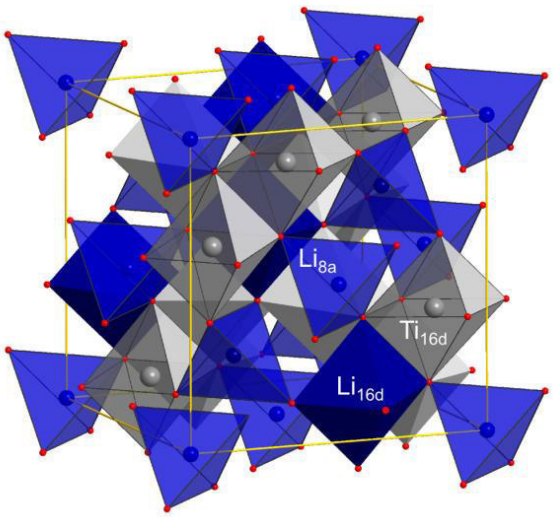

Abbildung 2: Spinell-Struktur von LTO, die Li-Ionen besetzen die Oktaederplätze 8a und 16d. Die freien 16c-Plätze verbinden je zwei Oktaederplätze durch gemeinsame Flächen.

LTO zeigt eine sehr geringe elektronische Leitfähigkeit, darum ist es für den Einsatz in einer Li Ionenbatterie nötig, analog zu Graphitelektroden, Leitruß beizumengen.

Bei einer insertierten (also geladenen) Graphitelektrode liegt das Potential nahe bei 0 gegen Li-Metall was zu einer raschen SEI[26,27,28] (*solid electrolyte interface*)-Bildung führt. Diese Schicht entsteht aus mit der Elektrodenoberfläche abreagierten Bestandteilen des Elektrolyten und überzieht die komplette Elektrode beim ersten Ladeschritt. Mit jedem Ladeschritt wächst die Schicht und die Zelle droht auszutrocknen. Die SEI weist je nach Elektrolyt eine andere Zusammensetzung auf und kann den Ionentransport stark beeinflussen. Wenn eine Graphitelektrode sich durch das Laden und Entladen ausdehnt und wieder zusammenzieht, kann immer wieder frische Elektrodenoberfläche mit dem Elektrolyten in Kontakt kommen oder die SEI abbröckeln. Diese Art Nachschub an frischer Elektrodenoberfläche beschleunigt dabei die Alterung.[29] Des Weiteren ist bei einer Graphitelektrode der irreversible Verlust an Aktivmaterial durch Volumenänderung[30] eine der Hauptursachen für Zellalterung und irreversiblem Kapazitätsverlust.

Im Gegensatz dazu liegt das Potential der geladenen LTO-Anode bei 1,55 V[31] gegen Li. Für die meisten Elektrolytsalze und organischen Elektrolytbestandteile liegt dieser Potentialbereich innerhalb ihres Stabilitätsfensters, das bedeutet die Bildung einer SEI findet bei einer LTO Anode weitestgehend nicht statt, somit fällt ein Bestandteil der Zellalterung an der Anodenseite weg.

Die kristalline Struktur von LTO erlaubt als dreidimensionaler Ionenleiter eine gut ablaufende Insertion und De-Insertion der Li Ionen,[32,33] während des Ladens wird zunehmend anstatt der Position 8a die Position 16c besetzt und die Struktur wechselt vom Spinell- zum Steinsalz-Typ. Die topotaktische Reaktion verläuft dabei ohne nennenswerte Volumenänderung - man bezeichnet LTO daher auch als *zero strain material*. Im vollgeladenen Zustand ist die Position 8a unbesetzt und sämtliche Li-Ionen sitzen auf den Positionen 16d und 16c. Die zugehörige Struktur lautet dann in der Wyckoff-Notation: $[Li_2]_{16c}[Ti_{5/3}Li_{1/3}]_{16d}[O_4]_{32e}$.

Dadurch fällt ein weiterer Alterungsmechanismus weg, nämlich das Loslösen von Aktivmaterial von der Elektrode durch den mechanischen Stress während des Zyklisierens. Besonders positiv wirkt sich das auf das Schnell-Ladeverhalten einer Zelle aus.

Ein weiteres Problem kann bei herkömmlichen Anodenmaterialien eine mangelnde thermische Stabilität darstellen. Bei LTO ist der Sauerstoff stark in die Struktur eingebunden, somit ist dieses Material bei einem Kurzschluss oder bei einem Tief- oder Überladen weniger reaktiv. Bei

tiefen Temperaturen neigen Graphitelektroden zum so genannten *plating*,[34] d.h. elementares Lithium scheidet sich über der Graphitelektrode ab; das führt zu einem schnelleren Altern und kann auch Kurzschlüsse oder Brände verursachen. LTO-Batterien lassen sich problemlos bis -40 °C betreiben. Titanate sind ungiftig und zeigen eine gute Umweltverträglichkeit.

Als Nachteil und wohl einer der Hauptgründe, warum sich LTO noch nicht stärker als Anodenmaterial durchgesetzt hat, liegt in der Tatsache, dass es eine relativ geringe Energiedichte von 70-90 Wh/kg aufweist. Dennoch bietet Toshiba bereits Titanatbatterien unter dem Handelsnamen Super Charge Ion Battery (SCiB)[35] für Elektroräder an. Für weitere mobile Applikationen scheint die geringe Energiedichte ein Hemmschuh zu sein, dennoch sollten die anderen genannten Vorteile insbesondere bei der Verwendung als stationärer Energiespeicher nicht außer Acht gelassen werden.

4 Festkörperelektrolyte-Granate

Um viele der oben genannten Nachteile von flüssigen Elektrolyten weitestgehend auszuschalten, hat die Entwicklung von Festkörperbatterien in den letzten Jahren zugenommen. Gerade in der Fahrzeugindustrie bieten Festkörperbatterien[36] nicht von der Hand zu weisende Vorteile: Sie erlauben, z. B. durch den Einsatz von Li-Metall als Anode, in der Regel eine weitaus höhere Energiedichte und ermöglichen im Gegensatz zu flüssigen Systemen ein kompakteres, platzsparendes Design. Durch eine Verschachtelung von Kathode, Anode und Festkörperelektrolyt[37] kann das so genannte Totvolumen auf ein Minimum beschränkt und der Energieinhalt der Batterie erhöht werden.

Die anorganischen Festkörperelektrolyte, an die natürlich *in puncto* elektronischer und ionischer Leitfähigkeit[38,39] dieselben Anforderungen gestellt werden wie an ihre flüssigen Pendants, weisen bezüglich thermischer Stabilität und mangelnder Brennbarkeit große Vorteile auf. Die strukturbedingten Unterschiede und die erhöhte Stabilität gegen hohe und tiefe Elektrodenpotentiale sorgen für eine erhöhte Zyklenstabilität. Bei den ersten Dünnschichtbatterien wurde LiPON (Lithium-Phosphor-Oxynitrid)[40,41,42] als Festkörperelektrolyt verwendet; diese Batterien zeichneten sich durch eine sehr hohe Zyklenfestigkeit aus: LiPON-Batterien können einige hunderte Male geladen und entladen werden. Ein weiteres Plus ist, dass ein fester Elektrolyt viele Nebenreaktionen einer Batterie, die eine Flüssigkeit naturgemäß ermöglicht, unterbindet. Solvatationsprozesse oder Bewegungsprozesse von anderen Ionen außer Lithium werden weitestgehend ausgeschaltet, d.h. die Li^+-Überführungszahl ist praktisch eins. Nicht vorhandenes Dendritenwachstum und eine erhöhte Stabilität gegen metallisches Lithium zeichnen Festkörperelektrolyte weiter aus. Ein weiterer Vorteil ist, das ausgeprägte Elastizitätsmodul, das den Einsatz in

Dünnschichtmikrobatterien erlaubt. Dennoch bleiben einige Punkte eine große Herausforderung für die Forschung. Bei sulfidischen[43] Festkörperelektrolyten zeigte sich, dass der Li-Ionen-Übergangswiderstand zwischen Kathode und Elektrolyt oft relativ hoch ist. In der Arbeit von Murugan *et al.*[11] wurden erstmals oxidische Lithiumionenleiter mit definierter Granatstruktur ($Li_5La_3M_2O_{12}$) vorgestellt, die eine sehr hohe Li-Ionenleitfähigkeit aufwiesen und elektrochemisch stabil waren.

Granate sind zudem chemisch äußerst stabil und kristallisieren vorwiegend in einer tetragonalen[44] Struktur. Vor allem weisen sie gegen ein Potential bis 5 V[45] eine ausgezeichnete Stabilität auf, was sie zu idealen Kandidaten für Festkörperelektrolyte macht. Eine ausreichende elektrochemische Stabilität kann ein Schwachpunkt von anorganischen Sulfiden darstellen, die z.B. reduzierbare Metallionen enthalten. Die Li-Ionenleitfähigkeit der heute bekannten Granate liegt in der Größenordnung von 10^{-4} S cm^{-1} bei Raumtemperatur, wobei eine Verbesserung durch gezieltes Dotieren mit beispielsweise Al oder Ga erreichbar ist. Dadurch wird zugleich die kubische[46] Phase, die erst bei höheren Temperaturen stabil ist, schon bei Raumtemperatur stabilisiert und zusätzliche Lithiumdiffusionswege[47] erschlossen. Je nach Reinheit des Granates liegt diese Umwandlungstemperatur zwischen 400 und 600 K[48,49]. Welche Diffusionswege möglich sind und die die genauen Wanderungsmechanismen aussehen, ist Thema aktueller Forschung.

5 Theoretische Grundlagen

5.1 Grundlagen von Sprungprozessen in Festkörpern

Jedes Teilchen befindet sich oberhalb des absoluten Nullpunktes in Bewegung. Die Gitterstruktur eines Festkörpers bietet je nach Kristallstruktur unterschiedliche Plätze, die die Atome einnehmen können. Die Kristallgitterplätze stellen stabile Senken der Potentiallandschaft dar, jedes Teilchen ist darin eingebettet; in Abhängigkeit der Temperatur zeigen die Teilchen thermisch angeregte Selbst-Diffusionsprozesse. Fehlstellen im Kristallgitter sind entscheidend und notwendig für den Teilchentransport; sie bestimmen seine grundlegenden Transporteigenschaften.

Protonen und Neutronen besitzen als Atomkernbestandteile einen Drehimpuls, der sich ausgleicht, wenn die Anzahl dieser Teilchen im Kern gerade ist. Bei einer ungeraden Anzahl resultiert ein effektiver Drehimpuls, der aufgrund der elektrischen Ladung der Teilchen ein magnetisches Moment erzeugt. Dieses Moment kann nun mit externen und internen Feldern interagieren und gemessen werden.

Diffusionsprozesse der spintragenden Teilchen führen zu elektrischen und magnetischen Feldfluktuationen, die mit Hilfe von Kernspinresonanzmethoden erfasst werden können. Somit sind indirekt Selbstdiffusionsprozesse spektroskopisch messbar. Die Bewegungsprozesse können dabei lokaler Natur oder langreichweitiger Natur sein.

5.2 Kernspinresonanz

Basis für die Messung der Kernspinresonanz ist der so genannte ZEEMANN Effekt. Er beschreibt die Aufspaltung der Kernniveaus in einem Magnetfeld. Besitzt der Kern einen Kernspin $\vec{I}$ so ergibt sich

$$\vec{\mu} = \gamma \cdot \vec{I} \qquad (5.1)$$

Das gyromagnetische Verhältnis γ besitzt einen für jedes Nuclid charakteristischen Wert und kann wie folgt ersetzt werden:

$$\gamma = \frac{1}{\hbar} \cdot g_K \cdot \vec{\mu}_N \qquad (5.2)$$

g_K ist dabei der dimensionslose g-Faktor und $\hbar$ die Planckkonstante mit einem Wert von 1,054 · 10^{-34} Js. In $\vec{\mu}_N$ fliesst die Protonenmasse m_p ein wie folgende Gleichung zeigt:

$$\mu_N = \frac{e \cdot \hbar}{2 \cdot m_P} = 5.05 \cdot 10^{-27}\ \mathrm{A\,m^2} \qquad (5.3)$$

γ und g_K sind dabei charakteristische Konstanten, die für jedes Elementarteilchen Gültigkeit haben. Für Protonen beispielsweise gilt: $g_K = 5.59$ und $\gamma = 2.675 \cdot 10^8$ 1/Ts

Wenn man den Betrag von I betrachtet, schreibt die Quantenmechanik vor, dass ausschließlich diskrete Werte verwendet werden dürfen

$$|I| = \sqrt{I \cdot (I+1) \cdot \hbar} \qquad (5.4)$$

während die magnetische Quantenzahl die Werte -*I*, - (*I* - 1),……., (*I* - 1), *I* durchläuft.

Durch das Anlegen eines äußeren Magnetfeldes B_0 spalten die einst energetisch entarteten Niveaus in unterschiedliche Zustände auf. Für die zugehörigen Energieeigenwerte ergibt sich:

$$E = -\mu \cdot B_0 = -\mu_z \cdot B_0 = -\gamma \cdot \hbar \cdot m_I \cdot B_0 \qquad (5.5)$$

Für beispielsweise einen 3/2 Kern führt dies zu einer Aufspaltung in 4 energetisch verschiedene Niveaus $(2 \cdot I + 1)$.

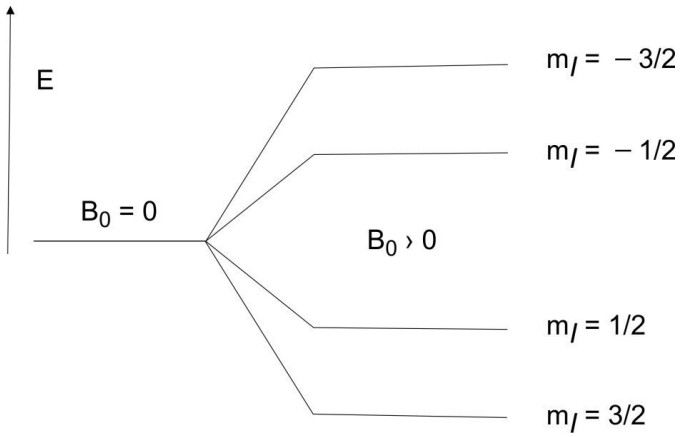

Abbildung 3: ZEEMANN-Niveaus im äußeren Magnetfeld eines Spin-3/2 Kerns; m_I repräsentiert die magnetische Quantenzahl

Betrachtet man das thermische Gleichgewicht, so sind alle Niveaus gemäß der BOLZMANN-Verteilung besetzt, folgende Übergänge sind erlaubt:

$$\Delta E = -\gamma \cdot \hbar \cdot B_0 \qquad (5.6)$$

Durch Einstrahlen von elektromagnetischer Strahlung (ν) kann man Übergänge zwischen den energetischen Niveaus anregen.

$$E_\gamma = \hbar \cdot \omega_L = \gamma \cdot \hbar \cdot B_0 \qquad (5.7)$$

Schließlich ergibt sich daraus die zentrale Resonanzbedingung

$$\omega_L = \gamma \cdot B_0 \qquad (5.8)$$

In vektorieller Schreibweise gilt: $\vec{\omega}_L = -\gamma \cdot \vec{B}_0$. In einer Probe mit dem Volumen *V* ergibt sich somit für die Gesamtmagnetisierung *M* aus der Summe aller magnetischen Momente

$$M = \frac{1}{V} \sum_i \mu_i \qquad (5.9)$$

Dabei gilt (*N* ist die Teilchendichte der Kernspins)

$$M_z = N \cdot \langle \mu_z \rangle = N \cdot \gamma \cdot \langle I_z \rangle \qquad (5.10)$$

Die BOLZMANN-Verteilung gilt im thermischen Gleichgewicht und lässt sich wie folgt darstellen

$$M_0 = N \cdot \frac{\gamma^2 \cdot \hbar^2 \cdot I\,(I+1)}{3\,k_B T} \cdot B_0 \qquad (5.11)$$

Wird nun, wie oben beschrieben, das thermische Gleichgewicht durch einen Radiofrequenz-Puls aus dem Gleichgewicht gebracht, benötigt es eine charakteristische Zeitkonstante T_1, um wieder in den ursprünglichen Gleichgewichtszustand zurück zu kehren.

$$\frac{dM_z}{dt} = \frac{M_0 - M_z}{T_1} \qquad (5.12)$$

Diese Zeitkonstante wird als longitudinale oder Spin-Gitter-Relaxationszeit bezeichnet. Das Spinsystem gibt während dieser Zeitspanne die aufgenommene Energie wieder an die Umgebung ab. Wurde die Magnetisierung zu Beginn komplett zerstört ($M_z = 0$ bei $t = 0$) gilt folgender Zusammenhang

$$M_z(t) = M_0 \cdot \left(1 - e^{\left(-\frac{t}{T_1}\right)}\right) \qquad (5.13)$$

Bei vorgegebener Temperatur und spezifisch für das vorhandene Magnetfeld kann die für jede Probe charakteristische Relaxationszeit T_1 im Bereich von einigen Mikrosekunden bis sogar zu Stunden liegen.

Im einfachen Vektormodell stellt sich der Fall wie folgt dar: Das magnetische Moment μ, das nicht parallel zum äußeren Magnetfeld B_0 ausgerichtet ist, ist einem Drehmoment τ ausgesetzt. Alle drei Größen sind Vektoren:

$$\vec{\tau} = \vec{\mu} \times \vec{B}_0 \qquad (5.14)$$

Durch Verwendung von Gleichung (5.1) und dem Differential *dI/dt* für τ erhält man die klassische Kreiselgleichung für das magnetische Moment μ

$$\vec{\mu} \times \vec{B}_0 = \frac{1}{\gamma} \cdot \frac{d\vec{\mu}}{dt} \qquad (5.15)$$

Diese Kreiselbewegung, auch Präzision genannt, findet um die z-Achse mit der so genannten Lamorfrequenz ω_L statt.

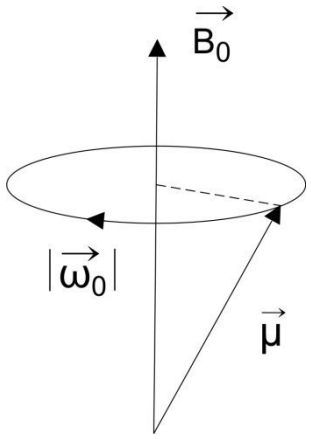

Abbildung 4 : Präzisionsbewegung des magnetischen Momentes μ im Magnetfeld B_0. Der Kreisfrequenzvektor ist nicht dargestellt.

Folgende Formel, s.o., ist dabei gültig

$$\vec{\omega}_L = -\gamma \cdot \vec{B}_0 \qquad (5.16)$$

Diese Frequenz entspricht genau der Resonanzfrequenz aus Gleichung 5.8. Für das Gesamtmoment *M* gilt analog:

$$\frac{d\vec{M}}{dt} = \gamma \cdot (\vec{M} \times \vec{B}_0) \qquad (5.17)$$

Dadurch erhält man die klassische Bewegungsgleichung für die Gesamtmagnetisierung *M*, wobei die Magnetisierung M_0 der longitudinalen Komponente im thermischen Gleichgewicht in z-Richtung entspricht und die transversalen Kompontenten null sind.

Betrachtet man die transversalen Komponenten der Magnetisierung M_x und M_y, wenn die einzelnen magnetischen Momente in Phase präzedieren, also nicht verteilt sind. In diesem Fall kann die Relaxationszeit T_2 ganz analog ermittelt werden.

$$\frac{dM_x}{dt} = \frac{-M_x}{T_2} \qquad \frac{dM_y}{dt} = \frac{-M_y}{T_2} \tag{5.18}$$

Diese transversale Relaxationszeit T_2 wird auch Spin-Spin-Relaxationszeit genannt. Wenn nun Spins miteinander wechselwirken, werden die magnetischen Momente M_x und M_y dadurch beeinflusst. Je mehr Wechselwirkungen stattfinden, desto weniger Spins bleiben in Phase und sie beginnen mit einer leicht unterschiedlichen Frequenz zu präzedieren.

Die BLOCH-Gleichungen für das statische Laborkoordinatensystem beschreiben die zeitliche Änderung der Komponenten von *M:*

$$\frac{dM_z}{dt} = \gamma \cdot (M \times B_0)_z + \frac{M_0 - M_z}{T_1}$$

$$\frac{dM_x}{dt} = \gamma \cdot (M \times B_0)_x - \frac{M_z}{T_2} \tag{5.19}$$

$$\frac{dM_y}{dt} = \gamma \cdot (M \times B_0)_y - \frac{M_z}{T_2}$$

Während eines NMR-Experimentes wirkt neben dem B_0-Feld auch das Wechselfeld B_1:

$$2\,B_1 \cdot \cos(\omega t) \cdot e_x \tag{5.20}$$

Das Radiofeld wird in der Messpraxis durch eine Spule erzeugt, in der sich die Probe befindet und z.B. in einem Winkel von 90° zum bestehenden B_0-Feld orientiert ist. Formal lässt sich B_1 in zwei gegensinnig rotierende Felder $B_1(\cos(\omega t)e_x + \sin(\omega t)e_y$ und $B_1(\cos(\omega t)e_x - \sin(\omega t)e_y$ auflösen. Der zweite Term rotiert gegenläufig zur präzedierenden Magnetisierung und kann somit in den weiteren Berechnungen gemäß der *rotating wave approximation* vernachlässigt werden.

Um nun die Bewegung der Magnetisierung in diesem sich bewegenden Magnetfeld effizient erfassen zu können, bietet sich die Betrachtung mithilfe eines rotierenden Koordinatensystems an. Das Koordinatensystem rotiert mit derselben Frequenz wie das rotierende Magnetfeld B_1 um das statische Magnetfeld B_0. Aus dieser Betrachtung heraus ergibt sich ein zusätzlicher Term, der sog. Coriolis-Term, in Gleichung 5.17.

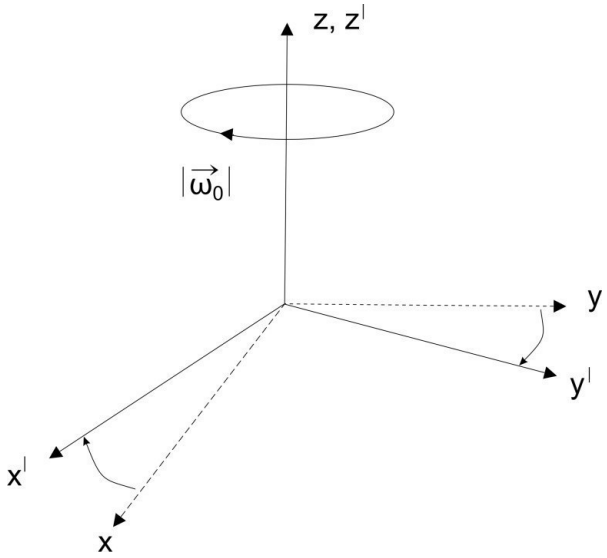

Abbildung 5: Das statische Laborkoordinatensystem und das rotierende Koordinatensystem. Der Übergang in das rotierende System ermöglicht es, die Präzessionsbewegung von *M* zu eliminieren.

$$\left(\frac{dM_y}{dt}\right)_{rot} = \gamma \cdot (M \times B) - (\omega \times B) = \gamma \cdot \left(M \times \left(B + \frac{\omega}{\gamma}\right)\right) = \gamma \cdot (M \times B_{eff}) \quad (5.21)$$

Im rotierenden Koordinatensystem wirkt ein effektives Magnetfeld B_{eff}:

$$B_{eff} = B + \frac{\omega}{\gamma} \quad (5.22)$$

Wenn man nun die Einheitsvektoren im rotierenden Koordinatensystem mit $e_{x'}$ und e_z bezeichnet, ergibt sich

$$B_{eff} = (B_0 - B_\omega) \cdot e_z + B_1 \cdot e_{x'} \quad \text{mit} \quad B_\omega = -\frac{\omega}{\gamma} \quad (5.23)$$

Durch die Rotation des Koordinatensystems wird das Magnetfeld zeitunabhängig und die Magnetisierung präzediert um B_{eff}. Für den Resonanzfall, $\omega = \omega_0$, verschwindet die z-Komponente von B_{eff} und es gilt $B_{\text{eff}} = B_1$. Somit präzediert die Magnetisierung um B_1 mit der Winkelgeschwindigkeit $\Omega = \gamma \cdot B_1$. Durch die Addition von Präzision und Rotation entsteht im Laborkoordinatensystem eine Spiralbewegung der Magnetisierung.

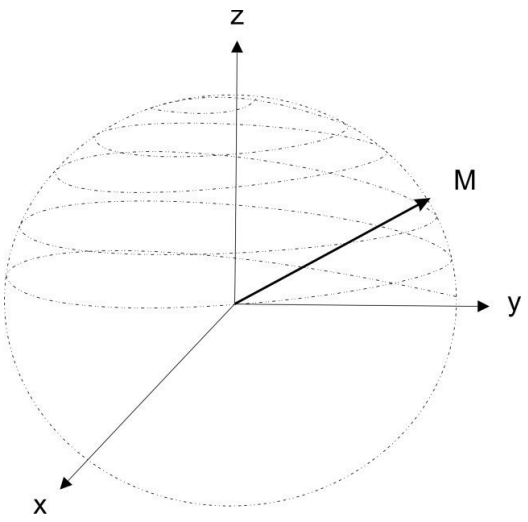

Abbildung 6: Spiralbewegung der Magnetisierung *M* im statischen Koordinatensystem

Der Zeitraum, wie lange das Hochfrequenzfeld B_1 aktiv ist, kann nun dazu benutzt werden, entlang der z-Achse die Magnetisierung zu variieren. Wenn man den Hochfrequenzpuls so einstellt, dass die Magnetisierung die (x,y)-Ebene erreicht hat, spricht man von einem 90° Puls ($\pi/2$-Puls). Die Magnetisierung der Spins präzediert dann um B_0 und induziert in der Spule ein Spannungssignal. Das Signal nimmt mit der Zeit ab, da die transversale Komponente der Magnetisierung der Spin-Spin-Wechselwirkung unterliegt. Die einzelnen magnetischen Momente geraten außer Phase, da sie z.B. lokal unterschiedlichen Magnetfeldern ausgesetzt sind. Beruht dies ausschließlich auf Spin-Spin Wechselwirkungen, so zerfällt die transversale Magnetisierung mit der Rate $1/T_2$. Meist führen Inhomogenitäten des äußeren Magnetfeldes zu einem noch schnelleren Zerfall als durch T_2 festgelegt.

In der Praxis kann man die longitudinale Relaxationszeit T_1 über die Pulsfolge π - τ - $\pi/2$ messen. Diese so genannte Inversion-Recovery-Pulsfolge bewirkt zuerst ein Kippen der Magnetisierung um 180° in z-Richtung. Daraufhin wächst die Magnetisierung wieder exponentiell entlang der z-Achse an und durchläuft einen Nulldurchgang. Aufgrund der Tatsache, dass die Empfängerspule lediglich die transversale Komponente der Magnetisierung detektieren kann, wird die Magnetisierung nach einer Wartezeit τ um 90° in die (x,y)-Ebene gekippt. Dort findet wieder Präzession statt und ein transientes Spannungssignal wird in der Empfängerspule induziert. Die Amplitude ist der Magnetisierung vor dem Puls proportional. Durch mehrmaliges Wiederholen dieses Experimentes mit unterschiedlichen Wartezeiten τ ist es möglich, durch ein Auftragen des FIDs gegen die Wartezeit, die Relaxationszeit T_1 zu ermitteln. Um die nötige Genauigkeit zu erreichen, ist es nötig zu warten, bis die Endmagnetisierung wieder erreicht wurde - dies lässt

sich durch eine ausreichende Wartezeit realisieren - mindestens 5 × T_1 im Falle einfach-exponentiellem Wiederaufbau.

Die Spin-Gitter Relaxationszeit T_1 gibt Auskunft über Spin-Bewegungsprozesse. Sie ist insbesondere sensitiv auf Bewegungsprozesse mit Korrelationsraten im MHz-Bereich. Um Sprungprozesse im niederen Frequenzbereich zu erfassen (z.B. im Hz- bis kHz-Bereich) wäre eine Messung bei einer geringen Magnetfeldstärke nötig, was das Signal-Rausch-Verhältnis jedoch empfindlich beeinflussen würde. Alternativ kann die Spin-Gitter-Relaxationszeit im rotierenden Koordinatensystem erfasst werden, sog. $T_{1\rho}$-NMR-Messungen ermöglichen es *per se* langsame Diffusionsprozesse zu erfassen.

Bei $T_{1\rho}$-Messungen wird die Magnetisierung im rotierenden Koordinatensystem durch einen 90° Puls in die (*x,y*)-Ebene gekippt und dort mit einem Radiopuls (B_1) fixiert. B_1 nimmt formal die gleiche Rolle wie B_0 bei den T_1-Experimenten ein. Die transversale Magnetisierung passt sich dem neuen, geringen Feld B_1 an und verringert sich mit der *locking*-Zeit, d.h. der Einstrahlzeit von B_1. Die Magnetisierung nimmt ausschließlich in der (*x,y*)-Ebene ab.

Analog zu den T_1-Experimenten wird die Restmagnetisierung nach unterschiedlichen Wartezeiten t_{SL} bei bestehendem *locking*-Puls detektiert. Durch Auftragen der FID-Flächen oder Amplituden gegen die Wartezeit kann $T_{1\rho}$ aus dem transienten Signal ermittelt werden.

$$M_{xy}(t_{SL}) = M_{xy}(0) \cdot e^{\left(-\frac{t_{SL}}{T_1\rho}\right)} \qquad (5.24)$$

t_{SL} entspricht dabei der Dauer des Radiofrequenzpulses.

5.3 Kernspinrelaxation und Diffusion

Ein Kernspin ist dem externen Magnetfeld unterworfen und wird durch dieses beeinflusst. Zudem „spürt“ der Kern *interne* Felder, wenn das Atom oder das Ion durch den Festkörper diffundiert. Die magnetischen und elektrischen Feldfluktuationen induzieren die transversale und longitudinale Relaxation. Sie dienen als Maß für die dynamischen Parameter eines sich bewegenden Teilchens.

Die spektrale Dichtefunktion *J* der Feldfluktuationen am Ort des Kernspins beschreibt die Spin-Gitter-Relaxation

$$T_1^{-1} \sim J(\omega_L) \qquad (5.25)$$

Dabei entspricht $J(\omega)$ der Fourier-Transformierten der Korrelationsfunktion $G(t)$. Das einfachste Modell von BLOMBERGEN, PURCELL, und POUND (BPP-Modell)[50] geht von einem exponentiellen Verhalten der Korrelationsfunktion aus,

$$G(t) = G(0) \cdot \exp\left(-\frac{|t|}{\tau_c}\right) \qquad (5.26)$$

Dabei wird der Parameter τ_c Korrelationszeit genannt. Für die spektrale Dichtefunktion ergibt sich dann

$$J(\omega) = G(0) \cdot \frac{2\tau_c}{1+(\omega\tau_c)^2} \qquad (5.27)$$

Trägt man die Dichtefunktion bei unterschiedlichen Temperaturen gegen die Lamorfrequenz auf, erkennt man, dass J ein Maximum bei festem ω_0 durchlaufen kann. Aufgrund von Gl. (5.27) gilt dies auch für die Spin-Gitter-Relaxationsrate.

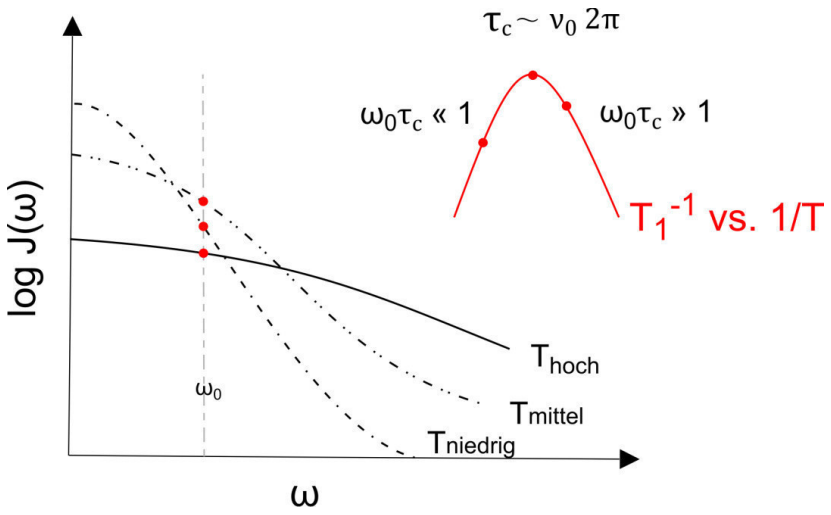

Abbildung 7: Verlauf der spektralen Dichtefunktion *J* als Funktion der Kreisfrequenz. Die zugehörige Spin-Gitter-Relaxationsrate durchläuft bei geeigneten Larmorfrequenzen ein Maximum, wenn die Rate gegen die inverse Temperatur aufgetragen wird.

Dabei zeigt die Korrelationszeit τ_c, die mit der mittleren Verweilzeit des Kernes verknüpft ist, im einfachsten Falle ARRHENIUS-Verhalten bezüglich der Temperatur.

$$\tau_c = \tau_{c0} \cdot \exp\left(\frac{E_A}{k_B T}\right) \qquad (5.28)$$

E_A ist dabei die Aktivierungsenergie des Diffusionsprozesses. Man kann erkennen, dass der Dichteanteil an der Stelle ω_L, der für die Spin-Gitter-Relaxation relevant ist, sich mit der Temperatur verschiebt. In Abbildung 8 ist die Frequenzabhängigkeit der NMR-Spin-Gitter-Relaxationsrate in einem ARRHENIUS-Diagramm dargestellt.

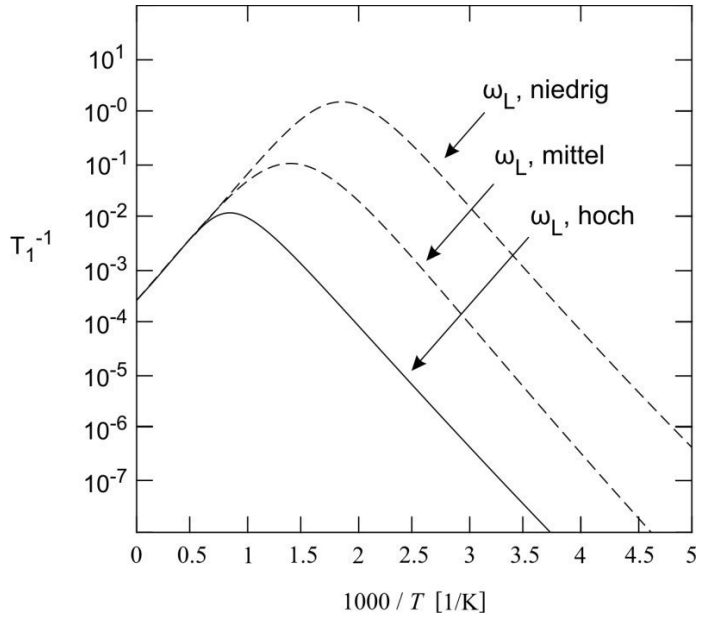

Abbildung 8: Verlauf der Relaxationszeit T_1 bei unterschiedlichen Lamorfrequenzen; die Ratenmaxima verschieben sich mit abhnehmender Larmorfrequenz zu niedrigeren Temperaturen. Untergrundeffekte, die nicht-diffusive Anteile darstellen sind nicht gezeigt.

Bei den drei gezeigten, verschiedenen Lamorfrequenzen kann man erkennen, dass sich die Flanke bei höheren Temperaturen nicht ändert, sie somit frequenzunabhängig ist. Die Tieftemperaturflanke ist frequenzabhängig und proportional zu ~ ω_L^{-2}. Die spektrale Dichtefunktion und auch die Spin-Gitter-Relaxationsrate werden maximal wenn

$$\omega_L \cdot \tau_C \approx 1 \qquad (5.29)$$

Dabei bedeutet, dass die Sprungrate τ^{-1} (in etwa) gleich der Lamorfrequenz ω_L wird.

Im Experiment wird die Temperatur variiert, um so das Maximum zu erfassen. Messungen bei verschiedenen Magnetfeldern liefern Informationen über die Frequenzabhängigkeit der Korrelationszeit. Sieht man sich die Erweiterungen des BPP-Modells an, so liefern Abweichungen vom idealen Kurvenverlauf Informationen über die Dimensionalität des Ionentransports (2-

dimensional oder 1-dimensional) bzw. über das Ausmaß von Korrelationseffekten wie z.B. die strukturelle Ordnung oder Coulomb-Wechselwirkungen, siehe Abbildung 9.

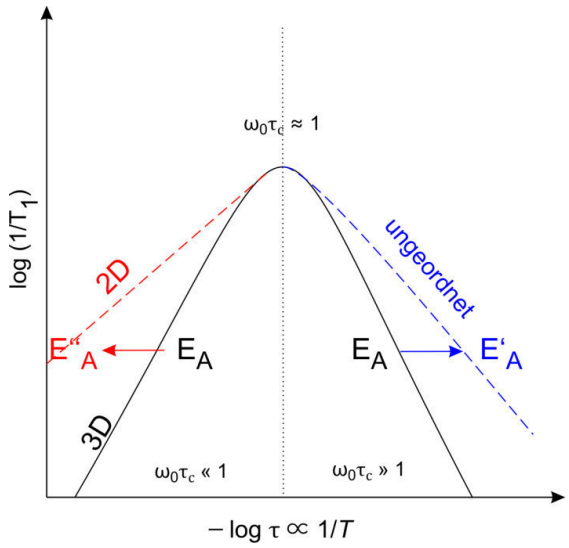

Abbildung 9: Abweichungen vom ‚einfachen' BPP-Modell, das weder Dimenionalitäts- noch Korrelationseffekten Rechnung trägt.

Über die Einstein-Smoluchovski-Gleichung[51] kann aus der Verweilzeit, bzw. der NMR-Korrelationszeit, ein mikroskopischer Diffusionskoeffizient abgeschätzt werden:

$$D^{SD} = \frac{a^2}{2 \cdot d \cdot \tau_C} \qquad (5.30)$$

Die Sprunglänge *a* wird mit der Gitterkonstante identifiziert, da sich Ionen in einem Festkörper z. B. über reguläre Leerstellen bewegen können. *d* (= 1, 2, 3) ist die Dimensionalität des Diffusionsprozesses.

Man kann so aus diffusionsinduzierten NMR-Relaxationsmessungen einen Diffusionskoeffizienten ermitteln und mit anderen Messmethoden vergleichen, wobei bei dieser Methode lediglich die Bewegung des gewünschten Ions beobachtet wird und andere Störeinflüsse eliminiert sind. Bei Impedanz- oder Leitfähigkeitsmessungen müssen z.B. elektronische Beiträge im Falle gemischtleitender Proben aufwändig eliminiert werden.

6 Experimentelle Details

6.1 Elektrochemische Untersuchungen

Zentrale Untersuchungsobjekte der Dissertationsschrift sind $Li_{4+x}Ti_5O_{12}$ in mikro- und nanokristalliner Form sowie Festelektrolyte mit Granatstruktur. Beide Materialklassen sind NMR-spektroskopisch untersucht worden. Im Falle von LTO stand auch seine elektrochemische Leistungsfähigkeit als Funktion des Defektgrades bzw. der Kristallitgröße im Fokus der Untersuchungen. Es wurde der Frage nachgegangen, wie sich die elektrochemischen Eigenschaften von LTO als Anodenmaterial verändern, wenn LTO zuvor in Hochenergiekugelmühlen mechanisch belastet wird.

Für die elektrochemischen Messungen wird aus dem als Pulver vorliegenden LTO zunächst ein *slurry* (teigige Masse aus Festkörper und Lösemittel) hergestellt; der *slurry* wird dann auf einen Cu-Stromableiter aufgetragen und so eine Elektrode gefertigt.

6.1.1 Probenvorbereitung

Trocknen der Probe:

LTO wird über Nacht in einem Trockenschrank (60 °C) vorgetrocknet und in einem Vakuumtrocknenofen (Büchi, Glasofen B-585 Kugelrohr) bei 60 °C und einem Vakuum von 10^{-3} mbar nachgetrocknet.

Nanostrukturierung der Proben:

Die Proben (4g) wurden in der Pulverisette (Fritsch P7) nach unterschiedlichen Vorgaben gemahlen. Bei Mahlvorgängen mit Lösemittel wurden 15 ml EtOH (reinst.) verwendet.

Slurryherstellung:

Für die Slurryherstellung sind folgende Elektrodenbestandteile eingewogen worden:

Aktivmaterial (LTO) - 80%, 13% Binder (Kynarflex 28019), 7% Leitruß (Super C 65)

Auf 1,5 g Einwaage wurden 4,5 ml NMP (wasserfrei) zugegeben und das Ganze in der Pulverisette 7 Premium Line dreimal 15 Minuten (mit *reverse mode*) homogenisiert. Dazu wurde ein Einwegbecher (45 ml) und 3 Kugeln (Durchmesser 1 cm, Zirkonoxid) verwendet.

Der Slurry wurde auf eine beidseitig aufgerauhte Kuperfolie (50 µm Dicke) mit einer Spaltdicke von 200 µm aufgerakelt (K-CONTROL-COATER-System K 101, Modell 623) und im Trockenschrank (60 °C) über Nacht getrocknet. Vor dem Einschleusen in die Glovebox wurden die Elektroden im Vakuumtrocknenofen (Büchi, Glasofen B-585 Kugelrohr) bei einem Vakuum von 10^{-3} mbar über Nacht bei 60 °C nachgetrocknet. Danach wurden Elektroden mit einem Durchmesser von 10mm ausgestanzt und danach abgewogen um die Schichtmasse zu ermitteln.

6.1.2 Meßzelle für elektrochemische Untersuchungen

Für elektrochemische Untersuchungen, wie z.B. alle Konstantstromzyklisierungen, wurden so genannte *Swagelok®-Zellen* (T-Zellen) verwendet. Dabei handelt es sich um eine 3-polige Zelle; das T-Stück besteht aus Teflon, während die Stempel aus einem speziellen antimagnetischen, sehr korrosionsbeständigen Spezialstahl (*U-Bootstahl*) bestehen. Die Arbeitselektrode, auf der die Elektrode mit dem Aktivmaterial angebracht wird, befindet sich gegenüber der Gegenelektrode. In einem Winkel von 90° dazu wird die Referenzelektrode angebracht. Die Arbeitselektrode wird mit einer Feder, die einen Druck von ca. 0.75 N/m² auf das Zellinnere ausübt, mit dem Stahlschaft verbunden. Die Swagelok-Zellen werden in einer Ar-gefüllten Glovebox (MBraun, O_2 < 1 ppm, H_2O < 1 ppm) gefüllt und entleert, da die verwendeten Materialien üblicherweise sehr Sauerstoff- und feuchtigkeitsempfindlich sind. Die Stahlschäfte verschließen das Zellinnere gasdicht und werden zusätzlich mit einem selbstdichtenden Schraubgewinde verschlossen. Die Gewinde werden dann noch zusätzlich mit Parafilm umwickelt.

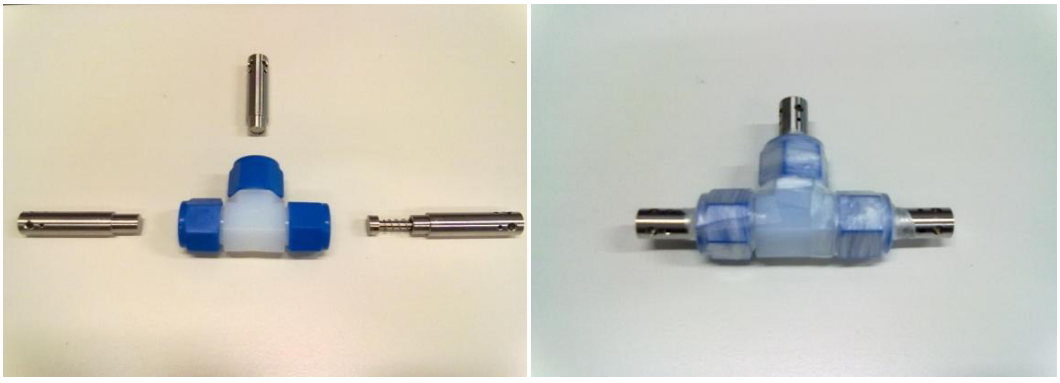

Abbildung 10: Swagelok-Zellen, mit der alle elektrochemischen Untersuchungen an mikro und nanokristallinem LTO durchgeführt wurden.

6.2 Elektrochemische Methoden

Um die Leistungsfähigkeit einer Halb- bzw. Vollzelle zu untersuchen, bedient man sich elektrochemischer Methoden wie z.B. der galvanostatischen Zyklisierung mit Potentiallimitierung.

6.2.1 GCPL (galvanostatic cycling with potential limitation)

Für diese Experimente wurde ein Potionstat (Biologic VMP3) verwendet. Ein konstanter Strom, der zuvor über das Faraday-Gesetz ermittelt wurde, wird vorab eingestellt. Die obere und untere Grenze werden durch Limitierung des Zellpotentials festgelegt. Innerhalb des Potentialbereiches wird die Zelle geladen und entladen und ihre Charakteristik bestimmt.

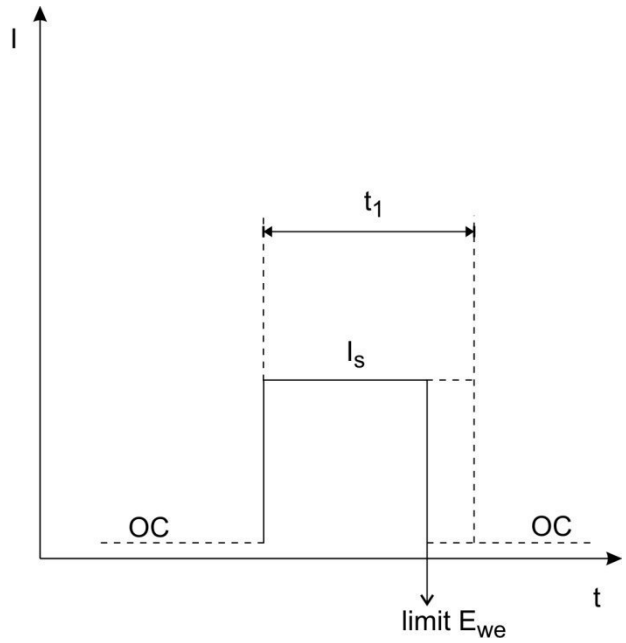

Abbildung 11: Zeitlicher Verlauf der Stromstärke beim Konstantstromzyklisieren.

Die konstante, nötige Stromstärke wird dabei aus dem Faraday-Gesetz abgeleitet:

$$I = \frac{m \cdot z \cdot F}{M \cdot t} \qquad (6.1)$$

Dabei gibt *m* die aktive Masse der Elektrode an, *z* die Anzahl der übertragenen Elektronen, und *F* die Faradaykonstante ($9.6485 \cdot 10^4$ C mol^{-1}). *M* steht für die Molmasse des Aktivmaterials und die Zeit *t* in diesem Fall für 3600 s.

Der C-Faktor ist für die Quantifizierung von Akkumulatoren eine wichtige Kenngröße, er ist folgendermaßen definiert

$$C = \frac{I_{max}}{C_N} \tag{6.2}$$

Dabei bedeutet I_{max} der Lade- bzw. Entladestrom und C_N die Nennkapazität des Akkumulators. Die Einheit des C-Faktors ist s^{-1}, wobei in der Praxis auf 1 h, also auf 3600 s referenziert wird. Bei höheren C-Raten verstärkt sich der kinetische, d.h. der durch den angelegten Strom beeinflussbare Anteil des Ionentransportes; dies bedeutet, dass die Gesamtkapazität nicht mehr diffusionskontrolliert, sondern kinetischer Hemmung unterworfen ist. Sie sinkt erwartungsgemäß mit Zunahme der C-Rate.

6.3 NMR-Relaxometrie und NMR-Spektroskopie: Techniken

Die Kernspinresonanzspektroskopie bietet im Vergleich zu anderen Methoden, mit denen Diffusionsparameter in Festkörpern gemessen werden können, den Vorteil der zerstörungs- und berührungsfreien Analyse.

Während eines NMR-Experimentes wird eine Probe in ein statisches, homogenes Magnetfeld gebracht. Die Kernspins der Probe richten sich dabei nach diesem Magnetfeld aus und besetzten die Zeeman-Niveaus gemäß der Boltzmann-Verteilung. Ein Radiofrequenzpuls mit der Lamorfrequenz regt ausschließlich den zu detektierenden Kernspin an und erzeugt einen Nichtgleichgewichtszustand. Die Rückkehr des Spin-Systems in das thermodynamische Gleichgewicht wird u.a. durch Bewegungsprozesse der Spins induziert und kann NMR-spektroskopisch erfasst werden. Die charakteristische Zeit kann technisch mit unterschiedlichen Methoden[52,53] experimentell erfasst werden. In dieser Arbeit wurden alle T_1-Messungen mit der Sättigungspulsfolge bestimmt, siehe Anhang.

Neben NMR-Relaxationsmessungen eignen sich Linienbreitenmessungen zur ersten Abschätzung von Li-Diffusionsparametern. Durch nichtselektive Einpulsexperimente kann aus der Fouriertransformierten die Breite und Form der NMR-Linien ermittelt werden.

Aufgrund der fehlenden schnellen Bewegung der Kernspins im Festkörper im Vergleich zu flüssigen Proben, werden dipolare Kopplungen, z.B. durch Molekülrotationen, nicht ausgemittelt und erzeugen breite Festkörper-Linien.[54] Erst bei erhöhten Temperaturen kommt es auch im Festkörper zu einer Ausmittelung der dipolaren Anteile. Wenn man Linienbreiten bei unterschiedlichen Temperaturen misst, setzt Linienverschmälerung ein, wenn die Sprungrate der Spins in den Bereich der Linienbreite des starren Gitters gelangt. Dieses so genannte *motional*

narrowing kann als qualitatives Maß zur Charakterisierung von Li-Ionenleitern genutzt werden. guten Ionenleiter handelt. Aus den gemessenen Halbwertsbreiten lassen sich relativ zueinander Proben unterschiedlicher Mobilität vergleichen.

Im Zuge dieser Arbeit wurde hauptsächlich die Mobilität von Lithiumkernen beobachtet. In erster Linie wurden ^{7}Li-NMR-Messungen herangezogen, der Quadrupolkern ist sowohl magnetischen und elektrischen Wechselwirkungen unterworfen und relaxiert schneller als der Spin-1 ^{6}Li-Kern, der aufgrund seines um den Faktor 50 kleineren Quadrupolmomentes für hochauflösende Messungen trotz seiner geringeren Häufigkeit (7.5 %), und somit Rezeptivität, der bevorzugte Kern ist. Auch die Dipol-Dipol Wechselwirkungen sind im Falle des ^{6}Li Isotopes geringer. Störende Spin-Diffusionseffekte (sog. flip-flop-Prozesse) sind unterdrückt, da die geringere natürliche Häufigkeit im Mittel gleichzeitig zu einer räumlichen Trennung der homonuklearen Kerne führt.

Hochauflösende Messungen wurden mittels *magic angle spinning* realisiert. Dabei wird die Probe in einen kleinen Rotor gefüllt und dieser in einem Winkel von 54.7° zum externen Magnetfeld gekippt und mittels eines N_2-Stromes in Rotation versetzt. Üblich sind dabei Rotationsfrequenzen von 20.000 bis 50.000 Umdrehungen pro Sekunde. Die spektrale Auflösung kann dadurch entscheidend verbessert werden, da alle verbreiternd wirkenden Wechselwirkungen der Kerne, die der Störungsrechnung 1. Ordnung unterliegen, eliminiert werden. Spin-Echo-Methoden unter statischen Bedingungen eignen sich hingegen zur Sichtbarmachung von schnell abfallenden Komponenten im FID, die durch Totzeiteffekte oft nicht detektiert werden können.

Um Li-Austauschprozesse zwischen magnetisch inäquivalenten Plätzen ‚direkt' sichtbar zu machen, werden üblicherweise im Falle diagmanetischer Materialien ^{6}Li-2D-Experimente durchgeführt.[55] Dabei wird auf zwei Achsen die chemische Verschiebung aufgetragen, während die Intensität der Linien z.B. als Konturlinie dargestellt wird. Auf der Diagonalen ist das 1D-Spektrum zu sehen, Intensitäten abseits der Diagonalen deuten auf eine Übertragung der Magnetisierung zwischen zwei Spin-Zuständen hin. Neben Spin-Diffusion, die im Falle von Proben mit natürlicher ^{6,7}Li-Isotopenverteilung gering gehalten werden kann, ist die Ionen-Diffusion eine der Ursachen, die zu *cross peaks* im 2D-Konturplot führt. Die unterschiedlichen NMR-Methoden[56,57,58,59,60] wurden in dieser Arbeit je nach Materialeigenschaften eingesetzt, um kurz- und langreichweitige Li-Diffusionsparameter sowie lokale Strukturen zu bestimmen.

7 Resultate: Publizierte und noch unveröffentlichte Arbeiten

Das folgende Kapitel enthält die Ergebnisse der Dissertation, die entweder bereits in *peer-reviewed* Fachjournalen publiziert worden sind bzw. bisher noch nicht veröffentlicht wurden. Zunächst werden die Ergebnisse aus den elektrochemischen Untersuchungen an den präparierten mikro- und nanokristallinen LTO-Proben kurz skizziert.

7.1 Alterungsuntersuchungen an Li-Zellen mit LTO-Anoden

7.1.1 Nanokristalline Materialien durch Kugelmahlen: Mahlparameter

Frühere Untersuchungen[61,62,63] zeigten, dass nanostrukturiertes LTO eine etwas bessere Leistungsfähigkeit als Anodenmaterial zeigt. In dieser Arbeit wurde das Alterungsverhalten von mikro- und nanokristallinem LTO durch Langzeitzyklisieren untersucht. Es wurden folgende Proben aus Charge 1037 durch Hochenergiekugelmahlen hergestellt und untersucht:

Tabelle 1: Übersicht der Mahlparameter

Probe		Drehzahl	Mahldauer	Pause	Wiederholungen	Lösemittel
EDX 1037	Nano 1	600 U/min	15 min	10 min	40	Trocken
	Nano 2	600 U/min	10 min	20 min	20	EtOH
	Nano 3	600 U/min	15 min	20 min	20	Trocken

Tabelle 2 zeigt Korngrößenverteilungen, die seitens des Hersteller gemessen wurden (Laser Diffraction: Mastersizer 2000, Malvern Instruments GmbH, in water using ultrasonic finger) und dem technischen Datenblatt entnommen wurden. Daneben sind die von uns ermittelten Daten (CILAS Granulometer 715) gezeigt.

Tabelle 2: Übersicht über die Korngrößenverteilung der LTO Proben

Durch-messer	EDX 1037	EDX 1979	EDX 1037			
	techn. Datenblatt		Mikro	Nano 1	Nano 2	Nano 3
d_{10}	ca. 0.9 µm	ca. 0.6 µm	0.67 µm	0.27 µm	0.17 µm	0.31 µm
d_{50}	ca. 2.3 µm	ca. 9 µm	1.64 µm	1.62 µm	0.99 µm	1.77 µm
d_{90}	ca. 4.7 µm	ca. 25 µm	3.16 µm	10.83 µm	3.29 µm	10.47 µm
d_{100}	ca. 7.5 µm	ca. 50 µm	-	-	-	-

Die Korngrößenverteilungen zeigen, dass die unter Lösemittel gemahlenen Proben eine deutliche Partikelverkleinerung und eine Verschmälerung der Verteilung zeigen. Die trocken gemahlenen Proben neigen zu einer stärkeren Agglomeration und bringen daher größere Partikel mit sich. Die Probe Nano 2 zeigt vor allem bei d_{50} schon, dass eine Verringerung der Partikelgröße erfolgreich war.

Laut den technischen Datenblättern weist EDX 1979 nach BET-Messung eine spezifische Oberfläche von 10 m²/g während EDX 1037 eine geringere Oberfläche von ca. 3 m²/g zeigt.

7.1.2 Röntgendaten

Zur Charakterisierung der Proben wurden XRD-Diffraktogramme aufgenommen, um Nebenphasen und Reinheiten zu bestimmen.

Aus den technischen Datenblättern ist laut XRD keinerlei Unterschied zwischen den beiden mikrokristallinen Chargen zu erkennen. In Abbildung 12 sieht man, dass das Mahlen bei den Proben Nano 1 und Nano 2 den amorphen Anteil erhöht; deutlich ist zudem zu erkennen, dass das trockene Mahlen bei diesen Parametern zu einem partiellen Abbau des LTO führt und sich eine neuen Phase ausbildet. Die neuen Reflexe konnten TiO_2 (Rutil) zugeordnet werden. Für die elektrochemischen Untersuchungen wurde neben den beiden Chargen des Herstellers nur mehr die Nanoprobe 2 verwendet.

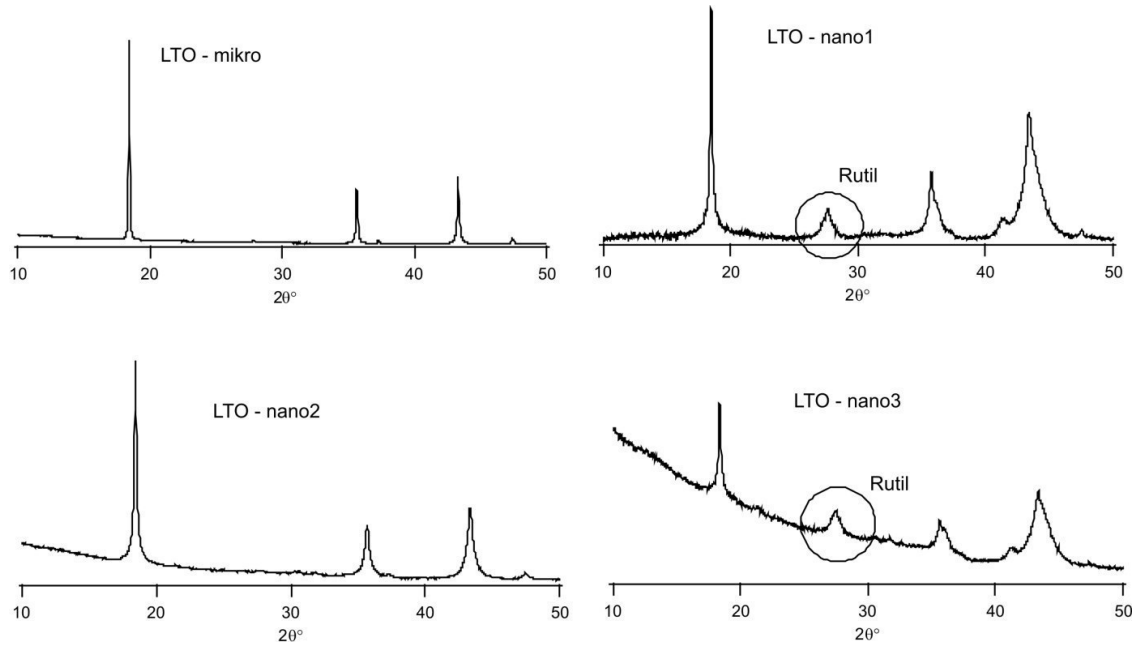

Abbildung 12 : XRD-Diffraktogramme der unterschiedlichen LTO-Proben; bei längerer mechanischer Behandlung zersetzt sich LTO zu Rutil.

7.1.3 Elektrochemische Untersuchungen

Für die elektrochemischen Untersuchungen wurden zwei unterschiedliche Chargen des Herstellers verwendet und wie in Kapitel 6.1 beschrieben, Elektroden hergestellt und Swagelok-Zellen gefertigt.

Über die ausgewogene Schichtmasse kann aus dem Faraday-Gesetz die zum Laden nötige Stromstärke errechnet werden. Die Stromstärke wurde so gewählt, dass die Zellen in einer Stunde ge- bzw. entladen wurden. Das entspricht einer C-Rate von 1. Die zugehörigen Formeln und Erläuterungen sind in Kapitel 6.2.1 kurz eingeführt.

Als untere Potentialgrenze wurde 1 V gewählt, als obere Grenze 2V.

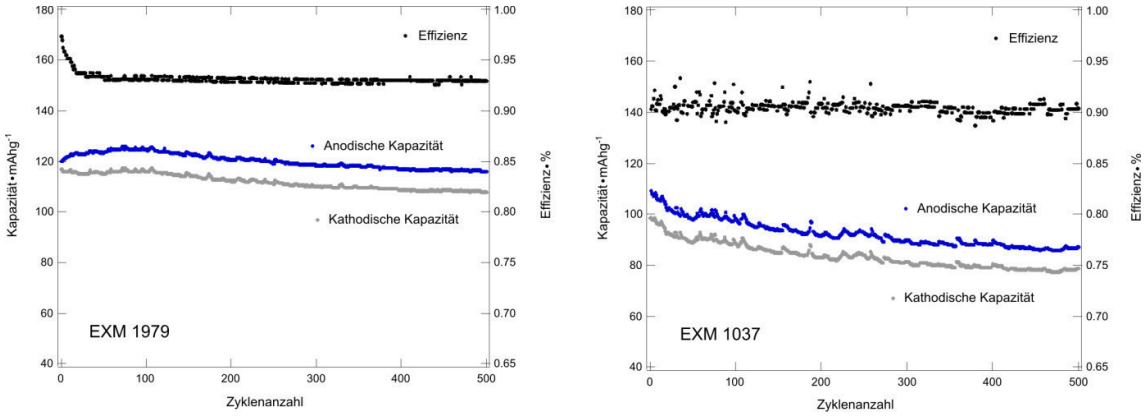

Abbildung 13: Kapazitätsverlauf der beiden mikro-LTO-Chargen, Gegenelektrode: Li-Metall; die aktive Masse betrug 80%, als Elektrolyt wurde LP30 (EC:DMC = 1:1; 1M $LiPF_6$) verwendet

Die Charge 1979 zeigt eine höhere Kapazität und gleichzeitig eine höhere Effizienz. Die Differenz zur Lade- und Entladekapazitäten liegen in einer vergleichbaren Größenordnung. Beide Zellen zeigen einen stetigen, sehr geringen Kapazitätsverlust.

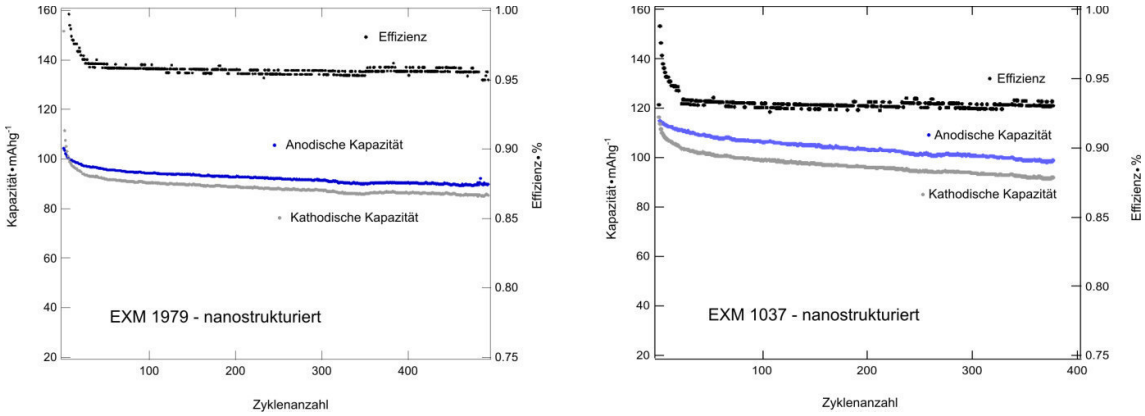

Abbildung 14: Kapazitätsverlauf der beiden nano-LTO-Chargen, Gegenelektrode: Li-Metall, die aktive Masse betrug 80%, als Elektrolyt wurde LP30 (EC:DMC = 1:1; 1M $LiPF_6$) verwendet

Die Partikelzerkleinerung führte bei EXM 1037 zu einer Verbesserung der Kapazität und Effizienz im Vergleich zur nicht gemahlenen Probe, während bei EXM 1979 ein umgekehrter Effekt zu beobachten war. Die Coulomb-Effizienz beider Proben konnte durch die Nanostrukturierung erhöht werden. Das bedeutet, dass die Reversibilität Li ein- und auszulagern bei den Nano-Proben verbessert werden konnte.

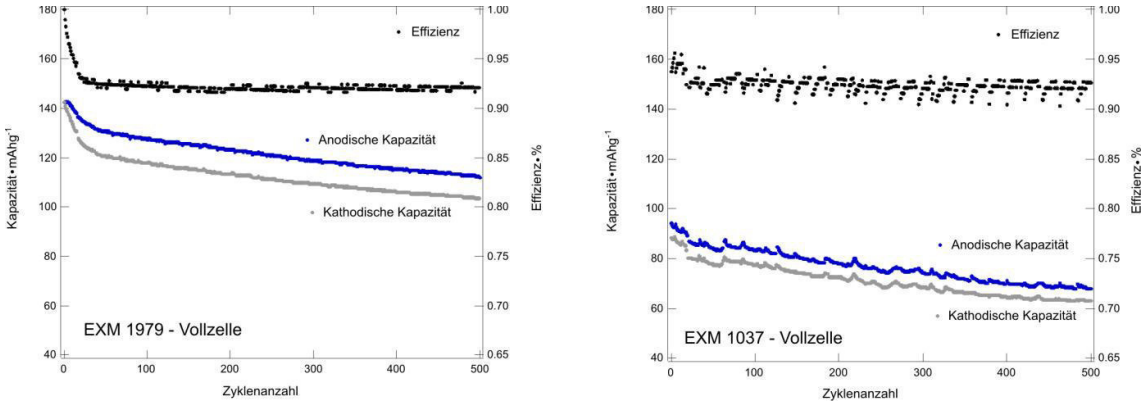

Abbildung 15: Kapazitätsverlauf der beiden LTO-Chargen in einer Vollzelle, Gegenelektrode: überdimensionierte NCA Elektrode (+30% aktive Masse), die aktive Masse an der Anode betrug 80%, als Elektrolyt wurde LP30 (EC:DMC = 1:1; 1M $LiPF_6$) verwendet

Beide Chargen zeigten einen Verlust betreffend der Startkapazität im Vergleich zu den Halbzellen. Der Kapazitätsverlust während des Zyklisierens ist bei beiden Vollzellen stärker ausgeprägt als bei den Halbzellen. Die C-Effizienz hat bei der Charge 1979 abgenommen, während die Effizienz bei 1037 zugenommen hat.

Bei allen Änderungen sieht man deutlich den Einfluss der Kathode auf das Zyklisierverhalten der Zelle. Unter Einbindung zusätzlicher Untersuchungsmethoden, wie beispielsweise elektrochemische Impedanzspektroskopie, könnte sich LTO somit sehr gut als eine Art Referenzanode eignen, um beispielsweise gezielt Alterungseffekte an der Kathode oder an den Grenzflächen zwischen Kathode und Elektrolyt zu untersuchen.

Es gab bereits intensive Anstrengungen, Modellsysteme mittels impedanzspektroskopischer Untersuchungen an Halb- und Vollzellen zu erstellen, doch konnten bis jetzt keine zufriedenstellenden, schlüssigen Ergebnisse erzielt werden.

Die Versuche symmetrische Zellen (d.h. LTO als Kathode und als Anode) zu zyklisieren, um gezielt Informationen über die Grenzflächen zu untersuchen, erwiesen sich auch nach etlichen Änderungen in den Versuchsbedingungen nicht zielführend, da kein stabiles System erhalten werden konnte.

7.2 Li-Diffusion in chemisch interkalierten LTO-Proben

Für alle Untersuchungen zur Li^+-Selbstdiffusion in $Li_{4+x}Ti_5O_{12}$ wurden ausschließlich Proben aus Charge EXM 1037 (SüdChemie) verwendet.

Im Hinblick auf frühere Arbeiten[25,33,23] hat sich die Frage gestellt, inwiefern die Festkörperdiffusionseigenschaften, d.h., die Selbstdiffusion der Li-Ionen in reinem und lithiiertem LTO, Einfluß auf die Leistungsfähigkeit von LTO-Anoden nimmt. Li-NMR-spektroskopische *time-domain* Verfahren sind in der Lage auch in gemischtleitenden Verbindungen wie z.B. $Li_7Ti_5O_{12}$, dem Ladeprodukt in einer Li-Ionen-Batterie, ausschließlich die ionischen Bewegungsprozesse zu detektieren und hinsichtlich mittlerer Aktivierungsenergie und Sprungraten zu quantifizieren.

7.2.1 Small Change - Great Effect: Steep Increase of Li Ion Dynamics in $Li_4Ti_5O_{12}$ at the Early Stages of Chemical Li Insertion

Die folgende Publikation hatte zum Ziel die dynamischen Änderungen der Li-Ionen[64] als Funktion des Lithiierungsgrades (x = 0 bis x = 3) insbesondere auch bei kleinen x-Werten präzise zu untersuchen.

Wichtig zu erwähnen ist, dass alle Proben chemisch mit Lithium interkaliert wurden, anstatt den Weg über die Elektrochemie zu gehen. Dadurch können Einflüsse von Binder und Leitruß ausgeschlossen werden. Buthyllithium ist ein Reagenz mit einem Potential von 1V vs. Li^+/Li, das sich vorzüglich zur chemischen Lithiierung anbietet.[18] Nach Trocknung der Proben bei 60 °C im Vakuum von 10^{-3} mbar (12 h) sind mehrere Zwischenstufen von $Li_{4+x}Ti_5O_{12}$ mit den folgenden Gehalten an Li hergestellt worden: x = 0; x = 0.1; x = 0.3; x = 1; x = 2; x = 3. Der Gehalt x = 3 stellt das vollständig interkalierte $Li_7Ti_5O_{12}$ dar. Dazu sind in einer mit Argon gefüllten Glovbox (MBraun; O_2 < 1 ppm; H_2O < 1 ppm) die LTO-Proben mit den dementsprechenden Mengen Butyllithium versetzt worden (Reaktion über Nacht). Danach wurden die Proben 3x mit Hexan gespült, Vakuumgetrocknet und in Glasampullen versiegelt. Die Proben wurden mittels ICP-OES analysiert und der eingestellte Li-Gehalt in der Probe bestätigt. Anschließend wurden sie mittels ^{7}Li NMR-Spektroskopie analysiert, d.h. vor allem mit Linienbreitenmessungen und *spin-lock*-Relaxometrie untersucht.

Small Change—Great Effect: Steep Increase of Li Ion Dynamics in $Li_4Ti_5O_{12}$ at the Early Stages of Chemical Li Insertion

Walter Schmidt[*]†‡, Patrick Bottke†, Michael Sternad†‡, Peter Gollob[§], Volker Hennige[§], and Martin Wilkening[*]†‡

[†]Institute for Chemistry and Technology of Materials, and [‡]Christian Doppler Laboratory for Lithium Batteries, Graz University of Technology (member of NAWI Graz), 8010 Graz, Austria

[§] AVL List GmbH, Hans-List-Platz 1, 8020 Graz, Austria

Chem. Mater., 2015, 27 (5), pp 1740-1750

DOI: 10.1021/cm504564k

Publication Date (Web): February 5, 2015

CHEMISTRY OF MATERIALS

Article

pubs.acs.org/cm

Small Change—Great Effect: Steep Increase of Li Ion Dynamics in $Li_4Ti_5O_{12}$ at the Early Stages of Chemical Li Insertion

Walter Schmidt,*[,†,‡] Patrick Bottke,[†] Michael Sternad,[†,‡] Peter Gollob,[§] Volker Hennige,[§] and Martin Wilkening*[,†,‡]

[†]Institute for Chemistry and Technology of Materials, and [‡]Christian Doppler Laboratory for Lithium Batteries, Graz University of Technology (member of NAWI Graz), 8010 Graz, Austria

[§]AVL List GmbH, Hans-List-Platz 1, 8020 Graz, Austria

ABSTRACT: Lithium titanate (LTO) is one of the most promising anode materials for large-scale stationary electrochemical storage of energy produced from renewable sources. Besides many other aspects, such as negligible formation of passivation layers and no volume expansion during lithiation, the success of LTO is mainly based on its ability to easily accommodate and release Li ions in a fully reversible way. This feature is tightly connected with Li self-diffusion. As yet, little information is available about microscopic Li diffusion properties and elementary steps of Li hopping at low intercalation levels, i.e., at values of x being significantly smaller than 1. Here, we used ^{7}Li spin-locking NMR relaxometry to probe absolute hopping rates of LTO (homogeneous) solid solutions in quasi-thermodynamic equilibrium. As a result, the largest increase of Li diffusivity is observed when small amounts of Li are inserted. Strong Coulomb repulsions caused by the simultaneous occupation of neighboring 8a and 16c sites serve as an explanation for the enhanced Li diffusivity found. At even larger values of x, Li mobility slows down but is still much faster than in the host material with $x = 0$. Our results experimentally corroborate the outcome of recently published calculations on the DFT level focusing on both dynamic and structural aspects. The findings favor the formation of LTO solid solutions upon chemical lithiation; the steep increase in Li diffusivity found might also help with understanding the flat insertion potential observed.

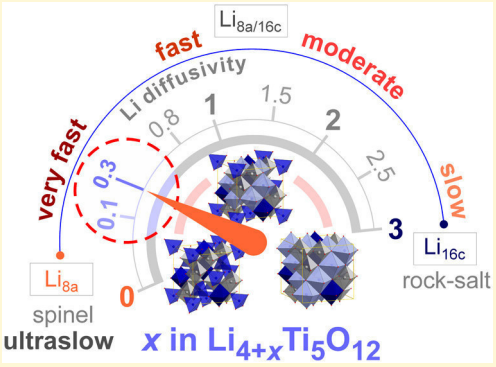

1. INTRODUCTION

Li-bearing energy materials play a vital role in developing batteries that store electricity from renewable sources.[1−5] Lithium titanate, $Li_{4+x}Ti_5O_{12}$ (LTO), is one of the most popular and abundant anode materials that offers facile and highly reversible Li insertion and deinsertion during charging and discharging lithium-ion batteries.[6−10] It allows many charge−discharge cycles without loosing significant performance; after thousands of cycles the retention is more than 90% of the original capacity making LTO a superior anode material for many applications.[10−13]

LTO is well-known to be a so-called zero-strain material with negligible volume expansion and stress generated during lithiation up to $x = 3$. The insertion potential of approximately 1.55 V (vs Li metal) leads to both a lower overall battery voltage and, for many common electrolytes, to negligible solid electrolyte interphase (SEI) formation because the working potential is above that of electrolyte decomposition.[7,11−15] Although its theoretical capacity is only 175 mAh/g, the titanate is, particularly in its mesoporous form as has been shown by Haetge et al.,[9] a promising material for high rate thin-film applications as well as large-scale stationary energy storage for the grid. The latter is because of its nontoxicity as well as long-term cyclability, i.e., its inherent resistance to aging effects.[10,13] For commercialization, of course, gas evolution[16,17] depending on the cathode materials used in a battery remains an issue that has to be carefully taken into account and brought under control in future studies, e.g., via carbon coating[16] or the use of AlF_3-modified LTO.[18]

Li insertion transforms the initially pure but poor[15] ionic conductor LTO, showing ultraslow Li^+ exchange,[19] into a mixed conducting oxide. During lithiation the originally colorless powder turns into a blue one; the darker the color, the larger the Li content x. In spinel-type LTO, crystallizing with the space group $Fd\bar{3}m$, the lithium ions occupy octahedral (16d) and tetrahedral (8a) sites according to the general formula (using Wyckoff notation) $[Li]_{8a}[Li_{1/3}Ti_{5/3}]_{16d}[O_4]_{32e}$ (see Figure 1). Wagemaker and co-workers have shown by thorough neutron diffraction measurements[20] that upon lithiation of LTO the Li^+ ions inserted occupy the initially empty (octahedral) 16c sites of the cubic structure. Simultaneously, the Li ions, originally residing on the 8a sites, are partly shifted to the 16c voids. Thus, during charging (discharging) an internal redistribution of the ionic charge carriers on the 16c and 8a sites takes place until at the composition of $x = 3$ rock-salt type $Li_7Ti_5O_{12}$

Received: December 12, 2014
Revised: February 3, 2015
Published: February 5, 2015

DOI: 10.1021/cm504564k
Chem. Mater. 2015, 27, 1740−1750

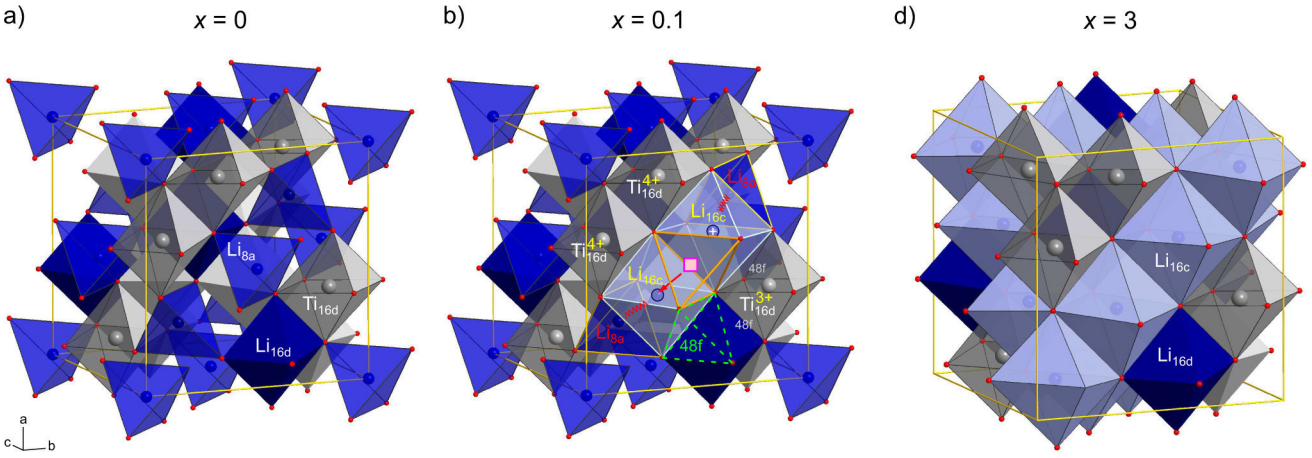

Figure 1. (a) Crystal structure of spinel-type $Li_4Ti_5O_{12}$ ($Fd\bar{3}m$); the Li ions occupy 16d and 8a positions; oxygen anions reside on 32e sites. (b) Inserting Li ions leads to a redistribution of the original Li ions nearby. The additional Li ions start to populate the 16c sites. In any case, Li−Li repulsions because of simultaneous occupation of neighbored (face-sharing) 16c and 8a polyhedra cannot be avoided at this insertion level even if some of the ions convert from 8a to 16c. This is because each 16c octahedron is connected to two 8a tetrahedra by face-sharing. At larger x levels the formation of nanometer-sized $Li_7Ti_5O_{12}$ domains may be energetically favored. During lithiation, titanium ions are partly reduced from Ti^{4+} to Ti^{3+}. (c) The crystal structure of $Li_7Ti_5O_{12}$ with all the 16c sites being fully occupied and the 8a sites being empty.

$([Li_2]_{16c}[Li_{1/3}Ti_{5/3}]_{16d}[O_4]_{32e})$ with empty 8a sites is formed via this topotactic reaction (see Figure 1). Rapid Li exchange between the 8a and 16c sites, sharing common faces, seems to be the relevant hopping mechanism in lithiated LTO.[19,21] This might, to a certain degree, also include the involvement of Li ions on 16d sites and thus 48f sites acting as transition states. Oxygen vacancies (32e) are expected to affect the 8a−16c exchange further.[22,23] More precisely, for nonlithiated LTO the pathway 8a−32e−32e−8a has also been discussed.[22,24]

The flat insertion potential observed for LTO, when used as a negative electrode material in a lithium-ion battery, is frequently explained in terms of kinetically induced two-phase regions or domains being rich ($Li_7Ti_5O_{12}$) and poor ($Li_4Ti_5O_{12}$) in Li concentration. Recently, the coexistence of Li rich and Li poor regions in locally lithiated single crystals of LTO has been reported by Kitta et al.[25] For comparison, in electrochemistry, which deals with powder samples, the situation might be different. As has been demonstrated by Wagemaker et al. such domains are formed at high charging rates; with time, however, the two-phase structure relaxes toward a homogeneous distribution of Li ions, that is, a solid−solution-like structure.[20] This is what is expected to take place in a charged battery for longer periods of time when stored at room temperature or above. If, on the other hand, Li is inserted chemically, which is usually done by stirring a suspension of LTO in *n*-butyllithium (*n*-BuLi) over many days at ambient conditions, quasi solid solutions are expected to be formed in the first place rather than spatially extensive domains differing in Li content.[20] At room temperature the existence of nanometer-sized domains of Li rich and Li poor regions is assumed; these domains have recently been visualized via aberration-corrected scanning transmission electron microscopy (STEM).[26] Lu et al. have shown that nanodomains of $Li_7Ti_5O_{12}$ in a sample with about 0.15 mol of Li insertion per formula unit shows diameters of ca. 6−8 nm. Moreover, sharp phase boundaries have been detected.[26]

Our investigation aims at understanding how Li diffusivity changes after very small amounts of Li have been inserted chemically into LTO that shows poor Li self-diffusivity.[19] Since a mixed conductor is formed immediately after intercalation, NMR was used in previous investigations to selectively study Li ion dynamics. The samples studied in the literature as yet are characterized by Li contents with x being larger or equal to 1. So far, little is known on how Li ion dynamics is influenced when x is kept well below $x = 0.5$. Such information is crucial if we are to overcome the limitations that face progress in electrochemical energy storage for both automotive and stationary applications.

Here, a series of samples has been prepared ($x = 0.1$, 0.3, 1, 2, 3) to unravel the change of Li diffusivity as a function of the degree of intercalation in thermodynamically stable solid solutions of LTO. NMR relaxometry, utilizing spin-lock fields in the kilohertz range,[27−31] was employed to directly measure the elementary diffusion parameters such as migration barriers and absolute hopping rates of the lithium ions. Special emphasis is put on samples with $x = 0.1$, 0.3.

2. EXPERIMENTAL SECTION

Polycrystalline $Li_{4+x}Ti_5O_{12}$, which is available from SüdChemie AG (Germany), EXM 1037, was treated with appropriate amounts of *n*-butyllithium in hexane. Samples with the following stoichiometries, $x =$ 0.1, 0.3, 1, 2 and $x = 3$, were prepared. The samples were rinsed with hexane and dried under vacuum at 333 K. The amount of Li inserted, i.e., the final Li content, was verified by inductively coupled plasma optical emission spectrometry (ICP-OES). It turned out that in each case the full amount of Li offered by the amount of *n*-butyllithium was inserted into LTO. *n*-Butyllithium reacts vigorously with LTO because it has a potential of 1 V vs Li. Note that all experiments were carried out in an Ar-filled glovebox (O_2 < 1 ppm, H_2O < 1 ppm, MBraun GmbH, Germany) to prevent any reaction with air or moisture. The final samples were fire-sealed in glass ampules under vacuum (2 cm in length and 4 mm in diameter).

NMR data were recorded using a Bruker 500 WB spectrometer operating at 11.7 T; this corresponds to a ^{7}Li Larmor frequency of 194.3 MHz. The 90° pulse lengths ranged from 3 to 5 μs in the temperature range from 223 to 448 K. Temperatures below room temperatures were reached with a flow of dry and cooled nitrogen gas; for temperatures above ambient, a stream of heated nitrogen gas was used.

To study Li ion dynamics, ^{7}Li NMR line shape studies and spin−lattice relaxation rate ($1/T_1$) measurements in both the laboratory frame and in the rotating frame ($1/T_{1\rho}$) were carried out.[32] While the first were recorded with a single pulse sequence, the well-known

DOI: 10.1021/cm504564k
Chem. Mater. 2015, 27, 1740−1750

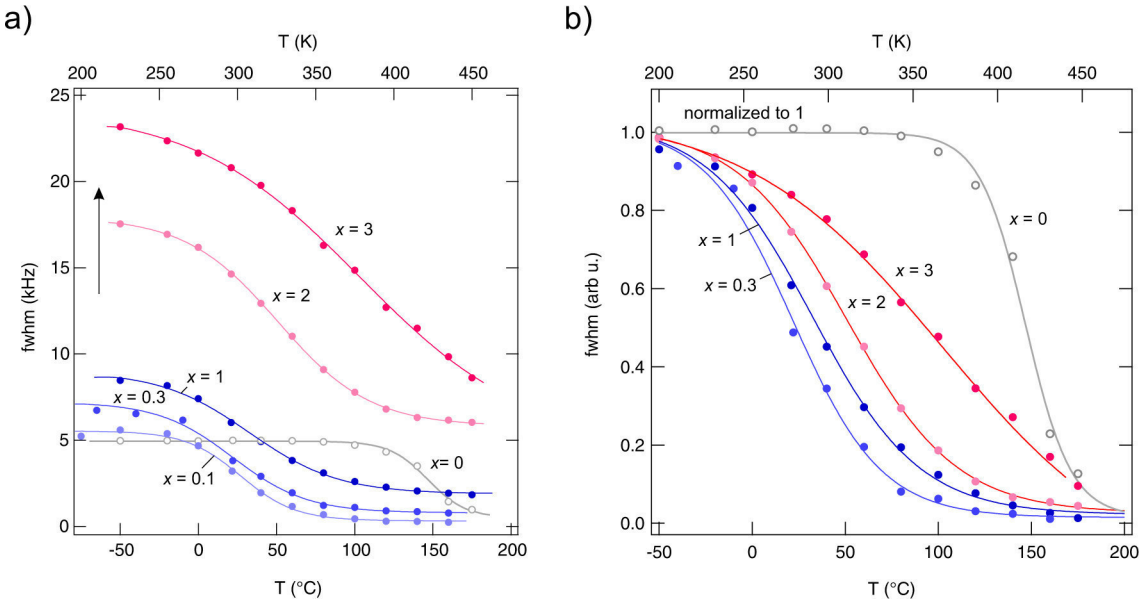

Figure 2. (a) Motional narrowing of the ^{7}Li NMR central lines of microcrystalline $Li_{4+x}Ti_5O_{12}$ with x = 0, 0.1, 0.3, 1, 2, 3. (b) Narrowing curves shown in (a) but scaled such that they are normalized to 1 at low temperatures. This scaling better illustrates the shape of the curves and locations of their inflection points. The lines are to guide the eye.

saturation recovery pulse sequence, $10 \times \pi/2 - t_d - \pi/2 -$ acquisition (acq.), was employed to record the rates $1/T_1$ as a function of temperature.[33] Here, the maximum value of t_d is chosen such that the transients well reached saturation of longitudinal magnetization ($t_d \approx 6T_1$); the curves obtained can be best approximated with single exponentials. For the $T_{1\varrho}$ measurements we used the spin-lock technique, $\pi/2$ p(t_{lock}) − acq., with a variable spin-lock pulse p(t_{lock}) as it was introduced by Ailion and Slichter.[34−36] The spin-locking frequency was set to approximately 20 kHz; this value disregards additional contributions of local magnetic fields[30] of the samples. The transients recorded in the rotating frame were parametrized with stretched exponentials to extract the "transversal" relaxation rates.

In addition to temperature-variable, time-domain NMR data, being sensitive to ion dynamics on the Ångström length scale, high-resolution ^{6}Li NMR lines were recorded under magic angle spinning (MAS) conditions with rotation frequencies of up to 30 kHz. For these measurements we employed a 2.5 mm MAS probe (Bruker); the spectra were recorded with ambient bearing gas pressure. If not stated otherwise, the corresponding ^{7}Li NMR spectra presented, which had been recorded under nonrotating conditions, were directly obtained by Fourier transformation of the free induction decays that were recorded with the saturation recovery sequence. Stimulated ^{7}Li NMR spectra,[37−40] on the other hand, were acquired with the three-pulse Jeener−Broekaert[41] pulse sequence, $\pi/2 - t_p - \pi/4 - t_m - \pi/4 -$ (acq.), optimized for spin-alignment echo (SAE) experiments on spin-3/2 nuclei such as ^{7}Li;[37,42] SAE NMR spectra were acquired with t_p = 10 μs and t_m = 100 μs to ensure negligible influence of Li diffusion on the shape of the lines.

3. RESULTS AND DISCUSSION

3.1. ^{7}Li NMR Line Shapes and Motional Narrowing. The easiest way to collect first information on the extent of Li self-diffusivity in LTO having different amounts of Li inserted is to record ^{7}Li NMR line shapes as a function of temperature T. At low T the central line of a powder ^{7}Li (spin-3/2) NMR spectrum is dipolarly broadened due to the absence of any diffusive motions. Li hopping motion usually leads to an averaging of dipolar couplings.[43−45] With increasing T, however, the Li jump rate $1/\tau$ increases and reaches the order of the rigid lattice line widths. As a consequence, significant NMR motional line narrowing is observed (see Figure 2).[43−45]

Starting our discussion with LTO (x = 0), diffusion-caused motional narrowing (MN) of the central line sets in at approximately T_{start} = 350 K (see Figure 2a). Temperatures T_{start} higher than room temperature roughly indicate very low Li diffusivity; this is particularly expected for crystal structures with the Li ions occupying tetrahedral sites connected by edge-sharing; $LiAlO_2$ may serve as an example here.[46] Below T_{start} the line width, i.e., the *rigid-lattice* line width of LTO, ν_0 (x = 0), is given by a full width at half-maximum (fwhm), ν_0, of ca. 5 kHz; hence, below T_{start}, the rate $1/\tau$ is estimated to be much smaller than 10^3 s^{-1}. This value illustrates the poor transport properties of nonlithiated LTO.[21]

With increasing Li content ν_0 increases from 5 to ν_0 (0.1) = 5.5 kHz and further to ν_0 (0.3) = 7 kHz. As has been shown by several studies, the Li ions additionally inserted occupy the octahedrally coordinated 16c sites within the spinel structure; note that the 16c octahedra share common faces with the 8a tetrahedra; see above. The increase in ν_0 can be explained by two reasons: (i) the decreasing Li−Li distance (8a−16c) leads to an increase of dipolar interaction according to van Vleck and (ii) the generation of Ti^{3+} centers is related to paramagnetic interactions with the lithium spins. Recently, the electron energy-loss spectroscopy (EELS) analysis presented by Lu et al.[26] showed that the Ti ions adopt locally different valences (Ti^{4+}, Ti^{3+}) upon lithiation; the results point to strong Li^+−e^- associations; this picture of severe valence heterogeneities has also been verified by calculations using density functional theory (DFT). The latter interactions dominate the increase in ν_0 when going from x = 0.3 to x = 1 (ν_0 = 8.5 kHz) and further to x = 2 (ν_0 = 17.5 kHz), finally reaching (ν_0 = 23.5 kHz) at x = 3; see Figure 2a). For x = 3, and in terms of a simple structural picture, all of the 16c sites of rock-salt $Li_7Ti_5O_{12}$ are filled with Li ions and the formerly occupied 8a sites are empty. The increase in ν_0 does also hold for the increase in $\nu_{(T\to\infty)}$, that is, the line width in the regime of *extreme narrowing*.

DOI: 10.1021/cm504564k
Chem. Mater. 2015, 27, 1740−1750

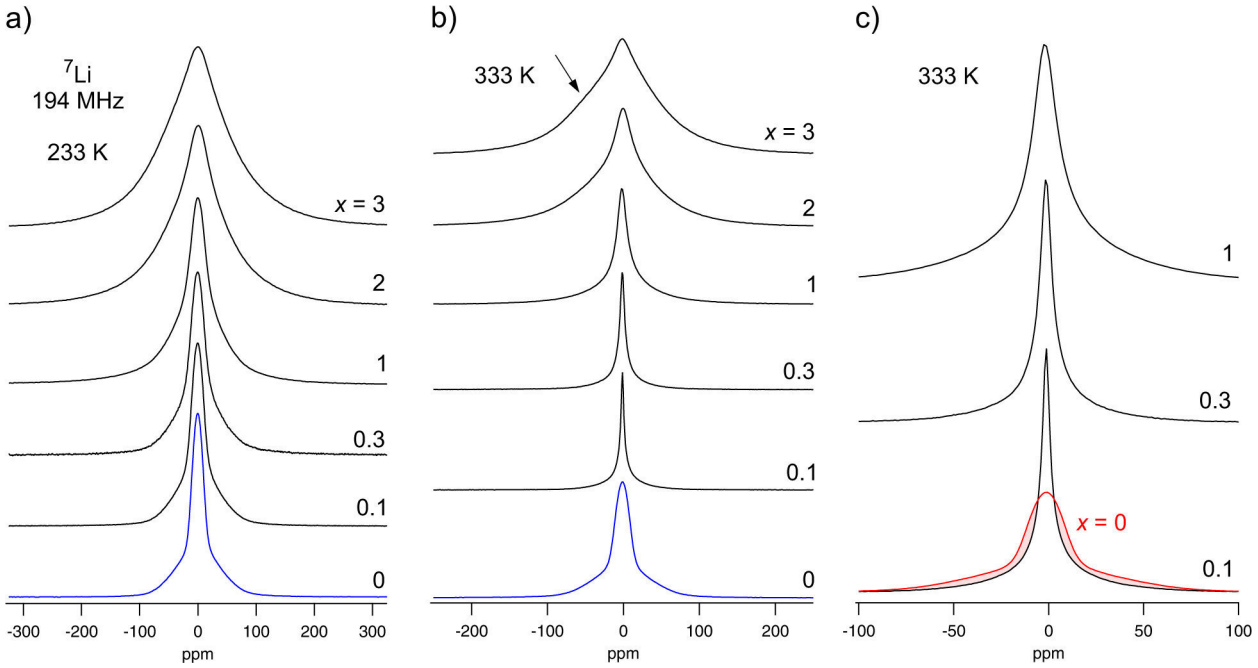

Figure 3. (a–c) ^{7}Li NMR spectra of $Li_{4+x}Ti_5O_{12}$ recorded at the temperatures and Li contents x indicated. In (c) a magnification of some of the spectra shown in (b) are shown. The small arrow in the spectrum of $Li_7Ti_5O_{12}$ recorded at 333 K indicates the NMR line that can be attributed to Li ions residing on 16c sites in the neighborhood of the Ti^{3+} centers. This component is clearly visible as a very broad but separated line in ^{6}Li MAS NMR centered at −9 ppm when referenced to LiCl(aq). See text for further explanation.

In Figure 2b, for a better comparison of onset temperatures and MN curve shapes, the line widths are scaled such that they range from 0 to 1, i.e., ν/ν_0 is plotted vs T. Increasing x from 0 to 0.1 (or 0.3), the onset temperature is drastically reduced to only 200 K, which is by approximately 150 K lower when compared to the sample with $x = 0$; see above ($T_{start}(x = 0)$ = 350 K). This indicates a steep increase in Li diffusivity at the early stages of Li intercalation. Most likely, it can be traced back to increased 8a–16c Coulomb interactions as is illustrated in Figure 1. Spin–lattice relaxation NMR—see below—will allow a quantitative determination of the increase in diffusivity observed.

In addition to the shift of the MN curves found, we also observed that the larger the x the more stretched the curves become. This means, instead of a "homogeneous" diffusion process in the case of $x = 0$, complex Li dynamics is sensed—even for the sample with $x = 3$. Hence, one should expect multiple Li diffusion pathways and a distribution of energy barriers present in samples with $x > 0$. The stepwise activation of these pathways with increasing T leads to line narrowing that finally proceeds over a temperature range of almost $\Delta T \approx 200$ K. These assumptions should also be reflected by the NMR line shapes themselves from which the line widths were deduced; they are shown in Figure 3. The spectra shown in (a) have been recorded at 223 K, thus in the same dynamic state, viz., the rigid lattice regime. It can be clearly seen that the spectrum of LTO ($x = 0$) is composed of a central line (from both the ions on 8a and 16d sites) and a so-called quadrupole powder pattern. This pattern stems from the interaction of the quadrupole moment of the ^{7}Li spins (spin quantum number 3/2) with a nonvanishing electric field gradient (EFG) at the Li sites.[37,40,43] The EFG is produced by the asymmetric electronic charge distribution in the direct neighborhood of the nucleus.

For comparison with this interpretation, Wagemaker et al. mentioned that the two contributions visible represent the *central* lines of the two crystallographically inequivalent Li sites.[49] According to our static ^{7}Li NMR measurements, which particularly included (stimulated, here, spin-alignment) echo techniques, we tend to interpret the broad contribution as follows. It is likely that it represents the quadrupole intensities of the Li ions on 8a and 16d rather than a central line because the intensity can easily be influenced by (refocusing) echo techniques optimized for spin-3/2 nuclei (see Figure 4). Additionally, the quadrupole signals undergo motional averaging and lose intensity with increasing T (see Figure 5); this observation, which is shown exemplarily for the sample with $x = 0.3$ in Figure 5, underlines once more its origin from electric interactions. In particular, the effect of motional averaging is seen in NMR stimulated echo spectroscopy.

The "overall ^{7}Li central line", on the other hand, cannot be separated into the two signals of Li ions on 8a and 16d sites. This is in contrast to ^{6}Li (MAS) NMR; compared to ^{7}Li, for the ^{6}Li nucleus second order quadrupole interactions are much smaller enabling high-resolution NMR. Hence, ^{6}Li MAS NMR lines definitely reveal the magnetically inequivalent Li sites showing up as two partly overlapping lines with distinct chemical shifts of 0.08 ppm and −0.26 ppm. These values are in perfect agreement with previous results reported by Irvine and co-workers.[50] Moreover, the areas under the two ^{6}Li NMR lines nicely agree with those expected from the crystal structure (see Figure 4b).

As mentioned above, with increasing x the spectra of $Li_{4+x}Ti_5O_{12}$ broaden due to the formation of paramagnetic Ti^3 centers; finally, at $x = 3$ the paramagnetic interactions dominate the spectrum and the quadrupole intensities can hardly be distinguished from the central line(s) (cf. Figure 3). Paramagnetic broadening and the increase in dipolar interactions are in competition with averaging of dipole–dipole couplings due to diffusive motions. Despite these three effects working in opposite direction, the drastic decrease in line width (see Figure

DOI: 10.1021/cm504564k
Chem. Mater. 2015, 27, 1740–1750

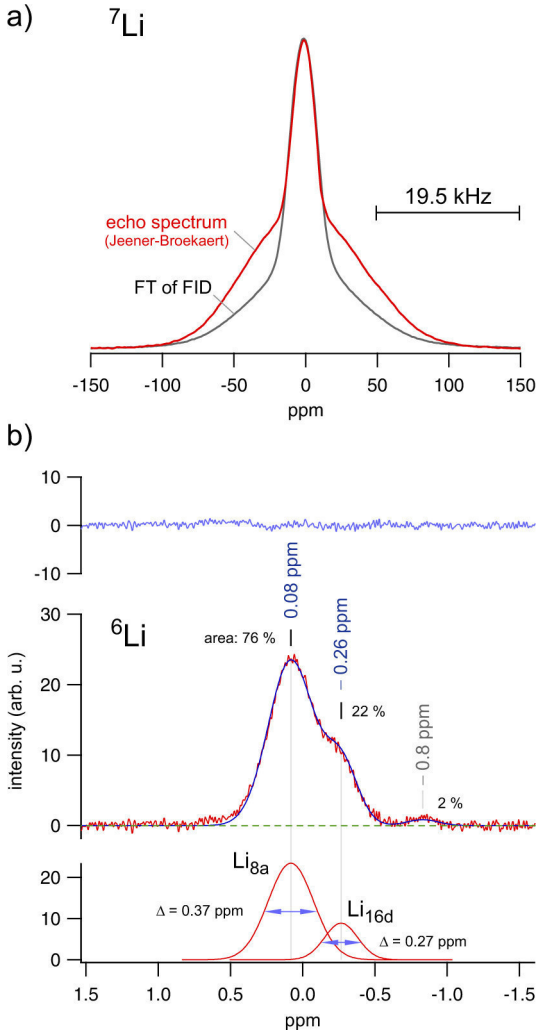

Figure 4. (a) ^{7}Li NMR spectrum of $Li_4Ti_5O_{12}$ obtained after Fourier transformation (FT) of an FID obtained via a single pulse experiment as well as obtained via FT of an Jeener-Broekaert echo with optimized phase cycling for spin-3/2 nuclei to enhance the intensity of quadrupole intensities. (b) ^{6}Li MAS NMR spectrum of $Li_4Ti_5O_{12}$ revealing the two magnetically different Li sites 8a and 16d; the whole spectrum, which is referenced to aqueous LiCl, can be deconvoluted with Gaussians that nicely reflect the population ratio expected for the two Li sites. The line at −0.8 ppm might be attributed to an (X-ray amorphous) impurity phase[47] such as Li_2TiO_3 or to a small fraction of Li ions residing already on the 16c sites. Traces of Li_2CO_3, which can build a thin film on the surface of the LTO particles, are hardly seen by NMR.[48] Δ denotes the MAS line width in ppm.

3b) that displays spectra recorded at 333 K) observed for x = 0.1 (and x = 0.3) can unequivocally be ascribed to a steep increase in Li ion dynamics setting in immediately after Li insertion. For the sake of completeness, in Figure 3c the shape of the ^{7}Li NMR spectrum LTO x = 0 is directly compared with those of the samples characterized by x = 0.1 and x = 0.3. Compared to the situation at x = 0, line narrowing of the central line and motional averaging of quadrupole intensities, as discussed above, can be observed for x = 0.1 and x = 0.3 (cf. also Figure 5). The averaging of EFGs can especially be recognized for the sample with x = 0.1; as is demonstrated via SLR NMR measurements presented below, at 333 K the mean Li jump rate (in Hz) becomes indeed comparable with the quadrupole splitting (ca. 20 kHz) causing the motional averaging of the corresponding quadrupolar powder pattern.

Before we discuss our SLR NMR measurements (see Figure 6) giving precise quantitative insights into the ion dynamics of Li-inserted LTO, we should have a look on the NMR spectrum of the sample with x = 2 recorded at 333 K; see Figure 3b. It represents the spectrum at the inflection point of the corresponding MN curve (see Figure 2). The line shape cannot be approximated with a single line; rather, it reflects a superposition of a motionally narrowed signal superimposed on a dipolarly broadened line. The width of the broad line is due to homonuclear Li−Li couplings that have not been averaged by Li exchange processes at the temperature given. The line is additionally broadened by Li^+−Ti^{3+} interactions. The emergence of a narrowed line on top of the NMR signal points to a stepwise MN, which is in many cases a signature of heterogeneous Li ion dynamics. For $Li_{4+x}Ti_5O_{12}$, this has already been observed by Wagemaker et al. in their ^{7}Li NMR spin−spin relaxation ($1/T_2$) study.[49] Such a two-component feature, however, should not necessarily result in pronounced two-component SLR NMR transients if sufficiently fast ^{7}Li−^{7}Li spin-diffusion mediated through flip-flop processes is present. Spin-diffusion has been indicated by Hain et al.[51] Indeed, our $T_{1\varrho}$ transients, and particularly those of the T_1 measurements, can be best fitted with single or slightly stretched exponentials rather than by a sum of two (single) exponential functions.

As a last remark, a slight asymmetry of the static line shapes of the samples with x = 2 and x = 3 recorded at 333 K can be seen; this is indicated by the small arrow drawn in Figure 3b. The shoulder showing up at negative ppm values reflects those Li ions residing on 16c sites nearby the Ti^{3+} centers. This component can be clearly resolved via ^{6}Li (as well as ^{7}Li) magic angle spinning NMR; it appears as a broad signal at NMR shifts ranging from −9 to −10 ppm when aqueous LiCl is used as a secondary reference; here, the primary reference was lithium acetate. Such a relatively large NMR shift can be understood as a direct consequence of the strong and localized Li^+−e^- associations described by Lu et al.[26]

3.2. ^{7}Li NMR Spin−Lattice Relaxation Rates. In Figure 6 the ^{7}Li NMR SLR rates recorded in the laboratory (a) and rotating frame (b) of reference are plotted vs the inverse temperature. The rates of the host material $Li_4Ti_5O_{12}$, when measured at a ^{7}Li Larmor frequency of 194.3 MHz, follow classical temperature behavior. Below 300 K a nondiffusive, weaker-than-activated regime shows up. The corresponding rate $1/T_{1,bgr}$ shows a $T^{1+\beta}$ behavior with β = 1.31(1); constant loss behavior, which refers to a frequency independent imaginary part of the complex permittivity $\hat{\epsilon}$, would lead to β = 1.[52] Thus, besides strictly localized Li motions, lattice vibrations and coupling to paramagnetic impurities may give rise to a β larger than 1. Nevertheless, in this low-T region successful translational jump processes are rare.

This behavior changes when the rates above 300 K are considered. They increase with temperature and follow the flank of a diffusion-induced rate peak. The associated activation energy of only 0.35 eV is linked with local motions of the Li spins including, for example, forward−backward jumps between 8a and vacant 16c sites. Note that the slope is also affected by correlation effects due to, e.g., electric Coulomb interactions. Hence, it does not reflect long-range ion transport that would be probed via conductivity spectroscopy in the frequency limit $\omega \rightarrow 0$.

DOI: 10.1021/cm504564k
Chem. Mater. 2015, 27, 1740−1750

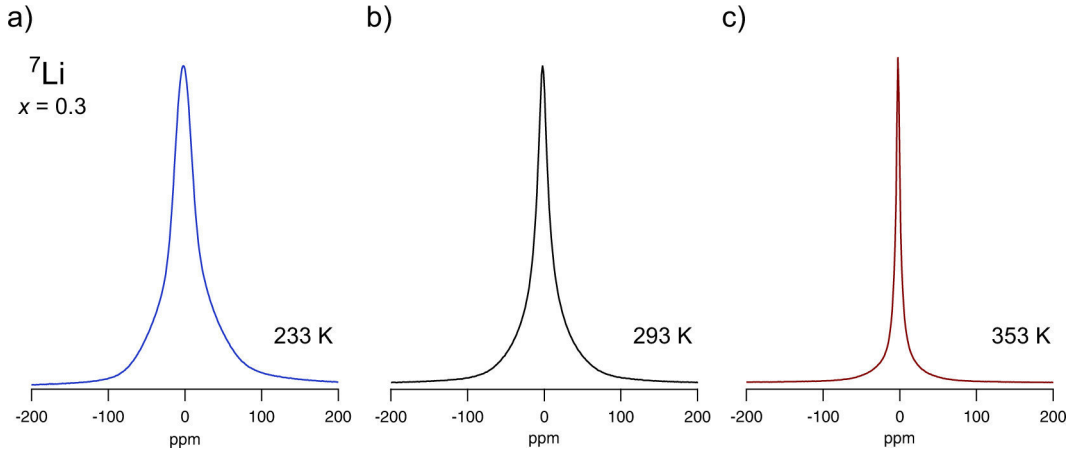

Figure 5. (a–c) ^{7}Li NMR spectra of $Li_{4+x}Ti_5O_{12}$ with x = 0.3 recorded at the temperatures indicated. With increasing T significant line narrowing sets in indicating rapid Li exchange at low Li contents. Noteworthy, the spectra have been recorded at extraordinary long recycle delays, t_d = 100 s ($\gg 5T_1$), to reveal any slowly relaxing components. Since they coincide with those recorded at t_d = 2 s ($\approx 5T_1$) shown in Figure 3, such components are evidently absent; see the discussion in section 3.2.3. Quadrupole intensities showing up at 233 K as a broad *foot* of the spectrum seem to be averaged due to rapid Li exchange at elevated temperatures; see section 3.2 for the quantification of the absolute Li jump rate via spin-lock NMR relaxometry.

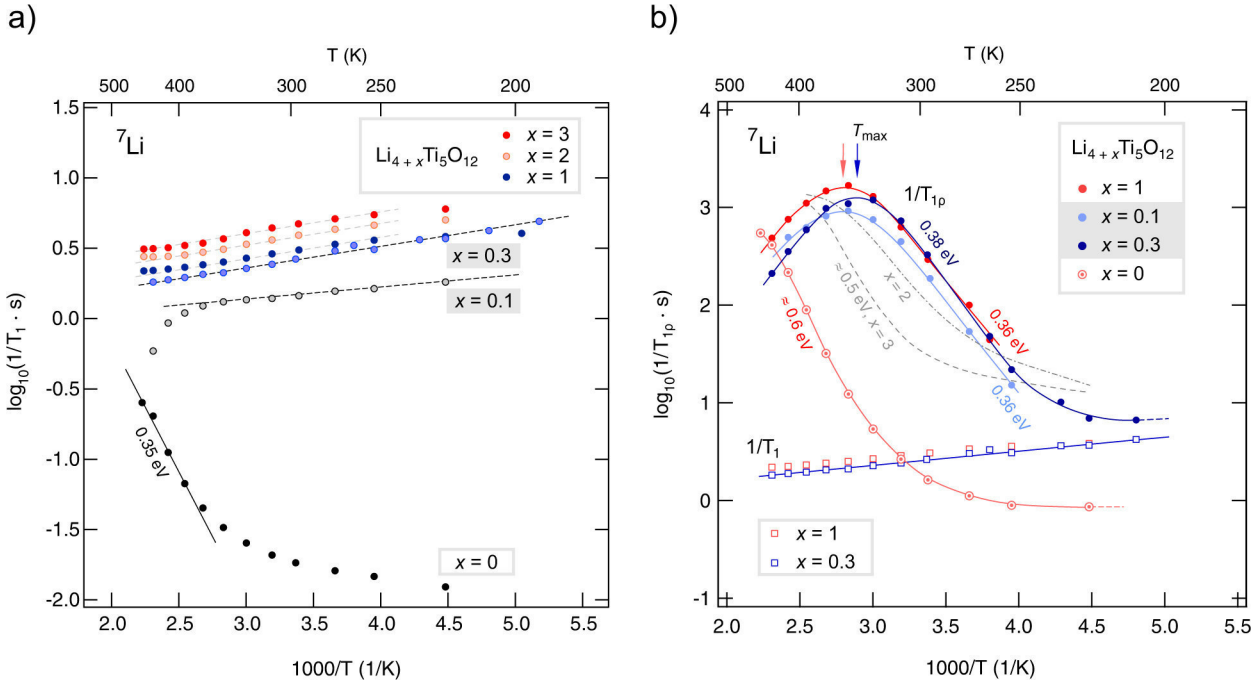

Figure 6. (a) ^{7}Li NMR relaxation rates of $Li_{4+x}Ti_5O_{12}$ that have been recorded in the laboratory frame of reference. Beginning with x = 0 they reveal the typical behavior seen for many ion conductors: a low-T nondiffusion induced background and an Arrhenius-activated flank (0.35 eV). This is in contrast to the samples with x > 0. Most likely they reveal Curie behavior and/or the segregation into a Li poor and Li rich phase well below room temperature as it was seen by neutron diffraction measurements.[20]

In contrast to SLR NMR performed at frequencies in the MHz range, $1/T_{1\varrho}$ rates, which have been recorded at locking frequencies in the kHz regime, are sensitive to slower Li motions; concomitantly they trace ion dynamics on a longer length scale as compared to $1/T_1$. Consequently, if an irregular potential landscape is present, larger (mean) activation energies are expected to be probed via $1/T_{1\varrho}$ measurements. Indeed this is the case here; from the slope of the low-T flank of the rate peak $1/T_{1\varrho}(1/T)$ an activation energy E_a of ca. 0.62 eV is obtained; see also the analysis presented in Figure 7.

Contrary to the nonlithiated host material, the rates $1/T_1$ of the samples with Li contents of x = 0.1 and larger reveal temperature dependencies that can be ascribed to paramagnetic relaxation according to Curie–Weiss behavior. One should keep in mind that additionally to the coupling of the Li spins with the Ti^{3+} centers generated, upon cooling, the solid solutions of $Li_{4+x}Ti_5O_{12}$ tend to segregate into Li rich ($Li_7Ti_5O_{12}$) and Li poor $Li_4Ti_5O_{12}$ regions. This has has been verified by neutron diffraction as mentioned above.[20] Since for $Li_7Ti_5O_{12}$ a shorter T_1 is expected than for $Li_4Ti_5O_{12}$, with decreasing T the formation of $Li_7Ti_5O_{12}$ domains might cause an overall increase of $1/T_1$. Above 250 K, however, the segregation process should play a minor role.

DOI: 10.1021/cm504564k
Chem. Mater. 2015, 27, 1740–1750

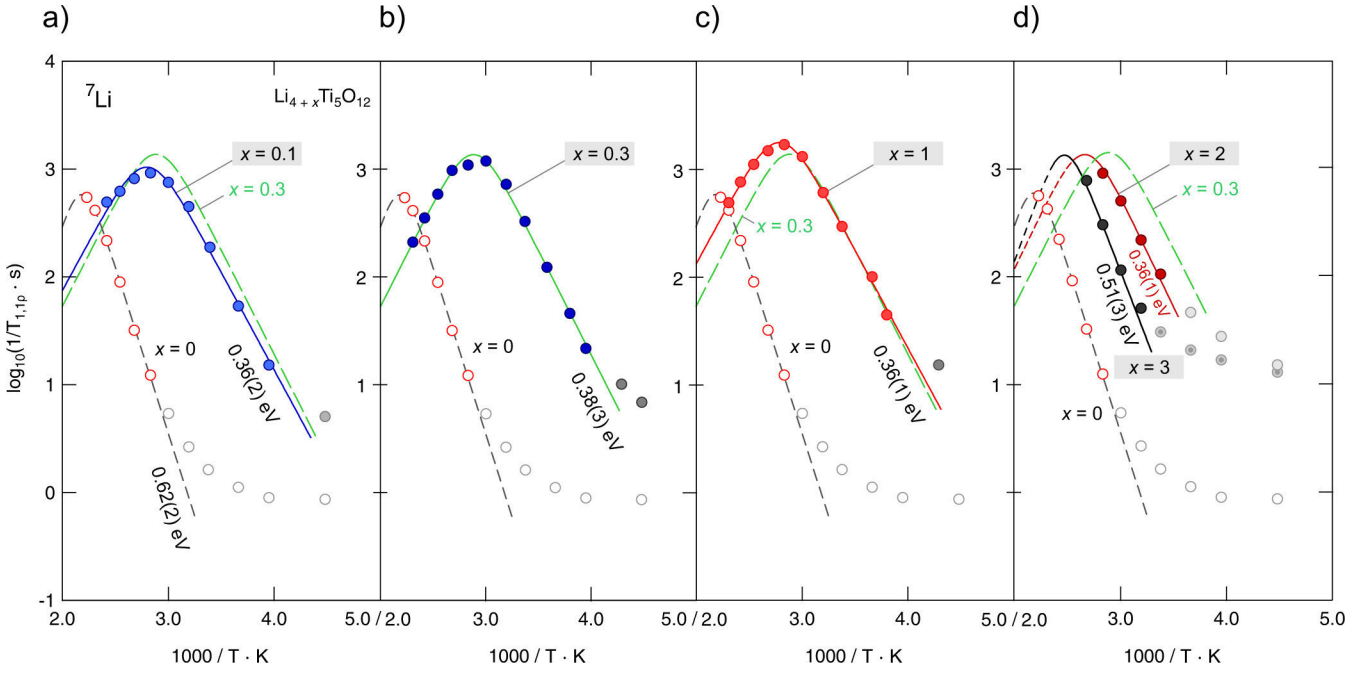

Figure 7. (a–d) ^{7}Li NMR SLR peaks of polycrystalline $Li_{4+x}Ti_5O_{12}$ recorded at a locking frequency of $\omega/2\pi$ = 20 kHz using a Larmor frequency of 194.3 MHz. The solid lines show fits with a BPP-type spectral density function being based on a single exponential correlation function. This leads to symmetric rate peaks; thus, activation energies (0.62–0.36 eV) can be obtained from the slope of the low-T flank, i.e., in the limit $\omega_1\tau \gg 1$. The individual peaks are compared with the SLR NMR rates of the sample with x = 0. The green dashed line in (a, c, and d) reflects the position and shape of the peak for x = 0.3.

Due to the increasing number fraction of Ti^{3+} centers with increasing x, the rates $1/T_1$ steadily increase at fixed temperature (Figure 6a). This is consistent with the line broadening observed in the rigid lattice regime, as presented above.

Most importantly, when regarding the corresponding diffusion-induced rates $1/T_{1\varrho}$ shown in Figure 6b), a drastic increase in Li ion dynamics is already observed for the sample with x = 0.1. While for the nonlithiated sample only the low-T flank of the rate peak is accessible up to temperatures of 450 K, for $Li_{4.1}Ti_5O_{12}$ almost the complete rate peak could be recorded. In general, the maximum in $1/T_{1\varrho}(1/T)$ shows up if the (mean) Li jump rate $1/\tau$, which is within a factor of 2 identical with the mean correlation rate $1/\tau_c$ of the underlying hopping correlation function, becomes similar to the angular locking frequency ω_1, i.e., $\omega_1\tau_c \approx 0.5$; in our case we have ω_1 = 125.7 kHz. Hence, at the temperatures T_{max} (see Figure 6b) where the rate passes through the rate maximum, the correlation rate $1/\tau_c$ is in the order of 2.5 × 10^5 s^{-1}; this corresponds to a mean residence time τ of the Li ions of ca. 4 μs (at T_{max} = 354(5) K for x = 0.1). Such a relatively high rate is capable to average EFGs at the nuclear site. In $Li_{4.1}Ti_5O_{12}$ the corresponding quadrupole splitting can be estimated to be in the order of 20 kHz (see above).

Increasing x to 0.3 shifts the rate peak toward even lower temperatures (T_{max} = 336(5) K). Remarkably, at x = 1 a revised point has already been passed and the rate peak shifts back toward larger T values; for x = 1 we obtained T_{max} = 360(5) K. This behavior is also seen for the samples with even larger Li contents; the low-T flanks appear at higher temperatures which directly reveals a slow down of Li diffusivity. Thus, starting from slow Li ion dynamics (x = 0), Li^+ diffusivity sharply increases at small x values reaching its maximum near x = 0.3; further lithiation, however, clearly slows down cation mobility once again (x = 1) until at larger Li contents, see x = 2 and particularly x = 3, a significant reduction in Li ion mobility is observed. The Li diffusivity finally reached for rock-salt type $Li_7Ti_5O_{12}$ is, however, higher than that found for the starting material with x = 0. The latter finding has recently been pointed out by detailed DFT calculations of Ziebarth et al.;[53] moreover, it has been shown in a qualitative way via temperature-variable T_2 NMR measurements by Wagemaker et al.[49]

The maximum passed through in Li diffusivity is also nicely reflected by the activation energies, which can be deduced by analyzing the rate peaks recorded. Whereas in Figure 6b the solid lines, comprising also the background rates, are simply drawn to guide the eye, in Figure 7 the $1/T_{1\varrho}(1/T)$ data have been analyzed with an NMR relaxation model according to Bloembergen, Purcell, and Pound (BPP). Here, a single-term fit, which is based on a Lorentzian shaped spectral density function $J(\omega_1) \propto 1/T_{1\varrho}$, served as a good approximation for our analysis: $1/T_{1\varrho} \propto \tau_c/[1 + (2\omega_1\tau_c)^\beta]$ with $1 < \beta \leq 2$. τ_c denotes the correlation time that is usually Arrhenius activated (see below). The best fits obtained are fully symmetric, i.e., β turned out to be 2. This points to an overall exponential (motional) correlation function $G(t)$ governing Li motion in $Li_{4+x}Ti_5O_{12}$ with x = 0.1, 0.3, and 1. Note that $J(\omega_1)$ is obtained from $G(t)$ via Fourier transformation.

Solid and dashed lines in Figure 7 show the BPP fits obtained; unfilled symbols or those in greyscale have been omitted for the analysis since they are not purely induced by Li jump diffusion. From x = 0 to x = 0.1 the BPP activation energy sharply decreases from E_a = 0.62 to 0.3 eV. For the samples with higher Li content (x = 0.3, 1) E_a takes similar values; upon further lithiation the flanks shift toward higher T and E_a increases again (0.51(3) eV for $x \rightarrow 3$). Thus, although Li diffusivity passes through a maximum, over a relatively large x range the mean value of E_a is almost constant. This is in

DOI: 10.1021/cm504564k
Chem. Mater. 2015, 27, 1740–1750

reasonable agreement with the results presented by Wagemaker and co-workers (0.31 eV, x = 0.3, 1, 2) deduced from T_2 measurements.[49] Consequently, the differences in Li hopping from x = 1 to x = 2 (and further to x = 3) have been looked for in the prefactor, τ_0^{-1}, of the underlying Arrhenius relation, $\tau^{-1} = \tau_0^{-1}\exp(-E_a/(k_B T))$. In particular, τ_0^{-1} is expected to increase from x = 1 to x = 2, and indeed this is observed (Table 1). Remarkably, the disordered samples with $0 < x < 3$ show rather small prefactors τ_0^{-1}, while for the end-members (x = 0 and x = 3) the factors are in the usual range of phonon frequencies (10^{13}–10^{14} Hz).

Table 1. Activation Energies and Pre-Factors Obtained from the BBP Fits Shown in Figure 7

$Li_{4+x}Ti_5O_{12}$	E_a, eV	τ_0, s	T_{max}, K
x = 0	0.62(2)	7.3×10^{-13}	>450
0.1	0.36(2)	3.4×10^{-11}	354(5)
0.3	0.38(2)	1.0×10^{-11}	336(5)
1	0.36(1)	3.4×10^{-11}	360(5)
2	0.36(1)	6.6×10^{-12}	>370
3	0.51(3)	8.8×10^{-13}	>400

3.2.1. Comparison with Results from Other NMR Studies Previously and Recently Published. Activation energies for x = 1 and x = 2 are in reasonable agreement with the value (0.43(2) eV) probed previously by our group on a $Li_{5.6}Ti_5O_{12}$ sample prepared in two different ways, viz., chemically with *n*-BuLi and electrochemically. Small differences in E_a have to be looked for in differences of the starting material such as crystallite size, crystallinity, morphology, and defect densities. Moreover, the value 0.43 eV was deduced from a complete peak $1/T_{1\varrho}(1/T)$ recorded at 13.8 kHz; compared with 0.36 eV for x = 1, the somewhat larger value for x = 1.6 already points to an increase in E_a reaching ca. 0.51 eV at x = 3.

The activation energies reported by Hain et al.,[51] who published a similar ^{7}Li NMR study, are 0.55(1) eV (x = 0), 0.39(1) eV (x = 2), and 0.45(1) eV (x = 3). The value for nonlithiated LTO turned out be rather low; it is in contrast to what is usually found by $1/T_{1\varrho}$ measurements and differs from results obtained by impedance spectroscopy in the low frequency limit. While E_a of $Li_6Ti_5O_{12}$ is similar to our result, we observed a steeper increase in activation energy for rock-salt $Li_7Ti_5O_{12}$.

Much more striking is another fact: Although Hain et al. also used LTO purchased from Süd-Chemie,[51] as we have done here and in our previous study that appeared in 2007,[21] the NMR relaxation rates presented by them are shifted toward much higher temperatures. They pass through peak maxima at temperatures as high as 570 K. For comparison, this is at 1.75 on the $1/T$ scale in Figure 7. In addition, the sample with x = 3 studied by Hain et al. suffers from interfering background relaxation while for the sample with x = 0 only four $1/T_{1\varrho}$ NMR data points were measured over a temperature range from 300 to 660 K.[51] Besides these peculiarities we should note that some of the samples of the investigation by Hain et al. were prepared electrochemically. Therefore, besides crystallinity, morphology, defect concentration (including also oxygen vacancies), and differences in NMR measurement procedures, at first the question arises whether the way Li is inserted in LTO can affect the final result. Let us keep in mind that samples prepared electrochemically may contain additives such as binders and conductive carbon. Since at sufficiently large potentials the formation of an SEI (see above) is almost negligible—in many cases LTO is called an SEI-free anode material—we do not expect that a possible thin SEI layer influences the NMR result as large as the additives mentioned.

To answer this question, we would like to refer to our previous study[21] focusing on a sample with x = 1.6 synthesized via both preparation routes—chemically and electrochemically. If properly prepared, bulk properties of $Li_{4+x}Ti_5O_{12}$ are available nonetheless. As we have shown previously, there was *no* difference observed in $1/T_{1\varrho}(1/T)$ for the two samples. The assumption of Aldon et al.[54] anticipating the occupancy of 48f sites in the case of *chemically* lithiated LTO (see the 48f tetrahedra marked in Figure 1) seems to be not supported by the neutron diffraction study carefully carried out by Wagemaker et al.[20] Of course, this does not rule out the possibility, or necessity, that 48f sites[19,54] are temporarily occupied or used as transition states when the Li ions jump from 16d to 16c sites and *vice versa* (see above).[19,53]

3.2.2. Comparison with Results from Theory, Self-Diffusion Coefficients. Let us come back to the activation energies found here and compare them with those calculated in various studies. The studies published so far have also focused on possible Li diffusion pathways in the host material LTO and in the lithiated phases; particular attention was put on the $Li_7Ti_5O_{12}$ phase. As has been pointed out by Ziebarth et al.,[53] who did calculations based on DFT (referring to 0 K), the random occupancy of 16d sites by both Li and Ti results in a couple of energetically different diffusion pathways leading to a distribution of activation energies. Moreover, this also includes that the profiles of the migration pathways are asymmetric. Here, via spin–lattice relaxation NMR *only* mean values over the possible migration pathways can be probed. Nevertheless, the calculations predict activation barriers for $Li_4Ti_5O_{12}$ ranging from 0.3 to 0.48 eV when pathways are considered that involve hops between 8a and 16c sites. Most interestingly, Li^+ exchange from 16d toward an empty 8a position is reported to be governed by an activation energy of approximately 0.92 eV. Hence, a mean value larger than 0.48 eV can be expected for x = 0. Indeed this is the case here and in our previous study. Moreover, via ^{7}Li spin-alignment echo NMR we were able to trace extremely slow Li exchange processes; the associated activation energy, which could be precisely measured via SAE NMR two-time correlation functions, was 0.86 eV.[19] Ziebarth et al. proposed that Li vacancies are trapped preferentially at 16d sites in the nonlithiated host material causing low Li diffusivity.[53] This is in contrast to the situation for x = 3 for which no trapping is reported; most of the activation energies calculated range from 0.2 to 0.51 eV. The involvement of 16d sites, however, leads to barriers between 0.56 and 0.94 eV.[53]

The results by Chen et al.,[55] who did similar ab initio calculations, as well as that of van der Ven and co-workers,[56] point to the same direction. Although only few pathways have been studied by Chen et al.,[55] the activation energies calculated for several Li migration routes in spinel-type LTO (x = 0) turned out to be larger than those predicted for $Li_7Ti_5O_{12}$ crystallizing with the rock-salt structure. In particular, for the diffusion pathway 8a–16c–8a′ in $Li_4Ti_5O_{12}$ the activation energy turned out to be 0.7 eV; for the pathway 16c–48f–16c′ (see Figure 1) a value of 1.0 eV was given. This confirms the relatively high barriers found for the sample with x = 0 here and in our previous SAE NMR study; note that SAE NMR is sensitive to very slow Li diffusion processes. For comparison, the barriers from macroscopic ac impedance spectroscopy,

DOI: 10.1021/cm504564k
Chem. Mater. 2015, 27, 1740–1750

which may also be affected by grain boundary effects, point to values as high as 0.96 eV.[9,19] Worth mentioning, the value calculated by Chen et al.[55] is, however, larger than those predicted by Ziebarth et al.[53] and by Bhattacharya et al.[56] Comparing the theoretical studies presented so far, there is still some disagreement about the existence and energetic level of metastable transition states.

Finally, the $1/T_{1\varrho}(1/T)$ peaks can be used to estimate self-diffusion coefficients from the hopping correlation rates directly determined (see above). With the value of 2.5×10^5 s^{-1}, as it has been found at 354(5) K for $x = 0.1$ (see above), with the Einstein−Smoluchowski equation a diffusion coefficient in the order of 1.35×10^{-15} m^2 s^{-1} can be estimated. The Einstein−Smoluchowski relation links τ with the self-diffusion coefficient D.[57] For 3D uncorrelated motion[24] we have $D = a^2/(6\tau)$; a denotes the (mean) jump distance.[57] Here, we have used a = 1.8 Å that is a good approximation for the 8a−16c distance. Using the Nernst−Einstein equation to relate D with the ion conductivity σ_{ion}, this corresponds to $\sigma_{ion} \approx 10^{-6}$ S cm^{-1} at 354 K ($Li_{4.1}Ti_5O_{12}$). For $x = 0.3$ the same value is reached at somewhat lower T; see above. Values in the order of 10^{-6} S cm^{-1} reflect transport properties that are characteristic for solids with modest ion conductivity.

3.2.3. Homogenous vs Nonhomogenous Spin-System. As a last remark, we recall the reader's attention to the nanodomain picture of $Li_{4+x}Ti_5O_{12}$. As has been shown by neutron diffraction,[20] the separation into $Li_4Ti_5O_{12}$ and $Li_7Ti_5O_{12}$ is kinetically driven by electrochemical lithiation (vide supra). As mentioned above, Lu et al. used STEM experiments to visualize the corresponding domain structure.[26] The phases, however, appear to be unstable at room temperature leading to a homogeneous solid solution.[20] In contrast, for chemical lithiation, usually carried out at ambient for several days, a morphology without a significant domain structure is expected. The vigorous reaction with *n*-BuLi might cause significant local heating leading to homogenized samples. Significant phase segregation, however, is anticipated at 100 K and below;[20] such a T range has not been covered here. Interestingly, the ^{7}Li 2D MAS exchange measurements presented by Wagemaker et al. on chemically lithiated samples have been interpreted in terms of a *nano*-domain structure with domain sizes of less than approximately 10 nm at 373 K.[49] The rather long correlation times in the ms time regime (2.3 ms) as deduced from ^{7}Li NMR exchange spectroscopy experiments on $Li_6Ti_5O_{12}$ (373 K) lead to this conclusion. In the meantime, however, it has been shown by Indris and co-workers that ^{7}Li 2D MAS NMR is largely influenced by spin-diffusion, at least below 323 K; note that very similar correlation times have been reported (2.1 ms, $Li_6Ti_5O_{12}$ (323 K)) even for samples with different compositions ($x = 2$, $x = 4$).[51]

Hence, in our opinion the "NMR picture" of nanodomains, as it was claimed from 2D exchange experiments, rests on unsound footing at least for samples prepared via chemical lithiation. We have to ask what signature a domain structure would leave behind in NMR relaxation rates and line shapes. Even if we (generously) consider spin-diffusion effects with correlation rates in the microsecond range, nanometer-sized Li rich domains ($Li_7Ti_5O_{12}$) embedded in $Li_4Ti_5O_{12}$ should result in a two-reservoir spin-system with spatially separated ensembles of relatively fast ($x > 0$) and slow ($x = 0$) Li ions. In other words, the transients of T_1 and $1/T_{1\varrho}$ should be composed of two contributions with two distinct SLR rates. In the case of T_1 the two rates should differ by approximately 2 orders of magnitude when ambient conditions are regarded (see Figure 6).

To shed light on this issue we have to ask the following question: Did we overlook the missing slowly relaxing component in our SLR NMR measurements for the samples with $x > 0$? Or, in other words, did we selectively excite only those Li ions residing in the Li rich (mixed conducting) domains proposed? To check whether there is a hidden component M_{slow} that behaves like that of the end-member $Li_4Ti_5O_{12}$, we carried out further SLR measurements taking advantage of extremely long waiting times t_d (see Figure 8).

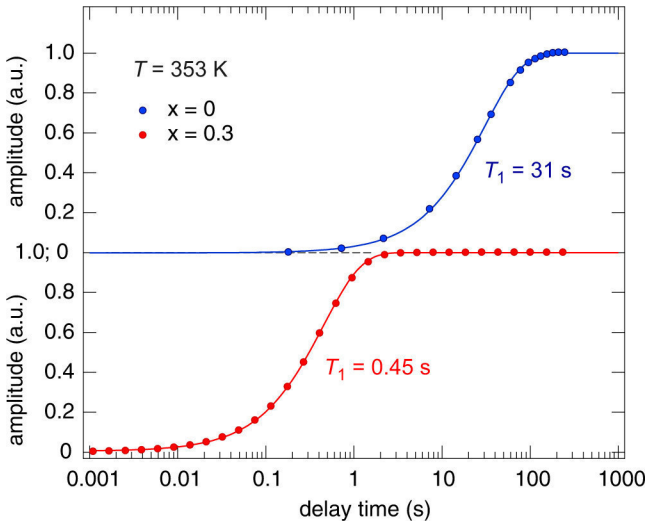

Figure 8. ^{7}Li NMR SLR magnetization transients of $Li_{4+x}Ti_5O_{12}$ with $x = 0$ and $x = 0.3$. Data have been recorded at 353 K for extraordinary long waiting times t_d of up to 250 s. The corresponding rates $1/T_1$ differ by approximately 2 orders of magnitude; see also Figure 6. Solid lines show fits with single exponential functions. Most importantly, the transient of the sample with $x = 0.3$, which was followed over six decades, already reached full saturation after 3 s. Any second contribution from a spatially separated $Li_{4+x}Ti_5O_{12}$ phase is missing. Such a contribution should significantly show up at delay times larger than 10 s. For $x = 0.3$, this Li poor phase would form the main volume of the sample. The transients shown here give evidence that all the 8a and 16c Li ions in $Li_{4.3}Ti_5O_{12}$ sense the Li^+−e^- coupling because of localized but, most likely, homogeneously distributed Ti^{3+} centers.

Even if we extend t_d to be much larger than $6T_1$ (see section 2), exactly the same single exponentially decaying transients, M_{fast}, were obtained as measured for $t_d = 6T_1$. As an example, the T_1 transients of $Li_{4.3}Ti_5O_{12}$ recorded at 293 and 353 K with t_d values of up to 100 s resulted in single exponentials with effective SLR rates in the order of T_1 = 450 ms only; see Figure 8. A magnetization component M_{slow} characterized by T_1 = 31 s (293 K), as expected for large domains of $Li_4Ti_5O_{12}$ completely free of Ti^{3+} centers, is most certainly absent. Note that one cannot distinguish between differently mobile Li ions residing regularly on 8a and 16d sites also. Most importantly, the comparison of the two transients proved that within our NMR relaxometry measurements, particularly including the $1/T_{1\varrho}$ data, the *entire* Li ensemble has been nonselectively excited. Note that the introduction of paramagnetic impurities during synthesis is a common practice to reduce T_1. Here, this effect enables us to excite the whole spin system; therefore, the diffusion-induced rate peaks $1/T_{1\varrho}(1/T)$ seem to reflect all of the Li ions present in the oxide. This view is supported by the

DOI: 10.1021/cm504564k
Chem. Mater. 2015, 27, 1740−1750

observation of fully motionally narrowed NMR lines at 373 K and above. Spin-diffusion would not cause such line narrowing.

In summary, so far, we could not find any convincing indications from SLR NMR for two magnetically decoupled or even spatially separated spin ensembles that can be described by distinct Li ion dynamics. Quite the contrary, even at very low x values, see particularly the sample with $x = 0.3$, *all* of the 8a and 16c Li ions seem to be mobile on the NMR time scale as evidenced by $1/T_{1\varrho}$ measurements. From a dynamic point of view, at least up to the composition of $x = 1$, a single and entirely homogeneous spin-system was detected. This strongly points to the formation of a solid solution with homogeneously distributed Li ions interstitially occupying the empty 16c sites in the spinel structure (Figure 1). Differently speaking, the Ti^{3+} centers generated during lithiation are expected to be distributed over the whole crystalline areas.

For larger Li contents ($x = 2$ and $x = 3$), cf. the NMR lines in Figure 3 b, so-called heterogeneous motional line narrowing is seen. To assign this feature to a domain structure is a speculative interpretation. As mentioned above, many structurally uniform spin-systems reveal complex, heterogeneous ion dynamics. A distribution of jump rates does not necessarily need a two-phase or many-phase picture on a nanometer length scale to be explained. In such cases a nonexponential (non-Debye) motional correlation function might be expected; here, however, this is not observed. The "simple" (isotropic) BPP model being based on a single exponential correlation function is sufficient to fully describe the $1/T_{1\varrho}$ peaks recorded. Moreover, we also checked the shape of the corresponding transients, as it was done for the $1/T_1$ magnetization curves of the sample with $x = 0.3$. Their shapes do not hint to a two-phase spin system. It is likely that the formation of Ti^{3+} centers affects the entire spin−lattice relaxation behavior in both the rotating and laboratory frame of reference. Hence, once again, all of the Li spins contribute to the diffusion-induced $1/T_{1\varrho}$ peaks obtained for $x = 2$ and $x = 3$.

Of course, the view drawn by NMR relaxometry should not be mixed with (i) the phase segregation observed and proven by neutron diffraction carried out at temperatures being much lower than ambient[20] and (ii) the known kinetically induced phase separation via electrochemical lithiation.[20] We assume that Lu et al.[26] (see above) studied a sample that was electrochemically intercalated to make visible the Li poor and Li rich phases via STEM. Although it is declared differentially in the main text, it was stated in the Supporting Information of their recent paper[26] that they performed STEM investigations on electrochemically lithiated samples

As a last remark, let us note that during the analysis the samples are heated above 423 K. Starting with a two-phase system such heat-treatment could cause homogenization of the Li environment. Here, however, even at room temperature or below, we did not find any evidence for a distinct two-phase scenario. In other words, the measurement order did not influence our analysis. The reproducibility of the results has been checked by several consecutive heating and cooling runs.

4. SUMMARY AND CONCLUSION

$Li_{4+x}Ti_5O_{12}$ belongs to one of the most promising anode materials. Zero-strain and highly reversible Li insertion/deinsertion guarantees an extremely long cycle life of lithium-ion batteries with moderate capacities. While nonlithiated $Li_4Ti_5O_{12}$ is a rather poor ion conductor with negligible electronic conductivity, small amounts of Li inserted ($x = 0.1$, $x = 0.3$) transform the material in a mixed conducting oxide that shows greatly improved Li ion diffusivities.

The steep increase in Li ion hopping rates, which is associated by a significant reduction of the mean activation barrier E_a from 0.62 to 0.36 eV ($x = 0.1$), was directly followed on the Ångström length scale by both ^{7}Li NMR line shape measurements and ^{7}Li NMR spin−lattice relaxation experiments. From the latter, activation energies and absolute hopping rates could be deduced. For the end-member, that is, rock-salt type $Li_7Ti_5O_{12}$, Li diffusivity slows down once again and E_a increases reaching approximately 0.51 eV.

We attribute the steep increase in Li diffusivity to the generation of strong repulsive Coulomb interactions because of the simultaneous occupation of (face-sharing) 8a and 16c sites within the spinel structure of LTO. Coupling of Li^+ and e^- migration is likely since upon lithiation LTO turns into a mixed conductor and both electronic and ionic conduction occur simultaneously. The significant reduction of the elementary Li ion jump barriers probed via NMR helps us understanding the superior insertion behavior of LTO at the early stages of Li insertion. Especially, it might be useful to consider also a solid-solution model if we want to understand the flat insertion potential observed in LTO.

Worth noting, the results from ^{7}Li NMR relaxometry and line shape analysis obtained refer to solid solutions of $Li_{4+x}Ti_5O_{12}$. Even if performed at sufficiently long delay times (or waiting times), our findings do not entail any evidence for the formation of a two-phase material with spatially extended and largely separated Li rich and Li poor regions. Excluding fast spin-diffusion being effective over large distances, there are no indications for the presence of two magnetically decoupled spin-ensembles in samples with $x \geq 0.1$; this is underlined by the observation of fully motionally narrowed NMR lines that appear upon Li intercalation; see $x = 0.1$ and $x = 0.3$.

The formation of a kinetically induced two-phase material, however, might be expected for samples that have been prepared electrochemically.[20,26] In contrast, in the case of *chemically* lithiated LTO, which we have synthesized at ambient temperature by treatment with *n*-BuLi, it seems likely that a homogeneous distribution of Li ions among the 8a and 16c sites is present at sufficiently high temperatures; such a scenario fully agrees with previous results from neutron diffraction measurements.[20] Quite recently, Pang et al.[23] have even used the solid solution model to explain their results from in situ neutron diffraction on Li ion transport in LTO working as electrode material in electrochemical cells.

AUTHOR INFORMATION

Corresponding Authors

*(W.S.) E-mail: w.schmidt@tugraz.at.

*(M.W.) E-mail: wilkening@tugraz.at.

Notes

The authors declare no competing financial interest.

ACKNOWLEDGMENTS

We thank our colleagues at the TU Graz for valuable discussions. Moreover, we gratefully acknowledge SüdChemie for providing the EXM 1037 sample. Financial support by the Austrian Federal Ministry of Science, Research and Economy, and the National Foundation for Research, Technology and Development is gratefully acknowledged. Moreover, we thank

DOI: 10.1021/cm504564k
Chem. Mater. 2015, 27, 1740−1750

the Deutsche Forschungsgemeinschaft (DFG) (Research Unit 1277, Grant No. WI3600/2-2 and 4-2) for financial support.

REFERENCES

(1) Whittingham, M. S. *Prog. Solid State Chem.* **1978**, *12*, 41−99.
(2) Whittingham, M. S. *Chem. Rev.* **2004**, *104*, 4271−4301.
(3) Aricó, A. S.; Bruce, P.; Scrosati, B.; Tarascon, J.-M.; Schalkwijc, W. V. *Nat. Mater.* **2005**, *4*, 366−377.
(4) Armand, M.; Tarascon, J.-M. *Nature* **2008**, *451*, 652−657.
(5) Palacín, M. R. *Chem. Soc. Rev.* **2009**, *38*, 2565−2575.
(6) Colbow, K.; Dahn, J.; Haering, R. *J. Power Sources* **1989**, *26*, 397−402.
(7) Ferg, E.; Gummow, R. J.; de Kock, A.; Thackeray, M. M. *J. Electrochem. Soc.* **1994**, *141*, L147−L149.
(8) Ohzuku, T.; Ueda, A.; Yamamoto, N. *J. Electrochem. Soc.* **1995**, *142*, 1431−1435.
(9) Haetge, J.; Hartmann, P.; Brezesinski, K.; Janek, J.; Brezesinski, T. *Chem. Mater.* **2011**, *23*, 4384−4393.
(10) Zhu, G.-N.; Wang, Y.-G.; Xia, Y.-Y. *Energy Environ. Sci.* **2012**, *5*, 6652−6667.
(11) Yi, T.-F.; Jiang, L.-J.; Shu, J.; Yue, C.-B.; Zhu, R.-S.; Qiao, H.-B. *J. Phys. Chem. Solids* **2010**, *71*, 1236−1242.
(12) Xia, H.; Luo, Z.; Xie, J. *Nanotechnol. Rev.* **2014**, *3*, 161−175.
(13) Chen, S.; Xin, Y.; Zhou, Y.; Ma, Y.; Zhou, H.; Qi, L. *Energy Environ. Sci.* **2014**, *7*, 1924−1930.
(14) Thackeray, M. *J. Electrochem. Soc.* **1995**, *142*, 2558−2563.
(15) Yonglong, Z.; Xuebu, H.; Yunlan, X.; Mingliang, D. *Acta Chim. Sinica* **2013**, *71*, 1341−1353.
(16) He, Y.-B.; Li, B.; Liu, M.; Zhang, C.; Lv, W.; Yang, C.; Li, J.; Du, H.; Zhang, B.; Yang, Q.-H.; Kim, J.-K.; Kang, F. *Sci. Rep.* **2012**, *2*, 913−1−913−8.
(17) Bernhard, R.; Meini, S.; Gasteiger, H. A. *J. Electrochem. Soc.* **2014**, *161*, A497−A505.
(18) Li, W.; Li, X.; Chen, M.; Xie, Z.; Zhang, J.; Dong, S.; Qu, M. *Electrochim. Acta* **2014**, *139*, 104−110.
(19) Wilkening, M.; Amade, R.; Iwaniak, W.; Heitjans, P. *Phys. Chem. Chem. Phys.* **2006**, *9*, 1239−1246.
(20) Wagemaker, M.; Simon, D. R.; Kelder, E. M.; Schoonman, J.; Ringpfeil, C.; Haake, U.; Lützenkirchen-Hecht, D.; Frahm, R.; Mulder, F. *Adv. Mater.* **2006**, *18*, 3169−3173.
(21) Wilkening, M.; Iwaniak, W.; Heine, J.; Epp, V.; Kleinert, A.; Behrens, M.; Nuspl, G.; Bensch, W.; Heitjans, P. *Phys. Chem. Chem. Phys.* **2007**, *9*, 6199−6202.
(22) Laumann, A.; Boysen, H.; Bremholm, M.; Fehr, K. T.; Hoelzel, M.; Holzapfel, M. *Chem. Mater.* **2011**, *23*, 2753−2759.
(23) Pang, W. K.; Peterson, V. K.; Sharma, N.; Shiu, J.-J.; Wu, S.-h. *Chem. Mater.* **2014**, *26*, 2318−2326.
(24) Dolotko, O.; Senyshyn, A.; Mühlbauer, M. J.; Boysen, H.; Monchak, M.; Ehrenberg, H. *Solid State Sci.* **2014**, *36*, 101−106.
(25) Kitta, M.; Akita, T.; Tanaka, S.; Kohyama, M. J. *Power Sources* **2014**, *257*, 120−125.
(26) Lu, X.; Zhao, L.; He, X.; Xiao, R.; Gu, L.; Hu, Y.-S.; Li, H.; Wang, Z.; Duan, X.; Chen, L.; Maier, J.; Ikuhara, Y. *Adv. Mater.* **2012**, *24*, 3233−3238.
(27) Epp, V.; Wilkening, M. *Phys. Rev. B* **2010**, *82*, 020301-1−020301-4.
(28) Epp, V.; Gün, O.; Deiseroth, H.-J.; Wilkening, M. *Phys. Chem. Chem. Phys.* **2013**, *15*, 7123−7132.
(29) Epp, V.; Nakhal, S.; Lerch, M.; Wilkening, M. *J. Phys.: Condens. Matter* **2013**, *25*, 195402-1−195402-7.
(30) Kuhn, A.; Narayanan, S.; Spencer, L.; Goward, G.; Thangadurai, V.; Wilkening, M. *Phys. Rev. B* **2011**, *83*, 094302-1−094302-11.
(31) Langer, J.; Epp, V.; Heitjans, P.; Mautner, F. A.; Wilkening, M. *Phys. Rev. B* **2013**, *88*, 094304-1−094304-9.
(32) Heitjans, P.; Schirmer, A.; Indris, S. In *Diffusion in Condensed Matter − Methods, Materials, Models*, 2nd ed.; Heitjans, P., Kärger, J., Eds.; Springer: Berlin, 2005; Chapter 9, pp 369−415.
(33) Fukushima, E., Roeder, S. *Experimental Pulse NMR*; Addison-Wesley: Reading, 1981.
(34) Ailion, D.; Slichter, C. P. *Phys. Rev. Lett.* **1964**, *12*, 168−171.
(35) Slichter, C. P.; Ailion, D. *Phys. Rev.* **1964**, *135*, A1099−A1110.
(36) Ailion, D. C.; Slichter, C. P. *Phys. Rev.* **1965**, *137*, A235−A245.
(37) Böhmer, R.; Jeffrey, K.; Vogel, M. *Prog. Nucl. Magn. Reson. Spectrosc.* **2007**, *50*, 87−174.
(38) Böhmer, R.; Jörg, T.; Qi, F.; Titze, A. *Chem. Phys. Lett.* **2000**, *316*, 419−424.
(39) Qi, F.; Jörg, T.; Böhmer, R. *Solid State Nucl. Magn. Reson.* **2002**, *22*, 484−500.
(40) Wilkening, M.; Heitjans, P. *Phys. Rev. B* **2008**, *77*, 024311-1−024311-13.
(41) Jeener, J.; Broekaert, P. *Phys. Rev.* **1967**, *157*, 232−240.
(42) Qi, F.; Diezemann, G.; Böhm, H.; Lambert, J.; Böhmer, R. *J. Magn. Reson.* **2004**, *169*, 225−239.
(43) Abragam, A. *The Principles of Nuclear Magnetism*; Clarendon: Oxford, 1961.
(44) Epp, V.; Gün, O.; Deiseroth, H.-J.; Wilkening, M. *J. Phys. Chem. Lett.* **2013**, *4*, 2118−2123.
(45) Wilkening, M.; Epp, V.; Feldhoff, A.; Heitjans, P. *J. Phys. Chem. C* **2008**, *112*, 9291−9300.
(46) Wohlmuth, D.; Epp, V.; Bottke, P.; Hanzu, I.; Bitschnau, B.; Letofsky-Papst, I.; Kriechbaum, M.; Amenitsch, H.; Hofer, F.; Wilkening, M. *J. Mater. Chem. A* **2014**, *2*, 20295−20306.
(47) Stenina, I. A.; Il'in, A. B.; Yaroslavtsev, A. B. *Inorg. Mater.* **2015**, *51*, 62−67.
(48) Gao, Y.; Wang, Z.; Chen, L. *J. Power Sources* **2014**, *245*, 684−690.
(49) Wagemaker, M.; van Eck, E. R. H.; Kentgens, A. P. M.; Mulder, F. M. *J. Phys. Chem. B* **2009**, *113*, 224−230.
(50) Kartha, J.; Tunstall, D.; Irvine, J. T. *J. Solid State Chem.* **2000**, *152*, 397−402.
(51) Hain, H.; Scheuermann, M.; Heinzmann, R.; Wünsche, L.; Hahn, H.; Indris, S. *Solid State Nucl. Magn. Reson.* **2012**, *42*, 9−16.
(52) Kanert, O.; Küchler, R.; Soares, P. C.; Jain, H. *J. Non-Cryst. Solids* **2002**, *307−310*, 1031−1038.
(53) Ziebarth, B.; Klinsmann, M.; Eckl, T.; Elsässer, C. *Phys. Rev. B* **2014**, *89*, 174301-1−174301-7.
(54) Aldon, L.; Kubiak, P.; Womes, M.; Jumas, J.; Olivier-Fourcade, J.; Tirado, J.; Corredor, J.; Vicente, C. *Chem. Mater.* **2004**, *16*, 5721−5725.
(55) Chen, Y.; Ouyang, C.; Song, L.; Sun, Z. *Electrochim. Acta* **2011**, *56*, 6084−6088.
(56) Bhattacharya, J.; van der Ven, A. *Phys. Rev. B* **2010**, *81*, 104304-1−104304-12.
(57) Mehrer, H. *Diffusion in Solids*; Springer: Berlin, 2006.

DOI: 10.1021/cm504564k
Chem. Mater. 2015, 27, 1740−1750

7.2.2 Discriminating the Mobile Ions from the Immobile Ones in $Li_{4+x}Ti_5O_{12}$: ^{6}Li NMR Reveals the Li^+ Diffusion Pathway and Proposes a Refined Lithiation Mechanism

Das folgende eingereichte Manuskript ergänzt die gewonnenen Erkenntnisse zur Li-Dynamik in LTO aus der ersten Publikation. In den ersten Schritten der Li-Interkalation steigert sich die Li-Diffusivität deutlich, das Material wandelt sich von einem schlechten Ionenleiter mit vernachlässigbarer elektrischer Leitfähigkeit zu einem Mischleiter mit relativ hoher Li-Ionenbeweglichkeit. ^{7}Li-NMR-Messungen der Linienbreiten und ^{7}Li-NMR-Gitter-Relaxationszeitmessungen bestätigen unabhängig voneinander die starke Zunahme der Diffusivität - die Aktivierungsenergie der Niedertemperaturflanke änderte sich von E_a = 0.62 eV (x = 0) zu E_a = 0.36 eV (x = 0.1). Das voll interkalierte $Li_7Ti_5O_{12}$ kristallisiert in der Steinsalz-Struktur, die im Vergleich zum ursprünglichen Spinell keine große Volumendifferenz aufweist. In Richtung x = 3 verlangsamt sich die Li-Diffusivität wieder und die Aktivierungsenergie ändert sich zu E_a = 0.51 eV; Die Li-7-Phase zeigt aber weiterhin eine höhere Li-Diffusivität im Vergleich zu nicht-lithiiertem LTO.

In der Literatur wurde die Frage aufgeworfen, ob es sich bei den Zwischenschritten um eine so genannte *solid solution*[23,64,65] handelt oder ob ein Zweiphasengemisch ($Li_4Ti_5O_{12}$ und $Li_7Ti_5O_{12}$) vorliegt. Unter einer *solid solution* versteht man einen Festkörper, bei dem unterschiedliche Phasenbereiche nicht feststellbar sind und Li homogen in der Kristallstruktur verteilt ist. Um im Falle von x = 0.1 oder x = 0.3 die möglichen langsamen Relaxationskomponenten des reinen LTOs sichtbar zu machen, sind NMR-Relaxationszeitmessungen bei sehr langen Wartezeiten durchgeführt worden, um das extrem langsam relaxierende Spin-System von LTO zu detektieren. Wir fanden jedoch ausschließlich schnelle NMR-Kernspinrelaxation - dies deutet daraufhin, dass im Falle der chemischen Interkalation kein Zweiphasengemisch unwahrscheinlich vorliegt.

Hochauflösende ^{6}Li-MAS-Messungen sollten dazu dienen, die kristallographischen Li-Positionen (8a, 16d, 16c) aufzulösen und als Funktion von x zu analysieren.[33] Die Messungen sollten Aufschluss über Besetzungsverhältnisse, mobile und immobile Li-Ionen bzw. Wanderungspfade liefern. Aus den Ergebnissen kann auf einen ‚verfeinerten' Lithiierungsmechanismus geschlossen werden.

Discriminating the Mobile Ions from the Immobile Ones in $Li_{4+x}Ti_5O_{12}$: ^6Li NMR Reveals the Li^+ Diffusion Pathway and Proposes a Refined Lithiation Mechanism

Walter Schmidt*,†,‡ and Martin Wilkening*,†,‡

†Institute for Chemistry and Technology of Materials, Stremayrgasse 9, Graz University of Technology (member of NAWI Graz), 8010 Graz, Austria

‡Christian Doppler Laboratory for Lithium Batteries, Graz University of Technology, 8010 Graz, Austria

under review: Energy & Environmental Science

Discriminating the Mobile Ions from the Immobile Ones in $Li_{4+x}Ti_5O_{12}$: ^6Li NMR Reveals the Li^+ Diffusion Pathway and Proposes a Refined Lithiation Mechanism

Walter Schmidt*,†,‡ and Martin Wilkening*,†,‡

†Institute for Chemistry and Technology of Materials, Stremayrgasse 9, Graz University of Technology (member of NAWI Graz), 8010 Graz, Austria

‡Christian Doppler Laboratory for Lithium Batteries, Graz University of Technology, 8010 Graz, Austria

ABSTRACT. One of the most widely known anode materials with excellent cycling performance in lithium-ion batteries is zero-strain lithium titanate $Li_4Ti_5O_{12}$ (LTO). This is based on the highly reversible insertion and de-insertion of Li ions varying the composition of $Li_{4+x}Ti_5O_{12}$ from $x = 0$ to $x = 3$. The facile incorporation of Li is tightly connected with bulk Li ion dynamics. Although macroscopic electrochemical properties have been studied in great detail, bulk Li ion diffusion pathways have rarely been probed experimentally from an atomic scale point of view. Here, we evaluated 1D and 2D ^6Li magic angle spinning (MAS) NMR spectra recorded as a function of x to make the local magnetic changes during Li insertion visible. This enabled us to directly show that rapid Li exchange involves the 8a and 16c sites, forming a 3D network throughout the LTO spinel structure. In contrast, considering the time scale set by our NMR experiments the Li ions residing on the mixed occupied octahedral positions 16d are quite immobile. Under the MAS conditions applied, they definitely do not participate in rapid Li self-diffusion as evidenced by rather long site-specific longitudinal relaxation times as well as the absence of any NMR coalescence effects. Based on the NMR spectra, we propose a refined Li insertion mechanism which includes the initial formation of a highly conducting solid solution characterized by very low values of x.

Keywords: *anode materials, solid-state NMR, local structures, diffusion, ion hopping*

1 Introduction

Without the numerous mobile energy storage systems we extensively use to communicate and to share information our modern society would look completely different. In most portable devices, Li-ion batteries (LIBs) serve as reliable and rechargeable power sources.[1–4] So far, many hundreds of studies appeared in the literature that deal with the synthesis and characterization of new active materials to improve existing concepts or to develop new generations of LIBs.[5–12] The most promising one among these materials, which already reaches the level of application in commercial batteries, is spinel-type lithium titanate $Li_{4+x}Ti_5O_{12}$ (LTO).[13–20]

Considering its electrochemical properties such as Li insertion behaviour in terms of charge/discharge performance it has already been extensively examined from a macroscopic electrochemical point of view.[16–24] Although the low energy density may be regarded as a disadvantage, zero-strain LTO benefits from a highly reversible and facile Li insertion/de-insertion process that gives rise to outstanding capacity retention resulting in many thousands of charge/discharge cycles. In particular, this qualifies LTO itself as superior material for use in emerging large-scale energy storage systems.[18]

The facile Li insertion and thus superior electrochemical performance observed[25–27] is tightly related to fast Li^+ self-diffusion.[28–30] Li ion insertion kinetics[19,31] and diffusion behavior in terms of mechanisms and atomic-scale interpretations is, however, far from being completely understood. Although extensively studied as an alternative to graphite[18,32] and investigated theoretically[33–35] the key Li ion diffusion pathway in LTO has so far not been proven *experimentally* in detail. If we, however, want to improve our understanding of the electrochemical performance of LTO a deeper know-

ledge on ion dynamics as well as on the electrochemically relevant diffusion pathways, *i.e.*, the geometry of Li diffusion, is definitely needed. Such information is also expected to fruitfully influence the development of similar or improved materials as well as to bring forward battery technology in general.

Since LTO turns into a mixed conductor upon lithiation,[22] the separation of bulk Li ion dynamics from electronic conduction is a challenging task. This fundamental obstacle can be overcome by employing other techniques[36] than impedance (or conductivity) spectroscopy to study ion dynamic properties. In contrast to conductivity measurements, Li nuclear magnetic resonance (NMR) spectroscopy,[30,37–43] is solely sensitive to ion translational dynamics. Here, we took advantage of high-resolution NMR techniques such as 1D and 2D NMR exchange to gather site-specific information on ion dynamics and, finally, to reveal the relevant diffusion pathway that is energetically preferred by the jumping ions. By using ^{6}Li magic angle spinning (MAS) NMR (see below), we were able to directly differentiate between the mobile and less mobile ions distributed among the various crystallographic sites in LTO.

In detail, upon *chemical* lithiation with *n*-BuLi a solid solution is most likely formed meaning that Li ions are distributed among the three magnetically different sites in the spinel structure (space group *Fd*3*m*), *i.e.*, the octahedral sites 16d and 16c, and the tetrahedral site 8a (see Fig. 1). According to the thorough neutron diffraction study by Wagemaker *et al.*[44] this also includes the redistribution of the 8a Li ions that partly move from their original positions toward the 16c sites. Only at sufficiently low temperatures (< 100 K) a segregation into Li rich and Li poor regions is seen as evidence by splitting of the corresponding diffraction reflections.[44] So far, this redistribution has not been followed systematically by NMR spectroscopy; moreover, there is no information available about the distribution of Li at very low Li contents.

As has recently been presented by NMR relaxometry, with respect to ion dynamics around room temperature and above lithiated LTO ($x > 0$) behaves like a single spin system.[28] While Li ion dynamics in non-lithiated LTO is rather poor,[29,30] minimal lithiation up to $x = 0.1$ only (or $x = 0.3$) converts the material immediately into a relatively fast Li ion conductor as has been shown previously by us.[28] In general, it has been anticipated that fast Li exchange occurs between the sites 8a and 16c, whose polyhedra share common faces (see Fig. 1),

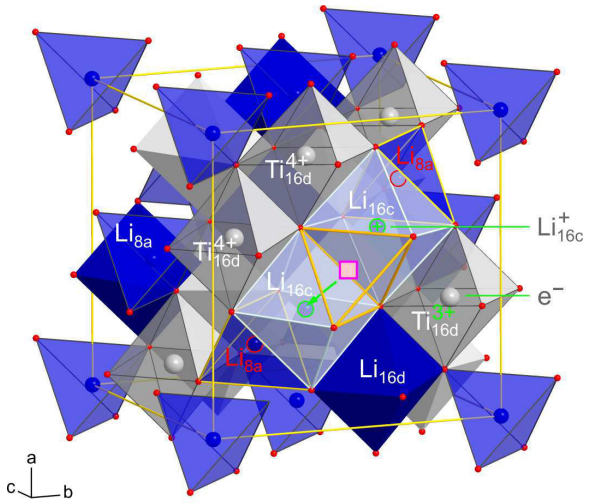

Fig. 1: Crystal structure of $Li_{4+x}Ti_5O_{12}$ (space group *Fd*3*m*); at $x = 0$ the Li ions occupy 8a and 16d sites. With $x > 0$ they start to occupy the 16c sites; simultaneously Li ions on 8a are shifted toward 16c site. See text for further explanation.

while the octahedrally coordinated ions on 16d are regarded as relatively immobile.[44,45] To the best of our knowledge, there is, however, no comprehensive experimental study available that was able to visualize the site-specific ion dynamics.

In the present investigation, we used high-resolution ^{6}Li (spin-1) MAS NMR to uncover local magnetic structures which are mostly hidden if ^{7}Li MAS NMR is applied. The latter is due to the larger electric quadrupole interactions of ^{7}Li spins (spin-3/2) that give rise to broadened central lines because of second order effects which cannot be eliminated by ordinary MAS, not even if ultrafast rotation speeds are applied to acquire the spectra. Here, ^{6}Li MAS NMR revealed the relevant Li diffusion pathway, *i.e.*, it allowed us to distinguish between the mobile and immobile Li spins in LTO. Our high-resolution spectra, particularly if recorded on samples characterized by low values of x, also contain information about the important question whether a two-phase or a single phase system is formed at the different stages of Li insertion.

2 Experimental

Polycrystalline $Li_{4+x}Ti_5O_{12}$ (EXM 1037), which is available from Süd Chemie AG (Germany), was chemically lithiated to yield several samples with varying Li content; the same samples have recently been studied via NMR relaxometry. Prior to chemical lithiation the powder was

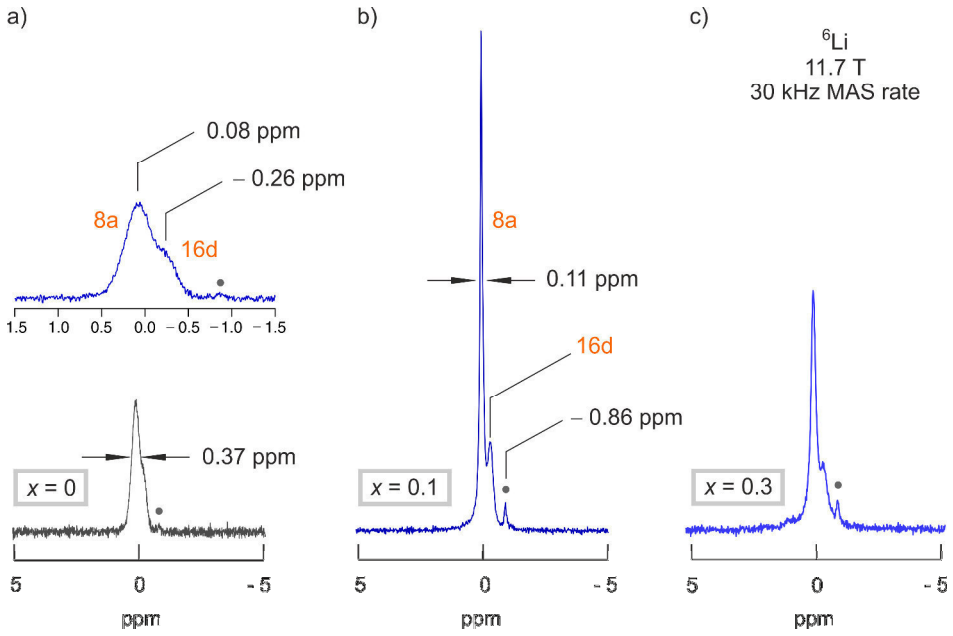

Fig. 2: a) - c) ^{6}Li MAS NMR spectra of $Li_{4+x}Ti_5O_{12}$ (73.6 MHz) recorded at ambient temperature; x ranges from 0 to 0.3. The upper graph in a) is a magnification of that shown below: The signal at 0.08 ppm corresponds to Li on 8a; the signal at – 0.26 ppm to Li on 16d. At $x = 0.1$ the sharp signal reflects a tremendous increase of all of the Li 8a ions. This points to the formation of a homogenous solid-solution with enhanced Li ion diffusivity. The absence of coalescence of the two signals (8a and 16d) points to extremely slow 16d Li ions. The signal marked with a dot (•) indicates the Li_2TiO_3 impurity serving as an internal reference; the spectra are scaled such that the areas under the NMR signals [a) - c)] is similar. See text for further explanation.

dried at 60 °C under vacuum for 12 hours; then treated with different amounts of *n*-butyllithium in hexane to obtain the following stoichiometries: $x = 0.1$, 0.3, 1, 2 and 3. Upon Li insertion the material immediately gets blue; this is because of the formation of Ti^{3+} centers. The more lithium is inserted the darker the colour. The samples were rinsed with hexane and dried under vacuum at ambient temperature. After that they were filled in 2.5 mm MAS rotors (Bruker). All experiments were carried out in an Ar-filled glovebox (M. Braun GmbH, Germany) since $Li_{4+x}Ti_5O_{12}$ ($x > 0.1$) is sensitive to air and traces of moisture. The final Li content was verified by inductively coupled plasma optical emission spectrometry (ICP-OES); for each sample it exactly agreed with the value expected, thus, quantitative Li insertion was observed.

^{6}Li MAS NMR spectra were recorded using a Bruker 500 WB spectrometer operating at 11.7 T; the corresponding Larmor frequency was 73.6 MHz. The rotating frequency used was 30 kHz; a standard 2.5-mm-probe head (Bruker) was employed. The 1D spectra were recorded with single pulse sequence; we accumulated up to 128 scans for one spectrum. Aqueous LiCl served as primary reference to determine the chemical shifts. In order to make slow diffusion processes visible and to obtain quantitative spectra, we varied the recycle delay between the consecutive scans from 3 s to 600 s. Long relaxation delays guarantee full longitudinal relaxation of all spectral components as well as extra phases (impurity phases) being characterized by rather long relaxation times (see below). The pulse length varied from 3 to 5 µs according to the electronic properties of the samples studied. We made sure that during the MAS experiments no reaction with water vapor occurred. ^{6}Li 2D MAS NMR spectra were recorded with ambient bearing gas temperature on the same spectrometer. To acquire the data we employed a three-pulse NOESY pulse sequence with appropriate phase cycling of 8 to 16 entries. The maximum number of data points chosen in the time domain in F1 direction was 256; for F2 the corresponding value varied from 1024 to 2048.

3 Results and Discussion

3.1 ^{6}Li MAS NMR spectra of $Li_{4+x}Ti_5O_{12}$

In Figs. 2 and 3 the ^{6}Li MAS NMR spectra of $Li_{4+x}Ti_5O_{12}$ are shown with the Li content being varied from very low ($x = 0.1$) to large values ($x = 3$). Before discussing the effect of Li insertion on the spectra we briefly analyze the spectrum of pure non-lithiated $Li_4Ti_5O_{12}$.

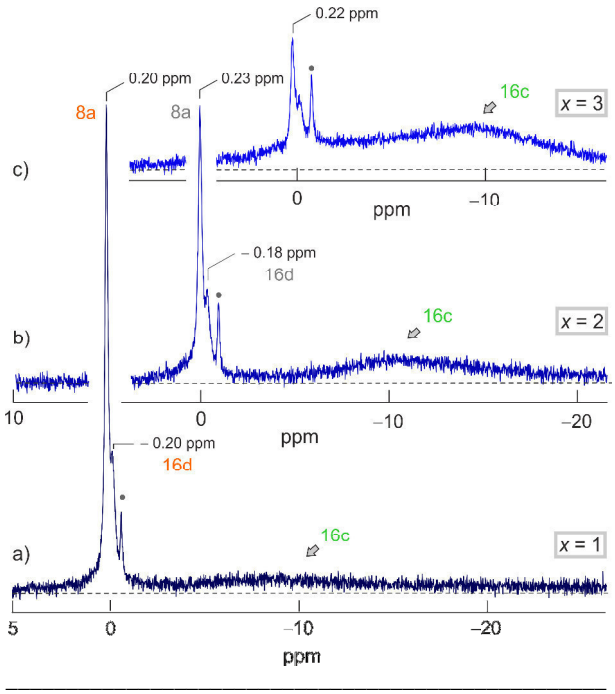

Fig. 3: (a-c) ^{6}Li MAS NMR spectra of of $Li_{4+x}Ti_5O_{12}$ with x ranging from 1 to 3. While the lines at 0.2 (8a Li) and – 0.2 ppm (16d Li) decrease in intensity, the signal at around – 10 ppm gains in intensity; it reflects Li on the 16c sites. The impurity signal of Li_2TiO_3 (•) serves to scale the spectra properly.

$Li_4Ti_5O_{12}$. The ^{6}Li MAS NMR spectrum of LTO is shown in Fig. 2 a). It is, in perfect agreement with that shown by Irvine *et al.*, composed of two components representing Li ions on the octahedral 16d sites and tetrahedral 8a sites in the spinel structure (space group Fd3m). [44,46] According to the well-known Wyckoff notation the general formula of spinel-type $Li_4Ti_5O_{12}$ reads $[Li_1]_{8a}$ $[Li_{1/3}Ti_{5/3}]_{16d}[O_4]_{32e}$, thus, in a titanate with ideal stoichiometry A_{8a} = 75% of the ions reside on the 8a sites and A_{16d} = 25% on the 16d sites, respectively.[46] This is, in our case, very well fulfilled, see the areas A shown in Fig. 4 a) that have been calculated by appropriate deconvolution of the spectrum with Gaussian and Lorentzian functions.

The two NMR lines show up at chemical shifts of 0.08 ppm and – 0.26 ppm when referenced to aqueous LiCl. The minor NMR intensity is attributed to a tiny amount of Li_2TiO_3 (– 0.87 ppm) that is known to be found in LTO samples prepared via solid state synthesis.[47] This signal is completely unaffected by Li intercalation and, thus, may serve as an internal calibration standard to scale the spectra properly. The extra phase could not been seen by X-ray powder diffraction; it is definitely an amorphous side phase. Its longitudinal NMR relaxation time is longer than that for the other two NMR lines. If not stated otherwise, in the following we will discuss spectra fully relaxed in terms of longitudinal recovery of the total magnetization, *i.e.*, we will focus on quantitative spectra.

$Li_{4.1}Ti_5O_{12}$. If x is increased from $x = 0$ to only $x = 0.1$ the ^{6}Li NMR spectrum clearly changes: the Li(8a) NMR line width is subject to further dipole-dipole averaging because of fast Li diffusion. The narrowed line starts to dominate the whole spectrum; this is also the case for the spectra characterized by, *e.g.*, $x = 0.3$ and $x = 1$ (Fig. 3). Finally, residual dipolar spin-spin interactions, which lead to broadening even under the MAS conditions chosen here, are completely averaged because of rapid Li exchange seen for $Li_{4.1}Ti_5O_{12}$.

As we have shown via ^{7}Li spin-lock NMR relaxometry quite recently, hopping Li ion dynamics sharply increase from $x = 0$ to $x = 0.1$.[28] The 1D ^{6}Li MAS spectrum shown here markedly reflects this impressive increase. The corresponding NMR line width at half maximum (FWHM), which is also included also in Fig. 4 and shown as a function of x in Fig. 5, decreases from Δ_{8a} ($x = 0$) = 0.37 ppm to Δ_{8a} ($x = 0.1$) = 0.11 ppm. On the other hand, almost no change in line width is observed for the Li(16d) line. At first glance, the ratio $A_{8a} : A_{16d}$ is almost unchanged; it still roughly reflects the 3:1 ratio expected for LTO. The rather slight decrease in A_{8a} found might be attributed to the re-distribution of the Li ions among the 8a and 16c sites while the occupancy of the 16d sites remains almost unchanged. As has been thoroughly shown by Wagemaker *et al.* via neutron diffraction, upon lithiation the Li ions inserted occupy the initially empty (octahedral) 16c sites;[45] simultaneously, part of the Li(8a) ions are shifted from 8a to the empty 16c voids. The higher x, the more pronounced the effect: in the extreme limit of $x = 3$ all of the 16d sites should be occupied occupied whereas the tetrahedral voids 8a are anticipated to be entirely empty. In other words, the crystal structure of the material changes from a spinel-type structure to a rocksalt one.[33]

Considering the Li(16d) signal, Δ_{16d} is almost unaffected by the change in x. Δ_{16d} slightly increases from 0.24 ppm to 0.28 ppm only. This is the first indication that Li(16d) ions behave quite differently with respect to self-diffusion in cubic $Li_{4.1}Ti_5O_{12}$ chemically lithiated: the 16d Li ions are much less mobile than their counterparts on 8a. This result is supported by theory[33,34] as well as by the absence of any coalescence effects, *i.e.*, verified by 2D EXSY

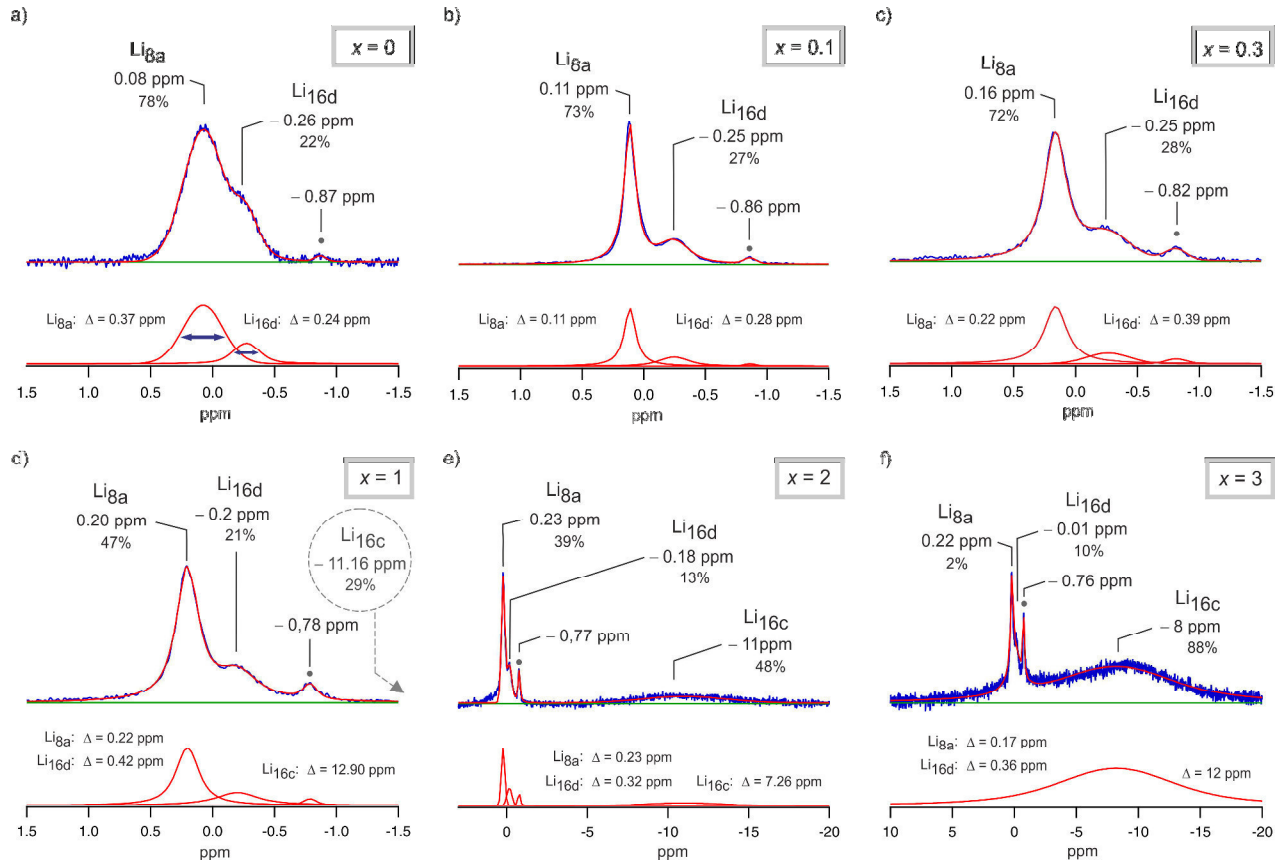

Fig. 4: Overview of the ^{6}Li 1D MAS spectra of $Li_{4+x}Ti_5O_{12}$ ($x = 0$ to $x = 3$) recorded with ambient bearing gas temperature. All NMR lines were deconvoluted with appropriate Gaussian and/or Lorentzian functions. The values in % denote the area fractions. The area of the side phase Li_2TiO_3 (– 0.8 ppm, •) did not change significantly; it was used as an internal reference for calibration of the spectra with respect to the area under the lines, see above. The most noticeable changes can been seen from a) to b) if the Li 8a NMR line is considered. Further, from d) to f) the line assigned to Li on 16c starts to dominate the spectra.

NMR (see below) which is sensitive to extremely slow Li exchange. Even such processes could not be observed.

Our recently published ^{7}Li NMR relaxometry study revealed that the corresponding magnetization transients, even if recorded at sufficiently long delay times, cannot be decomposed into a fast (8a) and a slowly (16d) relaxing component.[28] This is, most likely, due to sufficiently fast spin-diffusion between the ^{7}Li spins (see below). In other words, there is, in our opinion, no separation of the two dynamically distinct spin systems possible via ^{7}Li NMR relaxometry. Fortunately, the situation to separate the two magnetically and dynamically inequivalent spins is much more favorable in the case of 1D (and 2D) ^{6}Li (MAS) NMR, see also below.

Most importantly, since the area fraction of the motionally narrowed component assigned to Li_{8a} is still 73 %, all of the 8a spins undergo fast ion dynamics. This rules out a so-called two-phase scenario with Li poor ($Li_4Ti_5O_{12}$) and island-like Li rich ($Li_7Ti_5O_{12}$) regions, at least for small Li contents. The large regions of Li poor LTO are expected to give a broad NMR signal because of the slow Li diffusivity in $Li_4Ti_5O_{12}$. This is, however, not observed in our NMR study.

$Li_{4.3}Ti_5O_{12}$. By reaching the Li level of $x = 0.3$ an additional feature is revealed. As lithiation proceeds the number fraction of Ti^{3+} centers increases. The interaction between Li spins and (localized) e^- centers causes line broadening that surpasses the effect of motional line narrowing of the 8a signal (see Fig. 2 a) and Fig. 4 c)). As a consequence, the line broadens again and Δ_{8a} ($x = 0.1$) increases by a factor of 2. The same effect, but less pronounced, is

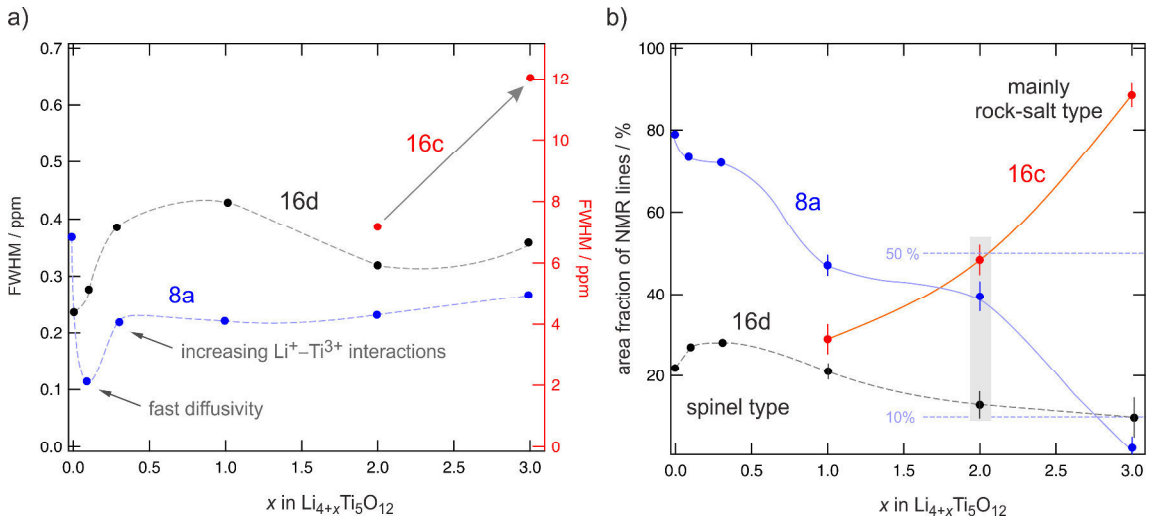

Fig. 5: a) Overview of the change of the full width at half maximum (FWHM) with increasing x; b) evolution of the area fractions of the Li NMR lines attributed to the 8a, 16c and 16d sites with increasing Li content. In a) the impressive line narrowing of the 8a Li NMR line can be clearly seen between $x = 0$ and $x = 0.1$. In b) a continuous depopulation of the 8a position is recognized while Li ions on 16d first increase to the value expected for stoichiometric LTO. As an example, a value of ca. 16.6 % (= 1/6) at $x = 2$ for 16d corresponds to $[Li_{5/3}]_{8a/16c}[Li_{1/3}Ti_{5/3}]_{16d}[O_4]_{32e}$, *i.e.*, the occupancy of the 16d site by Li ions remains almost unchanged as expected. At $x = 3$, $[Li_2]_{8a/16c}[Li_{1/3}Ti_{5/3}]_{16d}[O_4]_{32e}$, we expect the area fraction to be 14 % (= 1/7).

also seen for the NMR line representing the Li 16d ions, see Fig. 4 a) and b) as well as Fig. 5 a) for a comparison of the line widths. An additional source of broadening of the 8a NMR line might be due to the increase of the Li-Li distance leading, according to van Vleck's formalism, to stronger dipole-dipole interactions when Li ions occupy the 16c sites upon lithiation. Interestingly, while the chemical shift value of the 8a Li ions increases from 0.08 ppm ($x = 0$) to 0.11 ppm ($x = 0.1$) and then to 0.16 ppm ($x = 0.3$), that of the corresponding 16d line remains unaffected by x. This property is also seen for larger values of x presented next.

$Li_{4+x}Ti_5O_{12}$, $x = 1, 2, 3$. At even larger values of x (see the spectra in Fig. 3) the position of the Li 8a line is further shifted (0.2 ppm). In contrast, the line corresponding to the Li 16d ions remains once again almost untouched (– 0.2 ppm). At these intercalation levels it is still clearly separated from the other NMR line.

Within a few ppm the value reached for 8a seems to be the final one; further Li insertion does not change the position of the line drastically. Instead, a new and extremely broad resonance becomes detectable for $x > 1$. It is located at ca. – 11 ppm (see Fig. 3 a), b) and c)). For $x = 3$ its maximum is seen at – 8 ppm. The corresponding area fraction starts to dominate the spectra; for comparison, in Fig. 4 d), e) and f) the area fractions A of the three Li NMR lines are shown. In the ideal case, at $x = 3$ a rock-salt structure with full occupancy of the 16c sites is formed (see above). Thus, we assign this resonance to the Li ions on the 16c sites. This is in agreement with previous ^{7}Li MAS NMR results presented by Hain et al.[48]; the separate investigation of the lines 8a and 16d is, however, not possible via ^{7}Li MAS NMR suffering from second order quadrupole line broadening.[45,48]

As can be seen from Fig. 5, the 8a site is continuously depopulated while Li ions on 16d first slightly increase reaching the value expected for stoichiometric LTO. At larger x values the 16d site occupancy does not change much. As an example, a value of $A_{16d} = 16.7$ % (= 1/6) at $x = 2$ corresponds to $[Li_{5/3}]_{8a/16c}[Li_{1/3}Ti_{5/3}]_{16d}[O_4]_{32e}$, experimentally we observe $A_{16d} = 13$ %. For comparison, for $x = 3$, we expect an area fraction of $A_{16d} = 14$ % (16d) which is nicely fulfilled in our case if we consider both the 2 % deficiency observed for $x = 0$ (Fig. 4 a)) and the uncertainty of A, see Fig. 5 b).

Note that at $x = 2$ the sites 8a and 16c are almost equally occupied; this result from ^{6}Li site-specific NMR is in perfect agreement with the findings presented by Wagemaker et al. using neutron diffraction.[44]

3.2 The key diffusion pathway: mobile *vs* immobile Li ions

The ^{6}Li MAS NMR spectra recorded for the samples with very low amounts x of additional Li ions contain the key information to find out the most relevant diffusion pathway, which, at the same time, governs overall Li ion transport in LTO. In other words the spectra entail valuable information about mobile and less mobile Li ions in LTO.

As mentioned above, the narrowing of the 8a signal occurring immediately after Li insertion affects the whole NMR line. This is of course the most noticeable change showing up. It means that all of the 8a ions are exposed to fast Li ion dynamics. We studied this effect quantitatively via spin-lock ^{7}Li NMR relaxometry quite recently[28]; at ca. 354 K, this temperature is comparable to the present MAS NMR conditions, the average exchange rate is in the order of 10^5 jumps per second. The16d line, on the other hand, remains untouched after Li insertion: neither its position nor its width changes significantly. Since extra Li ions occupy the empty 16c sites, the most relevant diffusion pathway is given by the 8a-16c exchange process that causes averaging of homonuclear dipole-dipole interactions and, hence, pronounced motional line narrowing. The participation of the 32e sites seems also likely as porposed by Laumann *et al.* for high temperatures[49] and discussed by Elsässer and co-workers.[33]

Jumps involving the 16d sites are much less frequent. This perfectly corroborates the study of Ziebarth *et al.* who reported large activation energies for the 16d ions.[33] Rapid exchange between 8a (or 16c) and 16d would lead to coalescence of the lines participating in such an exchange process. They are, however, still well separated in our MAS NMR experiments. The spectral distance is given by 0.34 ppm which corresponds to 25 Hz only. Thus, the Li exchange rate is expected to be well below 10^3 s^{-1}, that is, at least two orders of magnitude lower than that found for the 8a ions. In order to detect extremely slow Li exchange processes, we performed 2D ^{6}Li MAS exchange spectroscopy (EXSY) experiments at 30 kHz spinning speed. Even in 2D EXSY NMR (as shown in Fig. 6) no off-diagonal intensities show up indicating no or ultra-slow Li exchange via the 16d sites in $Li_6Ti_5O_{12}$. This fully supports the view of Hain *et al.*[48] claiming that previous 2D ^{7}Li MAS spectra[45] suffer from spin-diffusion (*i.e.*, flip-flop) effects.

Additionally, the low mobility of the 16d ions is also reflected in a rather long site-specific ^{6}Li NMR

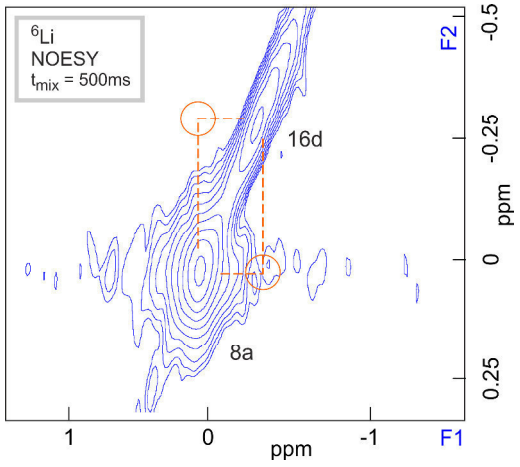

Fig. 6: 2D ^{6}Li MAS (NOESY, 76.3 MHz, 30 kHz) experiment on $Li_6Ti_5O_{12}$ revealing that no Li ion exchange between the 16d and 8a sites occurs on the time scale set by exchange spectroscopy. Even at a mixing time as long as 500 ms there is no evidence of notable Li ion hopping. This, in combination with the 1D NMR results on $Li_{4.1}Ti_5O_{12}$ (see Fig. 2), definitely proves the inactivity of the a6d ions in ion diffusion in LTO.

spin-lattice relaxation time. While the 8a line is subject to a fast longitudinal recovery within the frame of a saturation experiment, extremely long recycle delay times of up to 600 s are needed to fully detect the 16d resonance for $Li_{4.1}Ti_5O_{12}$ as is illustrated in Fig. 7. In terms of magnetization transients this leads to a two-component recovery of longitudinal ^{6}Li NMR magnetization. As mentioned above, because of effective spin-diffusion in the case of 1D and 2D (MAS) ^{7}Li,[48] which is eliminated in ^{6}Li NMR on samples with natural abundance (^{6}Li (7.5%) : ^{7}Li (92.5%)), this two-step behaviour is masked. This means that in ^{7}Li NMR the spin system excited appears as a homogenous one with respect to the Li ions on 8a and 16d. Only by means of ^{6}Li MAS NMR carried out on samples $Li_{4+x}Ti_5O_{12}$ with low x it is possible to obtain site-specific information and to identify the immobile 16d sub-ensemble, *i.e.*, to reveal the network of fast 8a-16c self-diffusion pathways possibly with vacant 32e oxygen sites involved.[49] Of course, depending on the exact defect configuration in the near proximity of the jumping ions this can lead to a variety of activation energies including different values for forward and backward jumps as pointed out by Ziebarth *et al.*[33]

Due to both fast ion exchange and neighboring Ti^{3+} centers the Li ions residing on 16c are also exposed to rapid longitudinal recovery. The 16c NMR

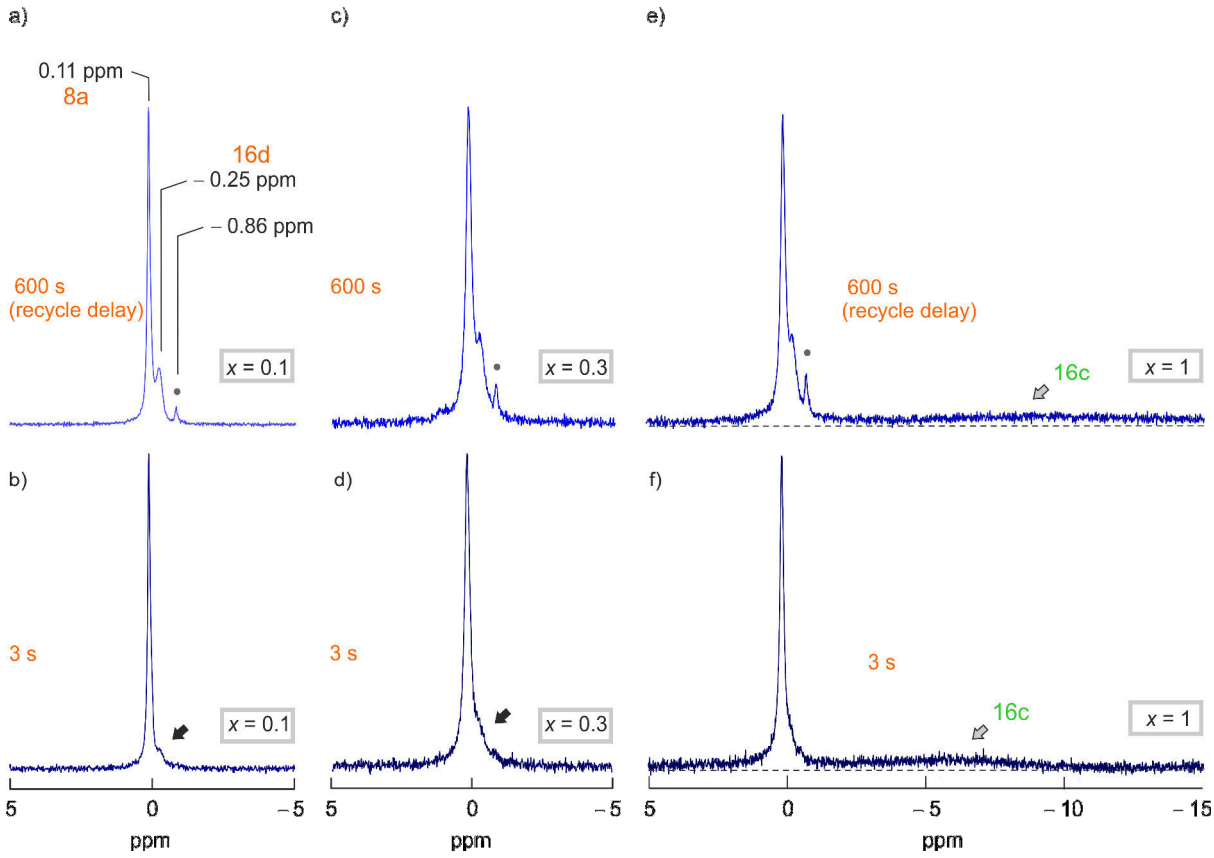

Fig. 7: Influence on spin-lattice relaxation on the individual ^{6}Li MAS NMR signals of $Li_{4+x}Ti_5O_{12}$; Li contents are indicated. While a) and c) represent spectra recorded at a long recycle delay of 600 s, short recycle delays were used to acquire the spectra shown at the bottom (b) and d)). Translational dynamics of the 16d Li ions is rather poor compared to those residing on 8a. This observation clearly shows Li ions trapped on the mixed 16d sites shared between Li^+ and Ti^{4+}. Fast ion exchange occurs via the 16c sites. (•) denotes the extra phase Li_2TiO_3.

signal is already fully developed at a recycle delay as short as 3 s. Since the 16c signal is extremely broadened because of paramagnetic interactions it is difficult to detect this line for samples with Li contents $x < 1$.

3.2 Solid solution *vs* two-phase system

In the literature, particularly if we consider *electrochemically* prepared $Li_{4+x}Ti_5O_{12}$, there is ongoing discussion about the question whether a solid-solution is formed during Li insertion or a so-called two-phase system is generated.[22,26,44,50–52] The latter means the formation of Li rich rock-salt type regions ($Li_7Ti_5O_{12}$) embedded or present in the grain boundary regions in Li poor spinel-type $Li_4Ti_5O_{12}$. If we remember that $Li_4Ti_5O_{12}$ is a rather poor ionic (and electronic) conductor,[28] the presence of better conducting $Li_7Ti_5O_{12}$ within a sample of the overall composition $Li_{4.1}Ti_5O_{12}$ should result in a ^{6}Li MAS NMR spectrum resembling that of $Li_4Ti_5O_{12}$ with a broad 8a NMR line (Li poor regions) and a narrower NMR line with a small area fraction representing the $Li_7Ti_5O_{12}$ phase (Li rich areas).[50,52] We have to keep in mind that the maximum Li ion diffusivity is found at $x = 0.3 \ldots x = 1.0$ while for larger x values (*e.g.*, $x = 2$) ion dynamics slow down once again.[28]

Here, for *chemically* lithiated samples the feature of a two-component (two-phase) line shape corresponding to a two-phase material is, however, not observed for $x = 0.1$ and $x = 0.3$. Importantly, for $x = 0.1$ all of the 8a ions participate in fast Li^+ diffusion and we do not find any evidences for a spatial separation of Li rich domains. This also holds for the situation characterized by $x = 0.3$. At $x = 0.1$ a motionally narrowed NMR line that comprises ca. 75% of the total area of the whole NMR spectrum would be in stark contradiction with a material consisting of two phases largely differing in Li content and also Li ion mobilities.[28]

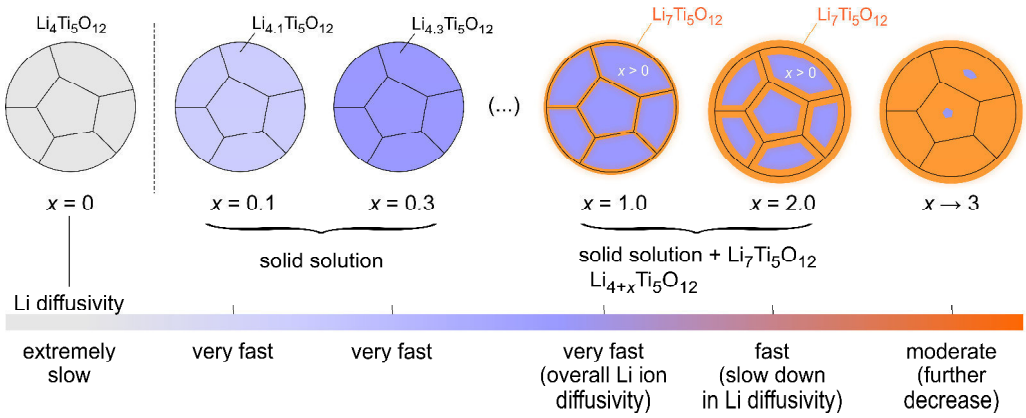

Fig. 8: Illustration of the lithiation model for LTO that is based on the ^{6}Li MAS NMR measurements. Initially a solid-solution is formed ($x = 0.1$, $x = 0.3$) which shows rapid Li ion diffusion. With increasing Li insertion regions rich in Li^{+} might show up that resemble the composition of rock-salt type $Li_7Ti_5O_{12}$. During further lithiation these regions grow; at $x = 3$ an almost fully rock-salt type oxide is formed. The latter scenario follows that proposed quite recently by Wagemaker and co-workers.[24]

From the point of view of NMR relaxometry, especially in the case of ^{7}Li NMR, sufficiently fast spin-diffusion might lead to a single magnetization transient even in the case of a two-phase scenario. Regarding our ^{6}Li MAS NMR data at low Li contents of x we find strong evidence for the existence of a solid solution that is immediately formed upon chemical lithiation. Extra Li ions seem to be distributed among the whole crystallites. Because of the repulsive Coulomb interactions generated between face-shared 8a and 16c polyhedra, all Li ions on 8a are subject to fast Li ion exchange.[28]

The situation for x values being much larger than $x = 1$, might be, however, quite different — even if we look at samples that were prepared via *chemical* Li insertion. It is well known for *electrochemically* synthesized samples that a two-phase behaviour[50,52] is kinetically induced that relaxes toward a solid solution with time.[44] Moreover, as mentioned above, phase segregation into Li rich and Li poor regions takes place at sufficiently low temperatures.[44] Considering the finding here, our ^{6}Li MAS NMR spectra point to the following Li insertion model for chemically lithiated LTO that would also be consistent with the flat insertion profile usually observed for LTO: After a solid solution has been formed, which is characterized by Li contents considerably smaller than $x = 1$, the additionally inserted ions might form Li rich regions.[52] This might happen if x reaches values of 2 and 3 as is evidently illustrated in Fig. 8 that shows the particularly highlights the abrupt change from $x = 0$ to $x = 0.1$. Li rich regions are anticipated to form first at the grain boundaries following the mechanism proposed by Wagemaker and co-workers recently.[24]

At such large intercalation degrees fast spin-diffusion in ^{7}Li NMR will however ensure that an average magnetization recovery shows up that does not allow for any separation of the Li rich regions formed.[28] The heavy formation of Ti^{3+} ions leading to line broadening complicates the situation further. On the other hand, via ^{6}Li MAS NMR it should be possible to see the signatures of the two different regions: a solid solution of $Li_{4+x}Ti_5O_{12}$ with $x > 0$ next to rock-salt type $Li_7Ti_5O_{12}$ formed. The latter shows significantly slower Li ion mobility than the spinel-type $Li_{4+x}Ti_5O_{12}$ solid solution. Because of the large Ti^{3+} concentration in $Li_7Ti_5O_{12}$ broad NMR signals should also result for ^{6}Li NMR and, indeed, the spectra recorded for $x = 2$ and $x = 3$ show these features (see Figs. 3 and 4): while the paramagnetically broadened signal at – 11 ppm and – 8 ppm reflects Li^{+} near the Ti^{3+} centers, the residual sharp signals near 0 ppm point to the Li poor regions of $Li_{4+x}Ti_5O_{12}$ with $x > 0$.

Considering overall, averaged Li ion diffusivity in LTO, with proceeding lithiation Li^{+} diffusivity is slowed down because vacant Li sites are increasingly filled up. At $x = 3$ it is yet still faster than that in the starting material with $x = 0$.[28] The fact that for $x = 3$ we still detect NMR lines corresponding to Li ions on 8a is most likely due to an incomplete lithiation process yielding a sample with regions characterized by $x < 3$ (see Fig. 8). Additionally, the NMR signal of 16d in $Li_7Ti_5O_{12}$ is assumed to be also broadened and partly hidden by the broad 16c

line.

4 Conclusions

The Li ion diffusion mechanism in the anode material $Li_{4+x}Ti_5O_{12}$ is far from being understood in detail. Elucidating the key elementary steps of ion hopping as well as shedding light on the general question about the stability of LTO solid solutions against a two-phase system might boost advancements in battery technology.

Here, temperature-variable 1D ^{6}Li MAS NMR spectroscopy was used to follow the local changes the ions are sensing during lithiation of LTO. Spectra recorded on samples with low values of x, that is, at the early stages of Li insertion, clearly reveal that all of the Li ions on the tetrahedral 8a sites are quite mobile on the NMR time scale. This is in contrast to the Li ions occupying the 16d sites that seem to trap Li ions. Obviously, for $Li_{4.1}Ti_5O_{12}$, and also for $Li_{4.3}Ti_5O_{12}$, chemical lithiation leads to the formation of solid solutions with the Li ions hopping between the sites 8a and 16c. With increasing level of lithiation the 16c octahedral sites are continuously occupied by the Li ions; simultaneously, to some extents the ions initially residing on the 8a sites move to 16c. At large values of x the Li rich $Li_7Ti_5O_{12}$ phase with rock-salt structure is formed; the corresponding ^{6}Li NMR spectrum is dominated by a broad, featureless NMR line at – 11 ppm. Partly, residues of $Li_{4+x}Ti_5O_{12}$ are seen, which are characterized by faster ion dynamics

In summary, by means of 1D ^{6}Li MAS NMR on LTO samples with varying Li content we were able (*i*) to trace the key Li^+ diffusion pathway as well as (*ii*), if LTO is chemically lithiated with *n*-BuLi, to directly prove the formation of LTO solid solutions at low Li contents. The Li ion self-diffusivity in the solid solutions greatly exceeds that of non-lithiated LTO. We proposed a new lithiation mechanism that comprises both the formation of solid solution and the separation into Li poor ($Li_{4+x}Ti_5O_{12}$, $x > 0$) and Li rich phases ($Li_7Ti_5O_{12}$). It may also be relevant for the goings-on in electrochemical cells.

Acknowledgements. We thank our colleagues at the Graz University of Technology for fruitful discussions during our weekly PhD seminar. In particular, we thank P. Bottke for his help with the 2D EXSY NMR measurements. Financial support by the Austrian Federal Ministry of Science, Research and Economy, and the National Foundation for Research, Technology and Development is gratefully acknowledged. Furthermore, we thank the Deutsche Forschungsgemeinschaft for support with this study (Research Unit 1277, WI-3600 4-2).

References

1 M. Armand and J.-M. Tarascon, *Nature*, 2008, **451**, 652–7.

2 M. R. Palacín, *Chem. Soc. Rev.*, 2009, **38**, 2565–2575.

3 F. T. Wagner, B. Lakshmanan and M. F. Mathias, *J. Phys. Chem. Lett.*, 2010, **1**, 2204–2219.

4 B. Dunn, H. Kamath and J.-M. Tarascon, *Science*, 2011, **334**, 928–35.

5 M. S. Islam and L. F. Nazar, *J. Mater. Chem.*, 2011, **21**, 9810.

6 B. L. Ellis, K. T. Lee and L. F. Nazar, *Chem. Mater.*, 2010, **22**, 691–714.

7 J. B. Goodenough and Y. Kim, *Chem. Mater.*, 2010, **22**, 587–603.

8 P. G. Bruce, B. Scrosati and J.-M. Tarascon, *Angew. Chem. Int. Ed. Engl.*, 2008, **47**, 2930–2946.

9 B. Scrosati and J. Garche, *J. Power Sources*, 2010, **195**, 2419–2430.

10 B. Scrosati, J. Hassoun and Y.-K. Sun, *Energy Environ. Sci.*, 2011, **4**, 3287.

11 D. G. Kwabi, N. Ortiz-Vitoriano, S. A. Freunberger, Y. Chen, N. Imanishi, P. G. Bruce and Y. Shao-Horn, *MRS Bull.*, 2014, **39**, 443–452.

12 N.-S. Choi, Z. Chen, S. A. Freunberger, X. Ji, Y.-K. Sun, K. Amine, G. Yushin, L. F. Nazar, J. Cho and P. G. Bruce, *Angew. Chem. Int. Ed. Engl.*, 2012, **51**, 9994–10024.

13 E. Ferg and R. Gummow, *J. Electrochem. Soc.*, 1994, **141**, 9–12.

14 M. M. Thackeray, *J. Electrochem. Soc.*, 1995, **142**, 2558.

15 K. Zaghib, M. Simoneau, M. Armand and M. Gauthier, *J. Power Sources*, 1999, **81-82**, 300–305.

16 L. Kavan and M. Grätzel, *Electrochem. Solid-State Lett.*, 2002, **5**, A39.

17 C. H. Chen, J. T. Vaughey, A. N. Jansen, D. W. Dees, A. J. Kahaian, T. Goacher and M. M. Thackeray, *J. Electrochem. Soc.*, 2001, **148**, A102.

18 T.-F. Yi, S.-Y. Yang and Y. Xie, *J. Mater. Chem. A*, 2015, **3**, 5750–5777.

19 S. Chen, Y. Xin, Y. Zhou, Y. Ma, H. Zhou and L. Qi, *Energy Environ. Sci.*, 2014, **7**, 1924.

20 T. Ohzuku, *J. Electrochem. Soc.*, 1995, **142**, 1431.

21 Y. Zhang, X. Hu, Y. Xu and M. Ding, *Acta Chim. Sin.*, 2013, **71**, 1341.

22 C. Kim, N. S. Norberg, C. T. Alexander, R. Kostecki and J. Cabana, *Adv. Funct. Mater.*, 2013, **23**, 1214–1222.

23 D. P. Singh, F. M. Mulder and M. Wagemaker, *Electrochem. commun.*, 2013, **35**, 124–127.

24 C. Wang, S. Wang, Y.-B. He, L. Tang, C. Han, C. Yang, M. Wagemaker, B. Li, Q.-H. Yang, J.-K. Kim and F. Kang, *Chem. Mater.*, 2015, 150803151628008.

25 W. J. H. Borghols, M. Wagemaker, U. Lafont, E. M. Kelder and F. M. Mulder, *J. Am. Chem. Soc.*, 2009, **131**, 17786–92.

26 Y. Sun, L. Zhao, H. Pan, X. Lu, L. Gu, Y.-S. Hu, H. Li, M. Armand, Y. Ikuhara, L. Chen and X. Huang, *Nat. Commun.*, 2013, **4**, 1870.

27 J. Haetge, P. Hartmann, K. Brezesinski, J. Janek and T. Brezesinski, *Chem. Mater.*, 2011, **23**, 4384–4393.

28 W. Schmidt, P. Bottke, M. Sternad, P. Gollob, V. Hennige and M. Wilkening, *Chem. Mater.*, 2015, **27**, 1740–1750.

29 M. Wilkening, R. Amade, W. Iwaniak and P. Heitjans, *Phys. Chem. Chem. Phys.*, 2007, **9**, 1239–46.

30 M. Wilkening, W. Iwaniak, J. Heine, V. Epp, A. Kleinert, M. Behrens, G. Nuspl, W. Bensch and P. Heitjans, *Phys. Chem. Chem. Phys.*, 2007, **9**, 6199–202.

31 N. Wu, Z.-Z. Yang, H.-R. Yao, Y.-X. Yin, L. Gu and Y.-G. Guo, *Angew. Chem. Int. Ed. Engl.*, 2015, **54**, 5757–61.

32 S. Goriparti, E. Miele, F. De Angelis, E. Di Fabrizio, R. Proietti Zaccaria and C. Capiglia, *J. Power Sources*, 2014, **257**, 421–443.

33 B. Ziebarth, M. Klinsmann, T. Eckl and C. Elsässer, *Phys. Rev. B - Condens. Matter Mater. Phys.*, 2014, **89**, 1–7.

34 Y. C. Chen, C. Y. Ouyang, L. J. Song and Z. L. Sun, *Electrochim. Acta*, 2011, **56**, 6084–6088.

35 J. Bhattacharya and A. Van der Ven, *Phys. Rev. B*, 2010, **81**, 104304.

36 P. Heitjans, *Solid State Ion.*, 1986, **18-19**, 50–64.

37 P. Heitjans, S. Indris and M. Wilkening, *Diffus. Fundam.*, 2005, **2**, 45.1–20.

38 O. Schulz, M. Martin, C. Argirusis and G. Borchardt, *Phys. Chem. Chem. Phys.*, 2003, **5**, 2308.

39 M. Wilkening and P. Heitjans, *J. Phys. Condens. Matter*, 2006, **18**, 9849–9862.

40 M. Wilkening, C. Lyness, a R. Armstrong and P. G. Bruce, *J. Phys. Chem. C*, 2009, **113**, 4741–4744.

41 P. Heitjans, A. Schirmer and S. Indris, in *Diffusion in Condensed Matter: Methods, Materials, Models*, eds. P. Heitjans and J. Kräger, Springer, 2005, pp. 367–415.

42 S. Narayanan, V. Epp, M. Wilkening and V. Thangadurai, *RSC Adv.*, 2012, **2**, 2553.

43 R. Böhmer, K. R. Jeffrey and M. Vogel, *Prog. Nucl. Magn. Reson. Spectrosc.*, 2007, **50**, 87–174.

44 M. Wagemaker, D. R. Simon, E. M. Kelder, J. Schoonman, C. Ringpfeil, U. Haake, D. Lützenkirchen-Hecht, R. Frahm and F. M. Mulder, *Adv. Mater.*, 2006, **18**, 3169–3173.

45 M. Wagemaker, E. R. H. Van Eck, A. P. M. Kentgens and F. M. Mulder, *J. Phys. Chem. B*, 2009, **113**, 224–230.

46 J. P. Kartha, D. P. Tunstall and J. T. S. Irvine, *J. Solid State Chem.*, 2000, **152**, 397–402.

47 I. Veljkovic, D. Poleti, L. Karanovic, M. Zdujic and G. Brankovic, *Sci. Sinter.*, 2011, 43, 343–351.

48 H. Hain, M. Scheuermann, R. Heinzmann, L. Wünsche, H. Hahn and S. Indris, *Solid State Nucl. Magn. Reson.*, 2012, **42**, 9–16.

49 A. Laumann, H. Boysen, M. Bremholm, K. T. Fehr, M. Hoelzel and M. Holzapfel, *Chem. Mater.*, 2011, **23**, 2753–2759.

50 M. Kitta, T. Akita, S. Tanaka and M. Kohyama, *J. Power Sources*, 2014, **257**, 120–125.

51 W. K. Pang, V. K. Peterson, N. Sharma, J.-J. Shiu and S. Wu, *Powder Diffr.*, 2014, **29**, S59–S63.

52 X. Lu, L. Zhao, X. He, R. Xiao, L. Gu, Y.-S. Hu, H. Li, Z. Wang, X. Duan, L. Chen, J. Maier and Y. Ikuhara, *Adv. Mater.*, 2012, **24**, 3233–3238.

7.2.3 Diffusion-induced ^{7}Li NMR spin-lattice relaxation of non-lithiated $Li_4Ti_5O_{12}$ and fully lithiated, mixed-conducting $Li_7Ti_5O_{12}$ battery materials

Die ^{6}Li-MAS Messungen, wie im vorherigen Manuskript gezeigt, ermöglichten es, die NMR-Linien der einzelnen kristallographischen Positionen, die Lithium einnehmen kann (8a, 16d und 16c) aufzulösen und zuzuordnen. Es ist klar ersichtlich, dass alle Li-Ionen auf der tetraedrischen Position 8a nach der zusätzlichen Lithiierung mit kleinsten Mengen Li (x = 0.1) enorm an Mobilität gewinnen. Die Halbwertsbreite des der Linie 8a sank auf ein Drittel der ursprünglichen LTO-Probe und ist, auch unter MAS-Bedingungen, ein deutliches Indiz für die hohe Mobilität der Ionen auf diesen Plätzen. Die Beweglichkeit der Li-Ionen auf 16d wurde im Laufe der Li-Insertion kaum beeinflusst; man kann davon ausgehen, dass sie an den schnelleren Diffusionsprozessen kaum teilnehmen. Mit zunehmender Lithiumkonzentration wird die Position 16c zunehmend besetzt. Dadurch kommt es zu einer Verringerung der durchschnittlichen Distanz zwischen den Lithiumionen, repulsive Wechselwirkungen induzieren hohe Diffusivität der Lithiumionen auf 8a. Bei höheren Li-Gehalten wird das 16c-Signal als breite Linie bei ungefähr -11 ppm sichtbar. Ab dem ersten Moment der Lithiierung ($Li_{4+x}Ti_5O_{12}$; $x > 0$) handelt es sich höchstwahrscheinlich um eine *solid solution* die sich ausbildet. Diese reichert sich zunehmend mit $Li_7Ti_5O_{12}$ an, bis bei der vollständigen Lithiierung ausschließlich die Kochsalzstruktur bestehen bleibt.

Für $Li_7Ti_5O_{12}$ und der nicht-lithiierten Phase sind im folgenden Beitrag die *spin-lock*-Experimente erweitert worden; mit einem Bruker-Hochtemperaturkopf konnte bei *locking*-feldern von ca. 30 kHz auch die sogenannte Hochtemperaturflanke und das Ratenmaximum erfasst werden. Das nachfolgende Manuskript ist zur Veröffentlichung eingereicht worden.

Diffusion-induced ^{7}Li NMR spin-lattice relaxation of non-lithiated $Li_4Ti_5O_{12}$ and fully lithiated, mixed-conducting $Li_7Ti_5O_{12}$ battery materials

Walter Schmidt*,†,‡ and Martin Wilkening*,†,‡
† Institute for Chemistry and Technology of Materials, Stremayrgasse 9, Graz

University of Technology (member of NAWI Graz), 8010 Graz, Austria

‡ Christian Doppler Laboratory for Lithium Batteries, Graz University of Technology, 8010 Graz, Austria

under review: Solid State Ionics

Diffusion-induced ^{7}Li NMR spin-lattice relaxation of non-lithiated $Li_4Ti_5O_{12}$ and fully lithiated, mixed-conducting $Li_7Ti_5O_{12}$ battery materials

Walter Schmidt*,†,‡ and Martin Wilkening*,†,‡

† *Institute for Chemistry and Technology of Materials, Stremayrgasse 9, Graz University of Technology (member of NAWI Graz), 8010 Graz, Austria*

‡ *Christian Doppler Laboratory for Lithium Batteries, Graz University of Technology, 8010 Graz, Austria*

ABSTRACT. $Li_4Ti_5O_{12}$ (LTO) belongs to one of the most promising anode materials for lithium-ion batteries. Its superior cycling performance and negligible ageing makes it a potential candidate to be used in, *e.g.*, stationary applications. Besides this application-oriented interest it serves as an excellent model system to study Li ion transport in a 3D mixed conducting host crystallizing with spinel structure. Whereas Li ion diffusion in $Li_4Ti_5O_{12}$ was the subject of several studies that appeared over the past years; Li ion transport in mixed conducting $Li_7Ti_5O_{12}$ crystallizing with rock-salt type structure is, however, much less frequently investigated. $Li_7Ti_5O_{12}$ is the compound that is formed after an LTO-type battery has been fully charged. In the present study we used spin-lock NMR relaxometry to quantify Li ion diffusion in terms of jump rates, activation energies and microscopic Li^+ ion self-diffusion coefficients. Compared to the non-lithiated source material $Li_4Ti_5O_{12}$, showing poor Li ion diffusivity, Li ion diffusivity in $Li_7Ti_5O_{12}$ is clearly enhanced but by far as high as recently reported for spinel-type $Li_{4+x}Ti_5O_{12}$, with x being significantly smaller than 1. Obviously, the small number of vacant 16c sites in $Li_7Ti_5O_{12}$ as well as repulsive 8a-16c interactions are responsible for the low Li ion diffusivity found.

Keywords: anode materials, solid-state NMR, local structures, diffusion, ion hopping

1 Introduction

Our daily life is to a great extent influenced by many small and mediums-sized electronic devices such as laptops and cell phones that rely on secondary Li ion batteries serving as electrochemical energy storage systems.[1-5] The performance ability of such devices strongly depends on the materials selected.[4-9]

Although numerous compounds have been examined and tested until now only few are able to reliably replace commercially applied materials.[10-14] Considering negative electrodes,[15-18] just few are able to replace graphite-based anodes.[12,19-22]

One of the materials suited, especially if we bear stationary systems in mind, is the spinel-type anode material lithium titanate $Li_{4+x}Ti_5O_{12}$ (LTO).[23-27] LTO has already reached commercial use because of its excellent long time stability during thousands of charging and discharging cycles.[23,28] It benefits from two further properties: it is a zero-strain material, *i.e.*, volume expansion during lithiation is negligible.[26,27] Moreover, because its high open circuit potential of 1.55 V *vs* Li metal no passivation layer is formed in lithium-based batteries.[23,26] This behavior is advantageous because it largely reduces ageing effects. While the relatively low capacity of LTO excludes the titanate from applications needing high energy densities, it is a promising electrode material in thin-film or micro-batteries as well as large-scale stationary applications.[28] The latter systems are urgently needed if we want to store electricity from intermittent, renewable sources in a decentralized way.[10]

In order to pave the way towards such applications, the electrochemical properties of LTO, which

change with the degree x of Li insertion $Li_{4+x}Ti_5O_{12}$, need to be investigated in detail. One of the crucial parameter that determines the performance of a given electrode material is its ion conductivity,[29] which is directly related to solid-state diffusion. As LTO turns into a mixed conductor during Li insertion, the study of Li ion conductivity in lithiated LTO via, *e.g.*, impedance spectroscopy,[30] is a challenging task since both contributions to overall conductivity, viz. the ionic and electronic contribution, have to be precisely separated. Fortunately, lithium nuclear magnetic resonance (NMR) can be applied that is solely sensitive to the motion of the Li spins.[31-36] In the present study, we took advantage of spin-lock NMR relaxometry[37-41] to shed light on microscopic self-diffusion parameters in both non-lithiated and lithiated LTO. These two compositions refer to the fully discharged ($x = 0$) and fully charged ($x = 3$) state of a lithium-ion battery. Note that spin-lock NMR measurements are sensitive to motional processes being characterized by diffusion coefficients in the order of 10^{-15} m^2 s^{-1} if we regard the relaxation rate maxima.[35,42]

Earlier NMR studies have shown that $Li_4Ti_5O_{12}$ ($x = 0$) is a poor ion conductor with a relatively low Li ion diffusivity.[43-47] As yet, the diffusion-induced spin-lock NMR rate peak has not been reported. As was shown by us recently, at the very early stages of Li insertion ($x = 0.3$) Li ion diffusivity sharply increases,[43] at large values of x, however, a decrease in diffusivity is seen. This behaviour can be understood in terms of a Li ion redistribution among the crystallographic sites 8a and 16c in LTO.[48] For $x = 0$ spinel-type LTO obeys the following site occupancy $[Li]_{8a}[Ti_{5/3}Li_{1/3}]_{16d}[O_4]_{32e}$ (Fd3m). During Li insertion Li ions start to occupy the empty octahedral 16c voids; simultaneously 8a Li ions move from 8a to 16c.[48] At $x = 3$, the 8a sites are empty and the 16c sites are fully occupied. This topotactic rearrangement leads to a rock-salt type structure according to $[Li_2]_{16c}[Ti_{5/3}Li_{1/3}]_{16d}[O_4]_{32e}$. The occupancy of the 16d sites is anticipated to be unchanged.

2 Experimental

Polycrystalline $Li_{4+x}Ti_5O_{12}$ (EXM 1037) was purchased from SüdChemie AG (Germany). Prior to our measurements the material was dried at 60 °C under vacuum for 12 hours; then it was transferred into an Ar-filled glovebox (M. Braun GmbH, Germany). The non-lithiated sample was fire-sealed in a small glass ampoule (3 cm in length, 5 mm in diameter). To prepare $Li_7Ti_5O_{12}$ the white powder was treated with an appropriate amount of *n*-butyllithium in hexane in Ar atmosphere. The sample was carefully rinsed with hexane and dried under vacuum at ambient temperature. Then, because of its sensitivity to air and moisture it was immediately sealed in a glass tube. To check the final composition of the sample chemically lithiated, its final Li content was verified by inductively coupled plasma optical emission spectrometry (ICP-OES). ICP-OES showed that a quantitative reaction took place meaning the composition $Li_7Ti_5O_{12}$ was indeed reached.

For the NMR measurements we used a Bruker 300 WB spectrometer connected to a 7-Tesla magnet. The ^{7}Li Larmor frequency was 116 MHz. NMR lines were recorded with a single pulse experiment using a 90° excitation pulse; its length ranged from 3 to 5 μs between 223 K and 573 K. In order to reach temperatures as high as 573 a Bruker high-temperature probe was employed. Temperatures below ambient were reached with a flow of dry and cooled nitrogen gas, while for higher temperatures a stream of heated dinitrogen gas was used.

While ^{7}Li NMR spin-lattice relaxation rates were recorded in the laboratory frame ($1/T_1$) with the well-known saturation recovery pulse sequence,[49] for the spin-lock NMR experiments we used the pulse sequence introduced by Ailion and Slichter:[50-52] directly after a π/2-pulse a spin-lock pulse $p(t_{lock})$ is applied that locks the magnetization M_ρ in the $(x,y)'$-plane. The immediate decay of M_ρ in the presence of the weak B_1 locking field, which is in our case characterized by a frequency of $\gamma B_1 = \omega_1 = 125$ kHz, is followed as a function of the duration of the locking pulse. The transversal decay of $M_\rho(t_{lock})$ is induced by slow jump processes of the Li ions. From variable-temperature experiments correlation rates and activation energies can be extracted.[49,53-57]

In general, the rate $1/T_{1\rho}$, which can be deduced from the transients $M_\rho(t_{lock}) \propto \exp(-(t_{lock}/T_{1\rho})^\alpha)$, with α being a stretching factor, is proportional to the

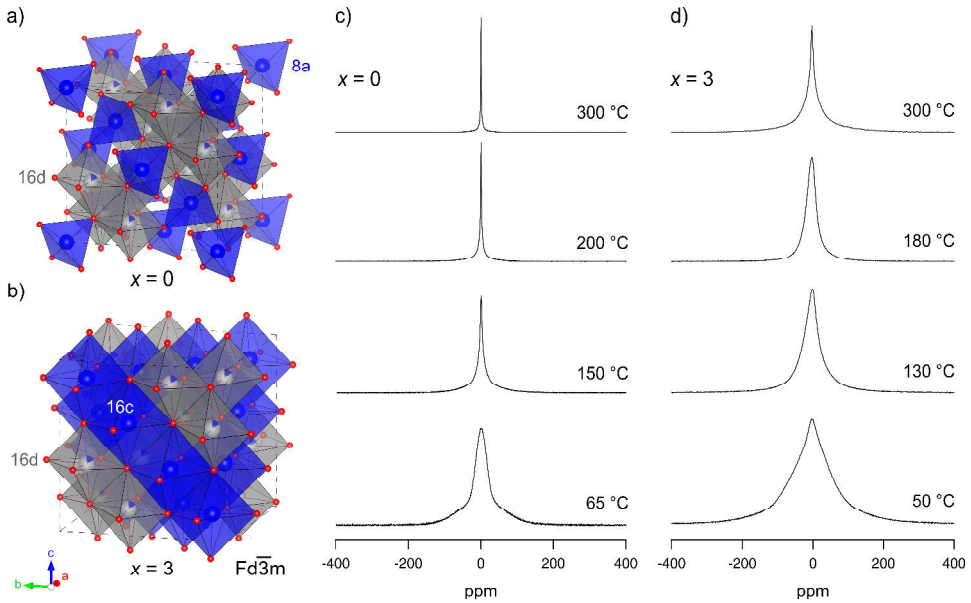

Fig. 1: a) and b) crystal structures of $Li_4Ti_5O_{12}$ and $Li_7Ti_5O_{12}$ (see text); c) and d) variable-temperature ^{7}Li NMR spectra (155 MHz) revealing diffusion-induced line narrowing. See text for further discussion.

spectral density function $J(\tau_c, \omega_1)$ containing the activation energy, E_a, and the pre-factor, $1/\tau_{c,0}$, of the underlying Arrhenius relation used to describe Li ion diffusion: $1/\tau_c = 1/\tau_{c,0} \exp(-E_a/(k_B T))$. The correlation rate $1/\tau_c$ is assumed to be in the order of the jump rate $1/\tau$. Usually, according to the model of Bloembergen Purcell and Pound (BPP),[58] $J(\tau_c, \omega_1)$ is given by a Lorentzian-type function (see below).

Between each scan we ensured that full longitudinal relaxation took place; thus, the recycle delay was at least $6T_1$. The resulting decay curves $M_\rho(t_{lock})$ could only be parameterized with stretching exponents α being smaller than 1. Such deviations from pure exponentiality are known for spin-lock experiments.[49]

3 Results and Discussion

Static ^{7}Li NMR spectra of $Li_4Ti_5O_{12}$ and $Li_7Ti_5O_{12}$ recorded at various temperatures are shown in Fig. 1. Because ^{7}Li is a spin-3/2 nucleus with a moderate quadrupole moment the spectra are, besides dipolar interactions, also governed by 1st order quadrupolar effects. In general, variable-temperature NMR give first insights into dynamic properties and local structures.[59,60] At low temperatures the ^{7}Li NMR spectrum of diamagentic $Li_4Ti_5O_{12}$, which is composed of a central line and a quadrupole powder pattern, is dipolarly broadenend. With increasing ion dynamics, *i.e.*, with increasing temperature, dipolar magnetic as well as quadrupolar electric interactions are, however, averaged[61] leading to a narrow NMR signal at sufficiently high T. This behaviour is expected for Li jump diffusion processes that are characterized by jump rates with values ranging from ca. 1 to 100 kHz, depending on the strengths of the respective interactions that need to be averaged. For very high temperatures (1173 K) Laumann *et al.* suggested involving the split site (32e) in Li ion diffusivity: 8a – 32e – 8a.[62,63]

In principle, the spectra of the lithiated sample, $Li_7Ti_5O_{12}$, obey the same characteristics of motional line narrowing. Due to the presence of paramagnetic Ti^{3+} centers, the rigid-lattice line is, however, much broader compared to $Li_4Ti_5O_{12}$. Most likely, this paramagnetic broadening also masks any quadrupole intensities. At elevated T the total line undergoes motional averaging and, even if the larger rigid-lattice line width compared to $Li_4Ti_5O_{12}$ is considered, the Li ions seems to be more mobile than in the non-lithiated compound. This behaviour was already inferred from the different inflexion points of the two motional narrowing curves recently.[43] In agreement

with line narrowing, the enhancement in Li^+ diffusivity is clearly seen if we take a look at the corresponding spin-lock NMR spin-lattice relaxation rates, as presented below. Note that a drastic increase in Li ion diffusivity is observed for LTO that was only slightly lithiated, *cf.* the result for $Li_{4.1}Ti_5O_{12}$ and $Li_{4.3}Ti_5O_{12}$ published recently. With increasing lithiation level, however, Li ion mobility decreases again, as is quantitatively proved in the present study for $Li_7Ti_5O_{12}$.

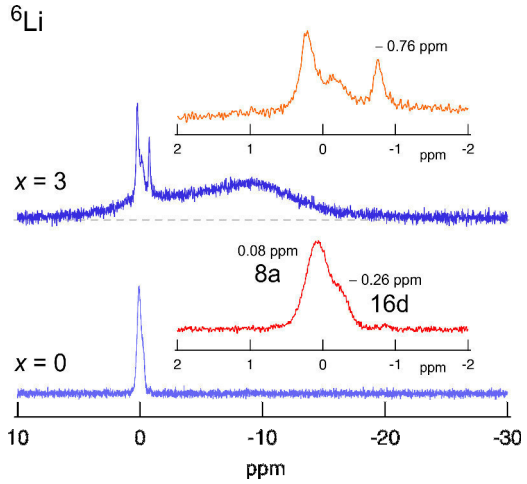

Fig. 2: ^{6}Li MAS NMR spectra (30 kHz) of $Li_{4+x}Ti_5O_{12}$ with x = 0 and 3. The $Li_7Ti_5O_{12}$ sample contains a tiny amount of non-reacted $Li_4Ti_5O_{12}$; the signal at – 0.76 ppm is attributed to γ-Li_2TiO_3 being an X-ray amorphous impurity. See text for further explanation.

Under static measurements conditions the broad, rigid-lattice NMR resonance of $Li_7Ti_5O_{12}$ shows an asymmetric shape. In the dynamic range of motional narrowing this asymmetry is increasingly averaged until an almost symmetric line is observed in the regime of so-called extreme narrowing.

The asymmetry of the line can be understood if we look at the corresponding ^{6}Li NMR spectrum that was recorded under fast magic angle spinning (MAS) conditions (see Fig. 2). The ^{6}Li MAS NMR spectrum reveals residual Li ions on 8a sites, Li ions on 16d (see above) as well as the majority of the Li ions on 16c. Due to the Li-Ti interactions a paramagnetic shift towards negative ppm values is seen: the main signal is rather broad; in agreement with literature its maximum shows up at – 10 ppm. For comparison, the signal of diamagnetic $Li_4Ti_5O_{12}$ is composed of two contributions with chemical shifts of 0.08 ppm (8a) and – 0.26 ppm (16d). The ratio of the areas under the lines (8a:16d) is 3:1; it is in excellent agreement with the Li ion distribution that we would expect for spinel-type $[Li]_{8a}[Ti_{5/3}Li_{1/3}]_{16d}[O_4]_{32e}$. In our opinion, any signal at ca. – 0.8 ppm (Fig. 2), which possesses extremely long T_1 relaxation times, has to be assigned to γ-Li_2TiO_3 impurities.[64] This is in agreement with Laumann *et al.* who do not found convincing arguments that the 16c sites are occupied by Li ions in non-lithiated LTO at lower T; instead, they confirmed full occupancy of the 8a sites.[62] At higher temperatures (> 973 K) Li ions in $Li_4Ti_5O_{12}$ start to occupy 32e sites instead of 16c sites[62] as claimed by others.[65] At temperatures as high as 1173 K a clear deficit of Li ions on 8a sites was seen. It might be related to the enhancement in Li ion conductivity found at elevated T.[29,66,67]

To quantify Li ion diffusivity in $Li_4Ti_5O_{12}$ and $Li_7Ti_5O_{12}$ we recorded spin-locking NMR spin-lattice relaxation rates over a large temperature range to fully access the corresponding diffusion-induced rate peaks $1/T_{1\rho}(1/T)$. This was possible by employing an NMR probe with a ceramic sample chamber that is designed for measurements at temperatures as high as 600 K. The Arrhenius plot presented in Fig. 3 shows the relaxation peaks obtained. While at temperatures below 300 K non-diffusive effects dominate spin-lock relaxation behaviour, the rates recorded at higher T pass through characteristic maxima located at T_{max}. At T_{max} the maximum condition $\omega_1\tau_c = 0.5$ is valid from which the correlation times τ_c of $Li_4Ti_5O_{12}$ and $Li_7Ti_5O_{12}$ can be determined. In our case, since we used ω_1 = 125 kHz, τ_c amounts to be approximately 4 µs at 430 K ($Li_7Ti_5O_{12}$) and 472 K ($Li_4Ti_5O_{12}$), respectively.

Irrespective of different activation energies for Li ion hopping in the two samples, the Li ion jump rate in $Li_7Ti_5O_{12}$ reaches values in the order of ω_1 at a significantly lower temperature T_{max} = 430 K compared to 472 K for $Li_4Ti_5O_{12}$. The higher diffusivity in the lithiated rock-salt phase $Li_7Ti_5O_{12}$ also manifests in a lower activation energy that can be deduced from analyzing the diffusion-induced relaxation rate peaks with an appropriate relaxation model. Assuming 3D Li ion diffusion we used a Lorentzian-type spectral density function, $J(\tau_c, \omega_1) \propto 1/T_1$, which relies on the

BPP model, to describe spin-lock NMR relaxation behavior in LTO:[46]

$$1/T_{1\varrho} = C \cdot \tau_c/[1 + (2\omega_1\tau_c)^{\beta}]$$

with $1/\tau_c = f(1/T)$, *i.e.*, following Arrhenius behaviour, see above. The pre-factor C contains the coupling constants describing magnetic dipolar and electric quadrupolar interactions. Restricting $J(\tau_c, \omega_1)$ to a single term served as a perfect approximation to obtain the best fitting results. The parameter β, which usually ranges from 1 to 2, turned out to be 2. This quadratic frequency dependence in the low-T limit ($\omega_1\tau_c \gg 1$) reflects typical BPP behaviour that is based on isotropic (3D), uncorrelated motion. $\beta = 2$ means that Li ion dynamics in the two titanates relies on an exponential motional correlation function $G(t)$ that describes the field fluctuations sensed by the Li ions; Fourier transformation of $G(t)$ directly yields $J(\tau_c, \omega_1)$. $\beta = 2$ also means that the corresponding rate peaks $1/T_{1\rho}(1/T)$ are fully symmetric.[38]

Table 1: Results obtained after using a BPP-type Lorentzian-shaped spectral density function to analyze the rate peaks in Fig. 3.

$Li_{4+x}Ti_5O_{12}$	β	E_a (eV)	τ_0 (s)	C (s^{-2})
$x = 0$	2	0.58(2)	$3(2)\times10^{-12}$	$3(2)\times10^{8}$
$x = 3$	2	0.48(3)	$5(2)\times10^{-12}$	$1(2)\times10^{9}$

The activation energies obtained (ca. 0.58 eV vs. ca. 0.48 eV, see Fig. 3) are in good agreement with those recently deduced just from the low-T flanks of the respective diffusion induced peaks.[43] In our recently published work,[43] however, we were not able to access the whole rate peaks as it is the case here. In particular, the value of 0.58 is in perfect agreement with results from DC conductivity measurements below temperatures of 500 K.[29]

Since the pre-factors are quite similar — note that values for $1/\tau_0$ in the order of 10^{12} s^{-12} are in agreement with phonon frequencies — the lower activation energy of 0.48 eV for $Li_7Ti_5O_{12}$ causes the rate peak to show up at lower temperature as compared to that of non-lithiated $Li_4Ti_5O_{12}$ (see Fig. 3)

The broader peak width in the case of $Li_7Ti_5O_{12}$ might be due to the mixed conductive nature of the lithiated phase that contains paramagnetic Ti^{3+} centers, in particular. The larger pre-factor C, could be explained by larger dipolar and/or quadrupolar coupling constants C which directly raise the absolute values of the relaxation rates. Most likely, paramagnetic Li-Ti interactions are also responsible for the enhanced relaxation rates. For comparison, below 270 K the background rates differ by somewhat more than order of magnitude, see the data points marked with a dot in Fig. 3.

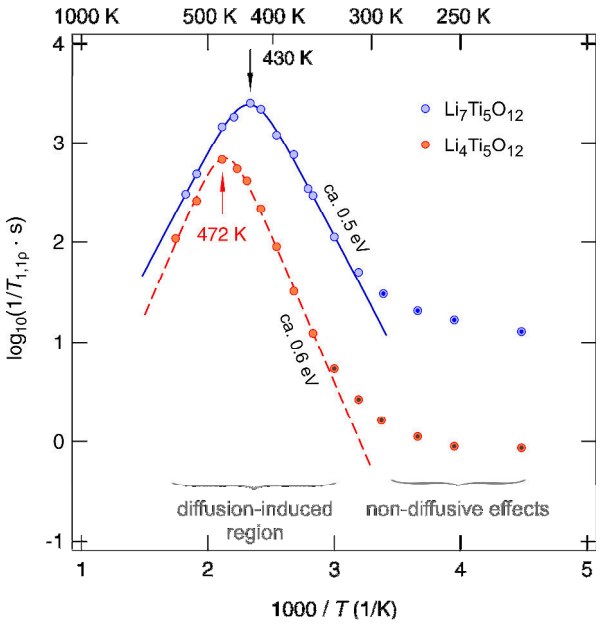

Fig. 3: Arrhenius plot of the ^{7}Li NMR spin-lattice relaxation rates of lithiated $Li_7Ti_5O_{12}$ and non-lithiated $Li_4Ti_5O_{12}$; the rates were recorded with the spin-lock technique using an angular frequency ω_1 of 125 kHz ($\omega_1/2\pi \approx 20$ kHz). The Larmor frequency was 155 MHz. The dashed line and the solid line represent fits with a BPP-type spectral density function. See text for further explanation.

With $\tau_c \approx 4$ µs, as obtained via the maximum condition mentioned above, diffusion coefficients D can be estimated for the two samples investigated. At the two different temperatures T_{max} (430 K and 472 K) we obtain $D = 1.35 \times 10^{-15}$ m^2 s^{-1}. At room temperature (300 K), considering the different activation energies, this yields 3.6×10^{-18} m^2 s^{-1} for $Li_7Ti_5O_{12}$ and 1.8×10^{-19} m^2 s^{-1} for the non-lithiated sample, $Li_4Ti_5O_{12}$. In earlier studies, performed by some of us, we reported even lower diffusion coefficients and higher activation energies for $Li_4Ti_5O_{12}$;[45] this is also the case for

the sample that was investigated by Hain et al.[47] Note that in our recent work a non-commercial sample of LTO was investigated.[45] The present results are obtained on a sample that is provided by SüdChemie; it is identical with those we used in a recent publication to study the effect of lithiation if x in $Li_{4+x}Ti_5O_{12}$ is only slightly enhanced.[43] Most importantly, based on the activation energies and D values deduced (see above), an estimation would predict D values in the order of 1.5×10^{-11} m^2 s^{-1} at 1173 K for LTO. This value is in good agreement with that found by neutron tracer experiments on $Li_4Ti_5O_{12}$: at 1173 K Takai *et al.* report $D_{1730\,K} \approx 2.2 \times 10^{-10}$ m^2 s^{-1}.[68] By comparing values over such a large temperature range one has to keep in mind, however, that the Li ions in LTO start to occupy a significant number of 32e (split) sites near the empty 16c sites.[62]

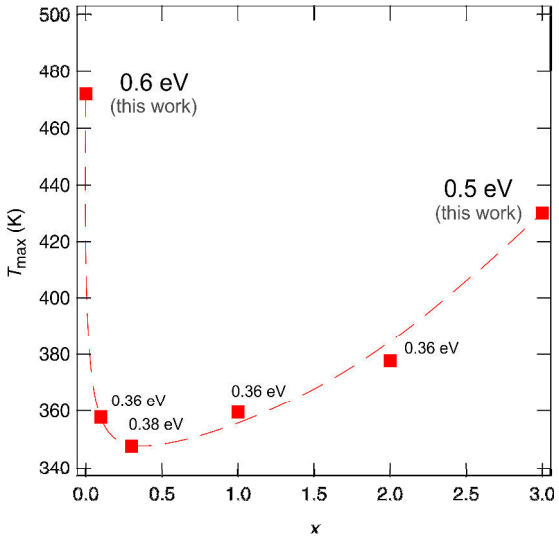

Fig. 4: Variation of the position of the diffusion-induced spin-lock NMR relaxation peaks of $Li_{4+x}Ti_5O_{12}$ with composition x. The change of activation energy is also included. The temperatures T_{max} refer to spin-lock experiments carried out at $\omega_1/2\pi \approx 20$ kHz.

The diffusion coefficients deduced from NMR in our study are, however, much lower than those presented by Sugiyama *et al.*[69] The authors used myon spin spectroscopy to estimate D values at 300 K: for the film samples investigated they present a coefficient in the order of ca. 3×10^{-15} m^2 s^{-1}.[69] This value is by four orders of magnitude higher than what is usually expected for poorly conducting $Li_4Ti_5O_{12}$. It also disagrees with conductivity measurements on LTO since it would predict values in the order of 10^{-6} S cm^{-1} at ambient temperature. Such a value is much too high for the almost stoichiometric $Li_4Ti_5O_{12}$ samples investigated so far: values in the order of 3×10^{-10} S cm^{-1} are, however, accepted, see the study by Fehr *et al.*[29] Earlier NMR studies also pointed to much lower Li diffusivities.[45,47,70]

Considering the activation energies published by Sugiyama et al.[69] values as low as 0.12 eV (film sample) and 0.09 eV (powder sample prepared by solid state reaction) are reported; once again, these barriers are clearly too low to serve as representative values for long-range ion transport in LTO. The same holds for the activation barriers presented by Vijayakumar *et al.*[65] As pointed out by the Sugiyama and coworkers,[69] variable-temperature susceptibility measurements down to 100 K indicate that they dealt with a Li deficient compound $Li_{4-\delta}Ti_{5+\delta}O_{12}$. If prepared under inert gas, *i.e.*, reducing, atmosphere or under low oxygen partial pressures[71] the defect chemistry might be significantly changed because of the formation of, *e.g.*, Li and/or O vacancies. Vacant Li or O sites may critically influence Li ion diffusivity in such non-stoichiometric compounds. As we have shown recently for the opposite direction, increasing x in $Li_{4+x}Ti_5O_{12}$ from $x = 0$ to $x = 0.1$ has a drastic effect on Li ion diffusivity. For $Li_{4.1}Ti_5O_{12}$, having a light blue color because of the Ti^{3+} centers generated, we obtained $D \approx 1.35 \times 10^{-15}$ m^2 s^{-1} at 354 K via spin-lock NMR.[43] This result corresponds to an increase of D by more than two orders of magnitude when going from $x = 0$ ($D_{354\,K} \approx 7.5 \times 10^{-18}$ m^2 s^{-1}) to $x = 0.1$. In terms of temperatures T_{max} this means that, at a locking frequency of 20 kHz, spin-locking NMR peak maxima show up in a temperature range from ca. 480 K to 340 K depending on x (see Fig. 5).

4 Summary

Li ion self-diffusion in both non-lithiated $Li_4Ti_5O_{12}$ and lithiated $Li_7Ti_5O_{12}$ was investigated by spin-locking NMR relaxometry. NMR Measurements in the rotating frame of reference are sensitive to jump rates in the order of 10^5 to 10^6 jumps per second if we use the maximum condition $\omega_1\tau_c = 0.5$ to estimate

the correlation rate $1/\tau_c$. While for spinel-type LTO Li ion diffusivity is extremely low, *i.e.*, characterized by diffusion coefficients in the order of 10^{-19} m^2 s^{-1}, Li^+ hopping in rock-salt type $Li_7Ti_5O_{12}$ is enhanced by two orders of magnitude. This change in Li ion diffusivity is also reflected by the two activation energies (0.6 eV vs. 0.48 eV) deduced from the corresponding diffusion-induced rate peaks. The peaks were evaluated with the BPP relaxation model introduced for 3D uncorrelated motion. They can be best described with the correlation parameter β being equal to 2 reflecting pure BPP behaviour. Non-BPP behaviour would result in asymmetric peaks with the slope of the low-T flank being smaller than that describing the high-T flank. Differing slopes might point to a distribution of energy barriers, while symmetric peaks could serve as an indication for a regular potential landscape the ions sense during the spin-lock experiment. Hence, we conclude that the Li ions sense a rather homogenous, regular potential landscape during diffusion.

Compared to a recently published myon spin spectroscopy study,[69] the diffusion coefficients measured in the present case are much lower. Very low diffusion coefficients as probed via NMR relaxometry are in perfect agreement with earlier studies including NMR and conductivity measurements, in particular.[29,43,46,47,70]

Acknowledgements. We thank our colleagues at the Graz University of Technology for fruitful discussions during our weekly PhD seminar. In particular, we thank P. Bottke for his help with some of the NMR measurements. Financial support by the Austrian Federal Ministry of Science, Research and Economy, and the National Foundation for Research, Technology and Development is gratefully acknowledged. Furthermore, we thank the Deutsche Forschungsgemeinschaft for financial support (Research Unit 1277, WI-3600 4-2).

References

1. D. Larcher and J. M. Tarascon, *Nature Chemistry*, 2015, **7**, 19-29.
2. M. S. Whittingham, *Chem. Rev.*, 2014, **114**, 11414-11443.
3. M. S. Whittingham, *Chem. Rev.*, 2004, **104**, 4271-4301.
4. P. G. Bruce, B. Scrosati and J. M. Tarascon, *Angewandte Chemie-International Edition*, 2008, **47**, 2930-2946.
5. A. S. Arico, P. Bruce, B. Scrosati, J. M. Tarascon and W. Van Schalkwijk, *Nat. Mater.*, 2005, **4**, 366-377.
6. Q. Zhang, E. Uchaker, S. L. Candelaria and G. Cao, *Chem. Soc. Rev.*, 2013, **42**, 3127-3171.
7. B. L. Ellis, K. T. Lee and L. F. Nazar, *Chem. Mater.*, 2010, **22**, 691-714.
8. J. B. Goodenough and Y. Kim, *Chem. Mater.*, 2010, **22**, 587-603.
9. M. R. Palacin, *Chem. Soc. Rev.*, 2009, **38**, 2565-2575.
10. B. Dunn, H. Kamath and J. M. Tarascon, *Science*, 2011, **334**, 928-935.
11. V. Etacheri, R. Marom, R. Elazari, G. Salitra and D. Aurbach, *Energy & Environmental Science*, 2011, **4**, 3243-3262.
12. R. Marom, S. F. Amalraj, N. Leifer, D. Jacob and D. Aurbach, *J. Mater. Chem.*, 2011, **21**, 9938-9954.
13. B. Scrosati and J. Garche, *J. Power Sources*, 2010, **195**, 2419-2430.
14. H. Li, Z. Wang, L. Chen and X. Huang, *Adv. Mater.*, 2009, **21**, 4593-4607.
15. M. V. Reddy, G. V. S. Rao and B. V. R. Chowdari, *Chem. Rev.*, 2013, **113**, 5364-5457.
16. W.-J. Zhang, *J. Power Sources*, 2011, **196**, 13-24.
17. L. Ji, Z. Lin, M. Alcoutlabi and X. Zhang, *Energy & Environmental Science*, 2011, **4**, 2682-2699.
18. M. Winter and J. O. Besenhard, *Electrochim. Acta*, 1999, **45**, 31-50.
19. L. W. Su, Y. Jing and Z. Zhou, *Nanoscale*, 2011, **3**, 3967-3983.
20. J. R. Szczech and S. Jin, *Energy & Environmental Science*, 2011, **4**, 56-72.
21. C.-M. Park, J.-H. Kim, H. Kim and H.-J. Sohn, *Chem. Soc. Rev.*, 2010, **39**, 3115-3141.
22. B. J. Landi, M. J. Ganter, C. D. Cress, R. A. DiLeo and R. P. Raffaelle, *Energy & Environmental Science*, 2009, **2**, 638-654.
23. T. F. Yi, S. Y. Yang and Y. Xie, *J. Mater. Chem. A*, 2015, **3**, 5750-5777.
24. K. M. Colbow, J. R. Dahn and R. R. Haering, *J. Power Sources*, 1989, **26**, 397-402.
25. E. Ferg, R. J. Gummow, A. de Kock and M. M. Thackeray, *J. Electrochem. Soc.*, 1994, **141**, L147-L150.
26. T. Ohzuku, A. Ueda and N. Yamamoto, *J. Electrochem. Soc.*, 1995, **142**, 1431-1435.
27. M. M. Thackeray, *J. Electrochem. Soc.*, 1995, **142**, 2558-2563.
28. G. N. Zhu, Y. G. Wang and Y. Y. Xia, *Energy & Environmental Science*, 2012, **5**, 6652-6667.
29. K. T. Fehr, M. Holzapfel, A. Laumann and E. Schmidbauer, *Solid State Ion.*, 2010, **181**, 1111-1118.
30. C. Wang, S. Wang, Y.-B. He, L. Tang, C. Han, C. Yang, M. Wagemaker, B. Li, Q.-H. Yang, J.-K. Kim and F. Kang, *Chem. Mater.*, 2015, **27**, 5647-5656.
31. M. Wilkening and P. Heitjans, *Chem. Phys. Chem.*, 2012, **13**, 53-65.

32. J. Langer, D. Wohlmuth, A. Kovalcik, V. Epp, F. Stelzer and M. Wilkening, *Ann. Phys.*, 2015, **527**, 523-530.
33. M. Wilkening, J. Heine, C. Lyness, A. R. Armstrong and P. G. Bruce, *Phys. Rev. B*, 2009, **80**.
34. M. Wilkening, C. Lyness, A. R. Armstrong and P. G. Bruce, *J. Phys. Chem. C*, 2009, **113**, 4741-4744.
35. M. Wilkening and P. Heitjans, *Phys. Rev. B*, 2008, **77**.
36. M. Wilkening, W. Kuchler and P. Heitjans, *Phys. Rev. Lett.*, 2006, **97**.
37. A. Kuhn, V. Epp, G. Schmidt, S. Narayanan, V. Thangadurai and M. Wilkening, *J. Phys.: Condens. Matter*, 2012, **24**.
38. A. Kuhn, S. Narayanan, L. Spencer, G. Goward, V. Thangadurai and M. Wilkening, *Phys. Rev. B*, 2011, **83**.
39. A. Dunst, V. Epp, I. Hanzu, S. A. Freunberger and M. Wilkening, *Energy & Environmental Science*, 2014, **7**, 2739-2752.
40. V. Epp, O. Gun, H. J. Deiseroth and M. Wilkening, *J. Phys. Chem. Lett.*, 2013, **4**, 2118-2123.
41. F. Preishuber-Pflügl, P. Bottke, V. Pregartner, B. Bitschnau and M. Wilkening, *Phys. Chem. Chem. Phys.*, 2014, **16**, 9580-9590.
42. M. Wilkening and P. Heitjans, *Solid State Ion.*, 2006, **177**, 3031-3036.
43. W. Schmidt, P. Bottke, M. Sternad, P. Gollob, V. Hennige and M. Wilkening, *Chem. Mater.*, 2015, **27**, 1740-1750.
44. W. Iwaniak, J. Fritzsche, M. Zukalova, R. Winter, M. Wilkening and P. Heitjans, *Defect Diffus. Forum*, 2009, **289-292**, 565-570.
45. M. Wilkening, R. Amade, W. Iwaniak and P. Heitjans, *Phys. Chem. Chem. Phys.*, 2007, **9**, 1239-1246.
46. M. Wilkening, W. Iwaniak, J. Heine, V. Epp, A. Kleinert, M. Behrens, G. Nuspl, W. Bensch and P. Heitjans, *Phys. Chem. Chem. Phys.*, 2007, **9**, 6199-6202.
47. H. Hain, M. Scheuermann, R. Heinzmann, L. Wunsche, H. Hahn and S. Indris, *Solid State Nucl. Magn. Reson.*, 2012, **42**, 9-16.
48. M. Wagemaker, D. R. Simon, E. M. Kelder, J. Schoonman, C. Ringpfeil, U. Haake, D. Lützenkirchen-Hecht, R. Frahm and F. M. Mulder, *Adv. Mater.*, 2006, **18**, 3169.
49. V. Epp, O. Gün, H. J. Deiseroth and M. Wilkening, *Phys. Chem. Chem. Phys.*, 2013, **15**, 7123-7132.
50. D. Ailion and C. P. Slichter, *Phys. Rev. Lett.*, 1964, **12**, 168.
51. D. C. Ailion and C. P. Slichter, *Phys. Rev.*, 1965, **137**, A235.
52. C. P. Slichter and D. Ailion, *Phys. Rev.*, 1964, **135**, 1099.
53. A. Dunst, M. Sternad, V. Epp and M. Wilkening, *J. Phys. Chem. C*, 2015, **119**, 12183-12192.
54. V. Epp and M. Wilkening, *Chem. Phys. Chem.*, 2013, **14**, 3706-3713.
55. J. Langer, V. Epp, P. Heitjans, F. A. Mautner and M. Wilkening, *Phys. Rev. B*, 2013, **88**.
56. V. Epp, O. Gün, H. J. Deiseroth and M. Wilkening, *J. Phys. Chem. Lett.*, 2013, **4**, 2118-2123.
57. V. Epp, S. Nakhal, M. Lerch and M. Wilkening, *J. Phys.: Condens. Matter*, 2013, **25**.
58. N. Bloembergen, E. M. Purcell and R. V. Pound, *Phys. Rev.*, 1948, **73**, 679-712.
59. V. Epp and M. Wilkening, in *Handbook of Solid State Batteries*, eds. Nancy Dudney, William C. West and Jagjit Nanda, World Scientific, Singapore, 2nd edn., 2015, ch. 5, pp. 133-190.
60. P. Heitjans, E. Tobschall and M. Wilkening, *European Physical Journal-Special Topics*, 2008, **161**, 97-108.
61. M. Wilkening, V. Epp, A. Feldhoff and P. Heitjans, *J. Phys. Chem. C*, 2008, **112**, 9291-9300.
62. A. Laumann, H. Boysen, M. Bremholm, K. T. Fehr, M. Hoelzel and M. Holzapfel, *Chem. Mater.*, 2011, **23**, 2753-2759.
63. W. K. Pang, V. K. Peterson, N. Sharma, J.-J. Shiu and S.-h. Wu, *Chem. Mater.*, 2014, **26**, 2318-2326.
64. H. Brandstätter, D. Wohlmuth, P. Bottke, V. Pregartner and M. Wilkening, *Z. Phys. Chem.*, 2015, **229**, 1363-1374.
65. M. Vijayakumar, S. Kerisit, K. M. Rosso, S. D. Burton, J. A. Sears, Z. G. Yang, G. L. Graff, J. Liu and J. Z. Hu, *J. Power Sources*, 2011, **196**, 2211-2220.
66. I. A. Leonidov, O. N. Leonidova, R. F. Samigullina and M. V. Patrakeev, *J. Struct. Chem.*, 2004, **45**, 262-268.
67. I. A. Leonidov, O. N. Leonidova, L. A. Perelyaeva, R. F. Samigullina, S. A. Kovyazina and M. V. Patrakeev, *Phys. Solid State*, 2003, **45**, 2183-2188.
68. S. Takai, M. Kamata, S. Fujine, K. Yoneda, K. Kanda and T. Esaka, *Solid State Ion.*, 1999, **123**, 165-172.
69. J. Sugiyama, H. Nozaki, I. Umegaki, K. Mukai, K. Miwa, S. Shiraki, T. Hitosugi, A. Suter, T. Prokscha, Z. Salman, J. S. Lord and M. Månsson, *Phys. Rev. B*, 2015, **92**, 014417.
70. M. Wagemaker, E. R. H. van Eck, A. P. M. Kentgens and F. M. Mulder, *J. Phys. Chem. B*, 2009, **113**, 224-230.
71. A. Kumatani, T. Ohsawa, R. Shimizu, Y. Takagi, S. Shiraki and T. Hitosugi, *Appl. Phys. Lett.*, 2012, **101**, 123103.

7.2.4 Einfluß von CO_2 auf die Ionenleitfähigkeit von mikrokristallinem LTO

In der Veröffentlichung von Yurui Gao et al. [66] wurde dargelegt, dass frisch synthetisiertes LTO bei Luftkontakt eine Reaktion mit CO_2 eingeht und oberflächlich mit einer Li_2CO_3-Schicht überzogen wird. Laut ihren Untersuchungen spielt diese oberflächliche Schicht keine signifikante Rolle für das elektrochemische Verhalten von LTO in einer Zelle. Uns interessierte die Frage, ob sich die Diffusionseigenschaften von Lithium dadurch ändern und ob die Defektstruktur in LTO nicht auch durch den O_2-Partialdruck verändert werden kann.

Wir ließen an der bei 60 °C getrockneten Proben eine TG-MS Messung durchführen (Zusammenarbeit mit der AG Prof. Sitte, Uni Leoben). Es ist ersichtlich, dass beim Aufheizen lediglich CO_2 abgegeben wird. Eine O_2-Abgabe wurde nicht beobachtet - im Gegenteil, die Daten deuten darauf hin, dass Spuren von O_2 aufgenommen wurden.

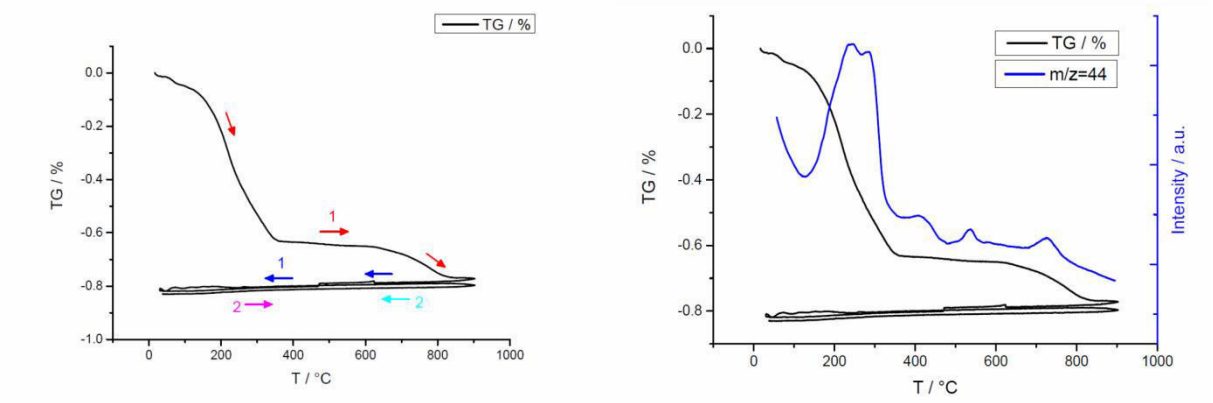

Abbildung 16: TG-MS Messung (links der Massenverlust, rechts das Signal des MS bei m/z = 44)

Also können wir davon ausgehen, dass alle unsere Proben von einer dünnen Li_2CO_3-Schicht umgeben waren, die allerdings auf die Interkalation keinen Einfluss hatte und sowohl bei den ^6Li als auch ^7Li NMR Messungen nicht in Erscheinung tritt. Die Spindichte der Karbonatschicht ist äußerst gering und kaum mit NMR-Messungen detektierbar.

Zusätzlich zu den schon durchgeführten statischen ^7Li-NMR Messungen an der LTO-Referenz, wurde eine weitere Probe vermessen, bei der die CO_2-Schicht durch Erhitzen im Vakuumtrockenofen zuvor bei 300 °C und 10^{-3} mbar entfernt wurde. Durch das Einschmelzen der Probe unter Vakuum konnte sie nicht mehr mit CO_2 reagieren.

Bei einer weiteren Probe haben wir, um die Reversibilität der CO_2-Aufnahme und Abgabe zu überprüfen, das Röhrchen mit LTO nicht wie üblich beidseitig verschlossen, sondern es wurde eine Seite offen gelassen. Durch das Vermessen der Probe wurde sie bis 300 °C erhitzt und somit „in situ“ CO_2 aus der Probe entfernt. Durch den inerten Stickstoffstrom, der das Röhrchen im Spektrometer umspült, konnte die Probe nicht erneut mit CO_2 aus der Luft reagieren. Beim ersten Erhitzen zeigte die Probe idente Werte zur Referenz. Danach wurde erneut von RT aus gemessen. Darüber hinaus wurde nach 2 Monaten Lagerung an Luft dasselbe Röhrchen wieder vermessen; es zeigte die anfänglichen Werte. Wir können also von einer vollständigen Reversibilität ausgehen.

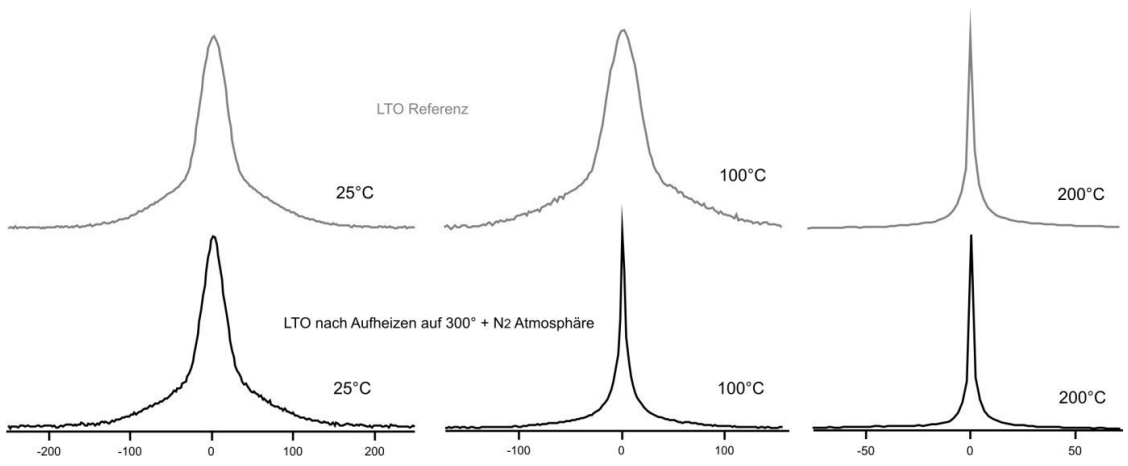

Abbildung 17: ^{7}Li-NMR-Linienbreiten der im N_2 Strom gelagerten Probe und der Referenz

Den signifikantesten Unterschied aller Proben gab es bezüglich der NMR-Linienbreiten beim Vergleich der Referenz mit der Probe, die im N_2-Strom des Spektrometers auf 300 °C aufgeheizt wurde. Schon bei Raumtemperatur weisen beide Proben einen leichten Unterschied auf, der sich bei 100 °C jedoch sehr ausgeprägt zeigt. Die Messung der Linienbreiten lässt erkennen, dass schon bei Raumtemperatur diffusionsbedingte Linienverschmälerung einsetzt, während diese bei der Referenz erst bei ca. 150 °C einsetzt.

Die zuvor bei 300 °C im Vakuum getrocknete Probe unterschied sich bezüglich der Linienbreiten und der Linienform unwesentlich vom Referenzmaterial.

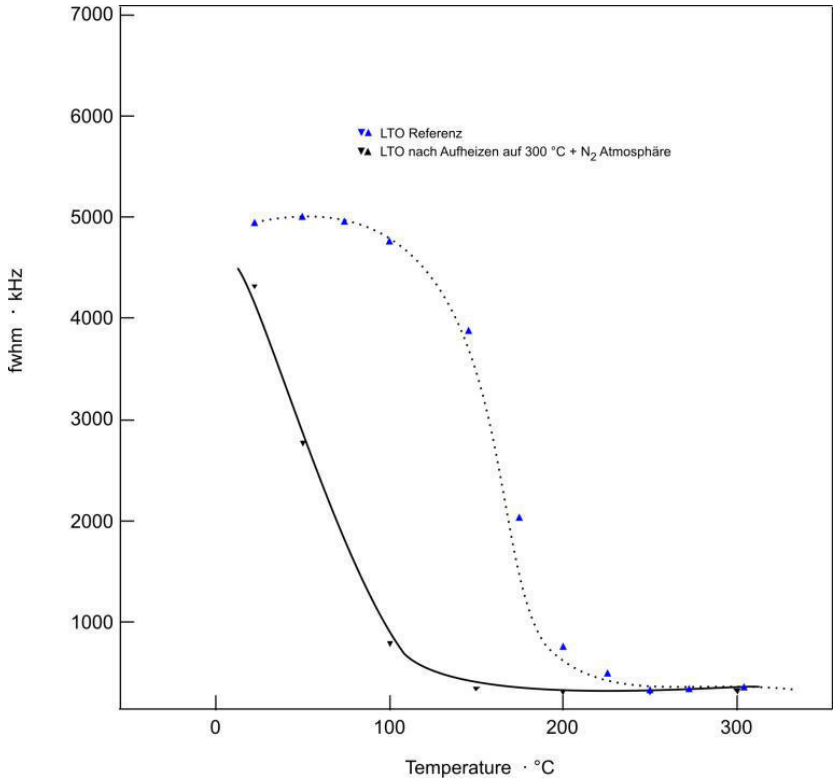

Abbildung 18: Halbwertsbreiten von LTO (Referenz) und LTO nach Erhitzen auf 300°C im N_2 Strom

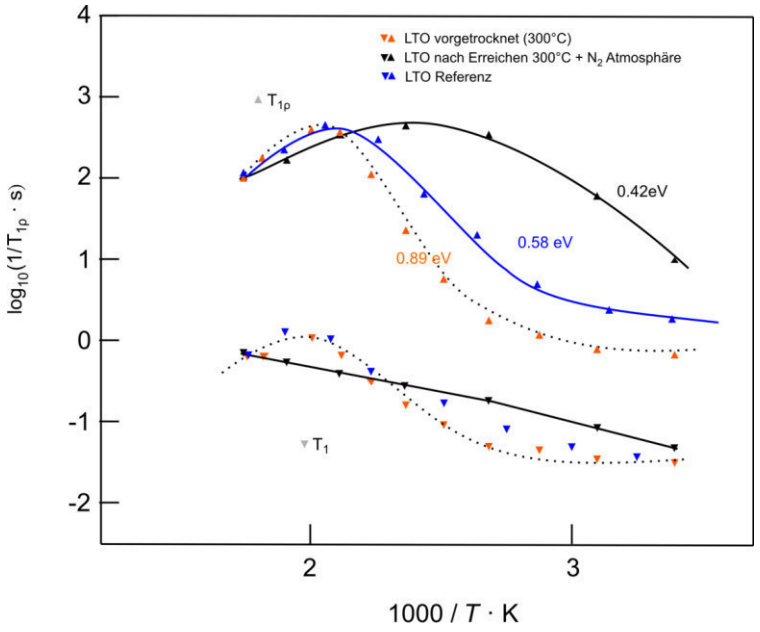

Abbildung 19: T_1- und $T_{1,\rho}$-NMR-Relaxationszeiten für LTO (Referenz), das vorgetrocknete LTO und LTO nach Erreichen von 300 °C im N_2-Strom des Spektrometers. Messungen bei 116 MHz (^{7}Li) und einer *locking*-Feldstärke von 30 kHz.

Abbildung 19 zeigt den Unterschied der T_1-^{7}Li-NMR-Relaxationszeiten zwischen den einzelnen Proben. Während bei der Referenz und der vorgetrockneten Probe keine Unterschiede bezüglich Ratenmaximum erkennbar sind, so weicht das Verhalten der Probe, die Kontakt zu N_2 hat, deutlich ab. Ein Ratenmaximum kann nicht mehr erfasst werden.

Weitaus drastischer sind die Änderungen, die die $T_{1,\rho}$-Messungen zeigen. Das Vortrocknen bei 300 °C führt zu einer Senkung der Relaxationszeiten, vor allem im Bereich des diffusionsunabhängigen Untergrundes. Das Temperaturmaximum und die Hochtemperaturflanke liegen sehr ähnlich wie bei der Referenzprobe. Die aus der Niedertemperaturflanke errechnete Aktivierungsenergie der Sprungprozesse hat sich jedoch fast um die Hälfte auf 0.89 eV erhöht. Das Temperaturmaximum der Probe die im N_2 Strom auf 300°C aufgeheizt wurde, hat sich um ca. 100 K von 500 K in Richtung niedrigerer Temperaturen verschoben; zudem ist der zugehörige Ratenpeak stark verbreitert, während die Aktivierungsenergie an der Niedertemperaturflanke auf 0.42 eV abfiel.

Zusammengefasst wäre folgender Mechanismus denkbar: Natives LTO könnte mit CO_2 nach folgender Gleichung reagieren:

$$Li_4Ti_5O_{12} + yCO_2 \rightarrow yLi_2CO_3 + Li_{4-2y}Ti_5O_{12-y}$$

Dadurch würden sowohl Li^+- als auch Sauerstofffehlstellen generiert werden, die theoretisch als zusätzlicher Migrationspfad zur Verfügung stehen könnten und die reduzierte Aktivierungsenergie für die Sprungprozesse an der Niedertemperaturflanke erklären könnten. Welche reversiblen Reaktionen bei 300 °C im N_2-Strom ablaufen, ist noch offen.

7.2.5 Untersuchungen an Nanostrukturierten Proben

Die die durch Hochenergiekugelmahlen erhaltene **Nanoprobe 1** wurde mittels statischen ^{7}Li-NMR-Messungen zusätzlich untersucht.

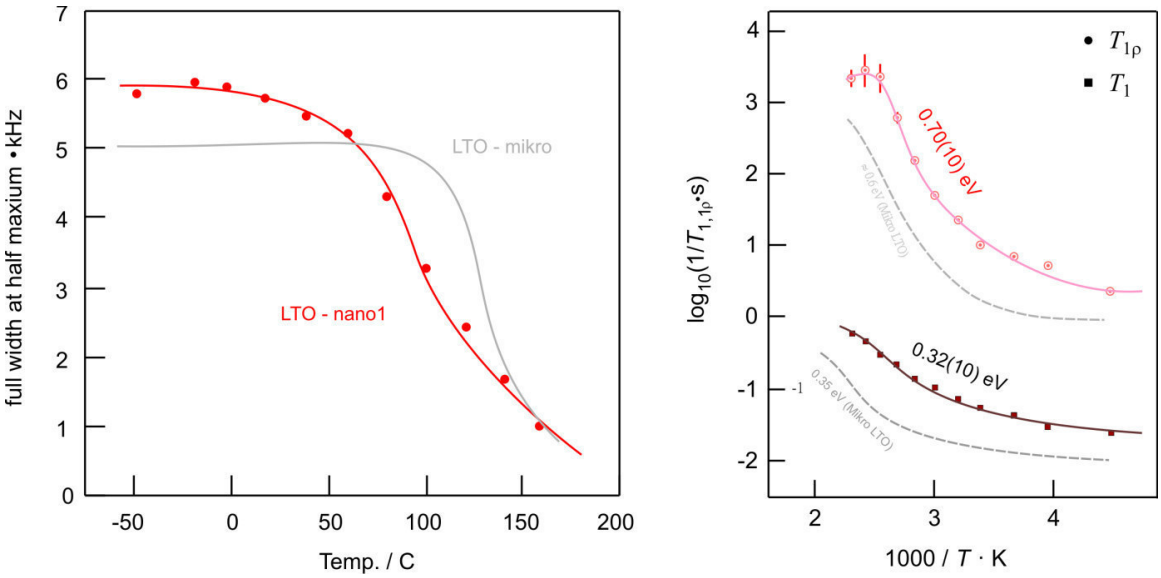

Abbildung 20: Linienbreiten, sowie T_1 und $T_{1\rho}$-Relaxationszeiten der Nanoprobe 1.

Von Beginn an liegen die gemessenen Linienbreiten der Nanoprobe 1 höher als bei der mikrokristallinen Probe. Die durch das Mahlen gebildeten Agglomerate dürften für diesen Effekt verantwortlich sein. Nichtsdestotrotz setzt die diffusionsinduzierte Linienverschmälerung bei etwa 50 °C früher ein als bei der mikrokristallinen Probe. Gleichzeitig verflacht die Kurve etwas.

Bei den T_1 Messungen kann man erkennen, dass die Kurve nach rechts, also zu niederen Temperaturen hin verschoben wurde. Die ermittelte Aktvierungsenergie ist geringfügig geringer geworden. Beide Messreihen deuten darauf hin, dass zumindest die kurzreichweitigen Li-Diffusionsparameter verbessert wurden. Bei den $T_{1\rho}$-Messungen sind die Resultate ähnlich. Ein mit einem relevanten Fehler behaftetes Maximum wurde erreicht, da die Kurve zu niederen Temperaturen verschoben wurde. Gleichzeitig sind auch hier die Relaxationszeiten kürzer geworden.

In der folgenden Abbildung 21 sind die NMR-Ergebnisse der **Nanoprobe 3** gezeigt. Bei dieser Probe war die Dauer der mechanischen Zerkleinerung in der Kugelmühle nur halb so lang.

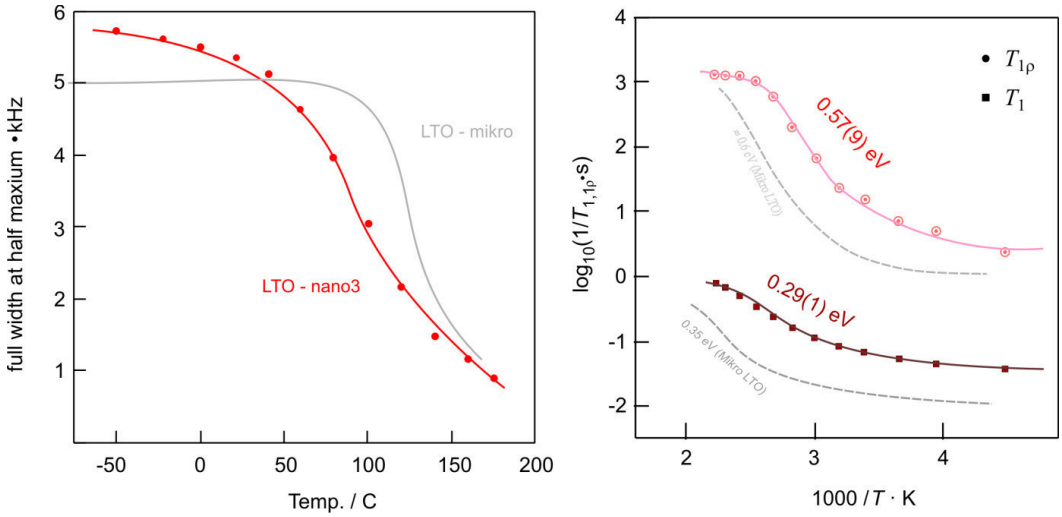

Abbildung 21: Linienbreiten, sowie T_1- und $T_{1,\rho}$-Relaxationszeiten der Nanoprobe 3

Die Linienbreiten liegen, ähnlich wie bei Nanoprobe 1, bei sehr niederen Temperaturen, über den Werten von kristallinem LTO. Die Linienverschmälerung setzt jedoch bereits bei 50 °C ein, die Steigung der durchgelegten Kurve ist jedoch flacher als bei der Referenzprobe. Die gemessenen Linienbreiten beider Proben nähern sich bei etwa 150°C einem gemeinsamen Wert, dem Wert des *extreme narrowing* an. Auch bei dieser Probe sind die T_1- und $T_{1,\rho}$-Kurven um etwa eine halbe Größenordnung nach oben verschoben, siehe Abbildung 21, rechts. Nanostrukturierung erhöht demnach auch in diesem Fall die Li-Diffusivität. Die T_1-Messungen bestätigen das Verhalten: Die T_1-Zeiten verändern sich über den gemessenen Temperaturbereich nicht so stark, sodass die resultierende Messkurve flacher wird. Ein Maximum konnte nicht durchlaufen werden, die Aktivierungsenergie bei der Niedertemperaturflanke liegt mit 0.29 eV unter dem Wert der Nanoprobe 1. Analog dazu liegen die $T_{1\rho}$-Werte beginnend von der Hintergrundrelaxation bei niederen Temperaturen bis zu höheren Temperaturen ebenfalls über den Werten von kristallinem LTO. Auch hier ist sichtbar, dass die diffusionsinduzierte Relaxation bereits bei tieferen Temperaturen beginnt. Ein Maximum konnte bei diesem Messaufbau nicht erreicht werden, die Steigung der Niedertemperaturflanke liegt mit 0.57 eV im Bereich des kristallinen LTO.

Die folgende **Nanoprobe 2**, die in EtOH gemahlen wurde, zeigte, wie schon gezeigt, im XRD keine zusätzlichen Phasen, und die gemessene Korngrößenverteilung wies eine deutliche Reduktion der mittleren Partikelgrösse auf. Daher wurde dieser Nanoprobe bei den NMR-Messungen etwas mehr Aufmerksamkeit gewidmet.

Analog zu den bereits publizierten Daten haben wir unterschiedliche Interkalationsgrade mittels Butyllithium eingestellt und dieselbe Messreihe wie im Falle von mikrokristallinem LTO vermessen.

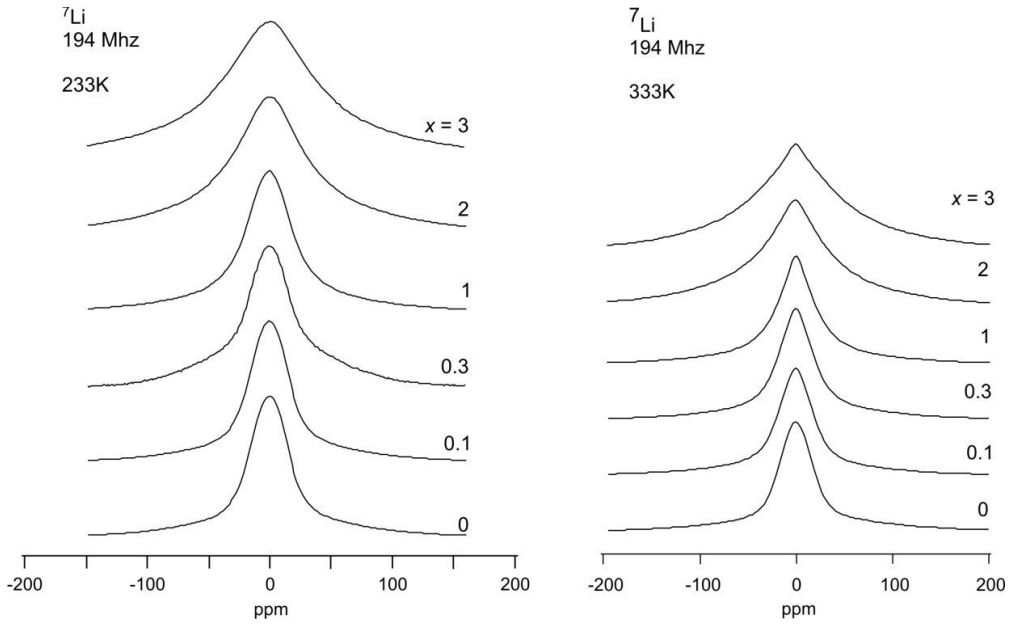

Abbildung 22: ^{7}Li-NMR-Linienbreiten der Probe $Li_{4+x}Ti_5O_{12}$ (Nanoprobe 2) bei 233 K und 333 K für x = 0, 0.1, 0.3, 1, 2 und 3.

Die Linien zeigen bei -50 °C ein Anwachsen der Halbwertsbreite analog mit dem Interkalationsgrad. Die Linien verbreitern sich aufgrund des Zunahme der Ti^{3+}-Zentrendichte. Je mehr Li eingelagert wird, desto mehr paramagnetische Ti^{4+}-Zentren werden generiert. Bei x = 0 ist der Quadrupolfuss des Spektrums gut sichtbar, der sich ebenfalls mit zunehmenden Anzahl an Ti^{3+}-Zentren ausprägt.

Vergleicht man die Linien bei 60 °C, fällt im Vergleich zum mikrokristallinen LTO auf, dass auch bei dieser Temperatur die Linienverbreiterung noch immer dem Interkalationsgrad folgt. Die diffusionsinduzierte Linienverschmälerung hat schon begonnen, aber der Unterschied zwischen Nanoprobe 2 bei den geringen Interkalationsgraden (x = 0.1 und x = 0.3) ist nur marginal. Analog zur Linie, die bei -50 °C aufgezeichnet wurde, zeigt sich auch hier bei höheren Interkalationsgraden der immer stärker ausgeprägte Quadrupolfuss.

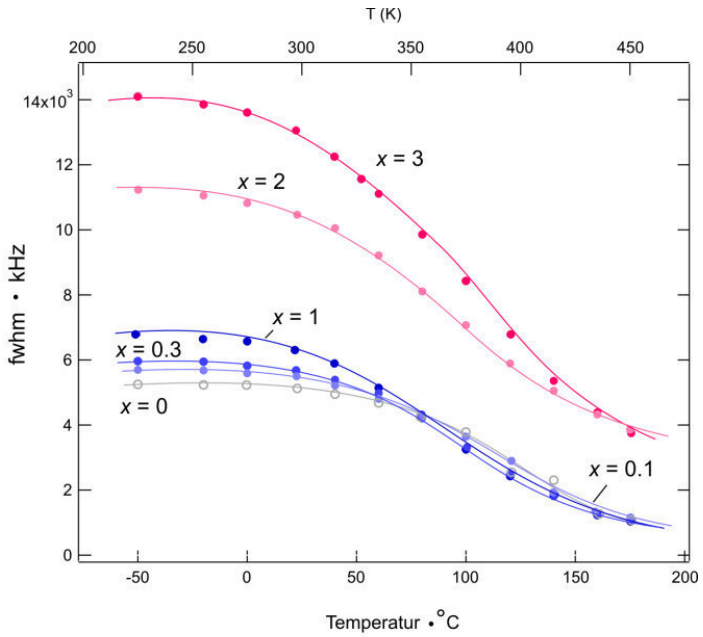

Abbildung 23: Halbwertsbreiten (fwhm) der unterschiedlichen $Li_{4+x}Ti_5O_{12}$ (Nanoprobe 2) für x = 0, 0.1,0.3, 1, 2 und 3 gegen die Temperatur aufgetragen

Abbildung 23 zeigt den Verlauf der Li-NMR-Halbwertsbreiten gegen die Temperatur aufgetragen. Im Gegensatz zum mikrokristallinen LTO beginnt die Linienverschmälerung schon bei niederen Temperaturen, dafür ist das Delta der Verschmälerung in Richtung höheren Temperaturen geringer ausgeprägt. Ab einer Temperatur von 75 °C liegt die Halbwertsbreite von LTO knapp über den Werten von x = 0.1 bis x = 1.

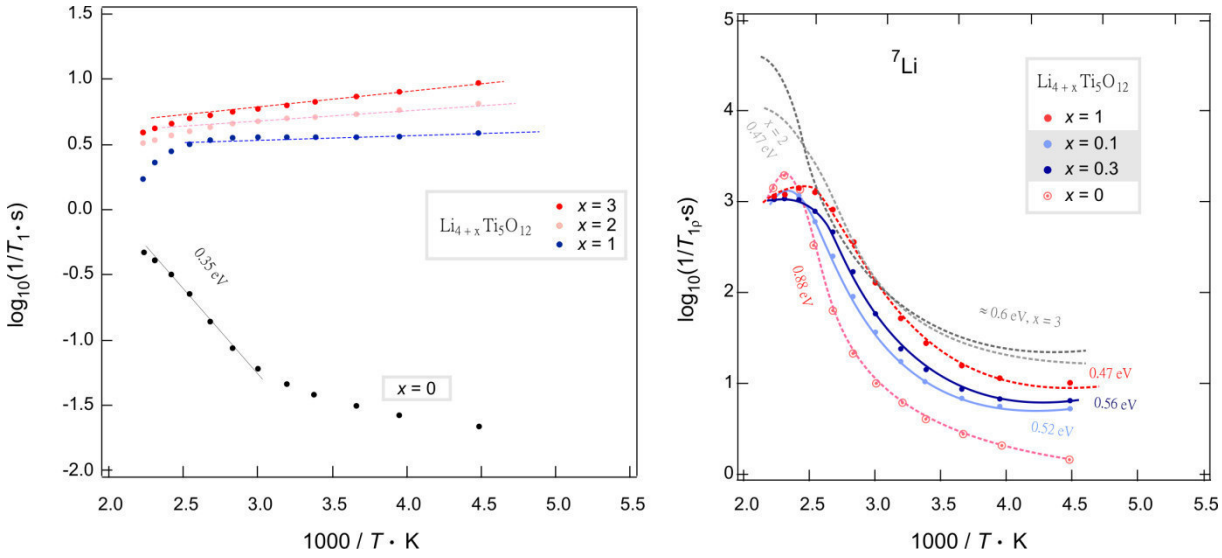

Abbildung 24: T_1-(links) und $T_{1\rho}$-Relaxationszeiten (rechts) der $Li_{4+x}Ti_5O_{12}$ (Nanoprobe 2) für x = 0, 0.1, 0.3, 1, 2 und 3.

Die T_1-Zeiten sind im Falle LTO (x = 0) analog zu den anderen Nano-Proben um eine halbe Größenordnung zu kürzeren Relaxationszeiten hin verschoben. Die aus der Steigung ermittelte Aktivierungsenergie bleibt für diese Sprungprozesse bei 0.35 eV und somit absolut gleich zur kristallinen Probe. Bei den interkalierten Nanoproben ist ein zu den kristallinen Proben analoges Verhalten zu beobachten. Die T_1-Zeiten zeigen ein beinahe temperaturunabhängiges Curie-Weiss-Verhalten, wobei sich die Werte mit zunehmendem Interkalationsgrad zu längeren Relaxationszeiten verschieben.

Die die $T_{1,\rho}$-Werte unterscheiden sich dahingehend vom Verlauf der mirkrokristallinen Proben, dass hierbei kein so eindeutiges Temperaturminimum im Verlauf der Interkalation durchlaufen wird. Charakteristisch ist bei den Werten auch, dass die nicht-interkalierte Nanoprobe 2 an der Niedertemperaturflanke eine höhere Aktivierungsenergie (0.75 eV) aufweist, als bei den nachfolgenden relativ niederen Interkalationsgraden. Bei x = 0.1 sind es 0.50 eV und bei x = 0.3 schließlich 0.48 eV. Bezüglich der Aktivierungsenergien wird auch bei den Nano-Proben hier ein Minimum in der Aktivierungsenergie in der Nähe von x = 1 durchlaufen. Die Absolutwerte der Relaxationszeiten im diffusionsbedingten Maximum liegen bei den Proben x = 0 bis x = 1 in einem vergleichbaren Bereich, während bei x = 2 das Maximum bei etwa einer Größenordnung darüber liegt und bei x = 3 gar nicht mehr detektierbar ist. Die $T_{1\rho}$-Werte der Hintergrundrelaxation nehmen über die Menge an eingelagertem Lithium kontinuierlich zu.

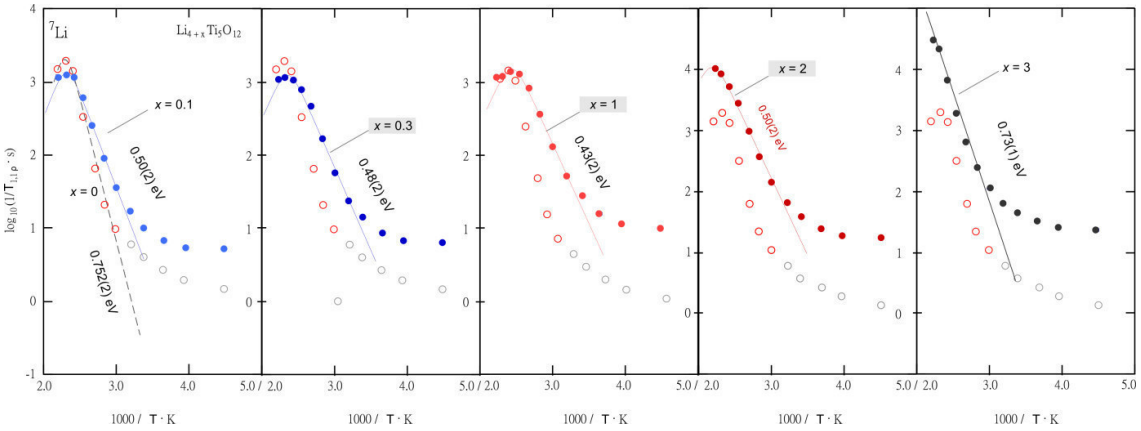

Abbildung 25: $T_{1\rho}$-Relaxationszeiten (rechts) der $Li_{4+x}Ti_5O_{12}$ (Nanoprobe 2) für x = 0, 0.1,0.3, 1, 2 und 3 im Detail aufgeschlüsselt.

Tabelle 3 zeigt nochmals eine Übersicht der charakteristischen Daten aus den $T_{1\rho}$-NMR-Experimenten und die Fitparameter aus den BPP-Fits. Hier muss man festhalten, dass ein BPP-Fit bei allen x nur mit einem relativ hohen Fehler möglich war, da die Hochtemperaturflanke bei manchen Proben außerhalb des Messbereichs lag.

Tabelle 3: Übersicht der Aktivierungsenergien, τ_0 und T_{max} bei x = 0, 0.1, 0.3, 1, 2, 3

$Li_{(4+x)}Ti_5O_{12}$ Nanoprobe 2	E_a, eV	τ_0,s	T_{max}, K
x = 0	0.75(2)	2.6×10^{-14}	~ 430
x = 0.1	0.50(2)	7.2×10^{-12}	~ 430
x = 0.3	0.48(2)	8.3×10^{-12}	~ 420
x = 1	0.42(2)	2.5×10^{-11}	~ 430
x = 2	0.50(2)	2.0×10^{-11}	> 430
x = 3	0.72(1)	3.6×10^{-11}	> 430

Analog zu den mikrokristallinen Proben haben wir auch bei diesen Proben hochauflösende ^{6}Li-MAS-Messungen durchgeführt.

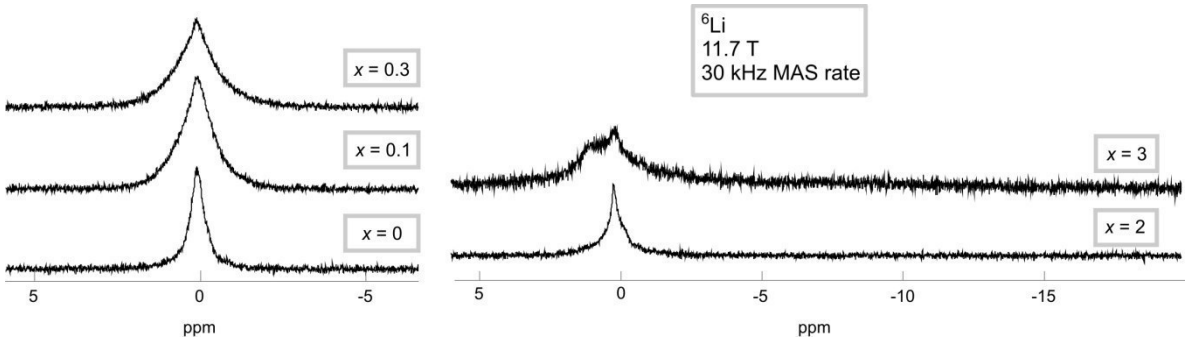

Abbildung 26: ^{6}Li MAS Spektren von $Li_{4+x}Ti_5O_{12}$ (Nanoprobe 2) für verschiedene x

Es war uns nicht möglich, die ^{6}Li-MAS--Spektren vor allem für kleine x nach den kristallographischen Positionen aufzulösen. Die Nanostrukturierung, d.h. der Eintrag hoher Defektdichte und damit struktureller Unordnung in das Material, lässt eine kristallographische Auflösung der einzelnen Positionen nicht mehr zu.

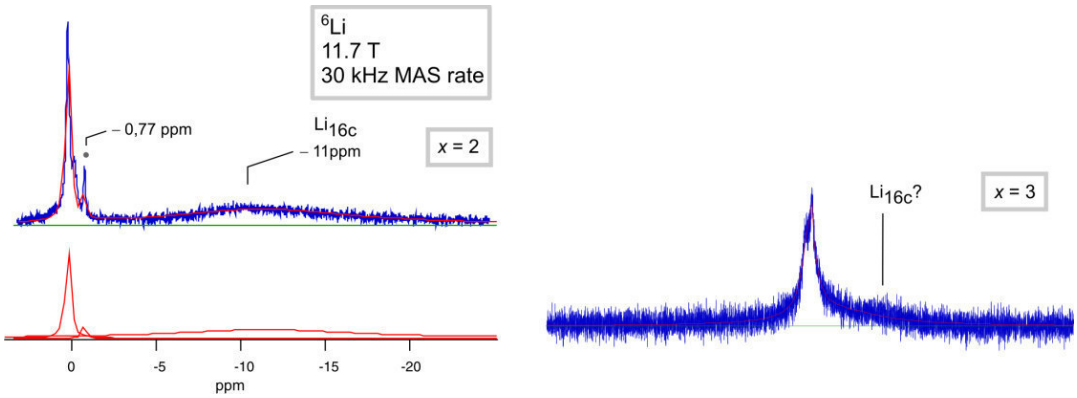

Abbildung 27: ^{6}Li-MAS-Detailspektren von $Li_{4+x}Ti_5O_{12}$ (Nanoprobe 2) $x = 2$ und $x = 3$

Abbildung 27 zeigt die Spektren für $x = 2$ und $x = 3$ noch im Detail. Immerhin war es im Falle der Probe mit $x = 2$ möglich, den 16c-Peak bei -11 ppm zu identifizieren und auch die Fremdphase von Li_2TiO_3 bei - 0.77 ppm.

7.3 Zusammenfassung der LTO-NMR-Ergebnisse

$Li_{4+x}Ti_5O_{12}$ zeichnet sich als ein sehr langlebiges Anodenmaterial aus, dass ein ausgezeichnetes Zyklenverhalten über hunderte und tausende Lade- und Entladeschritte ermöglicht. Das macht dieses Material mit seinem *zero strain*-Verhalten und dem recht hohen Potential von 1.5 V vs. Li^+/Li zu einem geeigneten Anoden-Kandidaten, der kaum Alterungsphänomenen, auch aufgrund der fehlenden SEI, unterworfen ist. Eine Nanostrukturierung ohne ein Lösemittel bewirkt eine teilweise Zerstörung des LTO, der amorphe Anteil und die Abbauprodukte bewirken eine Veränderung seiner Eigenschaften. Hochenergiekugelmahlen von LTO in reinem EtOH zeigt eine Verringerung der durchschnittlichen Partikel- und Kristallitgröße und führt in elektrochemischen Zellen einer leichten Verbesserung der Zykleneffizienz.

Aus den Li-NMR-Untersuchungen ergab sich, dass bei niedrigen, zusätzlichen Li-Gehalten in $Li_{4+x}Ti_5O_{12}$ die Lithiumdiffusivität gravierend gesteigert wird. LTO transformiert sich in einen guten Li-Ionenleiter. Die Aktivierungsenergie der Niedertemperaturflanke der gemessenen $T_{1\rho}$-NMR-Relaxationszeiten hat sich von $E_a = 0.62$ eV ($x = 0$) auf $E_a = 0.36$ eV ($x = 0.1$) reduziert, der Beginn der diffusionsinduzierten Linienverschmälerung hat sich um über 100 K zu kleineren Temperaturen hin verschoben. Die maximale Diffusivität wird zwischen $x = 0.3$ und $x = 1$ erreicht, dann nimmt sie wieder ab, wobei eine zusätzliche Linienverbreiterung von den generierten Ti^{3+}-Zentren herrührt. Das voll interkalierte $Li_7Ti_5O_{12}$ besitzt eine Steinsalz-Struktur; seine Aktivierungsenergie beträgt $E_a = 0.51$ eV; die Li-Diffusion ist noch immer ausgeprägter als im reinen LTO.

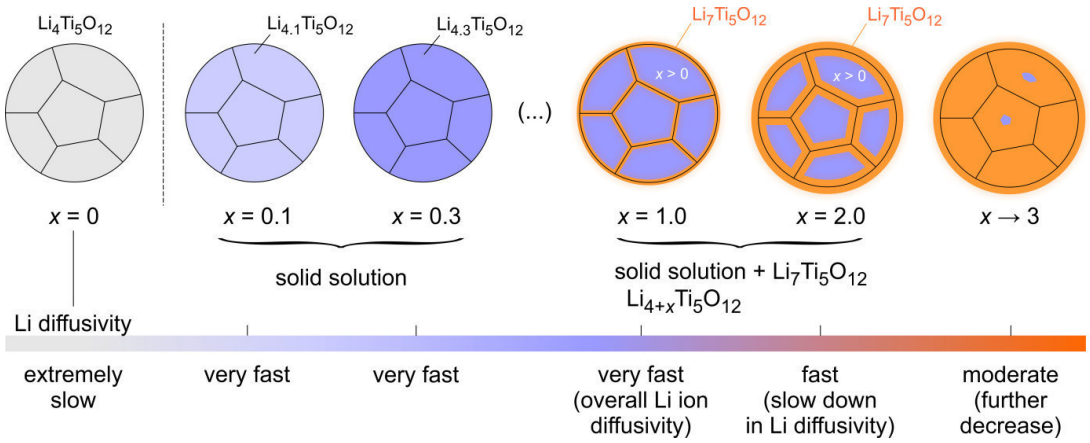

Abbildung 28: Das Lithiierungsmodell aufgrund der ^{6}Li-MAS-NMR Messungen, ab $x = 0.1$ bildet sich eine „solid solution", die sich langsam mit $Li_7Ti_5O_{12}$ anreichert, bis am Ende das reine $Li_7Ti_5O_{12}$ mit wenigen LTO-Bereichen übrigbleibt.

Die 1D-^{6}Li-MAS-NMR-Messungen deuten auf einen kombinierten Lithiierungsmechanismus hin, der eine anfänglich gebildete *solid solution* mit zunehmendem x in ein Zweiphasensystem übergehen lässt. Das bei den statischen ^{7}Li-NMR erhaltene recht breite Signal konnten wir in die kristallographischen einzelnen Positionen (8a, 16d, 16c) auflösen und eine Umverteilung bei unterschiedlichen Gehalten an Li beobachten. Bei x = 0.1 erfahren die Li-Ionen auf der Tetraederposition 8a eine deutliche Zunahme an Diffusiviät, während die Ionen auf 16d während der ganzen Lithiierung mehr oder weniger - auf der NMR-Zeitskala - immobil blieben. Mehr und mehr Ionen besetzten die Position 16c und die Besetzung der Position 8a nahm kontinuierlich ab. Bei voller Interkalation ($Li_7Ti_5O_{12}$) werden ausschließlich die Plätze 16d und 16c von Li okkupiert. Abbildung 28 fasst den erarbeiteten Lithiierungsmechanismus zusammen.

Im zur Publikation eingereichten Manuskript konnten wir mittels NMR-Hochtemperaturmessungen die $T_{1\rho}$-Ratenpeaks von $Li_4Ti_5O_{12}$ und $Li_7Ti_5O_{12}$ komplett aufzeichnen und auch die Hochtemperaturflanke erfassen. Aus diesen Messungen wurden zuverlässig die Diffusionskoeffizienten bestimmt, die der Größenordnung von 10^{-19} m^2 s^{-1} bei den entsprechenden Ratenmaximatemperaturen liegen. Aus den symmetrischen Ratenpeaks konnten wir Aktivierungsenergien in der Größenordnung von 0.6 eV und 0.48 eV ermitteln, die gut in die bereits veröffentlichten Daten passen. Die Annahme, dass es sich bei LTO um einen dreidimensionalen Ionenleiter handelt, in dem keine signifikanten Korrelationseffekte die Diffusion beeinträchtigen, konnte dadurch bestätigt werden.

Eine Nanostrukturierung durch Kugelmahlen kann je nach Betriebsmitteln und Dauer Vorteile oder Nachteile mit sich bringen. Die gesammelten Ergebnisse deuten darauf hin, dass die Li-Diffusivität in der gebildeten strukturell ungeordneten, z.T. amorphen Phase zugenommen hat.

7.4 Granate (LLZO) als Festkörperelektrolyte

Wie schon in Kapitel 4 erwähnt, bietet kristallines $Li_7La_3Zr_2O_{12}$ sehr interessante Materialeigenschaften, die es zu einem vielversprechenden Kandidaten für Festkörperbatterien macht. Murugan et al.[11] zeigten in ihrer Pionierarbeit, dass es sich um einen schnellen Li-Ionenleiter handelt. Die Arbeiten stimulierten Studien, Granate für Schutzschichten in Lithium-Luft und Li-Schwefelbatterien einzusetzen. Da LLZO eine ausreichende Stabilität gegen Lithium-Metall zeigt, erfahren Li-Anoden z.Zt. eine Renaissance in der Batterietechnologie, wenn an Festkörperbatterien gedacht wird. $Li_7La_3Zr_2O_{12}$ (LLZO) ist über Festkörpersynthese bei hohen Temperaturen darstellbar und thermisch sehr stabil. Allerdings existiert es in zwei Modifikationen. Bei Raumtemperatur ist die tetragonale Struktur stabil, während die kubische Phase nur bei sehr hohen Temperaturen synthetisiert werden kann und sich beim Abkühlen wieder in die tetragonale Phase umwandelt. Die Li-Ionenleitfähigkeit der beiden Phasen unterscheidet sich um etwa zwei Größenordnungen, die Leitfähigkeit der kubischen Phase liegt bei 10^{-3} bis 10^{-4} S cm^{-1}.[67] Die kubische Phase kann durch gezieltes Dotieren mit Al[68] oder Ga auch bei Raumtemperatur stabilisiert werden; in den letzten Jahren haben sich eine Fülle von Arbeiten der Dotierung von Granaten, d.h. der Synthese, und dem Studium der Transporteigenschaften gewidmet.[48]

7.4.1 Site Occupation of Ga and Al in Stabilized Cubic $Li_{7-3(x+y)}Ga_xAl_yLa_3Zr_2O_{12}$ Garnets As Deduced from ^{27}Al and ^{71}Ga MAS NMR at Ultrahigh Magnetic Fields

In der folgenden Publikation, die bei *Chemistry of Materials* erschienen ist, wurde zusammen mit der Forschergruppe um Prof. Amthauer und Dr. Rettenwander (Uni Salzburg) die Ionendynamik in Al- und Ga-stabilisierten, kubischen LLZO Phasen NMR-spektroskopisch untersucht. Die Proben wurden an der Uni Salzburg präpariert und ausführlich charakterisiert (XRD, SEM), die ^{7}Li-NMR-Messungen wurden an der TU Graz durchgeführt. Hochauflösende ^{27}Al- und ^{71}Ga-NMR-Messungen sind von Dr. J. Langer (TU Graz) bei ultrahohem Magnetfeld (21.7 T) in Canada, d.h. an der McMaster University in Hamilton und an der Universität von Ottawa, vermessen worden. Es wurden eine Reihe von Proben der Zusammensetzung $Li_{7-3(x+y)}Ga_xAl_yLa_3Zr_2O_{12}$ (x = 0.1, 0.2 ….. 0.8) hergestellt. Innerhalb jeder Serie von x wurden y nochmals variiert (y = 0, 0.1…..x) und x im Gegenzug reduziert.

Site Occupation of Ga and Al in Stabilized Cubic $Li_{7-3(x+y)}Ga_xAl_yLa_3Zr_2O_{12}$ Garnets As Deduced from ^{27}Al and ^{71}Ga MAS NMR at Ultrahigh Magnetic Fields

Daniel Rettenwander[*†], Julia Langer[*‡], Walter Schmidt[‡], Christian Arrer[†], Kristopher J. Harris[#], Victor Terskikh[§], Gillian R. Goward[#], Martin Wilkening[‡], and Georg Amthauer[†]

[†] Department of Materials Research and Physics, University of Salzburg, 5020 Salzburg, Austria

[‡] Christian Doppler Laboratory for Lithium Batteries, Institute for Chemistry and Technology of Materials, DFG Research Unit 1277 "molife", Graz University of Technology (NAWI Graz), 8010 Graz, Austria

[#] Department of Chemistry & Chemical Biology, McMaster University, Hamilton, Ontario L8S 4M1, Canada

[§] Department of Chemistry, University of Ottawa, Ottawa, Ontario K1N 6N5, Canada

Chem. Mater., 2015, 27 (8), pp 3135-3142

DOI: 10.1021/acs.chemmater.5b00684

Publication Date (Web): April 2, 2015

CHEMISTRY OF MATERIALS

Article

pubs.acs.org/cm

Site Occupation of Ga and Al in Stabilized Cubic $Li_{7-3(x+y)}Ga_xAl_yLa_3Zr_2O_{12}$ Garnets As Deduced from ^{27}Al and ^{71}Ga MAS NMR at Ultrahigh Magnetic Fields

Daniel Rettenwander,*[,†,⊥] Julia Langer,*[,‡,⊥] Walter Schmidt,[‡] Christian Arrer,[†] Kristopher J. Harris,[#] Victor Terskikh,[§] Gillian R. Goward,[#] Martin Wilkening,[‡] and Georg Amthauer[†]

[†]Department of Materials Research and Physics, University of Salzburg, 5020 Salzburg, Austria

[‡]Christian Doppler Laboratory for Lithium Batteries, Institute for Chemistry and Technology of Materials, DFG Research Unit 1277 "molife", Graz University of Technology (NAWI Graz), 8010 Graz, Austria

[#]Department of Chemistry & Chemical Biology, McMaster University, Hamilton, Ontario L8S 4M1, Canada

[§]Department of Chemistry, University of Ottawa, Ottawa, Ontario K1N 6N5, Canada

Supporting Information

ABSTRACT: Li-containing garnets, which are stabilized in their cubic modification by doping with Al or Ga, show very high Li-ion conductivities. This property qualifies them to be used as solid electrolytes in advanced all-solid-state batteries. The relation between local structures and dynamic properties, however, is still not fully understood. Here, cubic mixed-doped $Li_{7-3(x+y)}Ga_xAl_yLa_3Zr_2O_{12}$ garnet solid solutions with different portions of Al and Ga were synthesized. It turned out that the solubility of Ga is higher than that of Al; the evaluation of 42 different doping compositions indicated an increase of the lattice parameter a_0 with increasing Ga content. ^{71}Ga MAS NMR spectra recorded at 21.1 T revealed two ^{71}Ga NMR resonances, corresponding to Ga occupying both the 24*d* (243 ppm) and 96*h* sites (193 ppm). This behavior, which has been observed for the first time in this study, is very similar to that of Al. The ^{71}Ga NMR line at 193 ppm observed here remained invisible in previous NMR studies that were carried out at lower magnetic fields. The invisibility at lower field is because of large second-order quadrupolar broadening that has a lower effect on the ^{71}Ga NMR spectra at higher magnetic field. Most importantly, the similarity in site preference of Al and Ga found here inevitably raises a question about the significance of a blocking effect on long-range Li-ion transport. It weakens the assumption that the site preference of dopants is responsible for the higher Li diffusivity of Ga-doped samples compared to the Al-doped analogues. Concerning Li-ion dynamics, our ^{7}Li NMR line shape measurements indicate that the change in lattice constant a_0 with increasing doping level seems to have a larger influence on Li-ion dynamics than the Al:Ga ratio.

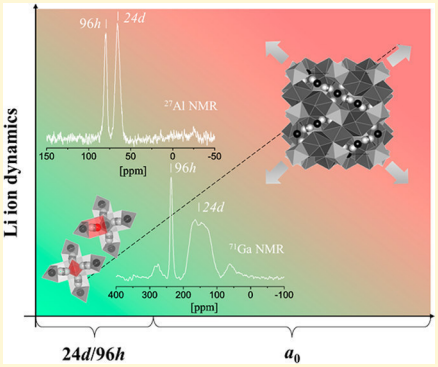

1. INTRODUCTION

Since the initial study by Murugan et al. in 2007, $Li_7La_3Zr_2O_{12}$ (LLZO) garnet has received much scientific attention as a fast Li-ion conductor.[1] Superior chemical and thermal stability, and electrochemical inertness in a wide potential window, particularly its stability against Li metal, make LLZO an excellent candidate to be used as solid electrolyte in both Li-ion and Li oxygen batteries.

The garnet-based structure occurs in at least two structural modifications, viz., a low-temperature tetragonal phase (space group $I4_1/acd$) and a non-quenchable high-temperature cubic phase (space group $Ia\bar{3}d$); the latter is shown in Figure 1.[2,3] Li-ion conductivity of the cubic polymorph is 2 orders of magnitude higher (10^{-3}–10^{-4} S cm^{-1}) compared to that of the tetragonal polymorph (10^{-6} S cm^{-1}). Fortunately, the cubic phase can be stabilized at room temperature (RT) by replacing Li with supervalent dopants (e.g., $Al^{3+} \leftrightarrow 3Li^+$), as has been previously demonstrated in many investigations.[4,5] Consequently, attention has been directed to other dopant cations, such as gallium. In the periodic table, Ga is located directly below Al; hence, it should show a crystal-chemical behavior similar to that of Al. Indeed, the successful stabilization of cubic garnet-type LLZO via the incorporation of Ga has been reported recently.[6−9]

Much experimental as well as theoretical effort has been undertaken to collect information on the local coordination as well as the site preferences of the dopants in LLZO. Some of our group have shown that Al preferentially occupies the tetrahedrally coordinated 24*d* sites as well as the distorted four-fold-coordinated 96*h* sites in LLZO.[10] For Ga, on the other hand, recent ^{71}Ga NMR studies indicated that only a single site (viz., the 96*h* site) is occupied by the dopant, irrespective of the

Received: February 22, 2015
Revised: March 30, 2015
Published: April 2, 2015

DOI: 10.1021/acs.chemmater.5b00684
Chem. Mater. 2015, 27, 3135−3142

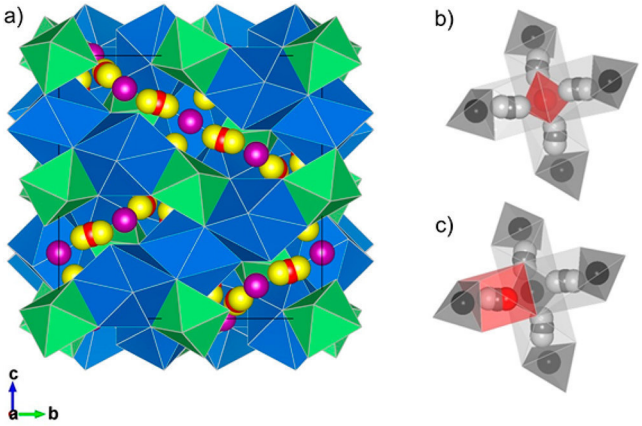

Figure 1. (a) Crystal structure of cubic LLZO ($Ia\bar{3}d$). Blue dodecahedra (24*c*) are occupied by La^{3+}, green octahedra (16*a*) by Zr^{4+}. The Li ions are distributed over three sites, viz., tetrahedrally coordinated (24*d*) sites represented by purple spheres, octahedrally coordinated (48*g*) sites represented by red spheres, and distorted four-fold-coordinated (96*h*) sites represented by yellow spheres. The figures on the right show the polyhedra of the main Li pathway. Red spheres/polyhedra indicate the occupation of one of the vacant sites, 24*d* (b) and 96*h* (c), by a dopant.

amount of Ga introduced.[7] Since the 24*d* site forms a junction between the loops of the Li-ion pathways in LLZO, the occupation of this site is suspected to act as a blockade for the mobile Li ions; this might be in contrast to the situation when only the 96*h* sites are occupied (see Figure 1).

Consequently, provided there is a significant site preference for Al and Ga, one might expect a measurable influence on Li-ion transport properties of LLZO, as discussed by Allen et al.[11]

In order to test this assumption, we synthesized mixed-doped LLZO:(Ga,Al) with varying portions of Al and Ga. Here, a series of $Li_{7-3(x+y)}Ga_xAl_yLa_3Zr_2O_{12}$ garnet solid solutions with intended mole fractions of x Ga and y Al, with $x, y \in \{0.0, 0.1, ..., 0.8 \wedge x + y \leq 0.8\}$ per formula unit (pfu) were synthesized by a conventional high-temperature sintering method.[12] For the sake of simplicity, samples are given with the following formulas:

$$Li_{6.4}Ga_{0.2-y}Al_yLa_3Zr_2O_{12} \rightarrow Ga_{0.2-y}Al_y, \quad \text{with } y = 0.0-0.2$$

$$Li_{6.1}Ga_{0.3-y}Al_yLa_3Zr_2O_{12} \rightarrow Ga_{0.3-y}Al_y, \quad \text{with } y = 0.0-0.3$$

$$Li_{5.8}Ga_{0.4-y}Al_yLa_3Zr_2O_{12} \rightarrow Ga_{0.4-y}Al_y, \quad \text{with } y = 0.0-0.4$$

$$Li_{5.5}Ga_{0.5-y}Al_yLa_3Zr_2O_{12} \rightarrow Ga_{0.5-y}Al_y, \quad \text{with } y = 0.0-0.5$$

$$Li_{5.2}Ga_{0.6-y}Al_yLa_3Zr_2O_{12} \rightarrow Ga_{0.6-y}Al_y, \quad \text{with } y = 0.0-0.6$$

$$Li_{4.9}Ga_{0.7-y}Al_yLa_3Zr_2O_{12} \rightarrow Ga_{0.7-y}Al_y, \quad \text{with } y = 0.0-0.7$$

$$Li_{4.6}Ga_{0.8-y}Al_yLa_3Zr_2O_{12} \rightarrow Ga_{0.8-y}Al_y, \quad \text{with } y = 0.0-0.8$$

Thereafter, the samples were investigated by X-ray powder diffraction (XRPD), scanning electron microscopy (SEM), and ^{27}Al (spin-quantum number $I = 5/2$) and ^{71}Ga ($I = 3/2$) magic angle spinning (MAS) nuclear magnetic resonance (NMR) spectroscopy. The latter was used to probe local magnetic and electronic structures. Finally, the Li-ion dynamics was studied by ^{7}Li ($I = 3/2$) NMR spectroscopy.

2. EXPERIMENTAL SECTION

Syntheses. The starting materials were Li_2CO_3 (99%, Merck), La_2O_3 (99.99%, Aldrich), ZrO_2 (99.0%, Aldrich), Ga_2O_3 (99.0%, Aldrich), and Al_2O_3 (99.0%, Aldrich).The well-ground powder was first calcinated at 900 °C and then reground, pelletized, and sintered at 1050 °C for 16 h. A small fragment taken from the middle of the sintered pellets was ground and used for the XRPD and NMR investigations. For SEM analysis, polycrystalline chips from the pellets were embedded in epoxy holders, and then the surface was ground and polished using diamond paste.

XRPD. Diffraction patterns were recorded with a Siemens D8 diffractometer using Cu Kα radiation. This was done to characterize the synthetic products in terms of all phases present and to determine the symmetry and unit-cell dimension of the garnet. Data were collected between 10° and 80° 2θ. The lattice parameter a_0 and the average grain size were obtained by Rietveld refinement using the program Topas V2.1 (Bruker).

SEM. Images were taken using a Zeiss Ultra Plus device. In particular, we put emphasis on the investigation of the phase composition and the chemical homogeneity, i.e., the distribution, of La, Zr, and Al, using a back-scattered electrons (BSE) detector and energy-dispersive spectroscopy (EDS) measurements, respectively.

Solid-State NMR. ^{27}Al and ^{71}Ga MAS NMR spectra, including the multiple quantum (MQ) MAS spectra, were acquired at RT using a high-performance Bruker Avance II 900-MHz spectrometer. The spectrometer is connected to a cryomagnet with a nominal field of 21.1 T; it is installed at the Canadian National Ultrahigh-Field NMR Facility. The value of 21.1 T corresponds to Larmor frequencies $\omega_0/2\pi$ = 234.5 MHz for ^{27}Al and 274.5 MHz for ^{71}Ga. All experiments were performed under MAS conditions at spinning rates of 25 kHz (^{27}Al), 31.25 kHz (^{27}Al triple quantum (3Q) MAS), and 30 kHz (^{71}Ga), using a Bruker 2.5 mm H/X probe. Chemical shift values, δ_{iso}, were referenced to 1 M aqueous solutions of $Al(NO_3)_3$ and $Ga(NO_3)_3$. The one-dimensional MAS spectra were recorded via single pulse excitation; very short pulse lengths of 1.0 μs (^{27}Al) and 0.5 μs (^{71}Ga) were used. For the ^{27}Al and ^{71}Ga measurements, the recycle delay was set to 0.5 s in both cases. The NMR acquisition conditions were tested to ensure quantitative spectra. ^{27}Al MAS NMR spectra were recorded with 640 scans, while ^{71}Ga spectra were acquired with 16k scans ($Ga_{0.4}Al_{0.0}$, $Ga_{0.3}Al_{0.1}$, $Ga_{0.2}Al_{0.2}$) or 32k scans ($Ga_{0.1}Al_{0.3}$).

^{27}Al 3QMAS NMR spectra were acquired using a standard three-pulse sequence with a Z-filter. The spectra were rotor-synchronized in the F1 dimension, and a relaxation delay of 2.5 s was used with 192 ($Ga_{0.0}Al_{0.4}$) or 288 ($Ga_{0.2}Al_{0.2}$) scans per each of the 128 td1 increments. The DMFit software was used to simulate the NMR line shapes and to determine chemical shift values as well as to estimate the corresponding coupling constants and asymmetry parameters.

Variable-temperature ^{7}Li NMR line shapes were recorded under non-MAS conditions at 11.7 T (193.4 MHz) using a Bruker Avance III spectrometer in combination with a commercial Bruker probe for broadband applications. Typically, the 90° pulse length was approximately 2 μs; we used a solid-echo pulse sequence to record the spectra.

DOI: 10.1021/acs.chemmater.5b00684
Chem. Mater. 2015, 27, 3135−3142

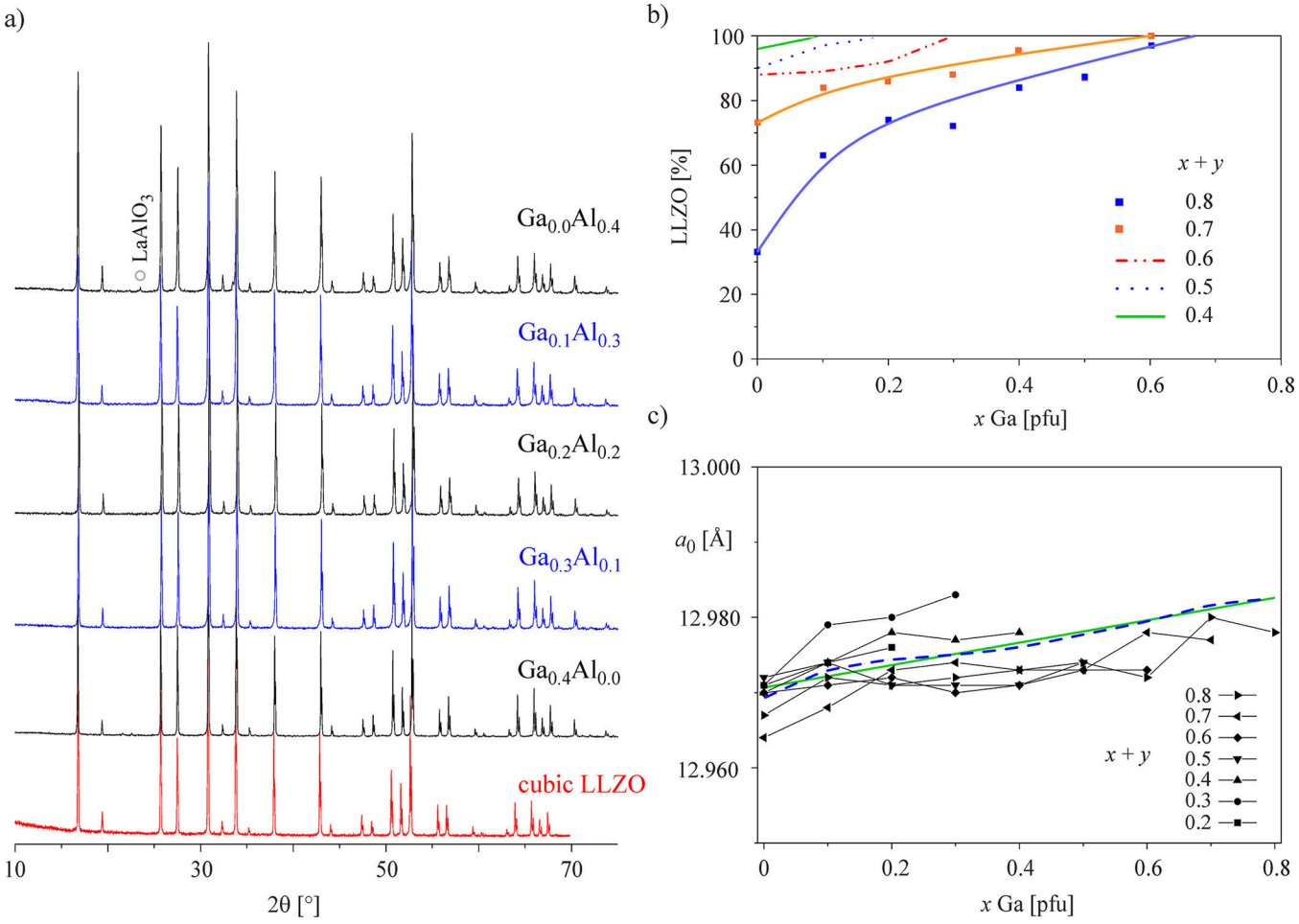

Figure 2. (a) XRPD patterns of $Ga_{0.4-y}Al_y$ with x = 0.0, 0.1, 0.2, 0.3, and 0.4. The diffraction pattern of cubic LLZO (red) is shown for comparison. (b) Portion of LLZO in the synthesis as a function of the Ga content. The lines, serving as guides to the eye, correspond to different solid solutions. Above these lines, phases other than LLZO are present. These extra phases are given in Table S1 in the Supporting Information. (c) Unit-cell parameter a_0 of Ga_xAl_y garnets as a function of Ga content. The dashed line represents the average of the multiple curves; the solid line is a linear fit of the multiple averaged curves.

3. RESULTS AND DISCUSSION

Phase Composition As Seen via XRPD. The XRPD patterns of $Ga_{0.4-y}Al_y$ are shown in Figure 2, together with the pattern of cubic LLZO.[5] For the patterns of all other solid solutions, we refer to Figure S1 in the Supporting Information.

Phase compositions were evaluated by Rietveld analysis, with the corresponding results summarized in Table S1. These data are also illustrated in Figure 2b, showing the portion of LLZO in the syntheses as a function of Ga content. The solid solutions synthesized exhibit reflections clearly showing cubic symmetry. There are no indications of any phases formed other than LLZO for $Ga_{0.4-y}Al_y$ with $y < 0.4$. The sample with $y = 0.4$ shows a low-intensity single reflection representing <1 wt % $LaAlO_3$. This impurity phase is also seen by ^{27}Al MAS NMR in the sample with $y = 0.3$; in that case it seems to be X-ray amorphous. The other samples are phase pure, independent of the intended portion of dopants. In all solid solutions with $x + y > 0.5$, the number and the amount of extra phases increase with the portion of Al. Typically, these extra phases are $LaAlO_3$, $Li_2Zr_2O_3$, and $La_2Zr_2O_7$; the more Al is present, the more easily those phases are formed. More details about the samples are given in the Supporting Information. The evaluation of the LLZO portion in the syntheses, as shown in Figure 2b, gives evidence for a lower incorporation limit of Al as compared to Ga. By increasing the Al portion (y) in $Ga_{x-y}Al_y$, with $x \leq 0.8$, the amount and the number of extra phases rise simultaneously. Phase-pure Ga-doped LLZO can be synthesized up to $x = 0.8$; this is in contrast to Al-doped LLZO, for which the incorporation limit turns out to be approximately 0.3 pfu.

Lattice Parameter (XRPD). The unit-cell constant, a_0, was evaluated by Rietveld analysis. Results are summarized in Table S1 and illustrated in Figure 2c. There is no indication that a_0 follows a general trend for the singly doped solid solution ($Ga_xAl_{0.0}$ and $Ga_{0.0}Al_y$). Our findings are in agreement with previous studies on Ga-doped LLZO, where the lattice parameter a_0 does not change systematically or significantly with the amount of dopants.[7,8] This is probably related to the aliovalent doping mechanism, where three Li^+ ions are substituted by one Ga^{3+}, and to the variation in site occupation. Interestingly, the a_0 value increases with the Ga portion by approximately 0.015 Å/Ga pfu. In our study, the Li content remains constant, but Al is continuously replaced by Ga within each series. Thus, in this case, the larger ionic radius of Ga seems to be responsible for the slight increase in a_0 observed.

Phase Stability and Solubility of Al and Ga. So far, efforts have been made to investigate the solubility of Al and Ga in LLZO and their influence on phase behavior. A detailed study on the role of the amount of Al and Li in cubic LLZO

DOI: 10.1021/acs.chemmater.5b00684
Chem. Mater. 2015, 27, 3135−3142

was presented by Rangasamy et al.[13] Those authors showed that the Al content has to be above a critical concentration of 0.20 pfu to stabilize the cubic garnet phase. Otherwise, if the Al content is above 0.39 pfu, two phases will form, cubic LLZO and $LaAlO_3$. Because Ga is located directly below Al in the periodic table, one may suspect Ga to have effects similar to those of Al on the stabilization of the cubic phase. Indeed, phase-pure cubic LLZO garnet can be obtained with a Ga content ranging from 0.16 to 0.72 pfu.[7]

Here, we were able to show that mixed doping with Al and Ga stabilizes the cubic phase in the same way as known for doping with a single element. It turned out that the solubility of Ga is higher than that of Al. Furthermore, the amount of extra phases increases with increasing Al portion. Most likely, the reason for the lower incorporation limit of Al compared to Ga can be related to the larger difference between the radii of Li ($r[4]$ = 0.59 Å; $r[6]$ = 0.74 Å) and Al ($r[4]$ = 0.39 Å; $r[6]$ = 0.53 Å) compared to the difference between Li and Ga ($r[4]$ = 0.47 Å; $r[6]$ = 0.62 Å).[14] According to Goldschmidt's rule, the maximum change in ionic radii should be below approximately 15% to fully substitute a given cation in solid solutions. Consequently, owing to the smaller radii of Al in different coordination spheres, one might expect a lower incorporation limit for Al ions than for Ga ions. Recently, the preparation of Al-doped LLZO samples with up to 1.78 Al pfu, namely $Li_{6.36}Al_{1.78}La_{2.27}Zr_{1.38}O_{12}$, has been tried via mechanosynthesis combined with calcination.[15] Here, 1.78 Al pfu means that 6.36 + 1.78 = 8.14 Al^{3+} cations are distributed over the Li sites (24*d*, 48*g*, and 96*h*). Because of repulsive Li^+−Li^+ and Li^+−Al^{3+} interactions, no more than 60 out of 168 available Li sites per unit cell (= 7.5 Li pfu) can be occupied by Li that is distributed among the available sites 24*d*, 48*g*, and 96*h*. This estimation is based on the assumption that, if a Li ion is located on a 24*d* site, Li ions in the immediate neighborhood will be displaced to a 96*h* void next to an empty 24*d* position. The value of 7.5 Li pfu is in agreement with the upper incorporation limit found experimentally by Rangasamy et al.[13]

Additional Al ions, however, might also be found in side products such as $LiAlO_2$ or $LaAlO_3$, as mentioned above.[12] If present in an amorphous form, they are expected to be invisible by X-ray diffraction but detectable by NMR spectroscopy. Due to signals overlapping in ^{27}Al MAS NMR, however, it can be difficult to detect such phases. As an example, δ_{iso} of crystalline or X-ray amorphous $LiAlO_2$ (the γ- or δ-form) shows up at ca. 82 ppm, which falls into the same ppm range of ^{27}Al on 96*h* in LLZO.[16] In ref 15, some of the ^{27}Al MAS NMR resonances at around 80 ppm, which should be interpreted as a single site in Al-LLZO, broaden with increasing Al content; in some cases a shoulder located at 82 ppm is visible for large Al portions. This feature might be attributed to the increasing formation of side products such $LiAlO_2$. Amorphous extra phases may work as a sintering aid and assist in connecting the LLZO particles, thus enabling long-range ion transport because of reduced ion-blocking effects stemming from low-conducting grain boundary regions.[8] Note that, in analogy to the Al-doped oxides, the formation of crystalline $LiGaO_2$ has also been observed during the synthesis of Ga-bearing garnets.[8]

Element Distribution (EDS Mapping). For illustration, Al and Ga incorporation and distribution were evaluated for a representative sample, $Ga_{0.2}Al_{0.2}$, by using BSE and EDS mapping (see Figure 3). The grains formed are smaller than 10 μm in diameter and are partly connected to each other. The element mapping of those grains clearly indicates that Al and Ga are successfully incorporated and homogeneously distributed throughout the garnet structure.

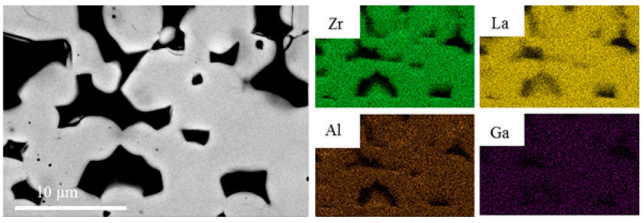

Figure 3. (Left) BSE image and (right) EDS element mapping of a representative sample, namely $Li_{5.8}Ga_{0.2}Al_{0.2}La_3Zr_2O_{12}$. The intensity of the color does not correspond to the amount of the element measured.

^{27}Al and ^{71}Ga MAS NMR. Selected NMR spectra of samples with the composition $Ga_{0.4-y}Al_y$, with y = 0.1, 0.2, 0.3, and 0.4, are shown in Figure 4. The position and the shape of the lines were evaluated with DMFit software; the results are summarized in Table 1.

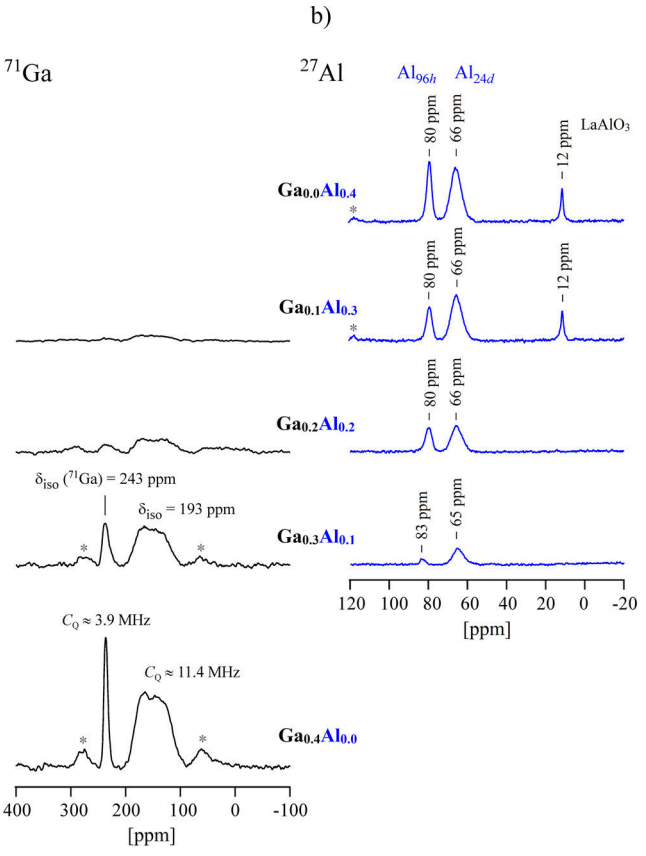

Figure 4. (a) ^{71}Ga (black) and (b) ^{27}Al (blue) MAS NMR spectra of $Li_{5.8}Ga_{0.4-y}Al_yLa_3Zr_2O_{12}$ garnets recorded at 21.1 T. Asterisks denote spinning side bands. See text for further details.

^{71}Ga (I = 3/2, natural abundance 39.6%) and ^{27}Al (I = 5/2, natural abundance 100.0%) are quadrupolar nuclei; the corresponding interaction of their quadrupole moments ($Q_{^{71}Ga}$ = 1.07 × 10^{-29} m^2 and $Q_{^{27}Al}$ = 1.466 × 10^{-29} m^2) with surrounding electric field gradients results in specific shapes of the NMR lines that depend on the interplay of the magnitude of the external magnetic field applied and the underlying coupling constant and asymmetry parameters characterizing the

DOI: 10.1021/acs.chemmater.5b00684
Chem. Mater. 2015, 27, 3135−3142

Table 1. NMR Parameters of $Li_{7-3(x+y)}Ga_xAl_yLa_3Zr_2O_{12}$ As Obtained by ^{27}Al and ^{71}Ga MAS NMR as Well as Static ^7Li NMR

sample	NMR	δ_{iso} (ppm)	C_Q (MHz)	assignment	fwhm[a] (Hz)
$Ga_{0.0}Al_{0.4}$	^{27}Al	65.9		24*d*	
		79.5		96*h*	5700
		11.7		$LaAlO_3$	
$Ga_{0.1}Al_{0.4}$	^{27}Al	65.9		24*d*	
		79.5		96*h*	
		11.6		$LaAlO_3$	5700
	^{71}Ga	–[b]		24*d*	
		–[b]		96*h*	
$Ga_{0.2}Al_{0.2}$	^{27}Al	65.5		24*d*	
		79.8		96*h*	4500
	^{71}Ga	–[b]		24*d*	
		–[b]		96*h*	
$Ga_{0.3}Al_{0.1}$	^{27}Al	65.2		24*d*	
		83.1		96*h*	3000
	^{71}Ga	193	11.1	24*d*	
		243	4.9	96*h*	
$Ga_{0.4}Al_{0.0}$	^{71}Ga	193	11.4	24*d*	2200
		243	3.9	96*h*	

[a]Full width at half-maximum, line widths as obtained from static ^7Li NMR line shape measurements at ambient temperature. [b]Signal observed but not simulated due to insufficient S/N.

interaction. While first-order electric quadrupole interactions are largely eliminated by sufficiently fast spinning, MAS is unable to remove the second-order effects.

^{27}Al NMR spectra of Al-doped LLZO have already been extensively analyzed in the past; see, e.g., refs 5 and 10. In accordance with previous reports, our ^{27}Al MAS NMR spectra of mixed LLZO show two characteristic resonances at ca. 66 ppm and ca. 81 ppm, irrespective of the amount of Al inserted. For the samples with high Al content, an additional resonance at 12 ppm was found; it reflects octahedrally coordinated Al ions in $LaAlO_3$, which is a known extra phase that forms during the synthesis of Al-doped LLZO.[5] As mentioned above, $LaAlO_3$ was also observed in XRPD for samples with high Al content. Since in our case the magnetic field interaction at B_0 = 21.1 T is much stronger than the quadrupole interactions, our ^{27}Al MAS NMR spectra benefit from a better resolution, resulting in sharp signals with almost isotropic line shapes. For this reason, the ^{27}Al NMR parameters C_Q and η_Q cannot be simulated well with DMFit; however, the apparent chemical shift values can be measured.

Here, also considering our recent study,[10] we assign the chemical shifts at 66 and 81 ppm (see Table 1) to Al ions residing on the 24*d* and 96*h* sites, respectively.[10] This assignment is in agreement with recent studies by other groups, focusing on the site preference of Al in LLZO; the resonance near 66 ppm has consistently been interpreted to reflect Al ions on the 24*d* position.[4,5,15,17] In one of those studies, the resonance was extraordinarily broad and, therefore, was interpreted as a superposition of two resonances assigned to two different 24*d* sites of LLZO phases, which had not yet reached thermodynamic equilibrium.[17]

In most of the published ^{27}Al MAS NMR spectra of LLZO, a second resonance shows up at approximately 80 ppm, being carefully assigned to the distorted, four-fold-coordinated 96*h* position. Because of the asymmetric line shape of this resonance, the signal was suspected to be a superposition of more than one NMR lines showing up in the region from 75 to 85 ppm. These results were afterward re-interpreted using DFT methods.[10]

In order to resolve potentially overlapping lines, we studied $Ga_{0.2}Al_{0.2}$ and $Ga_{0.0}Al_{0.4}$ with the help of ^{27}Al 3QMAS NMR (Figure 5). This technique increases the resolution of the

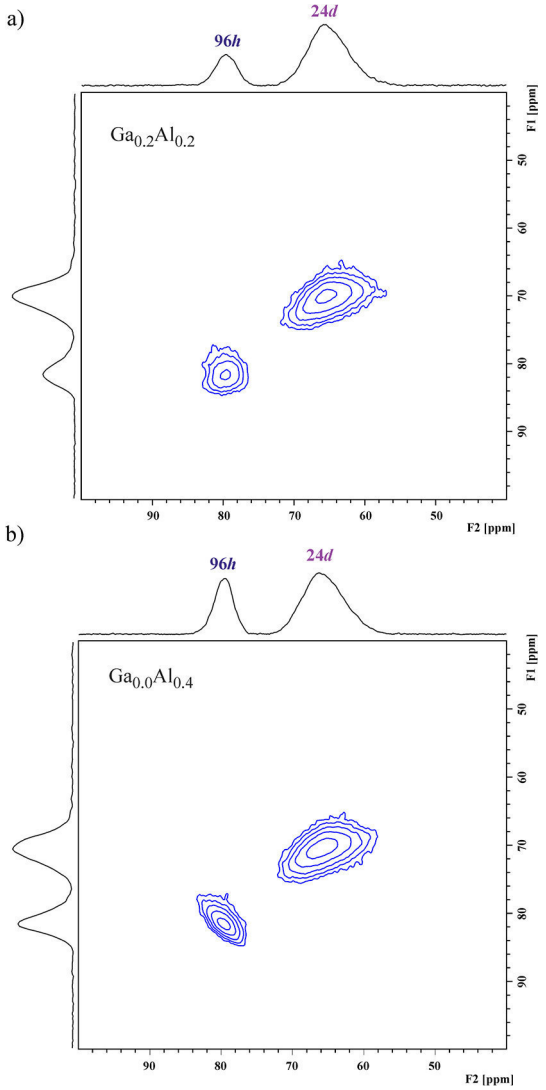

Figure 5. ^{27}Al 3QMAS NMR spectra of (a) $Ga_{0.2}Al_{0.2}$ and (b) $Ga_{0.0}Al_{0.4}$ recorded at 21.1 T and a spinning speed of 31.25 kHz.

spectra that are influenced by non-negligible second-order quadrupolar interactions which cannot be averaged by MAS, as mentioned above.

The ^{27}Al 3QMAS spectra of $Ga_{0.2}Al_{0.2}$ and $Ga_{0.0}Al_{0.4}$ essentially prove that the line broadening is not caused by distinct overlapping sites. However, it is worth noting that the diagonal streaking in the 2D projection indicates a certain distribution of chemical shifts reflecting a small amount of disorder or strain in the sample. This feature is even more pronounced in the ^{27}Al 3QMAS spectrum of $Ga_{0.0}Al_{0.4}$ for the

DOI: 10.1021/acs.chemmater.5b00684
Chem. Mater. 2015, 27, 3135−3142

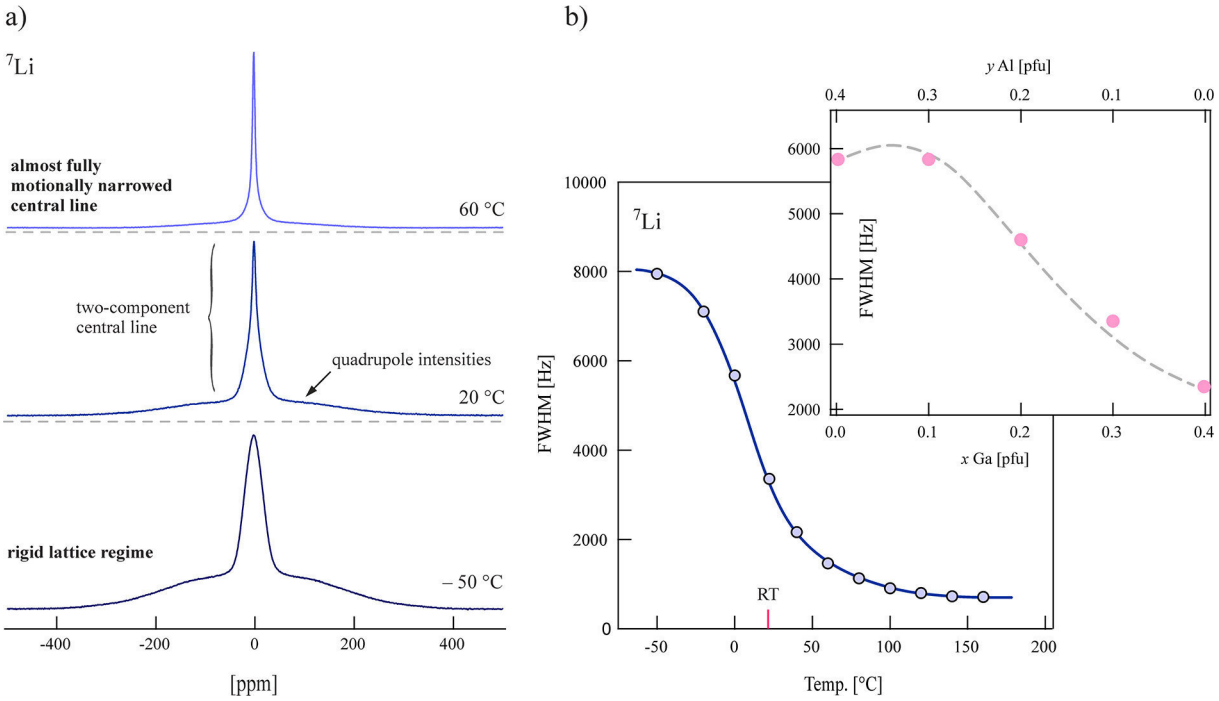

Figure 6. (a) ^{7}Li NMR line shape measurements and motional narrowing (non-rotating samples) of a sample with a Ga content of $x = 0.4$, recorded via a solid-echo pulse sequence at 194.3 MHz. At low temperatures the NMR line consists of a dipolarly broadened central line and a so-called quadrupole foot. The central line narrows with increasing temperature, indicating rapid Li exchange between the available crystallographic Li positions. (b) Motional narrowing of the ^{7}Li NMR line width (blue). Extreme narrowing is reached at temperatures slightly higher than 100 °C. (Inset) ^{7}Li NMR line width, determined at ambient temperature, as a function of the Ga:Al ratio of the garnets studied (full width at half-maximum). The solid line in (b) and the dashed line in the inset serve to guide the eye.

resonance at 81 ppm reflecting the distorted 96*h* site (see Figure 5). Thus, in agreement with previous works, the two signals observed reflect Al ions residing on only two distinct sites, viz., 24*d* and 96*h* voids, respectively.

Assignment for the ^{71}Ga MAS NMR resonances is not as well established in the literature as the ^{27}Al assignments. All previous publications have observed a single ^{71}Ga NMR resonance from doped LLZO, though the characteristics of the site break up into two distinct cases.[6,7,9] One publication, focusing on the complete solid solution of Ga-doped LLZO, with Ga contents up to 0.84 pfu, showed a single site with a large chemical shift (δ_{iso} = 244(2) ppm), a small quadrupole interaction (C_Q = 4.0(2) MHz), and an EFG tensor that deviates from axial symmetry (η_Q = 0.46(3)).[7] A different study revealed a single Ga site with a smaller chemical shift (δ_{iso} = 207(10) ppm), a larger C_Q (12.7(3) ppm), and an EFG tensor that is essentially axially symmetric (η_Q = 0.05(05)).[9] These characteristics mimic the two four-fold-coordinated dopant sites in the ^{27}Al system discussed above, as would be expected for two elements in the same group of the periodic table.[5]

It is, therefore, relatively straightforward to assign the higher chemical shift peak to Ga ions in the 96*h* site and the lower chemical shift peak to 24*d* dopant ions. This assignment is the only reasonable one, given that the local symmetry (S_4) at the 24*d* site enforces axial symmetry on the EFG tensor (η_Q = 0). However, we do note that local disorder (that may break this symmetry) probably varies somewhat with the preparation route; hence, some samples may display 24*d* site peaks that are better represented by a range of parameters rather than a single η = 0 site. Here, the ^{71}Ga NMR signal of the 24*d* site can be best simulated with η_Q < 0.3 (see below).

^{71}Ga MAS NMR spectra of the $Ga_{0.4}Al_{0.0}$ and $Ga_{0.3}Al_{0.1}$ samples recorded at 21.1 T (see Figure 4) clearly show both sites that were observed individually in different samples. The signal at high chemical shift, δ_{iso} = 243(1) ppm, is narrow under the ultrahigh magnetic field applied, though an upper limit of 4.4 MHz can still be placed on C_Q. The lower chemical shift site, δ_{iso} = 193(1) ppm, is estimated to have C_Q = 11.3(1) MHz, and an upper limit of 0.5 can be placed on η using line shape simulations. These parameters are in close agreement with the published ^{71}Ga values and mimic the ^{27}Al NMR results as well; therefore, we assign the 243 ppm peak to the 96*h* site, and the 193 ppm peak to the 24*d* site.

It is quite interesting that previous ^{71}Ga NMR studies of doped LLZO all reported that only one of the two sites was observed.[6,7,9] Howard et al. and Rettenwander et al. analyzed Ga-doped LLZO at an applied field of 9.4 T with relatively slow sample spinning and observed only the narrow 96*h* line.[6,7] On the other hand, Bernuy-Lopez et al. recently investigated LLZO doped with up to 0.3 Ga pfu at 11.75 T and fast sample spinning; they observed only the broad 24*d* signal.[9] While the broad 96*h* signal may have been obscured by the lower magnetic field and slower spinning rates applied in the first two of these studies, there is little doubt that the narrow peak from the 96*h* site would easily have been observed in the study by Bernuy-Lopez et al. if Ga populated this site in the material. The observation of both sites in the same material presented here provides the first evidence that Ga can populate both the 96*h* and 24*d* sites in the same doped LLZO. These data provide vital information on the structure and are important for developing the model of Li-ion dynamics of in the system.

Site Preferences of Al and Ga in Dopant-Stabilized LLZO. If we assume that the area under the NMR line is

DOI: 10.1021/acs.chemmater.5b00684
Chem. Mater. 2015, 27, 3135–3142

roughly proportional to the amount of the measured nuclei, the site distribution can be evaluated according to, e.g.,

$$24d \text{ pfu } [i, j] = \frac{A_{1i}}{\sum_{i=1}^{n} A_{1i}} c_1 + \frac{A_{2j}}{\sum_{j=1}^{m} A_{2j}} c_2$$

where i is the ith resonance of nucleus 1, A_{1i} denotes the area under the line i, and c_1 is the intended dopant concentration of nucleus 1, etc. The resulting site occupancies 24*d*:96*h* are quite similar and range from 0.2:0.1 ($Ga_{0.0}Al_{0.4}$, $Ga_{0.1}Al_{0.4}$) to 0.3:0.1 ($Ga_{0.2}Al_{0.2}$, $Ga_{0.3}Al_{0.1}$, $Ga_{0.4}Al_{0.0}$). Comparing the NMR spectra of the samples with a low amount of Ga incorporated (see Figure 4), there might be a tendency that, at first, the 96*h* position is preferentially occupied by Ga as compared to the 24*d* site. Considering the ^{27}Al MAS NMR spectrum of $Ga_{0.3}Al_{0.1}$, the Al ions seem to prefer to occupy the 24*d* sites at first. However, we found a rather similar site preference for Al and Ga; the dopant distribution among the available sites in LLZO may, of course, depend on the synthesis conditions chosen. This might also serve to explain differences in interpretation, where Bernuy-Lopez et al. reported that only the 24*d* site is occupied by Ga ions.[9]

Li-Ion Dynamics As Seen by ^{7}Li NMR. Narrowing of the ^{7}Li NMR central line with temperature, which is caused by thermally activated Li motion, is shown in Figure 6. If we look at the change of the line width as a function of Ga content at ambient temperature (Table 1), we observe a decrease of the ^{7}Li NMR line width with increasing Ga content. $Ga_{0.4}Al_{0.0}$ shows the highest Li-ion diffusivity found in this series. The regime of extreme narrowing is reached at temperatures slightly higher than 100 °C, this being an indication for high diffusivity in $Ga_{0.4}Al_{0.0}$.

The corresponding ^{7}Li (I = 3/2) NMR line shapes recorded under non-rotating conditions are composed of a central line and quadrupole intensities. Dipole−dipole as well as electric quadrupole interactions are increasingly averaged due to sufficiently fast Li exchange among the available crystallographic Li positions (see Figure 6).

The central line reveals heterogeneous line narrowing, pointing to complex ion dynamics. From a dynamic point of view, we have to deal with a relatively large distribution of jump rates. At sufficiently low temperatures, some of the Li ions distributed among the available sites in LLZO seem to be less mobile than others, meaning not all of them have access to the same fast diffusion pathway at the same time. This feature has also been found for Al-doped LLZO by some of our group recently;[4] it is also known for glassy ion conductors.[18] The fact that here the broad quadrupole powder pattern is affected by thermally activated Li hopping processes at temperatures as low as 20 °C indicates extremely rapid Li exchange (see below).

One might also think to interpret the overall line shape found in the motional narrowing regime as a result of the spin physics of spin-3/2 quadrupole nuclei that would lead to biexponential relaxation transients. In our case, however, the corresponding NMR spin−lattice and spin−spin relaxation transients do not show multiple components; instead, they can be well fitted with a single exponential function. Additionally, regarding the ^{7}Li NMR line shapes well above 60 °C, a single Lorentzian-shaped, motionally narrowed line shows up; hence, it is no longer possible to separate the two contributions. Thus, most likely the complex line shape observed in the line narrowing regime does indeed reflect heterogeneous dynamics.

Li jump rates can be estimated from NMR line narrowing. The inflection point of the motional narrowing curve of the NMR central line (see Figure 6b) is at 283 K. At this temperature the corresponding Li jump rate, $1/\tau$, can be roughly estimated according to $1/\tau = \nu_{rl}2\pi$, where ν_{rl} denotes the rigid lattice line width;[19] here we have ν_{rl} = 8 kHz. This leads to $1/\tau$ (283 K) $\approx 5 \times 10^4$ s^{-1}. Using an activation energy of 0.35 eV, which is commonly found for Al-doped, highly conducting LLZO,[4] this gives, at RT (300 K), a mean residence time between two successful hops in the order of 1−10 μs. This finding is consistent with the expected high room-temperature Li-ion conductivity of dopant-stabilized garnets, which typically ranges from 10^{-3} to 10^{-4} S/cm (see above).[4]

A possible influence of dopant cations on ionic conductivity was first proposed by Allen et al.[11] They discussed a possible blocking effect of dopants located at the Li-ion sublattice in garnets. In particular, the 24*d* site might act as a blockade for through-going ion diffusion, as already noted above. Allen et al. investigated garnets of the composition $Li_{6.75}La_3Zr_{1.75}Ta_{0.25}O_{12}$, with and without doping, using Al or Ga. The undoped garnet showed the highest total Li-ion conductivity, $\sigma_{total} = 8.7 \times 10^{-4}$ S cm^{-1} at RT, and the activation energy E_a = 0.22 eV. These values were compared to those of the Al-doped and the Ga-doped garnets, characterized by $\sigma_{total} = 3.7 \times 10^{-4}$ and 4.1×10^{-4} S cm^{-1}, with E_a = 0.30 and 0.27 eV, respectively.[11] The ionic conductivity of the undoped sample is reported to be twice that of the doped samples. The doped samples showed similar electrochemical performances. The lattice parameters of the doped and undoped samples are reported to be a_0 = 12.96 and 12.95 Å, respectively.[11]

In our opinion, the increase of σ_{total} observed and the slight decrease of E_a found for the undoped sample could also be related to the total amount of Li present or to the change in lattice constant a_0. Evidence for the latter is given in an earlier study by Murugan et al.,[20] who investigated the influence of the lattice parameter on Li-ion conductivity. Those authors were able to show that the partial substitution of La by divalent cations (e.g., Ba, Mg, Ca, and Sr) as well as by the use of higher sintering temperatures leads to an increase of a_0. This increase is accompanied by an increase of σ_{total} and a decrease of the E_a, as well as an increasing grain boundary resistance, R_{gb}. As an example, $Li_6SrLa_2Ta_2O_{12}$ and $Li_6BaLa_2Ta_2O_{12}$ are characterized by $\sigma_{total} = 3.05 \times 10^{-5}$ and 9.28×10^{-5} S cm^{-1}, as well as a_0 = 12.83 and 12.97 Å, respectively. This means that an increase in a_0 of 0.014 Å already leads to an increase of the ion conductivity by a factor of 2; this is similar to what Allen et al. have observed.[11]

In our study, we found a decrease in the ^{7}Li line width (fwhm) as a function of the Ga content; see the inset of Figure 6b. Since the RT line width can be regarded as a qualitative measure of translational Li-ion dynamics, it means that more Ga has been incorporated the higher the Li-ion diffusivity. Because (i) the Li content remains constant and (ii) no significant site preference of the dopants Al and Ga was found in NMR, we tend to connect the increase in Li-ion dynamics, as seen by the change in ^{7}Li NMR line widths, with the increase of a_0 rather than attributing this finding to the blocking effect of trivalent cations located on 24*d* sites.

■ ASSOCIATED CONTENT

Supporting Information

Table S1, summarizing unit cell parameters; XRPD analyses of phase composition; and Figure S1, showing XRPD patterns of

DOI: 10.1021/acs.chemmater.5b00684
Chem. Mater. 2015, 27, 3135−3142

the compounds studied. This material is available free of charge via the Internet at http://pubs.acs.org.

AUTHOR INFORMATION

Corresponding Authors

*E-mail: daniel.rettenwander@sbg.ac.at.
*E-mail: julia.langer@tugraz.at.

Author Contributions

⊥D.R. and J.L. contributed equally to this work.

Funding

The research was supported by Austrian Science Fund (FWF), project no. P25702. Further support was received from the Austrian Federal Ministry of Science, Research and Economy, and the Austrian National Foundation for Research, Technology and Development.

Notes

The authors declare no competing financial interest.

ACKNOWLEDGMENTS

D.R. thanks Peter R. Slater (Birmingham, UK) and Juan M. López del Amo (Miñano, Spain) for providing their NMR spectra. M.W. and W.S. thank the Austrian Federal Ministry of Science, Research and Economy, and the Austrian National Foundation for Research, Technology and Development for financial support. M.W. and J.L. thank the DFG Research Unit 1277 for additional financial support. Access to the 21.1 T NMR spectrometer was provided by the National Ultrahigh-Field NMR Facility for Solids (Ottawa, Canada), a national research facility funded by a consortium of Canadian universities, supported by the National Research Council Canada and Bruker BioSpin, and managed by the University of Ottawa (http://nmr900.ca).

REFERENCES

(1) Murugan, R.; Thangadurai, V.; Weppner, W. *Angew. Chem.* **2007**, *119*, 7925.
(2) Awaka, J.; Kijima, N.; Hayakawa, H.; Akimoto, J. *J. Solid State Chem.* **2009**, *182*, 2046.
(3) Awaka, J.; Takashima, A.; Hayakawa, H.; Kijima, N.; Idemoto, Y.; Akimoto, J. *Key Eng. Mater.* **2011**, *485*, 99.
(4) Buschmann, H.; Dölle, J.; Berendts, S.; Kuhn, A.; Bottke, P.; Wilkening, M.; Heitjans, P.; Senyshyn, A.; Ehrenberg, H.; Lotnyk, A.; Duppel, V.; Kienle, L.; Janek, J. *Phys. Chem. Chem. Phys.* **2011**, *13*, 19378.
(5) Geiger, C. A.; Alekseev, E.; Lazic, B.; Fisch, M.; Armbruster, T.; Langner, R.; Fechtelkord, M.; Kim, N.; Pettke, T.; Weppner, W. *Inorg. Chem.* **2011**, *50*, 1089.
(6) Howard, M. A.; Clemens, O.; Kendrick, E.; Knight, K. S.; Apperly, P. A.; Anderson, P. A.; Slater, P. R. *Dalton Trans.* **2012**, *41*, 12048.
(7) Rettenwander, D.; Geiger, C. A.; Tribus, M.; Tropper, P.; Amthauer, G. *Inorg. Chem.* **2014**, *53*, 6264.
(8) El Shinawi, H.; Janek, J. *J. Power Sources* **2013**, *225*, 13−19.
(9) Bernuy-Lopez, C.; Manalastas, W., Jr.; Lopez del Amo, J. M.; Aguadero, A.; Aguesse, F.; Kilner, J. A. *Chem. Mater.* **2014**, *26*, 3610.
(10) Rettenwander, D.; Blaha, P.; Laskowski, R.; Schwarz, K.; Bottke, P.; Wilkening, M.; Geiger, C. A.; Amthauer, G. *Chem. Mater.* **2014**, *26*, 2617.
(11) Allen, J. L.; Wolfenstine, J.; Rangasamy, E.; Sakamoto, J. *J. Power Sources* **2012**, *206*, 315.
(12) Vosegaard, T.; Massiot, D.; Gautier, N.; Jakobsen, H. J. *Inorg. Chem.* **1997**, *36*, 2449.
(13) Rangasamy, E.; Wolfenstine, J.; Sakamoto, J. *Solid State Ionics* **2012**, *206*, 28.
(14) Shannon, R. D.; Prewitt, C. T. *Acta Crystallogr.* **1969**, *B25*, 925.
(15) Düvel, A.; Kuhn, A.; Robben, L.; Wilkening, M.; Heitjans, P. *J. Phys. Chem. C* **2012**, *116*, 15192.
(16) Wohlmuth, D.; Epp, V.; Bottke, P.; Hanzu, I.; Bitschnau, B.; Letofsky-Papst, I.; Kriechbaum, M.; Amenitsch, H.; Hofer, F.; Wilkening, M. *J. Mater. Chem. A* **2014**, *2*, 20295.
(17) Hubaud, A. A.; Schroeder, D. J.; Key, B.; Ingram, B. J.; Dogan, F.; Vaughey, J. T. *J. Mater. Chem. A* **2013**, *1*, 8813.
(18) Faske, S.; Eckert, H.; Vogel, M. *Phys. Rev. B* **2008**, *77*, 104301.
(19) Wilkening, M.; Kuhn, A.; Heitjans, P. *Phys. Rev. B* **2008**, *78*, 054303.
(20) Murugan, R.; Thangadurai, V.; Weppner, W. *J. Electrochem. Soc.* **2008**, *155*, A90.

DOI: 10.1021/acs.chemmater.5b00684
Chem. Mater. 2015, 27, 3135−3142

7.4.2 Ion Dynamics in Solid Electrolytes: NMR Reveals the Elementary Steps of Li^+ Hopping in the Garnet $Li_{6.5}La_3Zr_{1.75}Mo_{0.25}O_{12}$

Neben der Substitutaion und Stabilisierung von kubischen LLZO-Granaten mit trivalenten Kationen wie z.B. Al oder Ga, bei der auch das Li-Untergitter direkt modifiziert wird, bleibt bei der Einfluss von Mo auf das Li-Untergitter geringer, da Mo im Gegensatz zu Al und Ga die Zr-Plätze besetzt. Die untersuchte Probe wurde an der Uni Salzburg mittels Hochtemperatursintern aus den einzelnen Metalloxiden und Li_2CO_3 hergestellt. Die Probe wurde dann kalziniert, gesintert und zu einem Pellet verpresst. Die Phasenreinheit wurde unter anderem durch Röntgenpulverdiffraktometrie und der Lithiumgehalt durch ICP-OES überprüft. Aus den statischen ^{7}Li-NMR-Messungen wurden die Linienbreiten über einen Temperaturbereich erfasst und so das *line narrowing* untersucht. Die Relaxationszeiten T_1 und $T_{1\rho}$ sowie Spin-Alignment-Echo Messungen gaben Auskunft über das Diffusionsverhalten und mögliche Migrationspfade. Die Messungen sind zum überwiegenden Teil von Dr. P. Bottke an der TU Graz durchgeführt worden. Der Verfasser dieser Schrift hatte Anteil an der Vorpräparation der Probe für die NMR-Messungen und den Linienbreitenmessungen.

Ion Dynamics in Solid Electrolytes: NMR Reveals the Elementary Steps of Li^+ Hopping in the Garnet $Li_{6.5}La_3Zr_{1.75}Mo_{0.25}O_{12}$

Patrick Bottke[*†‡], Daniel Rettenwander[¶], Walter Schmidt[†], Georg Amthauer[¶], and Martin Wilkening[*†‡]

[†] Christian Doppler Laboratory for Lithium Batteries, Institute for Chemistry and Technology of Materials, Graz University of Technology (NAWI Graz), 8010 Graz, Austria

[‡] DFG Research Unit 1277 'molife', Graz University of Technology, 8010 Graz, Austria

[¶] Department of Materials Research and Physics, University of Salzburg, 5020 Salzburg, Austria

Chem. Mater., 2015, 27 (19), pp 6571-6582

DOI: 10.1021/acs.chemmater.5b02231

Publication Date (Web): September 11, 2015

CHEMISTRY OF MATERIALS

Article

pubs.acs.org/cm

Ion Dynamics in Solid Electrolytes: NMR Reveals the Elementary Steps of Li^+ Hopping in the Garnet $Li_{6.5}La_3Zr_{1.75}Mo_{0.25}O_{12}$

Patrick Bottke,*[,†,‡] Daniel Rettenwander,[¶] Walter Schmidt,[†] Georg Amthauer,[¶] and Martin Wilkening*[,†,‡]

[†]Christian Doppler Laboratory for Lithium Batteries, Institute for Chemistry and Technology of Materials, Graz University of Technology (NAWI Graz), 8010 Graz, Austria

[‡]DFG Research Unit 1277 'molife', Graz University of Technology, 8010 Graz, Austria

[¶]Department of Materials Research and Physics, University of Salzburg, 5020 Salzburg, Austria

Supporting Information

ABSTRACT: Garnet-type oxides are considered to belong to the most attractive solid Li^+ electrolytes. This is due to their wide electrochemical stability window as well as their superior ionic conductivity, with a Li-ion transference number of almost one. Usually ionic conductivities are studied via impedance spectroscopy on a macroscopic length scale. Time-domain NMR methods, however, have been used much less extensively to shed light on the elementary hopping processes in highly conducting oxide garnets. Here, we used NMR relaxometry and stimulated echo NMR to study Li^+ self-diffusion in $Li_{6.5}La_3Zr_{1.75}Mo_{0.25}O_{12}$ (LLZMO), which served as a model compound to collect information on the ^7Li spin dynamics. It turned out that NMR spin−lattice relaxation (SLR) recorded in both the laboratory and rotating frame of reference shows features that seem to be a universal fingerprint for fast conducting garnets that have been stabilized in their cubic modification. In contrast to Al-doped garnet-type $Li_7La_3Zr_2O_{12}$ that modifies the Li sublattice, in LLZMO the Li sublattice remains intact, offering the possibility to get to the bottom of Li-ion dynamics in LLZO-based garnets. Most importantly, whereas NMR SLR rates measured at 194.3 MHz reflect an almost universal behavior of local hoppings being thermally activated by only 0.151(3) eV, the spin-lock technique (33.$\overline{3}$ kHz) gives evidence of two separate, overlapping rate peaks with activation energies on the order of 0.29 eV for the elementary steps of Li-ion hopping. This points to a less pronounced distribution of Li^+ jump rates on the kilohertz time scale than has been observed for the Al-stabilized LLZO samples. The NMR results obtained also entail information on both the Li^+ diffusion coefficients and the shape of the underlying motional correlation functions. The latter has been provided by ^7Li NMR spin-alignment echo correlation spectroscopy that also shows the involvement of 24d and 96h sites in Li^+ diffusion.

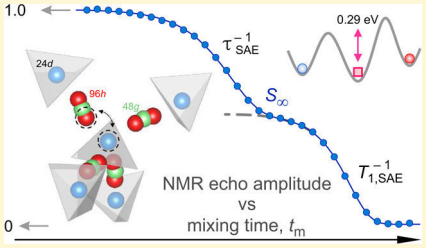

1. INTRODUCTION

Clean energy storage is one of the most urgent issues that has to be solved if we are to stop our dependency on fossil fuels. There is general agreement about the need to cut CO_2 emissions by storing electricity generated from renewable sources via, e.g., powerful and sustainable systems that store energy electrochemically.[1−5]

Ionically conducting solid electrolytes[6−8] are key to developing advanced all-solid-state batteries based on Li^+ as ionic charge carriers. In order to replace flammable liquid electrolytes, which are commonly used in lithium-ion batteries, Li-bearing sulfides and oxides are being feverishly searched to identify those that fulfill the requirements placed on solid electrolytes.[7−18] Considering oxides, garnet-type electrolytes are currently in the spotlight of materials science and battery research.[7,19]

In 2007, Murugan et al. reported on a very high Li-ion conductivity (10^{-3} to 10^{-4} S cm^{-1}) in garnet-type $Li_7La_3Zr_2O_{12}$ (LLZO) crystallizing with cubic symmetry (space group $Ia\overline{3}d$).[9] Since then, many papers have been published focusing on both synthesis and characterization of ion transport in Li-bearing garnets; an overview is given by Thangadurai and co-workers.[19] The electrochemical stability of LLZO has been studied recently by the Sakamoto group.[20] Nowadays, we know that aliovalent doping of LLZO with, e.g., Al, Ga, or even Fe,[21−26] is essential not only to stabilize the cubic modification[21,27,28] against the tetragonal one[29] with its lower conductivity but also to free the lithium ions from their fixed sites, enabling them to quickly diffuse along various pathways in the complex oxide network.[19,21]

While ionic transport properties in garnets are commonly studied by impedance spectroscopy,[19,30] some of us reported on a comprehensive time-domain nuclear magnetic resonance (NMR) study on Al-doped LLZO in 2011.[21] NMR relaxometry was used to corroborate the findings from impedance spectroscopy; moreover, it was helpful to deliver further insights on Li^+ self-diffusion from a microscopic point of view by taking advantage of methods that are sensitive to ion hopping on the Ångström scale.[21,31] Such information is crucial if we are to understand the extraordinary dynamic properties of garnets. Until now, however, NMR relaxometry has been used only rarely to characterize doped Li-containing garnets.[21,31,32]

Received: June 2, 2015
Revised: September 11, 2015
Published: September 11, 2015

DOI: 10.1021/acs.chemmater.5b02231
Chem. Mater. 2015, 27, 6571−6582

In our preceding work,[21] we discovered some NMR anomalies that are anticipated to be tightly linked with the high Li-ion diffusivity probed. For example, via spin-locking ^{7}Li NMR spin−lattice relaxation (SLR) rate measurements, an extremely broad diffusion-induced rate peak was observed,[21] pointing to high-temperature activation energies (ca. 0.34 eV) comparable with those from conductivity measurements. Unexpectedly, the shape of the corresponding peak in the lab frame turned out to be much different. Its so-called low-T flank followed Arrhenius behavior over a large temperature range characterized by an activation energy of only 0.12 eV

The present study is aimed at answering the question of whether this is a special feature of Al-doped LLZO or a universal one of fast Li-ion conducting garnets with cubic structure. Here, $Li_{6.5}La_3Zr_{1.75}Mo_{0.25}O_{12}$ (LLZMO) turned out to be a promising model system to shed light on this aspect. Most importantly, as compared to Al (or Ga)-doped LLZO,[21,25] for which the dopants on 24d sites might act as blocking ions for Li^+ transport, the cubic modification studied here is not stabilized by manipulating the Li sublattice; *au contraire*, in LLZMO the La−Zr sublattice is modified, leaving the Li sublattice untouched with respect to foreign dopants occupying the Li sites. In our opinion, this can be used to explain the differences found here when compared to the previous NMR relaxation studies on Al-doped LLZO.[21]

Moreover, compared to the available investigations on LLZO in the literature, in the present study we go one step further and apply spin-alignment echo (SAE) NMR correlation spectroscopy[33−40] to probe slow ion dynamics at temperatures well below ambient. ^{7}Li SAE NMR is able to provide more precise information on the nature of Li-ion dynamics since it directly measures a single-spin two-time hopping correlation function;[33,38,41−44] it takes advantage of the quadrupolar interaction of the Li spin with electric field gradients at the nuclear sites. From temperature-variable echo decay curves, both Li activation energies, i.e., hopping barriers, and correlation times can be deduced.[39,45−48] In addition, SAE NMR contains information on the shape of the underlying average motional correlation function that governs fast ion transport in LLZMO.

2. EXPERIMENTAL SECTION

Synthesis of $Li_{6.5}La_3Zr_{1.75}Mo^{6+}_{0.25}O_{12}$ was performed by high-temperature sintering methods according to Wagner et al.[49] The starting materials were Li_2CO_3 (99%, Merck), La_2O_3 (99.99%, Aldrich), ZrO_2 (99.0%, Aldrich), and MoO_3 (99.98%, Aldrich). Li_2CO_3 (with an excess of 10 wt % to compensate the loss of Li_2O during sintering) was mixed with the various oxides in the necessary proportions; they were ground intimately together using a hand mortar, a pestle, and isopropanol. This mixture was pressed uniaxially to a pellet and afterward calcined at 1123 K for 4 h with a heating rate of 5 K min^{-1}. The pellets were put in an alumina crucible. To avoid contamination with Al from the crucible, the samples were placed on a pellet of pure LLZO. The mixture was allowed to cool in the furnace to approximately 473 K. Then, the sample was milled in isopropanol using planetary ball mill (Fritsch Pulverisette 7) for 2 h (12 times 550 rpm for 5 min with a break of 5 min between each milling period). Finally, the powder was isostatically pressed (15 kbar) to yield pellets. Afterward, the pellets were sintered at 1500 K for 4 h sandwiched between pellets of pure LLZO to avoid Li-loss during sintering; the heating rate was 20.5 K min^{-1}; after the sintering period, the pellets were allowed to cool to room temperature. The phase purity was checked via X-ray powder diffraction, neutron diffraction (Table S1), and back scattered electrons as well as energy dispersive spectroscopy using a polished pellet: no phases other than LLZMO and no elements other than Li, La, Zr, Mo, O were observed.[49] Finally, the Li content was measured by means of ICP-OES, verifying the stoichiometry $Li_{6.5}La_3Zr_{1.75}Mo^{6+}_{0.25}O_{12}$. The sample investigated crystallizes with cubic symmetry, space group $Ia\bar{3}d$, see above.

A piece of the cylindrical pellet prepared was placed directly inside the NMR probe. A flow of dry nitrogen gas in combination with a heater inside the probe head was used to adjust the temperature inside the sample chamber. A preceding recuperator inserted in a dewar filled with liquid nitrogen was used to cool the sample below ambient conditions. We used an Avance 500 spectrometer (Bruker BioSpin) equipped with a shimmed magnet with a magnetic field B_0 of 11.7 T. The ^{7}Li resonance frequency $\omega_0/2\pi$ to record ^{7}Li NMR line shapes and SLR rates as a function of temperature was 194.3 kHz. While spectra under nonrotating conditions were recorded with a single 90° pulse, the SLR rates (R_1, $R_{1\varrho}$) were acquired either with the saturation recovery pulse sequence[50,51] or the spin-lock technique[13,51−58] that takes advantage of transversal relaxation along a locked B_1 field. For the latter, a locking frequency of $\gamma_m B_1 = \omega_1/2\pi = 33.\bar{3}$ kHz was used; here, γ_m denotes the magnetogyric ratio of ^{7}Li.

Additionally, spin−spin relaxation rates R_2 and Jeener−Broekaert[59] echo decay rates[33,36] were measured. We used a two-pulse quadrupole echo pulse sequence optimized for spin $^3/_2$ nuclei[41] to record transversal echo damping. Jeener−Broekaert echoes were generated with a 45° pulse following a 90° pulse after a short preparation time t_p of 10 μs.[33,34,37] The damping of the spin-alignment (quadrupolar) echo was monitored as a function of mixing time t_m. A 45° reading pulse was used to transfer magnetization back into in an observable signal. Optimized phase cycling[41] served to suppress unwanted coherence pathways; in general, a short preparation time[33,34,37] is necessary to eliminate dipolar contributions as effectively as possible (see below).

3. RESULTS AND DISCUSSION

3.1. Change of NMR Line Shapes. The garnet-type oxides studied by ^{7}Li NMR spectroscopy so far are characterized by a significant line narrowing that starts at temperatures much below room temperature. The same feature is seen for the present garnet, $Li_{6.5}La_3Zr_{1.75}Mo_{0.25}O_{12}$. In Figure 1, selected ^{7}Li NMR lines are shown; while Figure 1a focuses on the central transition, in Figure 1b, the satellite transitions are shown. Since ^{7}Li is a spin $^3/_2$ nucleus, the corresponding NMR line is composed of a central line ($+^1/_2 \rightleftarrows -^1/_2$) and satellite intensities that reflect the spin-transitions $+^3/_2 \rightleftarrows -^3/_2$. The

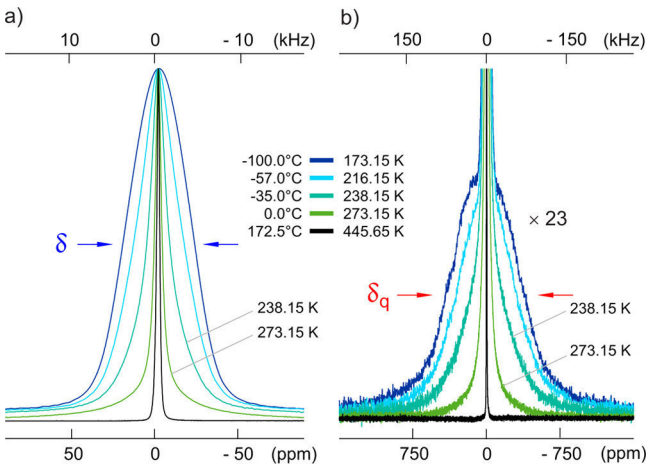

Figure 1. (a) ^{7}Li NMR spectra of garnet-type, Mo-bearing $Li_{6.5}La_3Zr_{1.75}Mo_{0.25}O_{12}$ recorded at 194.3 MHz at the temperatures indicated. The heights of the spectra are normalized; in (a), only the central line is shown. (b) Same spectra as in (a) but plotted with a magnification factor (23 times) to make the complete quadrupolar powder pattern visible.

DOI: 10.1021/acs.chemmater.5b02231
Chem. Mater. 2015, 27, 6571−6582

latter interaction is of electric quadrupolar nature; it is due to the interaction of the quadrupole moment of ^{7}Li with nonvanishing electric field gradients (EFGs) in the direct neighborhood of the nucleus.[60] This interaction alters the Zeeman levels, giving rise, in the case of a single crystal, to a central line flanked by two satellite transitions. For powder samples, on the other hand, the orientation dependence of the electric quadrupole interactions results in a broad quadrupolar powder pattern.[60] The more electrically inequivalent sites Li occupies, i.e., the more EFGs are present, the more complex the resulting overall line shape at low temperature will be. At sufficiently low T, where ion dynamics do not affect the line shape, called the *rigid lattice* regime, the quadrupole intensities can usually be approximated with a Gaussian function. Similarly, in this T regime, the central line, which reflects the magnetic dipolar interactions, shows, in many cases, a Gaussian shape.

With increasing mobility of the Li spins, however, magnetic dipolar as well as electric quadrupolar interactions are continuously averaged. This manifests itself in pronounced line narrowing,[61] which is shown in Figure 1a. While at 173.15 K the line recorded is as expected for the rigid lattice regime, ion dynamics start to affect the line widths already at 183.15 K. Above 273 K, the line is almost fully narrowed, indicating very fast Li-ion hopping processes. The ^{7}Li NMR line widths (fwhm, (overall) full width at half-maximum) are shown in Figure 2 as

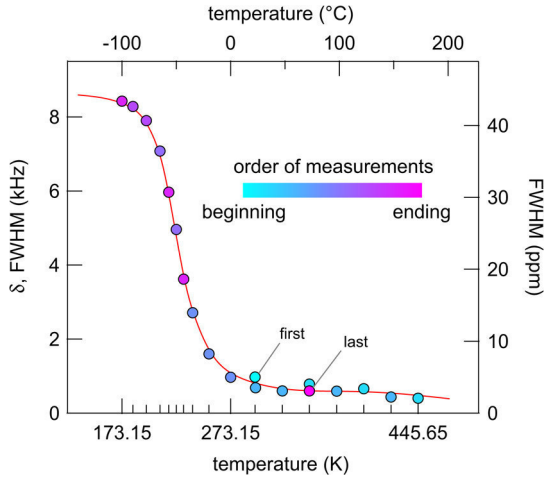

Figure 2. (a) The ^{7}Li NMR line width of the central transition (fwhm, full width at half-maximum) of $Li_{6.5}La_3Zr_{1.75}Mo_{0.25}O_{12}$ as a function of temperature. The color of the data points refer to the measuring order of the lines. It turned out that the powder sample, which was measured as a piece of the pellet in dry N_2 atmosphere, is stable over the whole T range investigated.

a function of temperature. Starting with a rigid lattice line width, δ_0, of ca. 9 kHz, the line reaches half of its initial value at ca. 240 K. At the inflection point of the motional narrowing curve, the Li^+ jump rate τ^{-1} is approximately given by $\tau^{-1} = \delta_0 \times 2\pi \approx 5.6 \times 10^4$ s^{-1}. At room temperature, which is the normal operation temperature for solid-state batteries, τ^{-1} is expected to be much larger (see below).

Interestingly, the ^{7}Li NMR line shapes, in contrast to what has been observed for Al-doped LLZO, undergo a relatively homogeneous motional narrowing. This means that almost the whole line is affected by the narrowing process; for Al-doped LLZO, we found a marked heterogeneous motional narrowing that points to mobile ions next to less mobile ions in the garnet structure. Here, the smooth transition from a Gaussian shape toward a Lorentzian line at elevated T indicates that the majority of Li ions take part in the diffusion process even at relatively low T. This is a noteworthy difference compared to Li-bearing garnets stabilized by aliovalent Al doping.

Line narrowing is sensitive to ion dynamics determined by the spectral width of the NMR component under investigation. While δ_0 is on the order of 9 kHz, the quadrupole intensities (see Figure 1b) span a spectral range of ca. 300 kHz. The width of the quadrupole foot, δ_q, is ca. 150 kHz. This is 10 times larger than δ_0. Hence, full averaging of the quadrupole intensities is expected if the jump rate reaches values (significantly) larger than δ_q. While at 273.15 K the satellite intensity has drastically lost in intensity, it has completely been vanished at 445.65 K. Already at 395.65 K the mean jump rate has increased to values much larger than 10^6 s^{-1} at least. The fact that averaging of quadrupole satellites sets in at relatively low temperatures and that it accompanies narrowing of the central line, which is sensitive to slower Li-ion diffusion, points to a subensemble of Li ions that are quite mobile on the time scale set by δ_q. This feature shows that we cannot interpret the data with the help of a single diffusion process only. Our ^{7}Li NMR SLR measurements, see next section, clearly underpin this view.

3.2. Diffusion-Induced NMR Spin–Lattice Relaxation Rates.

To quantify Li-ion diffusion parameters in crystalline $Li_{6.5}La_3Zr_{1.75}Mo_{0.25}O_{12}$, we recorded both ^{7}Li NMR SLR rates (T_1^{-1}) in (i) the laboratory frame of reference ($\omega_0/2\pi$ = 194.3 MHz) and (ii) in the so-called rotating frame of reference[56−58] ($T_{1\varrho}^{-1}$) by utilizing an angular spin-lock frequency $\omega_0/2\pi$ that is much lower than the Larmor frequency $\omega_0/2\pi$ (Figure 3). Hence, spin-lock NMR is sensitive to slower Li-ion dynamics as compared to that of T_1^{-1} NMR experiments.[39,40,62]

At first, we will present the T_1^{-1} results. The corresponding transients, which describe the recovery of longitudinal magnetization M_z as a function of delay time t_d, can be best parametrized with single exponentials: $M_z(t_d) \propto 1 - \exp(-(t/T_1)^{\gamma_1})$, where γ_1 deviates only slightly from 1. The rates T_1^{-1} and the corresponding stretching exponents γ_1 are shown in the Arrhenius plot of Figure 3. At low temperatures, T_1^{-1} deviates from Arrhenius behavior due to nondiffusive effects on $M_z(t_d)$. These can be lattice vibrations and coupling of the ^{7}Li spins to paramagnetic centers.[63] Above 250 K, the rates T_1^{-1} follow an Arrhenius law that is given by $T_1^{-1} \propto \exp(-E_a/(k_B T))$. k_B denotes Boltzmann's constant, and E_a is the activation energy. Here, we found E_a = 0.151(3) eV. Although it is slightly larger, this value is comparable with previous results on Al-doped garnets (0.12 eV).[21] Since E_a is smaller than the activation energy that is commonly found by conductivity spectroscopy, which is sensitive to long-range ion transport, the recovery of $M_z(t_d)$ is likely induced by short-range motions of the Li ions. These may also include unsuccessful, i.e., forward–backward, Li jumps that are accompanied by correlation effects.[64−66] The value of 0.151(3) eV might be closely related to the activation energy that represents the barrier of an elementary Li^+ jump process in LLZMO.

On the basis of the present result, the rather shallow increase of T_1^{-1} seems to be a universal feature of the highly conducting garnets with cubic symmetry investigated by NMR so far. This is in stark contrast to what is seen for the tetragonal modification of LLZO, whose ion conductivity is lower by 2 orders of magnitude.[29,31] For tetragonal LLZO, which does not

DOI: 10.1021/acs.chemmater.5b02231
Chem. Mater. 2015, 27, 6571−6582

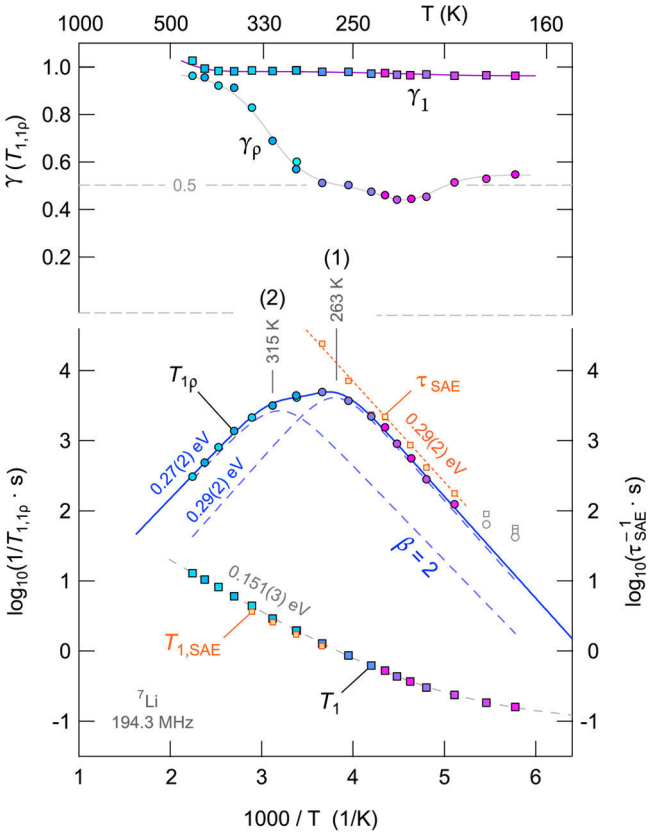

Figure 3. Arrhenius plot of the ^{7}Li SLR NMR rates T_1^{-1} and $T_{1\varrho}$ of crystalline $Li_{6.5}La_3Zr_{1.75}Mo_{0.25}O_{12}$. The Larmor frequency was 194.3 MHz, and we used a locking frequency of $\omega_1/2\pi$ of 33.$\bar{3}$ kHz to record the $M_\rho(t_{lock})$ transients that are shown in Figure 4. The continuous line represents the sum of two single rate peaks that are characterized by the dashed lines shown. The dashed line drawn through the T_1^{-1} data points is a combination of an Arrhenius fit with a power-law fit that takes into account background relaxation at low T. The solid lines in the upper part of the graph, which show the temperature dependence of γ_1 and γ_ϱ, respectively, are just to guide the eye. For comparison, decay rates obtained from SAE NMR are also shown. The dotted line is an Arrhenius fit yielding 0.29 eV; the corresponding rates $T_{1,SAE}^{-1}$, which coincide with T_1^{-1}, are also included.

need stabilization via Al doping, the rates T_1^{-1} follow a low-T flank of a diffusion-induced rate peak that is characterized by 0.32 eV.[31] The same low-T activation energy was found by $T_{1\varrho}^{-1}$. Altogether, a joint fit of $T_{1\varrho}^{-1}(1/T)$ and $T_1^{-1}(1/T)$ resulted in 0.48 eV.[31] This value is directly comparable with activation energies deduced from conductivity spectroscopy (0.47 eV).

By formally replacing ω_0 by ω_1, we are able to shift the low-T SLR rate flank toward lower temperatures.[39] This enables us to record the complete diffusion-induced rate peak $T_{1\varrho}^{-1}(1/T)$, as has been shown for tetragonal LLZO and Al-doped, cubic LLZO.[21,31] In general, the peak maximum shows up at $\omega_{0(1)}\tau_c \approx 1$, where the correlation time τ_c is identical with the jump rate τ within a factor of 2.[51] The corresponding rates $T_{1\varrho}^{-1}$ are included in Figure 3. They have been extracted from transversal magnetization transients $M_\rho(t_{lock})$ by varying the spin-lock time t_{lock} from 10 μs up to 0.5 s. The transients obtained are presented in Figure 4. Solid lines show fits with stretched exponentials according to $M_\rho(t_{lock}) \propto 1 - \exp(-(t/T_{1\rho})^{\gamma_\varrho})$. The stretching factor γ_ϱ strongly varies with temperature. It takes values of ca. 0.5 at low temperatures, where $\omega_1\tau \gg 1$ holds. Such a $\sqrt{(t_{lock})}$ decay behavior is expected for $T_{1\varrho}$ transients

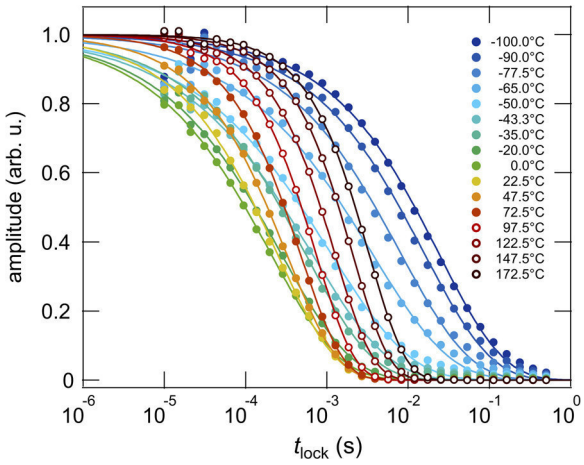

Figure 4. ^{7}Li NMR $T_{1\varrho}$ transients, M_ρ amplitude vs locking time normalized to range between 0 and 1, that were recorded with the spin-lock technique. The solid lines represent fits according to $M_\rho(t_{lock}) \propto \exp(-(t/T_{1\rho})^{\gamma_\varrho})$. The stretching exponents obtained, γ_ϱ, are shown in Figure 3. At the highest temperatures, $M_\rho(t_{lock})$ follows a single exponential.

that are governed by interactions of the Li spins with paramagnetic impurities.[67] At high temperatures, i.e., in the regime $\omega_1\tau \ll 1$, the exponent γ_ϱ strives toward $\gamma_\varrho = 1$, which is reached at approximately 450 K. The increase of γ_ϱ shows up when $T_{1\varrho}^{-1}$ has passed through the peak maximum, i.e., when reaching the limit $\omega_1\tau \ll 1$. It is likely that in this T range the shape of the underlying (averaged) motional correlation function resembles that of a pure exponential.

At first glance, the shape of the rate peak $T_{1\varrho}^{-1}(1/T)$ turns out to be rather broad. In the present case, however, it is much narrower than what has been observed for Al-doped (and Ga-doped) LLZO. For LLZO, this has been interpreted as a large distribution of jump rates and activation energies that leads to a superposition of many SLR rate peaks showing up at different temperatures. In the present case, instead, the shape of $T_{1\varrho}^{-1}(1/T)$ can be well-reproduced with a combination of only two individual rate peaks. The two peaks are shown in Figure 3 as dashed lines.

We used the SLR NMR model according to BPP theory that relies on a Lorentzian shaped spectral density function $J(\omega_{0(1)})$ to which the rate $T_{1(1\varrho)}^{-1}$ is proportional to[60]

$$J(\alpha\cdot\omega_{0(1)})_{\alpha=1,2} = C_{0(1)}\tau_c/(1 + (\alpha\cdot\omega_{0(1)}\tau_c)^\beta) \quad (1)$$

The data $T_{1\varrho}^{-1}(1/T)$ can be approximated with the following expression for 3D motion

$$T_{1\varrho}^{-1} = C_\varrho\left(J(2\omega_1) + \frac{5}{3}J(\omega_0) + \frac{2}{3}J(2\omega_0)\right) \quad (2)$$

The parameter β in eq 1 reflects deviations from the case of uncorrelated motion. τ_c is given by $\tau_c \approx \tau = \tau_0^{-1}\exp(-E_{a,\varrho}/(k_BT))$. Here, the best fits were obtained with $\beta = 2$, i.e., a simple BPP-type spectral density function is sufficient to reproduce the rate peaks. $\beta = 2$ leads to symmetric rate peaks.

Interestingly, the shape of the two peaks is rather similar. In the limit $\omega_1\tau \gg 1$, we obtain $E_{a,\varrho}^{low} \approx 0.29$ eV; almost the same value governs the rates in the regime $\omega_1\tau \gg 1$, for which $E_{a,\varrho}$ is given by 0.29(2) eV (peak 1) and 0.27(2) eV (peak 2). The latter value, which refers to the peak at lower T, is definitely smaller than the activation energy of tetragonal LLZO (0.42

DOI: 10.1021/acs.chemmater.5b02231
Chem. Mater. 2015, 27, 6571−6582

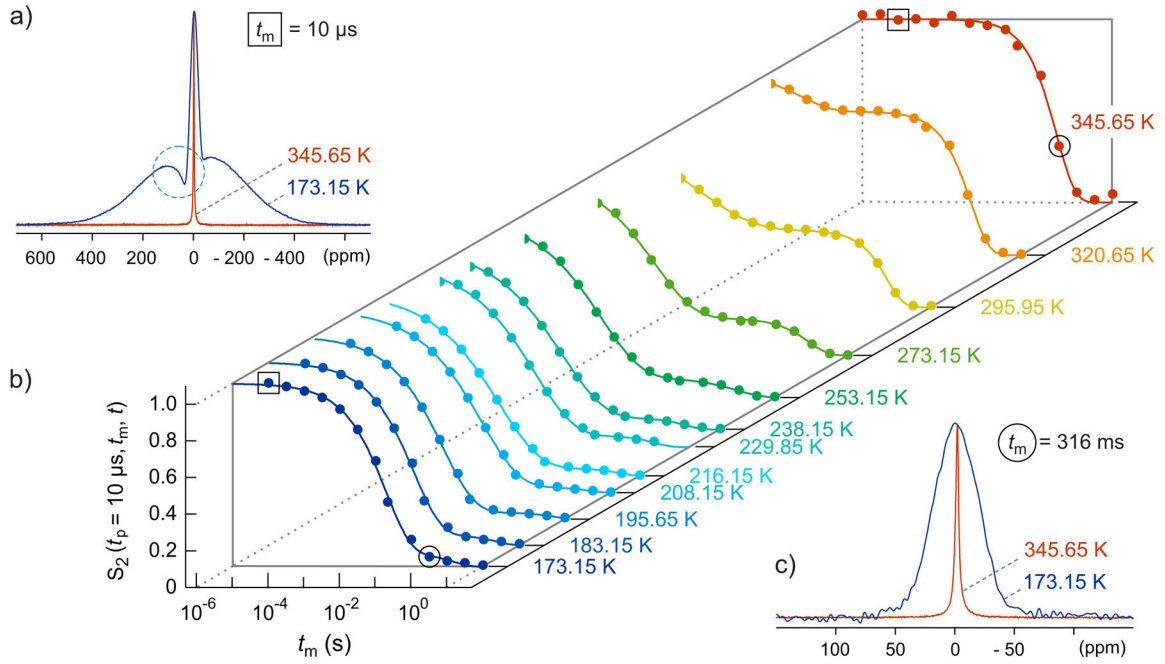

Figure 5. (a) Fourier transforms (173.15 and 345.65 K) of the ^{7}Li spin-alignment echoes of $Li_{6.5}La_3Zr_{1.75}Mo_{0.25}O_{12}$ that were recorded at t_p = 10 μs and short t_m = 10 μs, i.e., before ion dynamics has an effect on the echo amplitude; in (c), the Fourier transforms at t_m = 316 ms are shown for comparison. (b) Stacked plot of the ^{7}Li NMR SAE single-spin (sin−sin) two-time correlation functions recorded at t_p = 10 μs. From ca. 200 K to ca. 273 K, the first decay step is visible that contains the rate τ_{SAE}^{-1}, which can be identified with the Li$^+$ jump rate τ^{-1}. At 345.65 K, echo damping is governed solely by spin−lattice relaxation characterized by $T_{1,SAE}^{-1}$; the two rates are shown in Figure 3. See text for further details.

eV). This suggests high overall Li$^+$ diffusivity. The fact that peak 1 shows up at lower T is due to the larger prefactor obtained. Here, we have $\tau_0^{-1}(1) = 1.6 \times 10^{11}$ s^{-1} and a rather small value for $\tau_0^{-1}(2)$, viz., 8×10^9 s^{-1}.

Considering the fitting results, it is obviously possible to probe two different, quite fast, diffusion processes in LLZMO. Note that in the present case such information is neither available by T_1 nor by line shape measurements; it is seen solely in $T_{1\varrho}^{-1}(1/T)$. The separation into two peaks enables us to determine the temperatures of the peak maxima and to estimate Li$^+$ self-diffusion coefficients. Here, the rate peaks $T_{1\varrho}^{-1}(1/T)$ show up at $T_{max,1}$ = 263 K and $T_{max,2}$ = 315 K. With $\omega_0\tau \approx 0.5$, which is valid for $T_{1\varrho}$ at the peak maximum, the jump rate $\tau^{-1}(T_{max})$ is given by 4.2×10^5 s^{-1}. Using the Einstein−Smoluchowski equation, $D = a^2/(6\tau)$, this yields a self-diffusion coefficient D of ca. 1.9×10^{-11} cm^2 s^{-1} at 263 K (and 313 K, respectively). Here, we choose the jump distance a to be equal to the distance between the Li$^+$ sites 24d and 96h (a = 1.66 Å, see below).

3.3. Li Jumps in LLZMO as Seen via Stimulated Echo NMR. In order to find out whether the activation energy of 0.29 eV can also be seen by other NMR techniques, we employed stimulated echo correlation spectroscopy. In detail, we used the Jeener−Broeckaert three-pulse sequence[59] to record (sinus−sinus) two-time single-spin correlation functions[38] (see Figures 5 and 6).

3.3.1. SAE Decay Curves Recorded at Short Preparation Times. By using a short preparation time t_p of 10 μs between the first and second pulses, a spin state close to that of ideal spin-alignment can be reached, as has been shown by Wu and co-workers.[33] The corresponding spin-alignment echo (SAE) that is recorded after a variable mixing time t_m (10 μs $\leqslant t_m \leqslant$ 10 s) shows up after the reading pulse. Its amplitude, $S_2(t_p$ = const., t_m, $t = t_p)$, decays either (i) due to slow Li$^+$ jump processes between sites with different EFGs, i.e., $\tau_{SAE}^{-1} \approx \tau^{-1}$, (ii) because of ordinary (quadrupolar) NMR spin−lattice relaxation ($T_{1,SAE}^{-1}$), or (iii) because of spin-diffusion effects ($T_{1,sd}^{-1}$):[43,44]

$$S_2 \propto \exp[-(t_m/\tau_{SAE})^{\gamma}]\cdot A \quad (3)$$

with

$$A = \exp[-(t_m/T_{1,Q})^{\gamma'}]\exp[-(t_m/T_{1,sd})^{\gamma''}]$$

The pure SAE decay is given by $S_2' \propto \exp[-(t_m/\tau_{SAE})^{\gamma}]$. In many cases, the Li$^+$ jump process proceeds on a shorter time scale than the latter two effects; hence, it is possible to separate the term $S_2' \propto \exp[-(t_m/\tau_{SAE})^{\gamma}]$ from the nondiffusive ones. Indeed, this is the case here; as we will present below, a two-step decay shows up that can be attributed to S_2' and to the term $\exp[-(t_m/T_{1,Q})^{\gamma'}]$, where, in our case, $T_{1,Q}$ equals T_1.[44,48]

Another way of separation can be chosen if SAE curves have been recorded down to sufficiently low T. At low T, the damping is mainly governed by $T_{1,Q}$ or $T_{1,sd}$; this helps to estimate the influence of the two rates on the echo decay of interest.[43] Additional help is given by the fact that $T_{1,sd}^{-1}$ is expected to change only little with temperature. This is, however, in contrast to τ_{SAE}^{-1}, which, in the ideal case, resembles the temperature dependence of ionic conductivities, as has been shown for quite a large number of examples.[39,45−47,68,69] Hence, via SAE NMR, it is possible to access long-range (bulk) ion transport parameters with the help of a microscopic tool.[39] Moreover, in certain cases, it provides information on the geometry, that is, the diffusion pathways of Li ions.[40,63]

The ^{7}Li SAE NMR curves recorded for the oxide garnet $Li_{6.5}La_3Zr_{1.75}Mo_{0.25}O_{12}$ are shown in Figure 5. At the lowest temperatures, a one-step echo decay is seen; the SAE curve obtained can be parametrized with a stretched exponential function. With increasing temperature, the curves shift toward shorter mixing times, indicating that Li jumps between

DOI: 10.1021/acs.chemmater.5b02231
Chem. Mater. 2015, 27, 6571−6582

electrically inequivalent sites and increasingly causing echo damping. Simultaneously, at long mixing times, a second decay process gains in intensity. While the first process is leaving the accessible time window, the latter process dominates the S_2 curves at elevated T. This is also illustrated in Figure 6; for

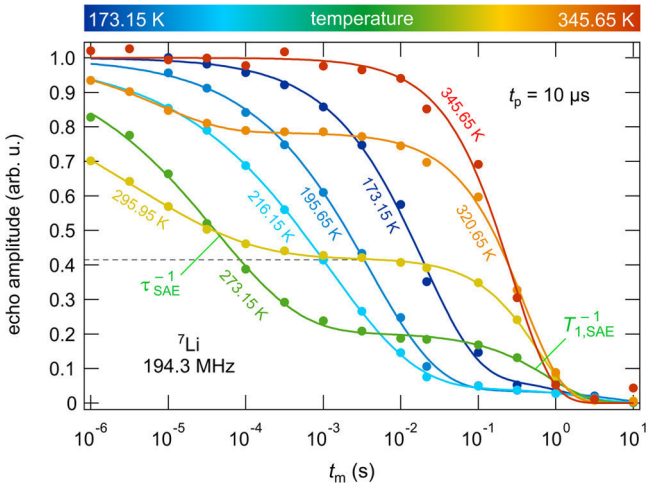

Figure 6. ^{7}Li SAE NMR two-time correlation functions $S_2(t_p = \text{const.}, t_m, t = t_p)$ recorded at t_p = 10 μs. The amplitude of the quadrupolar spin-alignment echo is plotted vs mixing time t_m. Data have been recorded at 194.3 MHz. The solid lines show fits being a sum of two exponential functions that contain the rates τ_{SAE}^{-1} and $T_{1,SAE}^{-1}$; the two-step decay feature is at best seen at 273.15 K. The emergence of the second decay step can have different origins; see text for further explanation.

example, the curve recorded at 273.15 K reveals the two-step decay behavior best. Note that for those recorded above 300 K the normalization turned out to be difficult; thus, arbitrary scaling is used for the data recorded at 320.65 and 345.65 K.

Analyzing the temperature dependence of the SAE NMR rates (see the Arrhenius plot in Figure 3) clearly reveals their origins. At the highest temperatures, the rates of the second decay step coincide with T_1^{-1}: $T_{1,Q}^{-1} = T_1^{-1}$. The rates of the first decay step, however, follow Arrhenius behavior down to ca. 200 K. Below this temperature, they deviate from Arrhenius behavior. It is most likely that spin-diffusion affects echo decay at low T. The fit shown in Figure 3, which does not take into account the last two data points, yields an activation energy, $E_{a,SAE}$, of 0.29 eV. This value is consistent with that deduced from SLR NMR in the rotating frame of reference ($E_{a,Q}$); see above. Moreover, it also agrees with that obtained from preliminary impedance spectroscopy measurements (ca. 0.3 eV) performed on the same sample.[49] In summary, the time-domain NMR methods applied tell us that at low temperatures (<300 K) bulk long-range lithium-ion transport in LLZMO is characterized by an activation energy of approximately 0.30 eV. This activation energy is slightly smaller than that found for Al-doped LLZO (0.34 eV).[21]

Coming back to the two-step decay behavior of our S_2 curves that evolves with increasing temperature, we have to ask the following question: what we can learn about the underlying spin system? As expected, the first decay step shifts toward shorter mixing times the faster the Li-ions jump between the available nonequivalent Li^+ sites in LLZMO. We should keep in mind that only a limited number of crystallographic sites are regularly occupied in our LLZMO sample: the tetrahedral site 24d and the split-atom site 96h; see below. Because of this circumstance, we have to consider, of course, the effect of final state amplitudes on echo decay, as will be discussed below. In addition, we have to consider the important effect of motional phase averaging as we deal with an ion conductor showing rapid Li diffusion at ambient temperature. As we can infer from the ^{7}Li NMR spectra shown in Figure 1b, the quadrupole interactions are indeed significantly averaged due to sufficiently fast Li exchange. This process sets in at relatively low temperatures. If some or all of the Li spins "sense" a single, averaged EFG, then no temporal fluctuations of the associated quadrupole frequency is given any longer during the time period t_m. This means at the same time, the Li ions have visited a number of sites during t_p if $\tau \lesssim t_p$, i.e., the evolution times is not short as compared to the hopping correlation time (as discussed below).[42] Sensing an averaged EFG or hopping directly between electrically inequivalent sites means that the prerequirement that makes SAE NMR work gets lost; consequently, there would be no SAE decay because the rate $\tau_{SAE}^{-1} \approx \tau^{-1}$ would be given by $\tau_{SAE}^{-1} \rightarrow 0$ (being equivalent to $\tau_{SAE} \rightarrow \infty$). Instead, the only reason for the decay of an echo formed would be because of (ordinary) spin−lattice relaxation.

Considering temperatures below ambient, we observe that the amplitude of the second step grows. This could be interpreted as follows: the spin system consists of two spin reservoirs, viz., a subsystem with slow Li spins for which SAE NMR works and a second one made up of very fast ions that already see an averaged EFG. The higher the temperature, the more ions convert into the fast reservoir. Consequently, the amplitude of the second decay step should steadily increase with temperature. For example, at 295.15 K, about 40% of the ions (Figure 6) would have access to a fast diffusion process that is invisible for SAE NMR. At 320.65 K and above, a reliable normalization of the S_2 curves is no longer possible. This is because the initial amplitude of the SAE echo lies out of the accessible time window if we use short preparation times to record the data.

Considering the shape of the first decay step, there are indeed indications of heterogeneous dynamics, although the ^{7}Li NMR spectra do not point to pronounced heterogeneous motional narrowing. For instance, only stretched exponentials are suitable to parametrize the first decay step; see, e.g., the curve recorded at 216.15 K (Figure 6). Between 200 and 280 K, a stretching exponent γ (see eq 3) of 0.4 is best suited to describe echo damping of S_2'. Obviously, heterogeneous dynamics is seen only if we use the site-specific electric quadrupolar information to identify the ions rather than to rely on homonuclear dipole−dipole interactions only. Of course, the distribution width of jump rates in LLZMO is assumed to be much narrower than that of Al-doped LLZO studied previously.[21] Compared to Al-stabilized $Li_7La_3Zr_2O_{12}$ in the case of LLZMO, no additional disorder on the Li sublattice is introduced. As noted above, in LLZMO the Mo ions share common sites with Zr residing on the Wyckoff position 16a; they do not directly influence the sites of the Li sublattice (24d, 96h).[49]

3.3.2. SAE Decay Curves Recorded at Long Preparation Times. Alternatively, one might think about another scenario that could explain the two-step S_2 decay: While at low T the Li ions could be exchanged over various ineqivalent sites, at higher temperatures a diffusion pathway connecting only electrically equivalent sites may play the dominant role. For instance, this could include direct jumps between 96h sites bypassing the 24d

DOI: 10.1021/acs.chemmater.5b02231
Chem. Mater. 2015, 27, 6571−6582

site, as illustrated below. Xu et al.,[70] however, pointed out that such a diffusion pathway is characterized by a much higher activation energy (>0.8 eV) than that found by rotating-frame SLR NMR here.

Thus, it seems more likely that echo damping is indeed affected by heterogeneous dynamics causing (partial) phase averaging. The plateau value reached at intermediate mixing times can also be interpreted as a so-called final state amplitude, S_∞. This means that if only a limited number of electrically inequivalent sites participate in Li diffusion then the loss of phase coherence is restricted. This would lead to a final amplitude S_∞ larger than 0. If S_2 is properly normalized to range between 0 and 1, then it is given by the inverse number $1/N$ of the quadrupole frequencies ω_Q involved, provided the available Li sites are equally populated. If equal population is not given, then S_∞ is calculated by the summation over the squared weighing factors w_i: $S_\infty = \sum_{i=1}^{N} w_i^2$.[38] Considering a powder average ($\langle \dots \rangle$), the pure SAE NMR decay is[38,43,44]

$$S_2'(t_m) \propto \langle (\sin[\omega_Q(0)t_p] \sin[\omega_Q(t_m)t_p]) \rangle \quad (4)$$

$$\propto \exp[-(t_m/\tau_{SAE})^{\gamma}] \quad (3')$$

relating the phase angles given by $\omega_Q(0)t_p$ and $\omega_Q(t_m)t_p$ (or their mean values $\bar{\omega}_Q$). The final value of $S_\infty(t_p \rightarrow \infty)$ is reached only at sufficiently large t_p; at shorter t_p, it will vary around the final value. In general, S_2 will be of the form of

$$S_2(t_m) = (A \cdot S_2' + B) \cdot \exp[-(t_m/T_{1,Q})^{\gamma'}] \quad (5)$$

provided we consider temperatures where $T_{1,SAE}$ equals $T_{1,Q}$, i.e., the two-step decay regime. The final state amplitude is then given by $S_\infty = B/(A + B)$. Thus, to determine S_∞, echoes at large t_p have to be recorded. For ^{7}Li, however, this will simultaneously create (unwanted) dipolar order. This disadvantage is less important in ^{2}H SAE NMR because of the much larger quadrupole interaction in deuteron NMR, but it is important in ^{7}Li NMR. Therefore, SAE decay curves, and echoes as well, recorded at preparation times significantly larger than, e.g., 10 μs will be affected by dipole−dipole interactions. Such interactions also play a role at t_p = 10 μs if we consider the Fourier transforms shown in Figure 5a. The apparent "central" line that shows up at low T and short t_p and t_m reflects dipolar coupling of the Li spins.[41] Note that at short t_m the influence of ion dynamics on echo formation is kept as low as possible. For comparison, the Fourier transforms of the second decay step (see Figure 5c) is composed of a single line that no longer contains the quadrupole intensities. In short, before we can discuss any results for S_∞, we have to know the influence that large t_p values have on the $S_2'(t_m)$ decay.

If t_p is increased, i.e., if t_p is (much) larger or equal to τ_{SAE}, then phase averaging during t_p might affect echo damping. This would shift the $S_2'(t_m)$ curve back toward longer mixing times, and, indeed, this is found here (see Figure 7). In contrast, as expected, the term $\exp[-(t_m/T_{1,SAE})^{\gamma'}]$ is not influenced by t_p, and the increase in preparation time affects τ_{SAE}^{-1} since $\tau_{SAE} \gg t_p$ is no longer valid. The higher the temperature, the larger the effect because τ_{SAE} decreases with T. In the ideal case, during a short t_p, no Li$^+$ exchange occurs, guaranteeing the storage of all of the necessary phase information on the spins. Here, below 240 K, overall Li exchange is slow and an increase of t_p has little effect on τ_{SAE}^{-1} (and on the amplitude S_∞), ensuring that the rate is useful to derive a reliable activation energy; see Figure 3. At 273 K and above, the effect of motional phase averaging during t_p is, however, apparent,[42] limiting the detection of all of the Li$^+$ jump processes (this is best seen at 295 K and above.) The limitation, on the other hand, can be used to estimate the order of magnitude of τ_{SAE}^{-1}: at ambient temperature, it is definitely on the order of 10^5 s^{-1}. This is in perfect agreement with the result derived from spin-lock SLR NMR. In particular, it is in perfect agreement with the jump rate (4.2×10^5 s^{-1}) estimated from

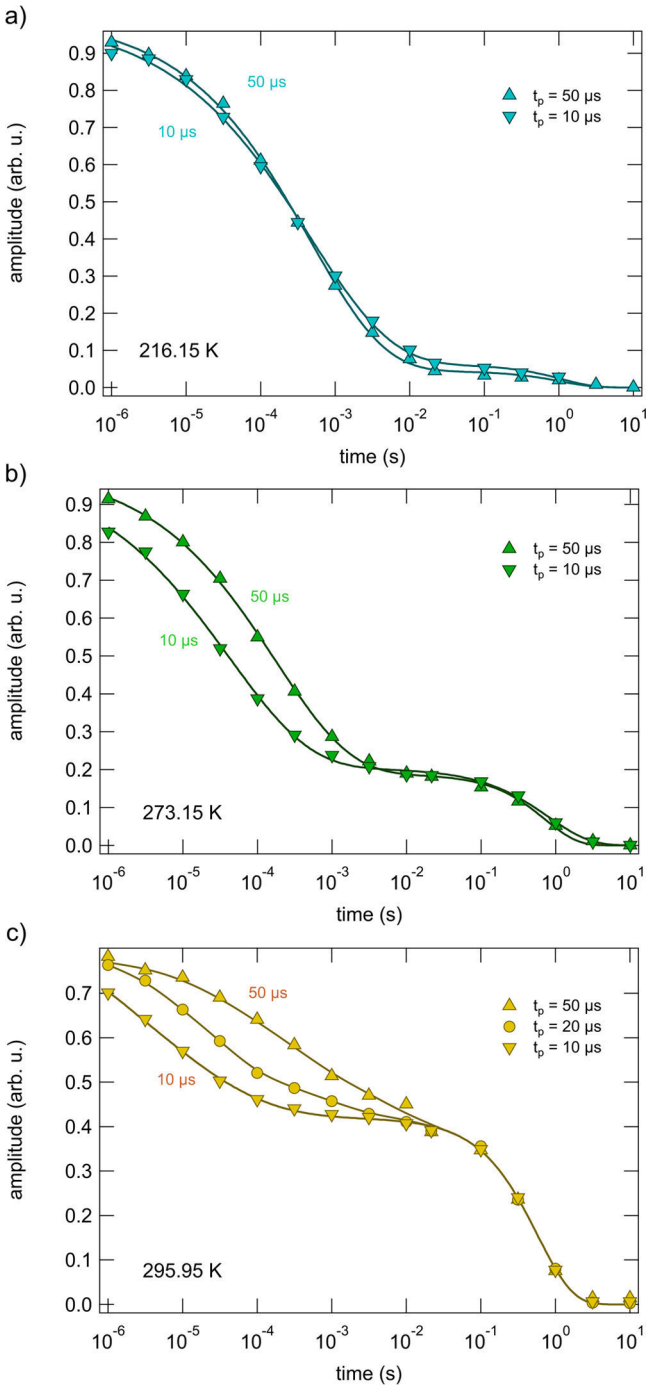

Figure 7. ^{7}Li SAE NMR echo decay curves, $S_2(t_p,t_m)$ vs t_m, that have been recorded at preparation times t_p equal to or larger than 10 μs but shorter than 50 μs. With increasing t_p, the first decay step shifts toward larger mixing times t_m. This is because of motional phase averaging that takes place during the evolution period t_p. The higher T is, the more pronounced the effect because Li diffusivity steadily increases with T.

DOI: 10.1021/acs.chemmater.5b02231
Chem. Mater. 2015, 27, 6571−6582

the second SLR NMR rate peak showing up at 313 K (see above).

Knowing about the t_p dependence on $S_2'(t_m)$, we can analyze the associated final state amplitudes. At sufficiently large preparation times, the complete SAE NMR curves are measurable, i.e., proper normalization is possible. In Figure 8,

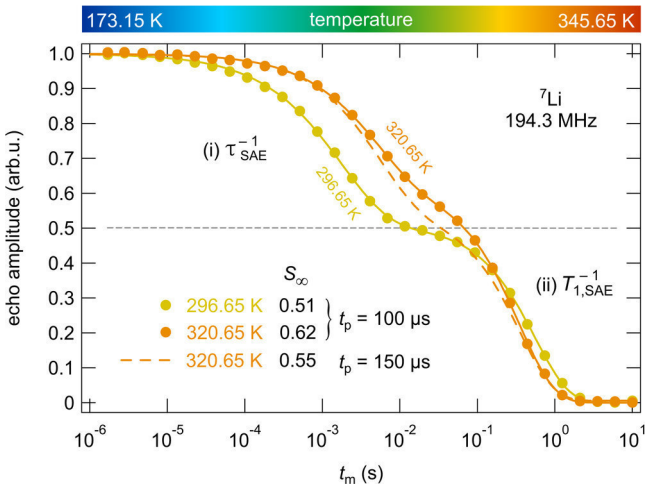

Figure 8. ^{7}Li SAE NMR decay curves, $S_2(t_p,t_m)$ vs t_m, recorded at large preparation times t_p of up to 150 μs. As is evident from the normalization of S_2 final state amplitudes, S_∞ between 0.5 and 0.6 show up. The slight increase of $T_{1,SAE}$ reflects the temperature dependence of T_1. The data points refer to the amplitude of the quadrupolar spin-alignment echo. Note that at such large preparation times the whole echo is composed of both a qudrupolar and a dipolar part. The dipolar part, however, behaves very similar compared to the sharp alignment echo. Note that the slight temperature dependence of the second decay step reflects the diffusion-induced increase of R_1 with T (see Figure 3).

results are shown for 296.65 and 320.65 K; at these temperatures, dipole−dipole interactions, which may affect S_∞,[41] are largely eliminated through rapid Li^+ exchange; increasing T further has no effect on the curves.

The corresponding final state amplitudes S_∞ range from 0.5 to 0.6. Taking into account the site occupancy as derived from neutron diffraction (0.50 (24d), 0.36 (96h), see Table S1), S_∞ is expected to take a value of 0.62 if we assume this two-site jump process to be mainly responsible for SAE decay. This good agreement with experiment (Figure 8) points to the involvement of the two electrically inequivalent sites in LLZMO. Moreover, the pronounced phase averaging during t_p indicates that the quadrupole frequencies associated with the sites 24d and 96h are quite different. In such a case, a small number of jumps suffices to cause averaging. Because of dipolar couplings (to some extent, the amplitude S_∞ depends on T),[41] only at sufficiently high T are these couplings fully averaged.

As a last remark: of course, at temperatures equal to or higher than 270 K, the condition $t_p \ll \tau_{SAE}$ is violated. Thus, the influence of phase averaging, which predominantly affects the fraction of species moving fast on the scale set by the evolution time, cannot be neglected, as is shown in Figure 7. Thus, there might be a fast spin reservoir because of heterogeneous dynamics rather than uniform Li^+ exchange that leads to $\bar{\omega}_Q(t_m)$ = const. giving rise to the second decay step seen.

3.4. Possible Li Ion Diffusion Pathways and Comparison of NMR Activation Energies with Findings from Theory. In order to ascribe the activation energies found to possible (microscopic) Li^+ diffusion pathways or elementary jump processes, we first have to look at the crystal structure of LLZMO. The crystal structure ($Ia\bar{3}d$) and, most importantly, the Li site occupancies of our sample have been revealed by neutron diffraction. According to the refinement of neutron powder diffraction data, Mo and Zr ions are distributed over the 16a sites, and La ions occupy the dodecahedra (24c). As mentioned above, according to the best refinement, Li ions reside on two sites, viz., 24d positions with 4-fold coordination (site occupancy 0.5) and 96h sites with distorted 4-fold coordination (site occupancy 0.36). The occupancy of these two sites is in agreement with that found for other LLZO-type garnets.[71] Possible Li^+ diffusion pathways, simply connecting sites 24d and 96h,[70,71] are shown in Table 1.

The distribution of vacancies, ordered or disordered over the Li^+ sites,[72,73] as well as repulsive Li^+−Li^+ Coulomb interactions (note that each occupied 24d site (see Figure 9) blocks the occupation of next-neighbored 96h sites)[74] are expected to vary with the synthesis conditions.[75] Annealing temperatures and cooling rates may critically influence lithium ordering[75] and, thus, ionic conductivity that is assumed to depend on total Li^+ concentration rather than on the kind of doping ions present.[19] In particular, the thermal history of the samples may also cause nonequilibrium Li^+ distributions over the available voids in garnet-type cubic LLZO that crucially influences its ion transport properties.[75] Thus, coming from real systems, the comparison with results from calculations is by far not straightforward. We should also keep in mind that diffusion pathways chosen by the ions may change with increasing temperature, as has been pointed out by Lai and co-workers for $Li_5La_3Ta_2O_{12}$ using classical molecular dynamics simulations.[76]

Table 1. Possible Elementary Steps of Li Ion Hopping in LLZMO between Next Neighbors and Tentative Assignment of Activation Energies

sites	a (Å)	E_a (eV)	method	type/comment
96h−48g−96h″[a]	0.7	<0.1	T_1 (low-T)	"caged dynamics"[b]
24d−96h[c]	1.66	0.15	T_1	forward, backward jumps[d]
96h−24d(−96h′)	1.66	0.15	T_1	also detectable by SAE NMR (0.29 eV)
24d−[96h]−24d[e]	2.34, 3.12	0.27−0.29	$T_{1\varrho}$; τ_{SAE}	
96h−96h′[f]	2.47, 2.9, 3.1, 3.47	⩾0.29	$T_{1\varrho}$; (τ_{SAE})	including paths bypassing the 24d site; curved pathway

[a]Very fast jump process between similar sites most likely invisible for SAE NMR even at extremely low T. [b]Strictly localized motions of split site 48g. Only one of the three sites within the pocket can be occupied by Li. E_a is expected to be extremely small. Note that this movement has not been detected by NMR so far. [c]Fast jump process between similar sites most likely invisible for SAE NMR. [d]Localized two-site jump process. [e]Here, [96h] denotes the split-atom site 96h−48g−96h″; see the first line in the table. [f]Presumably, this process, which bypasses the 24d site, involves temporary occupation of voids connecting the two 96h sites; it is most likely also visible by SAE NMR at low temperatures.

DOI: 10.1021/acs.chemmater.5b02231
Chem. Mater. 2015, 27, 6571−6582

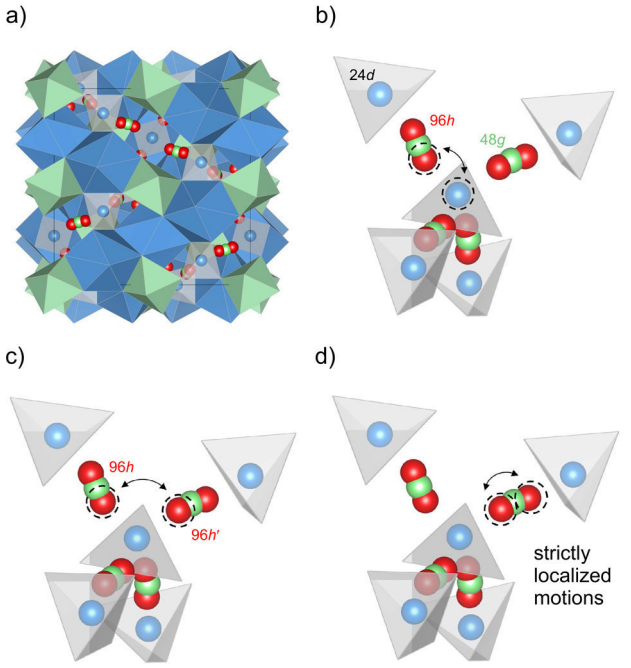

Figure 9. (a) Crystal structure of cubic LLZO (view along the *a*-axis); (b–d) selected Li elementary hopping steps between sites 24d and 96h that are occupied by Li in LLZMO, as evidenced from neutron diffraction. In (b), the 24d–96h jump process is shown; in (c), Li^+ diffusion between 96h sites of two different octahedral voids is illustrated. (d) Strictly localized Li motions within the 96h–48g–96h″ arrangement.

Recent theoretical investigations on overall ion conductivity, diffusion pathways, and local hopping barriers reflect a highly complex picture of ion transport through LLZO. Long-range ion transport in cubic LLZO, to which (dc)-conductivity measurements are sensitive, is reported to be governed by an average activation energy of ca. 0.32 to 0.34 eV. The final result of Adams and co-workers (0.34 eV),[74] who studied the 3D network pathway consisting of connected local 24d–96h–24d paths (see Table 1 and Figure 9), agrees well with the study performed by Jalem et al.[77] that reported on a concerted diffusion mechanism (0.33 eV); both groups used molecular dynamics simulations to describe Li^+ motions in the stabilized cubic polymorph at high temperatures. For Ta-bearing LLZO, Ceder and co-workers reported an activation energy of 0.19 eV by considering the 96h–24d(–96h′) pathway; this value points to the activation energy we observed via T_1 SLR NMR that is sensing short-range ion dynamics.[78]

Two further studies have been published that focus on the *elementary* steps of ion hopping in LLZO-type garnets. The *ab initio* calculations based on density functional theory performed by Xu et al.[70] differentiate between two possible Li-ion hopping pathways. The first route describes Li-ion hopping between (96h/48g) and (96h/48g)′ voids in garnets (Figure 9c); this pathway is characterized by a rather large hopping barrier. According to the second route,[70] the Li ion moves through the (96h/48g)–24d border (Figure 9c), thus crossing the shared triangular face (0.25 eV). Then, the ion shortly stays at the corner of the 24d site before climbing over the other barrier and finally reaching the empty 24d site (cf. also the considerations of Awaka et al.[71]). This (edge pass-type) pathway would be consistent with that roughly denoted 96h–24d(–96h′) in Table 1. The overall barrier reported by Xu et al.[70] is 0.26 eV, which is in excellent agreement to that seen via NMR relaxometry on our sample; see above. As suggested by Lai et al.,[76] in $Li_5La_3Ta_2O_{12}$ there might be a change from this edge-passing mechanism at low temperatures to a center-passing one at higher *T*. In the case of $Li_5La_3Ta_2O_{12}$, the authors, who used reverse Monte Carlo modeling and classical molecular dynamics to understand local lithium structure and dynamics, do not find any evidence for direct jumps between the octahedral voids, i.e., bypassing the 24d bottleneck.[76] The latter has also been observed by Miara et al.[78]

Coming back to our results from NMR relaxometry, we indeed observe two different relaxation rate peaks ($R_{1\varrho}$). This points to two types of Li-ion motional processes in our sample. Tentatively, we would assign the rate peak showing up at lower *T* to Li motions between 24d and 96h sites (Figure 9b). The corresponding sites are separated by ca. 1.66 Å; because of Coulomb repulsion, it is expected that they cannot be occupied simultaneously. Likely, this hopping process also influences the R_1 rates (0.15 eV). From our measurements, we find no indications that the Li ions on 24d sites do not participate in Li^+ diffusion, as assumed for, e.g., $Li_5La_3Nb_2O_{12}$ on the basis of ^{6}Li 2D exchange NMR.[79] For comparsion with theory, it is common in theoretical investigations to observe that 24d sites do indeed participate in Li^+ diffusion (see above). The second NMR relaxation rate peak observed via $R_{1\varrho}$ might be attributed to Li-ion hopping between 96h sites either temporarily occupying or even bypassing the 24d sites (see Table 1). As pointed out by Meier et al.,[80] short-distance jumps between face-sharing tetrahedra (24d) and octahedra (96h/48g) exhibit a slightly smaller energetic barrier than jumps between the neighboring, edge-sharing polyhedra (96h).

In detail, Meier et al. used *ab inito* molecular dynamics simulation, metadynamics, and nudged-elastic band calculations to systematically describe Li-ion hopping in cubic and tetragonal LLZO.[80] While for the tetragonal modification the motion of Li ions is reported to be influenced by collective nature, they identified an asynchronous mechanism dominated by single-ion jumps and induced collective motion for cubic LLZO. On the assumption of individual jumps, the activation energies for a series of elementary hopping processes along the Li^+ diffusion path in LLZO, involving the 24d and (96h/48g) sites, in particular, are on the order of ca. 0.10 to 0.30 eV.[80] The activation energies of our NMR measurements perfectly agree with this range. For comparison, these barriers are significantly lower than the mean activation energy for Li-ion hopping in the tetragonal modification (0.4 eV), for which 0.32 eV ($\omega_1\tau_c \gg 1$) and 0.48 eV ($\omega_1\tau_c \ll 1$) was recently found using spin-lock NMR relaxometry (as mentioned above).[31]

As a last remark, the Li ions in the (96h/48g) void, i.e., the split site 96h–48g–96h′, which can be occupied only by a single Li ion, might give rise to strictly localized Li^+ displacements (Figure 9d). Such caged dynamics would give rise to a phenomenon that is frequently related to a nearly constant loss, that is, a frequency-independent ϵ'' being the imaginary part of the complex permittivity. This translates into a temperature-independent conductivity that linearly increases with frequency at sufficiently low *T*. For such motions, activation energies below 0.1 eV are reasonable. Further studies are needed to clarify whether this phenomenon can indeed be detected in LLZO-type garnets.

DOI: 10.1021/acs.chemmater.5b02231
Chem. Mater. 2015, 27, 6571–6582

4. CONCLUSIONS

$Li_{6.5}La_3Zr_{1.75}Mo_{0.25}O_{12}$ represents a new, fast lithium-ion conductor that crystallizes with cubic symmetry. The fact that it is stabilized in its cubic modification without doping with trivalent cations such as Al or Ga, leaves the Li sublattice untouched by any dopants that could possibly disturb the 3D network pathway used by Li ions for long-range diffusion.

We used various ^{7}Li solid-state NMR spectroscopic tools to analyze Li-ion dynamics on both the short- and long-range length scales. It is difficult to obtain such information from impedance spectroscopy that is usually applied to characterize ion transport in LLZO-based materials. Li diffusivity in LLZMO turns out to be remarkably high but has to be described by multiple Li-ion dynamic processes taking place. Depending on the time window to which the different NMR methods are sensitive, (mean) activation energies were extracted that range from 0.15 eV (R_1) to 0.29 eV ($R_{1\varrho}$, SAE NMR).

In particular, the two-step damping of variable-temperature sin−sin correlation functions of SAE NMR reveals heterogeneous dynamics. The applicability of SAE NMR, which is sensitive to ion hopping between electrically inequivalent sites in LLZO, shows that both 24d and 96h sites are involved in Li^+ diffusion. This is underlined by the two-step behavior observed. Echo damping at large preparation times might be adduced to find indications that a two-site jump process, 96h−24d−96h′, is present in LLMZO. At least for LLZMO, this rules out previous considerations about immobile Li ions residing on 24d.

The behavior of the $R_{1\varrho}$ rates with temperature can be approximated at best with two BPP fits. The peak at 313 K points to an Li^+ jump rate of 4.2×10^5 s^{-1}. This value is in perfect agreement with the jump rate expected from SAE NMR if we extrapolate the τ_{SAE}^{-1} rates toward higher T. The rate transforms into a self-diffusion coefficient D of ca. 1.9×10^{-11} cm^2 s^{-1}. Interestingly, the diffusion-induced rate peaks $R_{1\varrho}(1/T)$ observed appear to be sharper than has been observed for Al-doped LLZO, indicating a less broad distribution of jump rates for LLZMO with a dopant-free Li sublattice. Extremely broad $R_{1\varrho}(1/T)$ peaks seem to be characteristic merely for Al- or Ga-stabilized LLZO. The activation energies found have tentatively been assigned to possible elementary Li-ion hopping processes between neighboring Li^+ sites 24d and 96h. Remarkably, our results agree very well with local hopping barriers that have been calculated on the basis of density functional theory.

■ ASSOCIATED CONTENT

Supporting Information

The Supporting Information is available free of charge on the ACS Publications website at DOI: 10.1021/acs.chemmater.5b02231.

Results from neutron diffraction experiments including the site occupancies found (PDF).

■ AUTHOR INFORMATION

Corresponding Authors

*(P.B.) E-mail: bottke@tugraz.at.

*(M.W.) E-mail: wilkening@tugraz.at.

Notes

The authors declare no competing financial interest.

■ ACKNOWLEDGMENTS

We thank our colleagues at the TU Graz for valuable discussions. Financial support by the Deutsche Forschungsgemeinschaft (DFG Research Unit 1277, grant nos. WI3600/2-2 and 4-1) as well as by the Austrian Federal Ministry of Science, Research and Economy, and the Austrian National Foundation for Research, Technology and Development is greatly appreciated. Moreover, we thank the Austrian Science Fund (FWF), project no. P25702 (D. Rettenwander, G. Amthauer), for financial support.

■ REFERENCES

(1) Larcher, D.; Tarascon, J.-M. Towards Greener and More Sustainable Batteries for Electrical Energy Storage. *Nat. Chem.* **2015**, *7*, 19−29.

(2) Adelhelm, P.; Hartmann, P.; Bender, C. L.; Busche, M.; Eufinger, C.; Janek, J. From Lithium to Sodium: Cell Chemistry of Room Temperature Sodium-Air and Sodium-Sulfur Batteries. *Beilstein J. Nanotechnol.* **2015**, *6*, 1016−1055.

(3) Bruce, P. G.; Freunberger, S. A.; Hardwick, L. J.; Tarascon, J.-M. Li-O_2 and Li-S Batteries with High Energy Storage. *Nat. Mater.* **2012**, *11*, 19−29.

(4) Aricó, A. S.; Bruce, P.; Scrosati, B.; Tarascon, J.-M.; van Schalkwijc, W. Nanostructured Materials for Advanced Energy Conversion and Storage Devices. *Nat. Mater.* **2005**, *4*, 366−377.

(5) Whittingham, M. S. Lithium Batteries and Cathode Materials. *Chem. Rev.* **2004**, *104*, 4271−4301.

(6) Knauth, P. Inorganic Solid Li Ion Conductors: An Overview. *Solid State Ionics* **2009**, *180*, 911−916.

(7) Cao, C.; Li, Z.; Wang, X.-L.; Zhao, X.; Han, W.-Q. Recent Advances in Inorganic Solid Electrolytes for Lithium Batteries. *Front. Energy Res.* **2014**, *2*, 25.

(8) Jung, Y. S.; Oh, D. Y.; Nam, Y. J.; Park, K. H. Issues and Challenges for Bulk-Type All-Solid-State Rechargeable Lithium Batteries using Sulfide Solid Electrolytes. *Isr. J. Chem.* **2015**, *55*, 472−485.

(9) Murugan, R.; Thangadurai, V.; Weppner, W. Fast Lithium Ion Conduction in Garnet-Type $Li_7La_3Zr_2O_{12}$. *Angew. Chem., Int. Ed.* **2007**, *46*, 7778−7781.

(10) Kamaya, N.; Homma, K.; Yamakawa, Y.; Hirayama, M.; Kanno, R.; Yonemura, M.; Kamiyama, T.; Kato, Y.; Hama, S.; Kawamoto, K.; Mitsui, A. A Lithium Superionic Conductor. *Nat. Mater.* **2011**, *10*, 682−686.

(11) Mizuno, F.; Hayashi, A.; Tadanaga, K.; Tatsumisago, M. New, Highly Ion-Conductive Crystals Precipitated from Li_2S-P_2S_5 Glasses. *Adv. Mater.* **2005**, *17*, 918−921.

(12) Deiseroth, H.-J.; Kong, S.-T.; Eckert, H.; Vannahme, J.; Reiner, C.; Zaiß, T.; Schlosser, M. Li_6PS_5X: A Class of Crystalline Li-Rich Solids With an Unusually High Li^+ Mobility. *Angew. Chem., Int. Ed.* **2008**, *47*, 755−758.

(13) Epp, V.; Gün, O.; Deiseroth, H.-J.; Wilkening, M. Highly Mobile Ions: Low Temperature NMR Directly Probes Extremely Fast Li^+ Hopping in Argyrodite-Type Li_6PSe_5Br. *J. Phys. Chem. Lett.* **2013**, *4*, 2118−2123.

(14) Kaib, T.; Haddadpour, S.; Kapitein, M.; Bron, P.; Schröder, C.; Eckert, H.; Roling, B.; Dehnen, S. New Lithium Chalcogenidotetrelates, LiChT: Synthesis and Characterization of the Li^+-Conducting Tetralithium ortho-Sulfidostannate Li_4SnS_4. *Chem. Mater.* **2012**, *24*, 2211−2219.

(15) Bron, P.; Johansson, S.; Zick, K.; Schmedt auf der Günne, J.; Dehnen, S.; Roling, B. $Li_{10}SnP_2S_{12}$: An Affordable Lithium Superionic Conductor. *J. Am. Chem. Soc.* **2013**, *135*, 15694−15697.

(16) Sahu, G.; Lin, Z.; Li, J.; Liu, Z.; Dudney, N.; Liang, C. Air-Stable, High-Conduction Solid Electrolytes of Arsenic-Substituted Li_4SnS_4. *Energy Environ. Sci.* **2014**, *7*, 1053−1058.

(17) López, M. C.; Ortiz, G. F.; Arroyo-de Dompablo, E. M.; Tirado, J. L. An Unnoticed Inorganic Solid Electrolyte: Dilithium Sodium

DOI: 10.1021/acs.chemmater.5b02231
Chem. Mater. 2015, 27, 6571−6582

Phosphate with the Nalipoite Structure. *Inorg. Chem.* **2014**, *53*, 2310−2316.
(18) Brant, J. A.; Massi, D. M.; Holzwarth, N. A. W.; MacNeil, J. H.; Douvalis, A. P.; Bakas, T.; Martin, S. W.; Gross, M. D.; Aitken, J. A. Fast Lithium Ion Conduction in Li_2SnS_3: Synthesis, Physicochemical Characterization, and Electronic Structure. *Chem. Mater.* **2015**, *27*, 189−196.
(19) Thangadurai, V.; Narayanan, S.; Pinzaru, D. Garnet-Type Solid-State Fast Li Ion Conductors for Li Batteries: A Critical Review. *Chem. Soc. Rev.* **2014**, *43*, 4714−4727.
(20) Wolfenstine, J.; Allen, J. L.; Read, J.; Sakamoto, J. Chemical Stability of Cubic $Li_7La_3Zr_2O_{12}$ with Molten Lithium at Elevated Temperature. *J. Mater. Sci.* **2013**, *48*, 5846−5851.
(21) Buschmann, H.; Dölle, J.; Berendts, S.; Kuhn, A.; Bottke, P.; Wilkening, M.; Heitjans, P.; Senyshyn, A.; Ehrenberg, H.; Lotnyk, A.; Duppel, V.; Kienle, L.; Janek, J. Structure and Dynamics of the Fast Lithium Ion Conductor "$Li_7La_3Zr_2O_{12}$. *Phys. Chem. Chem. Phys.* **2011**, *13*, 19378−19392.
(22) Rettenwander, D.; Geiger, C. A.; Tribus, M.; Tropper, P.; Amthauer, G. A Synthesis and Crystal Chemical Study of the Fast Ion Conductor $Li_{7-3x}Ga_xLa_3Zr_2O_{12}$ with x = 0.08 to 0.84. *Inorg. Chem.* **2014**, *53*, 6264−6269.
(23) Wolfenstine, J.; Ratchford, J.; Rangasamy, E.; Sakamoto, J.; Allen, J. L. Synthesis and High Li-Ion Conductivity of Ga-Stabilized Cubic $Li_7La_3Zr_2O_{12}$. *Mater. Chem. Phys.* **2012**, *134*, 571−575.
(24) Allen, J. L.; Wolfenstine, J.; Rangasamy, E.; Sakamoto, J. Effect of Substitution (Ta, Al, Ga) on the Conductivity of $Li_7La_3Zr_2O_{12}$. *J. Power Sources* **2012**, *206*, 315−319.
(25) Jalem, R.; Rushton, M.; Manalastas, W.; Nakayama, M.; Kasuga, T.; Kilner, J. A.; Grimes, R. W. Effects of Gallium Doping in Garnet-Type $Li_7La_3Zr_2O_{12}$ Solid Electrolytes. *Chem. Mater.* **2015**, *27*, 2821−2831.
(26) Rettenwander, D.; Geiger, C. A.; Amthauer, G. Synthesis and Crystal Chemistry of the Fast Li-Ion Conductor $Li_7La_3Zr_2O_{12}$ Doped with Fe. *Inorg. Chem.* **2013**, *52*, 8005−8009.
(27) Bernstein, N.; Johannes, M. D.; Hoang, K. Origin of the Structural Phase Transition in $Li_7La_3Zr_2O_{12}$. *Phys. Rev. Lett.* **2012**, *109*, 205702.
(28) Rangasamy, E.; Wolfenstine, J.; Sakamoto, J. The Role of Al and Li Concentration on the Formation of Cubic Garnet Solid Electrolyte of Nominal Composition $Li_7La_3Zr_2O_{12}$. *Solid State Ionics* **2012**, *206*, 28−32.
(29) Awaka, J.; Kijima, N.; Hayakawa, H.; Akimoto, J. Synthesis and Structure Analysis of Tetragonal $Li_7La_3Zr_2O_{12}$ with the Garnet-Related Type Structure. *J. Solid State Chem.* **2009**, *182*, 2046−2052.
(30) Ramakumar, S.; Satyanarayana, L.; Manorama, S. V.; Murugan, R. Structure and Li^+ Dynamics of Sb-Doped $Li_7La_3Zr_2O_{12}$ Fast Lithium Ion Conductors. *Phys. Chem. Chem. Phys.* **2013**, *15*, 11327−11338.
(31) Kuhn, A.; Narayanan, S.; Spencer, L.; Goward, G.; Thangadurai, V.; Wilkening, M. Li Self-Diffusion in Garnet-type $Li_7La_3Zr_2O_{12}$ as Probed Directly by Diffusion-Induced ^{7}Li Spin-Lattice Relaxation NMR Spectroscopy. *Phys. Rev. B: Condens. Matter Mater. Phys.* **2011**, *83*, 094302.
(32) Kuhn, A.; Epp, V.; Schmidt, G.; Narayanan, S.; Thangadurai, V.; Wilkening, M. Spin-Alignment Echo NMR: Probing Li^+ Hopping Motion in the Solid Electrolyte $Li_7La_3Zr_2O_{12}$ with Garnet-Type Tetragonal Structure. *J. Phys.: Condens. Matter* **2012**, *24*, 035901.
(33) Tang, X.-P.; Wu, Y. Alignment Echo of Spin-3/2 ^{9}Be Nuclei: Detection of Ultraslow Motion. *J. Magn. Reson.* **1998**, *133*, 155−165.
(34) Tang, X.-P.; Busch, R.; Johnson, W.; Wu, Y. Slow Atomic Motion in Zr-Ti-Cu-Ni-Be Metallic Glasses Studied by NMR. *Phys. Rev. Lett.* **1998**, *81*, 5358−5361.
(35) Tang, X.-P.; Geyer, U.; Busch, R.; Johnson, W.; Wu, Y. Diffusion Mechanisms in Metallic Supercooled Liquids and Glasses. *Nature* **1999**, *402*, 160−162.
(36) Böhmer, R.; Jörg, T.; Qi, F.; Titze, A. Stimulated Echo NMR Spectroscopy of Slow Ionic Motions in a Solid Electrolyte. *Chem. Phys. Lett.* **2000**, *316*, 419−424.
(37) Qi, F.; Jörg, T.; Böhmer, R. Stimulated-Echo NMR Spectroscopy of ^{9}Be and ^{7}Li in Solids: Method and Application to Ion Conductors. *Solid State Nucl. Magn. Reson.* **2002**, *22*, 484−500.
(38) Böhmer, R.; Jeffrey, K.; Vogel, M. Solid-state Lithium NMR with Applications to the Translational Dynamics in Ion Conductors. *Prog. Nucl. Magn. Reson. Spectrosc.* **2007**, *50*, 87−174.
(39) Wilkening, M.; Heitjans, P. From Micro to Macro: Access to Long-Range Li^+ Diffusion Parameters in Solids via Microscopic ^{6}Li/^{7}Li Spin-Alignment Echo NMR Spectroscopy. *ChemPhysChem* **2012**, *13*, 53−65.
(40) Wilkening, M.; Küchler, W.; Heitjans, P. From Ultraslow to Fast Lithium Diffusion in the 2D Ion Conductor $Li_{0.7}TiS_2$ Probed Directly by Stimulated-Echo NMR and Nuclear Magnetic Relaxation. *Phys. Rev. Lett.* **2006**, *97*, 065901.
(41) Qi, F.; Diezemann, G.; Böhm, H.; Lambert, J.; Böhmer, R. Simple Modeling of Dipolar Coupled ^{7}Li Spins and Stimulated-Echo Spectroscopy of Single-Crystalline β-Eucryptite. *J. Magn. Reson.* **2004**, *169*, 225−239.
(42) Qi, F.; Rier, C.; Böhmer, R.; Franke, W.; Heitjans, P. Ion Hopping in Crystalline and Glassy Spodumene $LiAlSi_2O_6$: Spin-Lattice Relaxation and ^{7}Li Echo NMR Spectroscopy. *Phys. Rev. B: Condens. Matter Mater. Phys.* **2005**, *72*, 104301.
(43) Wilkening, M.; Heine, J.; Lyness, C.; Armstrong, A. R.; Bruce, P. G. Li Diffusion Properties of Mixed Conducting TiO_2-B Nanowires. *Phys. Rev. B: Condens. Matter Mater. Phys.* **2009**, *80*, 064302.
(44) Wilkening, M.; Gebauer, D.; Heitjans, P. Diffusion Parameters in Single-Crystalline Li_3N as Probed by ^{6}Li and ^{7}Li Spin-Alignment Echo NMR Spectroscopy in Comparison with Results from ^{8}Li β-Radiation Detected NMR. *J. Phys.: Condens. Matter* **2008**, *20*, 022201.
(45) Wilkening, M.; Mühle, C.; Jansen, M.; Heitjans, P. Microscopic Access to Long-Range Diffusion Parameters of the Fast Lithium Ion Conductor Li_7BiO_6 by Solid State ^{7}Li Stimulated Echo NMR. *J. Phys. Chem. B* **2007**, *111*, 8691−8694.
(46) Faske, S.; Koch, B.; Murawski, S.; Küchler, R.; Böhmer, R.; Melchior, J.; Vogel, M. Mixed-Cation $Li_xAg_{1-x}PO_3$ Glasses Studied by ^{6}Li, ^{7}Li, and ^{109}Ag Stimulated-Echo NMR Spectroscopy. *Phys. Rev. B: Condens. Matter Mater. Phys.* **2011**, *84*, 024202.
(47) Brinkmann, C.; Faske, S.; Koch, B.; Vogel, M. NMR Multi-Time Correlation Functions of Ion Dynamics in Solids. *Z. Phys. Chem.* **2010**, *224*, 1535−1553.
(48) Böhmer, R.; Qi, F. Spin Relaxation and Ultra-Slow Li Transport in an Aluminosilicate Glass Ceramic. *Solid State Nucl. Magn. Reson.* **2007**, *31*, 28−34.
(49) Wagner, R.; Rettenwander, D.; Welzl, A.; Schmidt, W.; Fleig, J.; Wilkening, M.; Amthauer, G. A comparative study of the synthesis of coarse-grained $Li_{6.4}M_{0.2}La_3Zr_2O_{12}$ with M = Al, Ga, or Fe, to be published.
(50) Fukushima, E.; Roeder, S. *Experimental Pulse NMR*; Addison-Wesley: Reading, MA, 1981.
(51) Heitjans, P.; Schirmer, A.; Indris, S. In *Diffusion in Condensed Matter: Methods, Materials Models*, 2nd ed.; Heitjans, P., Kärger, J., Eds.; Springer, Berlin, 2005; Chapter 9, pp 369−415.
(52) Ailion, D.; Slichter, C. P. Study of Ultraslow Atomic Motions by Magnetic Resonance. *Phys. Rev. Lett.* **1964**, *12*, 168−171.
(53) Ailion, D. C.; Slichter, C. P. Observation of Ultra-Slow Translational Diffusion in Metallic Lithium by Magnetic Resonance. *Phys. Rev.* **1965**, *137*, A235−A245.
(54) Slichter, C. P.; Ailion, D. Low-Field Relaxation and the Study of Ultraslow Atomic Motions by Magnetic Resonance. *Phys. Rev.* **1964**, *135*, A1099−A1110.
(55) Epp, V.; Gün, O.; Deiseroth, H.-J.; Wilkening, M. Long-Range Li Dynamics in the Lithium Argyrodite Li_7PSe_6 as Probed by Rotating-Frame Spin-Lattice Relaxation NMR. *Phys. Chem. Chem. Phys.* **2013**, *15*, 7123−7132.
(56) Stanje, B.; Epp, V.; Nakhal, S.; Lerch, M.; Wilkening, M. Li Ion Dynamics along the Inner Surfaces of Layer-Structured 2H-Li_xNbS_2. *ACS Appl. Mater. Interfaces* **2015**, *7*, 4089−4099.
(57) Dunst, A.; Epp, V.; Hanzu, I.; Freunberger, S. A.; Wilkening, M. Short-Range Li Diffusion vs. Long-Range Ionic Conduction in

DOI: 10.1021/acs.chemmater.5b02231
Chem. Mater. 2015, 27, 6571−6582

Nanocrystalline Lithium Peroxide Li_2O_2 - the Discharge Product in Lithium-Air Batteries. *Energy Environ. Sci.* **2014**, *7*, 2739−2752.
(58) Langer, J.; Epp, V.; Heitjans, P.; Mautner, F. A.; Wilkening, M. Li Motion in the Anode Material LiC_6 as Seen via Time-domain ^{7}Li NMR. *Phys. Rev. B: Condens. Matter Mater. Phys.* **2013**, *88*, 094304.
(59) Jeener, J.; Broekaert, P. Nuclear Magnetic Resonance in Solids: Thermodynamic Effects of a Pair of rf Pulses. *Phys. Rev.* **1967**, *157*, 232−240.
(60) Abragam, A. *The Principles of Nuclear Magnetism*; Clarendon: Oxford, 1961.
(61) Wilkening, M.; Epp, V.; Feldhoff, A.; Heitjans, P. Tuning the Li Diffusivity of Poor Ionic Conductors by Mechanical Treatment: High Li Conductivity of Strongly Defective $LiTaO_3$ Nanoparticles. *J. Phys. Chem. C* **2008**, *112*, 9291−9300.
(62) Küchler, W.; Heitjans, P.; Payer, A.; Schöllhorn, R. ^{7}Li NMR Relaxation by Diffusion in Hexagonal and Cubic Li_xTiS_2. *Solid State Ionics* **1994**, *70/71*, 434−438.
(63) Wilkening, M.; Heitjans, P. Li Jump Process in *h*-$Li_{0.7}TiS_2$ Studied by Two-Time ^{7}Li Spin-Alignment Echo NMR and Comparison with Results on Two-Dimensional Diffusion from Nuclear Magnetic Relaxation. *Phys. Rev. B: Condens. Matter Mater. Phys.* **2008**, *77*, 024311.
(64) Bunde, A.; Dieterich, W.; Maass, P.; Meyer, M. In *Diffusion in Condensed Matter: Methods, Materials, Models*, 2nd ed.; Heitjans, P., Kärger, J., Eds.; Springer, Berlin, 2005; Chapter 20, pp 813−856.
(65) Funke, K. Jump Relaxation in Solid Electrolytes. *Prog. Solid State Chem.* **1993**, *22*, 111−195.
(66) Meyer, M.; Maass, P.; Bunde, A. Spin Lattice Relaxation: Non-BPP-Behavior by Structural Disorder and Coulomb Interactions. *Phys. Rev. Lett.* **1993**, *71*, 573−576.
(67) Tse, D.; Hartmann, S. R. Nuclear Spin-Lattice Relaxation via Paramagnetic Centers without Spin Diffusion. *Phys. Rev. Lett.* **1968**, *21*, 511−514.
(68) Ruprecht, B.; Billetter, H.; Ruschewitz, U.; Wilkening, M. Ultra-Slow Li Ion Dynamics in Li_2C_2 - On the Similarities of Results from ^{7}Li Spin-Alignment Echo NMR and Impedance Spectroscopy. *J. Phys.: Condens. Matter* **2010**, *22*, 245901.
(69) Ruprecht, B.; Wilkening, M.; Uecker, R.; Heitjans, P. Extremely Slow Li Ion Dynamics in Monoclinic Li_2TiO_3 - Probing Macroscopic Jump Diffusion via ^{7}Li NMR Stimulated Echoes. *Phys. Chem. Chem. Phys.* **2012**, *14*, 11974−11980.
(70) Xu, M.; Park, M. S.; Lee, J. M.; Kim, T. Y.; Park, Y. S.; Ma, E. Mechanisms of Li^+ Transport in Garnet-Type Cubic $Li_{3+x}La_3M_2O_{12}$ (M = Te, Nb, Zr). *Phys. Rev. B: Condens. Matter Mater. Phys.* **2012**, *85*, 052301.
(71) Awaka, J.; Takashima, A.; Kataoka, K.; Kijima, N.; Idemoto, Y.; Akimoto, J. ystal Structure of Fast Lithium-ion-conducting Cubic $Li_7La_3Zr_2O_{12}$. *Chem. Lett.* **2011**, *40*, 60−62.
(72) Cussen, E. J. The structure of lithium garnets: cation disorder and clustering in a new family of fast Li^+ conductors. *Chem. Commun.* **2006**, 412−413.
(73) Li, Y.; Han, J.-T.; Wang, C.-A.; Vogel, S. C.; Xie, H.; Xu, M.; Goodenough, J. B. Ionic Distribution and Conductivity in Lithium Garnet $Li_7La_3Zr_2O_{12}$. *J. Power Sources* **2012**, *209*, 278−281.
(74) Adams, S.; Rao, R. P. Ion Transport and Phase Transition in $Li_{7-x}La_3(Zr_{2-x}M_x)O_{12}$ (M = Ta^{5+}, Nb^{5+}, x = 0, 0.25. *J. Mater. Chem.* **2012**, *22*, 1426−1434.
(75) Rao, R. P.; Gu, W.; Sharma, N.; Peterson, V. K.; Avdeev, M.; Adams, S. In Situ Neutron Diffraction Monitoring of $Li_7La_3Zr_2O_{12}$ Formation: Toward a Rational Synthesis of Garnet Solid Electrolytes. *Chem. Mater.* **2015**, *27*, 2903−2910.
(76) Wang, Y.; Klenk, M.; Page, K.; Lai, W. Local Structure and Dynamics of Lithium Garnet Ionic Conductors: A Model Material $Li_5La_3Ta_2O_{12}$. *Chem. Mater.* **2014**, *26*, 5613−5624.
(77) Jalem, R.; Yamamoto, Y.; Shiiba, H.; Nakayama, M.; Munakata, H.; Kasuga, T.; Kanamura, K. Concerted Migration Mechanism in the Li Ion Dynamics of Garnet-Type $Li_7La_3Zr_2O_{12}$. *Chem. Mater.* **2013**, *25*, 425−430.
(78) Miara, L. J.; Ong, S. P.; Mo, Y.; Richards, W. D.; Park, Y.; Lee, J.-M.; Lee, H. S.; Ceder, G. Effect of Rb and Ta Doping on the Ionic Conductivity and Stability of the Garnet $Li_{7+2x-y}(La_{3-x}Rb_x)(Zr_{2-y}Ta_y)O_{12}$ ($0 \leqslant x \leqslant 0.375$. $0 \leqslant y \leqslant 1$) Superionic Conductor: A First Principles Investigation. *Chem. Mater.* **2013**, *25*, 3048−3055.
(79) van Wüllen, L.; Echelmeyer, T.; Meyer, H.-W.; Wilmer, D. The Mechanism of Li-Ion Transport in the Garnet $Li_5La_3Nb_2O_{12}$. *Phys. Chem. Chem. Phys.* **2007**, *9*, 3298−3303.
(80) Meier, K.; Laino, T.; Curioni, A. Solid-State Electrolytes: Revealing the Mechanisms of Li-Ion Conduction in Tetragonal and Cubic LLZO by First-Principles Calculations. *J. Phys. Chem. C* **2014**, *118*, 6668−6679.

DOI: 10.1021/acs.chemmater.5b02231
Chem. Mater. 2015, 27, 6571−6582

7.5 Zusammenfassung: LLZO-basierte Festelektrolyte

Das relativ leicht herzustellende LLZO in seiner kubischen Phase mittels statischer und MAS-NMR-Messungen an den Kernen ^{7}Li, ^{27}Al und ^{71}Ga untersucht; dabei sind mögliche kristallographische Besetzungsverhältnisse im Detail studiert worden, die Aufschluss über Li-Wanderungspfade in der Granatstruktur geben.

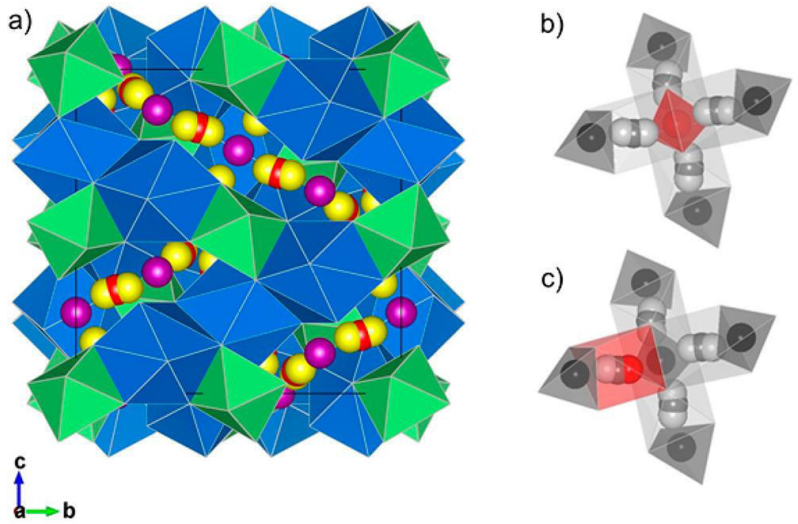

Abbildung 29: (a) Kristallographische Struktur von kubischem LLZO, Li besetzt 3 mögliche Stellen (24d, purpur; 48g, rot und 9h, gelb) (b+c) zeigt die möglichen Plätze, die z.B. für Dotierelemente zur Verfügung stehen; (b) 24d und (c) 96h

In Abbildung 29 sind mögliche Li-Migrationspfade für Li dargestellt und in (b) und (c) die kristallographischen Positionen gezeigt, die dotierte Elemente einnehmen können. Die ^{27}Al-MAS-NMR-Linien zeigten zwei Resonanzen bei 66 und 81 ppm, die den Positionen 24d und 96h zugeordnet werden konnten. Bei Variation des Al-Gehaltes war bei beiden Linien keine klare Präferenz hinsichtlich der Besetzung zu sehen. Zusammen mit den ^{71}Ga-MAS-NMR-Messungen ist das Signal bei höheren ppm-Werten dem 96h-Platz und das Signal bei kleineren ppm-Werten dem Platz 24d zugeordnet worden. Die Messdaten deuten darauf hin, dass Ga bevorzugt die 94h Position besetzt und erst bei höheren Konzentrationen 24d. Wenn man sich die Li-Diffusivität im Vergleich zur Dotierungskonzentration ansieht, fällt auf, dass die ^{7}Li-Linienbreiten mit dem Al-Gehalt zunehmen: Al-Gehalt und Li-Diffusivität korrelieren miteinander. Unter der Annahme, dass es keine Platzpräferenz der Al- und Ga-Kationen gibt, zeigt der NMR-Linienbreitentrend, dass die Zunahme der Li-Transportparameter höchstwahrscheinlich auf eine Zunahme der Gitterkonstanten als auf den (z.T. als blockierend angenommenen) Einfluss von Ga oder Al zurückzuführen ist.

8 Resümee und Ausblick

Ziel dieser Dissertation war es, mittels unterschiedlicher NMR-Methoden das Anodenmaterial $Li_4Ti_5O_{12}$ genauer hinsichtlich seiner Li-Diffusivität zu untersuchen und die Zwischenprodukte der entladenen und geladenen Anode genauer zu charakterisieren. Die publizierten und noch unveröffentlichten Arbeiten enthüllen ein komplexes Bild der Lithiierung und Li-Diffusivität in LTO, das entscheidende Impulse für die angewandte Batterieforschung beinhaltet. In weitergehenden Studien sollten impedanzspektroskopische Messungen einfließen, die sowohl an den mikro- als auch an den nanostrukturierten Proben Aufschluss über langreichweitige Li-Transportparameter geben könnten.

Die NMR-Untersuchungen an granatartigen Festkörperelektrolyten offenbaren ebenfalls eine komplexe von der Dotierung beeinflussbare Li-Dynamik, die mit den komplementären NMR-Methoden auf unterschiedlichen Längenskalen gut erfasst werden konnte. Insbesondere in Dünnschichtbatterien[69,70] könnten Granate eine wichtige Rolle als Festelektrolyt spielen. Nachdem es bereits Veröffentlichungen zu einer Festkörperbatterie mit LTO und einem sulfidischen Festkörperelektrolyten gab[71], wäre es sicherlich sehr interessant ein Aufeinandertreffen von LTO und LLZO in einem solchen System näher zu charakterisieren und vor allem elektrochemische Stabilitäten und Grenzflächenprozesse zu beschreiben.

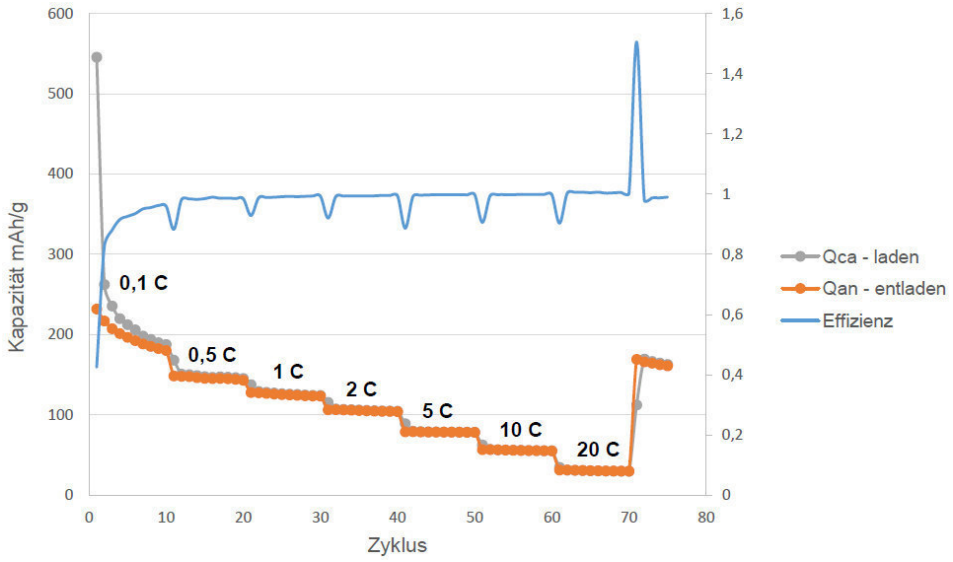

Abbildung 30: Kapazitätsverlauf von nanostrukturiertem LTO (EXM 1037), Gegenelektrode war Na-Metall, die aktive Masse betrug 80%, als Elektrolyt wurde 1M $NaClO_4$ in PC verwendet

Neben Li als neben Wasserstoff kleinstem Ladungsträger ist in letzter Zeit das Thema Natriumbatterien in den Fokus der Forschung gerückt. Auch hier bietet sich LTO vorzüglich als Anodenmaterial an.[72,73,74] Im Zuge eine Bachelorarbeit konnten wir in der Arbeitsgruppe bereits erste Resultate erzielen, wie Abbildung 30 zeigt. Man sieht, dass LTO bei der Interkalation vergleichbare Kapazitäten bei dieser Probe erreichen kann. Es wäre sehr interessant, an $Li_4Na_xTi_5O_{12}$ für $x = 0$ bis $x = 3$ statische und Li-MAS-NMR Messungen durchzuführen, um sowohl die Li- als auch in Na-Diffusivität im Material getrennt voneinander zu untersuchen und den Lithiierungsmechanismus zu erfassen.

LTO kann zukünftig vor allem für stationäre Anwendungen[75] oder auch für Festkörperdünnschichtbatterien eine wichtige Rolle als Aktivmaterial spielen. Es ist auch zu erwarten, dass es sich im Bereich der Na-Ionenbatterien einen festen Platz als Anodenmaterial sichern wird.

A. Anhang

A.1 Geräte für die NMR-Messungen

Für alle NMR-Experimente, die an der TU Graz durchgeführt wurden, wurden Bruker Avance III Festkörper-NMR-Spektrometer eingesetzt: ein WB 300 mit einem 7 T Magneten (Lamorfrequenz für ^{7}Li 116 MHz) und ein WB 500 mit einem 11 T Magneten (Lamorfrequenz für ^{7}Li 194 MHz). Der verfügbare Teflonprobenkopf für das WB 500 ist für maximale Temperaturen von 450 K ausgelegt. Ein weiterer Keramikprobenkopf ermöglichte Experimente bis zu einer Temperatur von bis zu 600 K. Die Temperaturkontrolle erfolgte an beiden Spektrometern über ein Typ-T-Thermoelement, das mit einem Temperaturregler und somit mit der Steuerungssoftware verbunden ist.

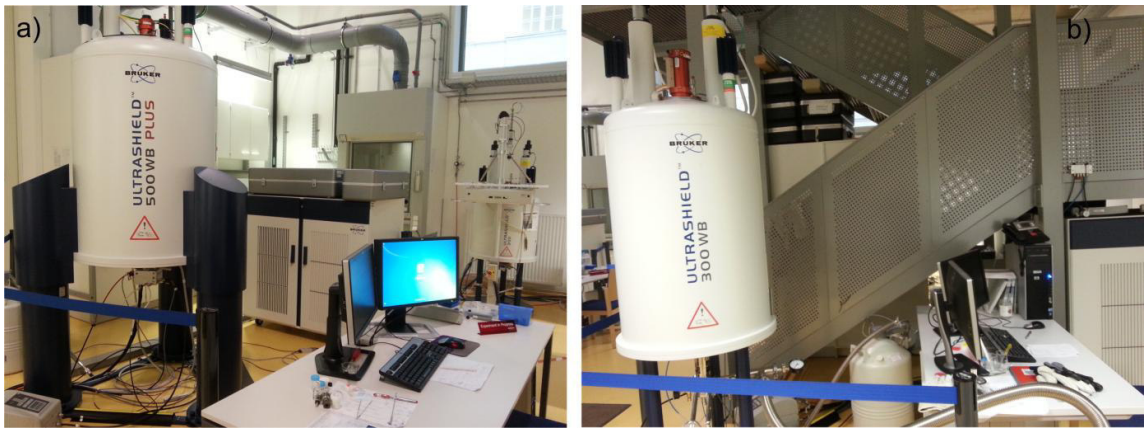

Abbildung 31: Festkörper-NMR-Spektrometer an der TU Graz; a) Bruker 500 WB; b) Bruker 300 WB

A.2 Geräte zur Homogenisierung / Nanostrukturierung

Abbildung 32: a) Pulverisette premium line (zum Nanostrukturieren); b) Pulverisette classic line (zum Homogenisieren von *slurries*)

Um Materialien mechanisch zu zerkleinern, wurde eine Fritsch *Pulverisette 7 Premium line* mit einem verschließbaren 45 ml Probenbecher aus ZrO_2 (mit 180 Kugeln, 5 mm Durchmesser) aus demselben Material verwendet (siehe Abbildung 33). Zum Homogenisieren der *slurries* ist eine Fritsch Pulverisette Classic Line eingesetzt worden, die mit Einwegbechern aus PP und 3 Kugeln aus ZrO_2 ausgestatte war (siehe Abbildung 34).

Abbildung 33: a) Mahlbecher aus ZrO_2; b) offener Mahlbecher gefüllt mit 180 Kugeln (∅: 5mm)

Abbildung 34: a) Einmalbecher verschlossen; b) Einmalbecher gefüllt mit 3 Kugeln (∅: 3cm ; ZrO_2)

A.3 Rakelautomat

Abbildung 35: Erichsen Multicator 411 zum Aufbringen der Elektrodenslurries

Um *slurries* mit einer definierten Schichtdicke aufzutragen, kann der Rakelaufsatzes des Erichsen Multicators 411 justiert werden (siehe Abbildung 35). Anschließend wurde mit einer Vorschubgeschwindigkeit von 100 mm s^{-1} der *slurry* durch den Spalt auf die Folie aufgerakelt.

A.4 Gloveboxen

Abbildung 36: Gloveboxen der TU Graz, gefüllt mit Argon; Toleranzen O_2 und H_20 < 1 ppm; a) Mbraun Model 150B-G; b) Mbraun Model Labmaster Pro SP

Arbeiten mit luft- oder feuchtigkeitsempfindlichen Materialien oder Substanzen wurden in einer der beiden Gloveboxen der TU Graz durchgeführt.

A.5 Software

Folgende Software wurde im Laufe dieser Dissertation verwendet:

Topspin 3.1 (Bruker Biospin GmbH): Diese Auswertesoftware der Bruker Spektrometer WB 300 und WB 500 diente zur Fouriertransformation der gemessenen Daten und zur Phasenkorrektur.

IGOR Pro 6.37: Diese mathematische Software wurde verwendet, um alle erhaltenen Daten zu bearbeiten und auszuwerten.

Diamond 3.2 und Vesta: Programme zur Darstellung von Kristallstrukturen

DMFIT: Programm zum Umwandeln von Rohdaten beispielsweise aus TopSpin 3.1 in ASCII-Dateien

CorelDRAW X7: Grafikprogramm zum Bearbeiten von Bildern, Grafiken und Abbildungen

Mircosoft Word 2010: Textprogramm zum Verfassen von Texten

A.6 NMR-Pulsfolgen

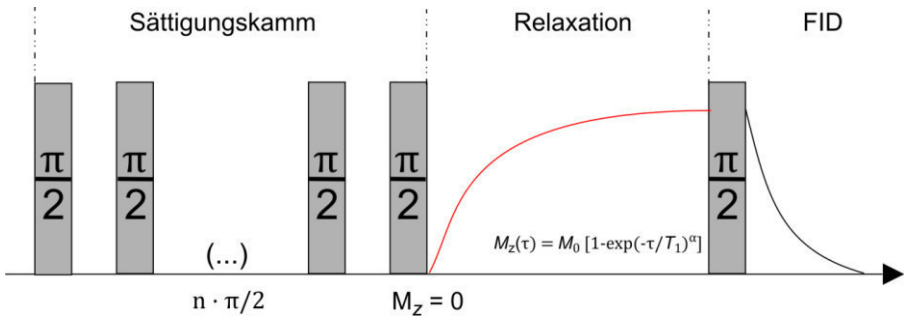

Abbildung 37 : Schema einer T_1 Messung mit Sättigungspulsfolge

Sättigungspulsfolge:

Sättigungspulsfolgen können bei der Messung der NMR-Spin-Gitter-Relaxationszeiten im Laborkoordinatensystem T_1 sicherstellen, dass die Magnetisierung zerstört wurde. Anfangs wird, wie in Abbildung 37 gezeigt, eine Reihe von Zerstörungspulsen in unterschiedlichen *x,y,z*-Richtungen eingestrahlt, um die Magnetisierung zu zerstören. Anschließend nach der Wartezeit T_1 ist die Magnetisierung vollständig wiederhergestellt und die Messung der Magnetsierungsamplitude kann mittels $\pi/2$-Puls durchgeführt werden.

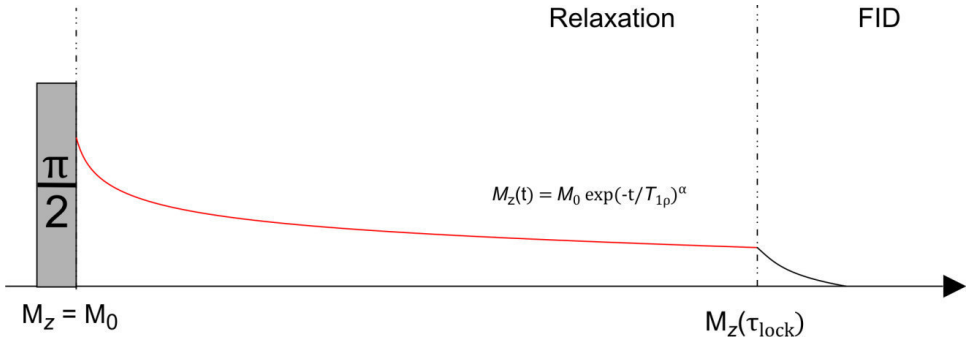

Abbildung 38: Schematische Darstellung des Spin - Lock Pulses

Die Spin-Lockpulsfolge diente zur Messung der Spin-Gitter-Relaxationszeit $T_{1\rho}$ im rotierenden Koordinatensystem[76,77,78,79] wie Abbildung 38 zeigt. Der erste $\pi/2$-Puls kippt die transversale Magnetisierung in die (*x,y*)-Ebene und für eine variable Zeit wird dieser Spin-*lock* aufrechterhalten. Während dieser Zeit nimmt die Magnetisierung innerhalb der Ebene ab und kann nach einer Wartezeit durch einen erneuten $\pi/2$-Puls ausgelesen, detektiert werden.

B. Konferenzbeiträge und Publikationen

B.1 Posterbeiträge

Schmidt, W.; Bottke, P.; Hennige, V.; Gollob, P.; Hanzu, I.; Wilkening, M.

Small change — great effect: Steep increase of Li ion dynamics in $Li_4Ti_5O_{12}$ at the early stages of chemical Li insertion ($x = 0.1$, $x = 0.3$), ECSSC, Wien (2015)

Schmidt, W.; Bottke, P.; Gollob, P.; Hennige, V.; Hanzu, I.; Wilkening, M.

Small change — great effect: Steep increase of Li ion dynamics in $Li_4Ti_5O_{12}$ at the early stages of chemical Li insertion ($x = 0.1$, $x = 0.3$), 12th Conference on Material Chemistry, York (2015)

Rettenwander, D.; Schmidt, W.; Langer, J.; Arrer, C.; Wilkening, M.; Amthauer, G.

The Site Preference of Al and Ga in Mixed Doped Li $_{7-3(x+y)}Ga_xAl_yLa_3Zr_2O_{12}$ Garnet Solid Solutions with x, y {0.1, 0.2, …, 0.8 ; $x + y \leq 0.8$} and its Influence on Li-Ion Mobility, Bunsen Colloquium, Hannover (2014)

Schmidt, W.

In Situ Impedance Study of the Long-time Cycling Behaviour of $Li_4Ti_5O_{12}$ Anodes in Li - Ion Batteries, 15. Österreichischen Chemietage, Graz (2012)

B.2 Vorträge

Schmidt, W.; Bottke, P.; Hennige, V.; Gollob, P.; Hanzu, I.; Wilkening, M.

Small change — great effect: Steep increase of Li ion dynamics in $Li_4Ti_5O_{12}$ at the early stages of chemical Li insertion, DocDays, Graz (2015)

Schmidt, W.; Bottke, P.; Hennige, V.; Gollob, P.; Hanzu, I.; Wilkening, M.

Small change — great effect: Steep increase of Li ion dynamics in $Li_4Ti_5O_{12}$ at the early stages of chemical Li insertion ($x = 0.1$, $x = 0.3$), Materials Day, Graz (2015)

Schmidt, W.; Bottke, P.; Volker, H.; Gollob, P.; Hanzu, I.; Wilkening, M.

Steep increase of Li diffusivity in the anode material $Li_{4+x}Ti_5O_{12}$ at low amounts of Li Insertion ($x = 0.1$, $x = 0.3$), DIMAT 2014, Münster (2014)

Schmidt, W.; Bottke, P.; Uitz, M.; Hanzu, I.; Freunberger, S.; Wilkening, M.

New *vs* Old — Li insertion in the anode material $Li_{4+x}Ti_5O_{12}$ probing the change of Li diffusivity via ex situ NMR relaxometry, Evaluation of the Christian Doppler Laboratory for Li-Ion Batteries, Graz (2014)

B.3 Publikationen

Steps of Li^+ Hopping in the Garnet $Li_{6.5}La_3Zr_{1.75}Mo_{0.25}O_{12}$

Bottke P., Rettenwander D., Schmidt W., Amthauer G., Wilkening M., Chemistry of materials 27 (2015), S. 6571 − 6582

Rettenwander, D.; Langer, J.; Schmidt, W.; Arrer, C.; Harris, K.; Terskikh, V.; Goward, G.; Wilkening, M.; Amthauer, G.

Site occupation of Ga and Al in stabilized cubic Li $_{7-3(x+y)}Ga_xAl_yLa_3Zr_2O_{12}$ garnets as deduced from ^{27}Al and ^{71}Ga MAS NMR at ultrahigh magnetic fields, Chemistry of materials 27 (2015) 8, S. 3135 - 3142

Schmidt, W.; Bottke, P.; Sternad, M.; Gollob, P.; Hennige, V.; Wilkening, M.

Small Change—Great Effect: Steep Increase of Li Ion Dynamics in $Li_4Ti_5O_{12}$ at the Early Stages of Chemical Li Insertion, Chemistry of materials 27(5) (2015), S. 1740 - 1750

B.4 Eingereichte Manuskripte

Discriminating the Mobile Ions from the Immobile Ones in $Li_{4+x}Ti_5O_{12}$: ^6Li NMR Reveals the Li^+ Diffusion Pathway and Proposes a Refined Lithiation Mechanism

Schmidt W., Wilkening M. (eingereicht)

Diffusion-induced ^7Li NMR spin-lattice relaxation of non-lithiated $Li_4Ti_5O_{12}$ and fully lithiated, mixed-conducting $Li_7Ti_5O_{12}$ battery materials

Schmidt W., Wilkening M. (eingereicht bei *Solid State Ionics*)

Literaturverzeichnis

1. König, W. Ein galvanisches Element aus der Partherzeit? *Forschungen und Fortschritte* **14,** 8–9 (1938).

2. Armand, M. & Tarascon, J.-M. Building better batteries. *Nature* **451,** 652–657 (2008).

3. Dell, R. M. Batteries - fifty years of materials development. *Solid State Ionics* **134,** 139–158 (2000).

4. Besenhard, J. 0. *Handbook of Battery Materials*. (1999).

5. Nishi, Y. The development of lithium ion secondary batteries. *Chem. Rec.* **1,** 406–413 (2001).

6. Goodenough, J. B. & Kim, Y. Challenges for Rechargeable Li Batteries †. *Chem. Mater.* **22,** 587–603 (2010).

7. Hayes, J. G., Oliveira, R. P. R. De, Vaughan, S. & Egan, M. G. Simplified electric vehicle power train models and range estimation. *2011 IEEE Veh. Power Propuls. Conf.* 1–5 (2011).

8. Dunn, B., Kamath, H. & Tarascon, J.-M. Electrical Energy Storage for the Grid: A Battery of Choices. *Science* **334,** 928–935 (2011).

9. Tarascon, J. M. & Armand, M. Issues and challenges facing rechargeable lithium batteries. *Nature* **414,** 359–367 (2001).

10. Thackeray, M. M. Spinel Electrodes for Lithium Batteries . *J. Am. Ceram. Soc* **82,** 3347–3354 (1999).

11. Murugan, R., Thangadurai, V. & Weppner, W. Schnelle Lithiumionenleitung in granatartigem Li7La3Zr2O12. *Angew. Chemie* **119,** 7925–7928 (2007).

12. Kuhn, A. *et al.* NMR relaxometry as a versatile tool to study Li ion dynamics in potential battery materials. *Solid State Nucl. Magn. Reson.* **42,** 2–8 (2012).

13. Winter, M. & Besenhard, J. O. Wiederaufladbare Batterien. *Chemie unserer Zeit* **33,** 252–266 (1999).

14. Winter, M. & Brodd, R. J. What are batteries, fuel cells, and supercapacitors? *Chem. Rev.* **104,** 4245–4269 (2004).

15. Linden, D. *Handbook Of Batteries*. (2002).

16. Yoshio, M., Brodd, R. J. & Kozawa, A. *Lithium-Ion Batteries*. *Science and Technologies* (2009).

17. Winter, M., Besenhard, J., Spahr, M. E. & Novák, P. Insertion electrode materials for rechargeable lithium batteries. *Adv. Mater.* **10,** 725–763 (1998).

18. Whittingham, M. S. Lithium batteries and cathode materials. *Chem. Rev.* **104,** 4271–4301 (2004).

19. Hill, R. J., Craig, J. R. & Gibbs, G. V. PHYSICS I] CHEMISTRY MIHERALS Systematics of the Spinel Structure Type. *Phys. Chem. Miner.* **4,** 317–339 (1979).

20. Kataoka, K. *et al.* A single-crystal study of the electrochemically Li-ion intercalated spinel-type Li4Ti5O12. *Solid State Ionics* **180,** 631–635 (2009).

21. Aldon, L. *et al.* Chemical and Electrochemical Li-Insertion into the Li 4 Ti 5 O 12 Spinel. 5721–5725 (2004).

22. Leonidov, I. a *et al.* Structure , Ionic Conduction , and Phase Transformations in Lithium Titanate Li 4 Ti 5 O 12. *Phys. Solid State* **45,** 2183–2188 (2003).

23. Wagemaker, M. *et al.* A Kinetic Two-Phase and Equilibrium Solid Solution in Spinel Li4+xTi5O12 - ResearchGate.pdf. *Adv. Mater.* **18,** 3169–3173 (2006).

24. Colin, J.-F., Godbole, V. & Novák, P. In situ neutron diffraction study of Li insertion in Li4Ti5O12. *Electrochem. commun.* **12,** 804–807 (2010).

25. Wilkening, M. *et al.* Microscopic Li self-diffusion parameters in the lithiated anode material Li4+xTi5O12 ($0 \leq x \leq 3$) measured by 7Li solid state NMR. *Phys. Chem. Chem. Phys.* **9,** 6199 (2007).

26. Peled, E. the Electrochemical-Behavior of Alkali and Alkaline-Earth Metals in Non-Aqueous Battery Systems - the Solid Electrolyte Interphase Model. *J. Electrochem. Soc.* **126,** 2047–2051 (1979).

27. Peled, E. Film forming interface. *J. Power Sources* **9,** 253 – 266 (1983).

28. Lin, C., Tang, A., Mu, H., Wang, W. & Wang, C. Aging Mechanisms of Electrode Materials in Lithium-Ion Batteries for Electric Vehicles. **2015,** (2015).

29. Vetter, J. *et al.* Ageing mechanisms in lithium-ion batteries. *J. Power Sources* **147,** 269–281 (2005).

30. Winter, M., Moeller, K.-C. & Besenhard, J. O. in *Lithium Batteries - Science and Technology* 145–194 (2003).

31. Ferg, E., Gummow, R. J. & Kock, A. De. Spinel Anodes for Lithium-Ion Batteries. *J. Electrochem. Soc.* **141,** 10–13 (1994).

32. Ding, Z. *et al.* Towards understanding the effects of carbon and nitrogen-doped carbon coating on the electrochemical performance of Li4Ti5O12 in lithium ion batteries: a combined experimental and theoretical study. *Phys. Chem. Chem. Phys.* **13,** 15127 (2011).

33. Hain, H. *et al.* Study of local structure and Li dynamics in Li(4+x)Ti(5)O(12) ($0 \leq x \leq 5$) using (6)Li and (7)Li NMR spectroscopy. *Solid State Nucl. Magn. Reson.* **42,** 9–16 (2012).

34. Broussely, M. *et al.* Aging mechanism in Li ion cells and calendar life predictions. *J. Power Sources* **97-98,** 13–21 (2001).

35. Jeong, G., Kim, Y.-U., Kim, H., Kim, Y.-J. & Sohn, H.-J. Prospective materials and applications for Li secondary batteries. *Energy Environ. Sci.* **4,** 1986 (2011).

36. Takada, K. Progress and prospective of solid-state lithium batteries. *Acta Mater.* **61,** 759–770 (2013).

37. Li, J., Ma, C., Chi, M., Liang, C. & Dudney, N. J. Solid Electrolyte: the Key for High-Voltage Lithium Batteries. *Adv. Energy Mater.* **5,** 1401408 (2015).

38. Knauth, P. Inorganic solid Li ion conductors: An overview. *Solid State Ionics* **180,** 911–916 (2009).

39. Cao, C., Li, Z.-B., Wang, X.-L., Zhao, X.-B. & Han, W.-Q. Recent Advances in Inorganic Solid Electrolytes for Lithium Batteries. *Front. Energy Res.* **2,** 1–10 (2014).

40. Bates, J. B. *et al.* Fabrication and characterization of amorphous lithium electrolyte thin films and rechargeable thin-film batteries. *J. Power Sources* **43,** 103–110 (1993).

41. Whitacre, J. F., West, W. C., Brandon, E. & Ratnakumar, B. V. Crystallographically Oriented Thin-Film Nanocrystalline Cathode Layers Prepared Without Exceeding 300°C. *J. Electrochem. Soc.* **148,** A1078 (2001).

42. Schwenzel, J., Thangadurai, V. & Weppner, W. Developments of high-voltage all-solid-state thin-film lithium ion batteries. *J. Power Sources* **154,** 232–238 (2006).

43. Jung, Y. S., Oh, D. Y., Nam, Y. J. & Park, K. H. Issues and Challenges for Bulk-Type All-Solid-State Rechargeable Lithium Batteries using Sulfide Solid Electrolytes. *Isr. J. Chem.* **55,** 472–485 (2015).

44. Awaka, J., Kijima, N., Hayakawa, H. & Akimoto, J. Synthesis and structure analysis of tetragonal Li7La3Zr2O12 with the garnet-related type structure. *J. Solid State Chem.* **182,** 2046–2052 (2009).

45. Kraytsberg, A. & Ein-Eli, Y. Higher, Stronger, Better… A Review of 5 Volt Cathode Materials for Advanced Lithium-Ion Batteries. *Adv. Energy Mater.* **2,** 922–939 (2012).

46. Awaka, J. *et al.* Crystal Structure of Fast Lithium-ion-conducting Cubic Li7La3Zr2O12. *Chem. Lett.* **40,** 60–62 (2011).

47. Meier, K., Laino, T. & Curioni, A. Solid-state electrolytes: Revealing the mechanisms of Li-Ion conduction in tetragonal and cubic LLZO by first-principles calculations. *J. Phys. Chem. C* **118,** 6668–6679 (2014).

48. Geiger, C. A. *et al.* Crystal Chemistry and Stability of '$Li_7La_3Zr_2O_{12}$' Garnet: A Fast Lithium-Ion Conductor. *Inorg. Chem.* **50,** 1089–1097 (2011).

49. Kuhn, A. *et al.* Li self-diffusion in garnet-type Li7La3Zr2O12 as probed directly by diffusion-induced 7Li spin-lattice relaxation NMR spectroscopy. *Phys. Rev. B* **83,** 094302 (2011).

50. Bloembergen, N., Purcell, E. M. & Pound, R. V. Relaxation Effects in Nuclear Magnetic Resonance Absorption. *Phys. Rev.* **73,** 679–712 (1948).

51. Einstein, A. Über die von der molekularkinetischen Theorie der Wärme geforderte Bewegung von in ruhenden Flüssigkeiten suspendierten Teilchen. *Ann. Phys.* **322,** 549–560 (1905).

52. Herzig, C. & Mishin, Y. *Diffusion in Condensed Matter. Diffusion in Condensed Matter: Methods, Materials, Models* (Springer - Verlag, 2005).

53. Indris, S. & Heitjans, P. Li Ion Dynamics in a LiAlO2 Single Crystal Studied by 7Li NMR Spectroscopy and Conductivity Measurements. *J. Phys. …* 7–11 (2012).

54. Duer, M. J. *Solid-State NMR Spectroscopy*. *Analysis* (2002).

55. Jeener, J. & Meier, B. Investigation of exchange processes by two-dimensional NMR spectroscopy. *J. Chem. …* **71,** 4546–4553 (2008).

56. E. Fukushima, S. B. W. R. *Experimental Pulse NMR: A Nuts and Bolts Approach*. (1981).

57. Mehring, M. *Principles of High Resolution NMR in Solids*. *Springer, Berlin* **212,** (Springer - Verlag, 1983).

58. Puddephat, M. *Principles of magnetic resonance imaging*. (Springer - Verlag, 2014).

59. Keeler, J. *Understanding NMR spectroscopy*. *8* (2004).

60. L.R. *The principles of nuclear magnetism*. *Nuclear Physics* **28,** (1961).

61. Wang, G. *et al.* Influence of high-energy ball milling of precursor on the morphology and electrochemical performance of Li4Ti5O12–ball-milling time. *Solid State Ionics* **179,** 946–950 (2008).

62. Shi, Y., Wen, L., Li, F. & Cheng, H.-M. Nanosized Li4Ti5O12/graphene hybrid materials with low polarization for high rate lithium ion batteries. *J. Power Sources* **196,** 8610–8617 (2011).

63. Wang, F. *et al.* Nitrogen-doped carbon decorated Li $_4$ Ti $_5$ O $_{12}$ composites as anode materials for high performance lithium-ion batteries. *RSC Adv.* **5,** 46359–46365 (2015).

64. Wagemaker, M., van Eck, E. R. H., Kentgens, A. P. M. & Mulder, F. M. Li-Ion Diffusion in the Equilibrium Nanomorphology of Spinel Li4+xTi5O12. *J. Phys. Chem. B* **113,** 224–230 (2009).

65. Kitta, M., Akita, T., Tanaka, S. & Kohyama, M. Two-phase separation in a lithiated spinel Li4Ti 5O12 crystal as confirmed by electron energy-loss spectroscopy. *J. Power Sources* **257,** 120–125 (2014).

66. Gao, Y., Wang, Z. & Chen, L. Stability of spinel Li4Ti5O12 in air. *J. Power Sources* **245,** 684–690 (2014).

67. Buschmann, H. *et al.* Structure and dynamics of the fast lithium ion conductor ‘Li7La3Zr2O12’. *Phys. Chem. Chem. Phys.* **13,** 19378 (2011).

68. Kuhn, A. *et al.* Li Ion Dynamics in Al-Doped Garnet-Type Li 7 La 3 Zr 2 O 12 Crystallizing with Cubic Symmetry. *Zeitschrift für Phys. Chemie* **226,** 525–537 (2012).

69. Tan, J. & Tiwari, a. Fabrication and Characterization of Li7La3Zr2O12 Thin Films for Lithium Ion Battery. *ECS Solid State Lett.* **1,** Q57–Q60 (2012).

70. Teng, S., Tan, J. & Tiwari, A. Recent developments in garnet based solid state electrolytes for thin film batteries. *Curr. Opin. Solid State Mater. Sci.* **18,** 29–38 (2014).

71. Kim, J. G. *et al.* A review of lithium and non-lithium based solid state batteries. *J. Power Sources* **282,** 299–322 (2015).

72. Yu, X. *et al.* A size-dependent sodium storage mechanism in Li4Ti 5O12 investigated by a novel characterization technique combining in situ X-ray diffraction and chemical sodiation. *Nano Lett.* **13,** 4721–4727 (2013).

73. Zhao, L., Pan, H.-L., Hu, Y.-S., Li, H. & Chen, L.-Q. Spinel lithium titanate (Li 4 Ti 5 O 12) as novel anode material for room-temperature sodium-ion battery. *Chinese Phys. B* **21,** 028201 (2012).

74. Sun, Y. *et al.* Direct atomic-scale confirmation of three-phase storage mechanism in Li4Ti5O12 anodes for room-temperature sodium-ion batteries. *Nat. Commun.* **4,** 1870 (2013).

75. Xu, T., Wang, W., Gordin, M. L., Wang, D. & Choi, D. Lithium-ion batteries for stationary energy storage. *Jom* **62,** 24–30 (2010).

76. Wilkening, M., Epp, V., Feldhoff, A. & Heitjans, P. Tuning the Li Diffusivity of Poor Ionic Conductors by Mechanical Treatment: High Li Conductivity of Strongly Defective LiTaO3 Nanoparticles. *J. Phys. Chem. C* **112,** 9291 (2008).

77. Heitjans, P., Masoud, M., Feldhoff, A. & Wilkening, M. NMR and impedance studies of nanocrystalline and amorphous ion conductors: lithium niobate as a model system. *Faraday Discuss.* **134,** 67–82; discussion 103–118, 415–419 (2007).

78. Heitjans, P., Tobschall, E. & Wilkening, M. Ion transport and diffusion in nanocrystalline and glassy ceramics. *Eur. Phys. J. Spec. Top.* **161,** 97–108 (2008).

79. Slichter, C. P. & Ailion, D. Low-Field Relaxation and the Study of Ultraslow Atomic Motions by Magnetic Resonance. *Phys. Rev.* **135,** A1099–A1110 (1964).